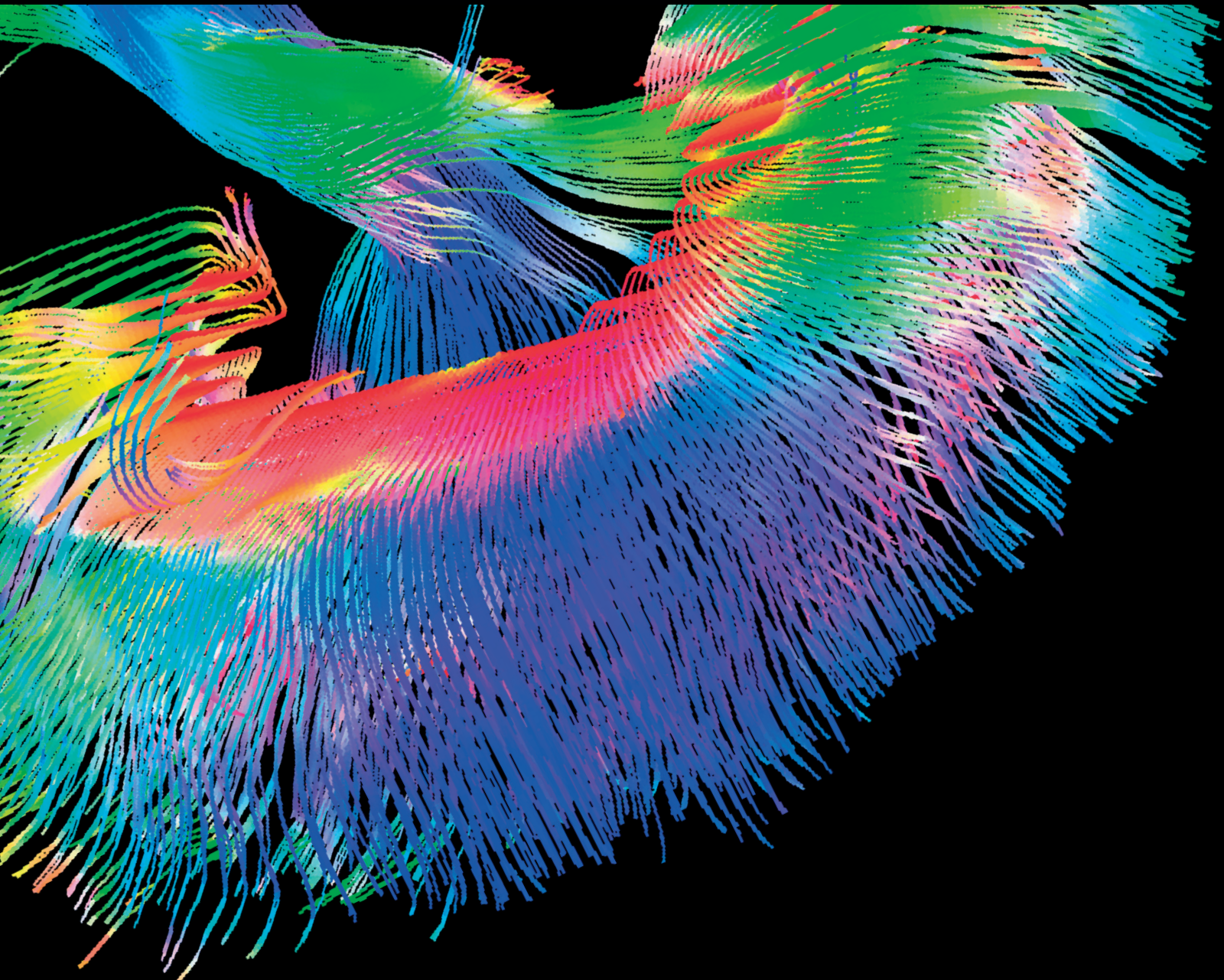


Contrast Media & Molecular Imaging

Development and Application of Nanoparticles in Biomedical Imaging

Lead Guest Editor: Fernando Herranz

Guest Editors: Maria P. Morales, Paulo H. Rosado-de-Castro,
Pedro M. Pimentel-Coelho, and Rosalia Mendez-Otero





Development and Application of Nanoparticles in Biomedical Imaging

Contrast Media & Molecular Imaging

Development and Application of Nanoparticles in Biomedical Imaging

Lead Guest Editor: Fernando Herranz

Guest Editors: Maria P. Morales, Pedro M. Pimentel-Coelho,
and Rosalia Mendez-Otero



Copyright © 2018 Hindawi. All rights reserved.

This is a special issue published in “Contrast Media & Molecular Imaging.” All articles are open access articles distributed under the Creative Commons Attribution License, which permits unrestricted use, distribution, and reproduction in any medium, provided the original work is properly cited.

Editorial Board

Peter Bannas, Germany

Giorgio Biasiotto, Italy

Dinesh K. Deelchand, USA

Françoise Kraeber-Bodéré, France

Kazuo Kubota, Japan

Gaurav Malviya, UK

Isabelle Miederer, Germany

Barbara Palumbo, Italy

Giancarlo Pascali, Australia

Maria Joao Ribeiro, France

Anne Roivainen, Finland

Pedro Rosa-Neto, Canada

Giuseppe Rubini, Italy

Barbara Salvatore, Italy

Ralf Schirmacher, Canada

Fijs W. B. Van Leeuwen, Netherlands

Luc Zimmer, France

Contents

Development and Application of Nanoparticles in Biomedical Imaging

Paulo H. Rosado-de-Castro , Maria del Puerto Morales, Pedro M. Pimentel-Coelho ,
Rosalia Mendez-Otero , and Fernando Herranz 

Volume 2018, Article ID 1403826, 2 pages

Neural Induction Potential and MRI of ADSCs Labeled Cationic Superparamagnetic Iron Oxide Nanoparticle In Vitro

Weiqiong Ma, Qi Xie , Baolin Zhang , Huixian Chen, Jianyi Tang, Zhengxian Lei, Minyi Wu,
Dingxuan Zhang, and Jiani Hu

Volume 2018, Article ID 6268437, 11 pages

Carboxyl of Poly(D,L-lactide-co-glycolide) Nanoparticles of Perfluorooctyl Bromide for Ultrasonic Imaging of Tumor

Shengjuan Luo , Jinsong Ding , Peiqi Wang , Zheng Wang, Xiaoqian Ma , Cejun Yang ,
Qi Liang, Pengfei Rong , and Wei Wang 

Volume 2018, Article ID 2957459, 10 pages

Gallium-68 Labeled Iron Oxide Nanoparticles Coated with 2,3-Dicarboxypropane-1,1-diphosphonic Acid as a Potential PET/MR Imaging Agent: A Proof-of-Concept Study

Maria-Argyro Karageorgou, Sanja Vranješ-Djurić, Magdalena Radović, Anna Lyberopoulou, Bratislav Antić,
Maritina Rouchota, Maria Gazouli, George Loudos, Stavros Xanthopoulos, Zili Sideratou,
Dimosthenis Stamopoulos, Penelope Bouziotis, and Charalampos Tsoukalas

Volume 2017, Article ID 6951240, 13 pages

Brain Tumor Diagnostics and Therapeutics with Superparamagnetic Ferrite Nanoparticles

Fahmeed Hyder and S. Manjura Hoque

Volume 2017, Article ID 6387217, 17 pages

Key Parameters on the Microwave Assisted Synthesis of Magnetic Nanoparticles for MRI Contrast Agents

Maria Eugênia Fortes Brollo, Sabino Veintemillas-Verdaguer, Cesar Menor Salván,
and Maria del Puerto Morales

Volume 2017, Article ID 8902424, 13 pages

Mapping Extracellular pH of Gliomas in Presence of Superparamagnetic Nanoparticles: Towards Imaging the Distribution of Drug-Containing Nanoparticles and Their Curative Effect on the Tumor Microenvironment

Samuel Maritim, Daniel Coman, Yuegao Huang, Jyotsna U. Rao, John J. Walsh, and Fahmeed Hyder

Volume 2017, Article ID 3849373, 15 pages

Iron Oxide Nanoradiomaterials: Combining Nanoscale Properties with Radioisotopes for Enhanced Molecular Imaging

Juan Pellico, Jordi Llop, Irene Fernández-Barahona, Riju Bhavesh,
Jesús Ruiz-Cabello, and Fernando Herranz

Volume 2017, Article ID 1549580, 24 pages



Erbium-Based Perfusion Contrast Agent for Small-Animal Microvessel Imaging

Justin J. Tse, P. Joy Dunmore-Buyze, Maria Drangova, and David W. Holdsworth

Volume 2017, Article ID 7368384, 10 pages

One-Pot Aqueous Synthesis of Fluorescent Ag-In-Zn-S Quantum Dot/Polymer Bioconjugates for Multiplex Optical Bioimaging of Glioblastoma Cells

Alexandra A. P. Mansur, Herman S. Mansur, Sandhra M. Carvalho, and Anderson J. Caires

Volume 2017, Article ID 3896107, 15 pages

Editorial

Development and Application of Nanoparticles in Biomedical Imaging

Paulo H. Rosado-de-Castro ^{1,2}, **María del Puerto Morales**,³ **Pedro M. Pimentel-Coelho** ⁴,
Rosalía Mendez-Otero ⁴, and **Fernando Herranz** ⁵

¹*Instituto de Ciências Biomédicas, Universidade Federal do Rio de Janeiro, Av. Carlos Chagas Filho 373, 21941-590 Rio de Janeiro, RJ, Brazil*

²*D'Or Institute for Research and Education, 22281-100 Rio de Janeiro, RJ, Brazil*

³*Departamento de Energía, Medioambiente y Salud, Instituto de Ciencia de Materiales de Madrid, CSIC, Sor Juana Inés de la Cruz 3, Cantoblanco, 28049 Madrid, Spain*

⁴*Instituto de Biofísica Carlos Chagas Filho, Universidade Federal do Rio de Janeiro, Av. Carlos Chagas Filho 373, 21941-590 Rio de Janeiro, RJ, Brazil*

⁵*CIBER Enfermedades Respiratorias (CIBERES) and Fundación Centro Nacional de Investigaciones Cardiovasculares (CNIC), Melchor Fernández-Almagro 3, 28029 Madrid, Spain*

Correspondence should be addressed to Fernando Herranz; fherranz@cnic.es

Received 27 February 2018; Accepted 27 February 2018; Published 1 April 2018

Copyright © 2018 Paulo H. Rosado-de-Castro et al. This is an open access article distributed under the Creative Commons Attribution License, which permits unrestricted use, distribution, and reproduction in any medium, provided the original work is properly cited.

The combination of the size-dependent properties of nanomaterials with the noninvasive characterisation in molecular imaging is a powerful combination that is being successfully applied across disciplines. In the past ten years, we have witnessed the development of, literally, hundreds of nanoparticle-based probes for molecular imaging. All major imaging techniques have been enhanced by the use of nanoparticles, particularly magnetic resonance imaging (MRI), positron emission tomography (PET), and optical imaging. The use of iron oxide nanoparticles for T_1 -weighted and/or T_2 -weighted MRI, the design of radioisotope chelator-free particles for PET, and new developments in fluorescent nanoparticles (carbon dots and upconverting nanoparticles) are important milestones in the field. There are two key features in nanoparticle-based probes which are seldom found in traditional imaging probes: multimodality and multifunctionality. The use of, at least, two complementary imaging techniques (multimodality) like PET/MRI or MRI/Fluorescence and the possibility of incorporating several vectors on the surface and/or drugs (multifunctionality) expand the use of these probes. Furthermore, the properties

of some nanoparticles can be used to create new imaging techniques, for example, the superparamagnetism of iron oxide nanoparticles for magnetic particle imaging.

In this issue, we have aimed to provide a platform for high-quality contributions on nanoparticles application to molecular imaging. Original papers and review articles focusing on the latest application of nanoparticle-based imaging probes were submitted. The topics treated include the application of iron oxides for MRI, for PET/MRI, and for drug delivery; new synthesis approaches to obtain magnetic nanoparticles-based contrast agents; polymeric nanoparticles for ultrasound imaging; new computed tomography (CT) contrast agents; and quantum dots for multiplex optical imaging. We received a total of 16 submissions, and after two rounds of rigorous review, 9 papers were accepted for publications in this special issue.

Acknowledgments

The guest editorial team thanks the authors submitting their contributions to this special issue. The editors also thank

the reviewers for their precious help with review assignments.

Paulo H. Rosado-de-Castro
María del Puerto Morales
Pedro M. Pimentel-Coelho
Rosalía Mendez-Otero
Fernando Herranz

Research Article

Neural Induction Potential and MRI of ADSCs Labeled Cationic Superparamagnetic Iron Oxide Nanoparticle In Vitro

Weiqiong Ma,^{1,2} Qi Xie ,¹ Baolin Zhang ,³ Huixian Chen,¹ Jianyi Tang,¹ Zhengxian Lei,¹ Minyi Wu,¹ Dingxuan Zhang,¹ and Jiani Hu⁴

¹Medical Imaging Department, Nan Sha Center Hospital, Guangzhou Municipal First People's Hospital, Guangzhou Medical University, The Second Affiliated Hospital of South China University of Technology, Guangzhou, Guangdong 511457, China

²Department of Radiology, Huizhou Municipal Central Hospital, Huizhou, Guangdong 516001, China

³School of Materials Science and Engineering, Guilin University of Technology, Guilin, Guangxi 541004, China

⁴Karmanos Cancer Institute, Wayne State University, 3990 John R. Street, Detroit, MI 48201, USA

Correspondence should be addressed to Qi Xie; xieqi8@yeah.net and Baolin Zhang; baolinzhang@ymail.com

Received 24 August 2017; Revised 21 December 2017; Accepted 31 December 2017; Published 14 February 2018

Academic Editor: Maria P. Morales

Copyright © 2018 Weiqiong Ma et al. This is an open access article distributed under the Creative Commons Attribution License, which permits unrestricted use, distribution, and reproduction in any medium, provided the original work is properly cited.

Magnetic resonance imaging (MRI) combined with contrast agents is believed to be useful for stem cell tracking in vivo, and the aim of this research was to investigate the biosafety and neural induction of SD rat-originated adipose derived stem cells (ADSCs) using cationic superparamagnetic iron oxide (SPIO) nanoparticle which was synthesized by the improved polyol method, in order to allow visualization using in vitro MRI. The scan protocols were performed with T2-mapping sequence; meanwhile, the ultrastructure of labeled cells was observed by transmission electron microscopy (TEM) while the iron content was measured by inductively coupled plasma-atomic emission spectrometry (ICP-AES). After neural induction, nestin and NSE (neural markers) were obviously expressed. In vitro MRI showed that the cationic PEG/PEI-modified SPIO nanoparticles could achieve great relaxation performance and favourable longevity. And the ICP-AES quantified the lowest iron content that could be detected by MRI as 1.56~1.8 pg/cell. This study showed that the cationic SPIO could be directly used to label ADSCs, which could then inductively differentiate into nerve and be imaged by in vitro MRI, which would exhibit important guiding significance for the further in vivo MRI towards animal models with neurodegenerative disorders.

1. Introduction

Stem cell transplantation in treatment of central nervous system (CNS) diseases has the capacity to replace damaged nerve tissues so as to halt the progression of diseases and restore their physiological functions and then ultimately create favorable conditions for the clinical treatment [1–3]. However, stem cell biology remains incompletely understood despite significant advances in the field of neuroscience, including their migration, homing, survival, proliferation, and directed differentiation in vivo. Cell imaging has provided a feasible platform to solve the above-mentioned problems [4–6].

Cell imaging has used superparamagnetic nanoparticles coupled with magnetic resonance imaging to follow the

fate of labeled cells in the organs and tissues. Therefore, it has become one of the most ideal analytical techniques of molecular imaging [7, 8]. The first widely applied strategy was to combine the commercial iron oxide nanoparticles (e.g., Feridex® or Resovist®) with the commercial transfection agents (e.g., liposomes, polylysine, or protamine sulfate) for the efficient labeling, but such shortcomings as imprecise surface properties and noncompletely consistent sizes of combinations influenced the results of tracing and imaging [9, 10]. Thus, various strategies had been explored to improve the stability of superparamagnetic nanoparticles. Laurent et al. [11] found that thermal decomposition in organic solvents could produce nanoparticles with precise control of charge and size relative to the combinations with transfection agents.

TABLE 1: The characteristics of the two types of functionalized nanoparticles.

Agent	Coating	Hydrodynamic size (nm)	Zeta potential (mV)
PEG/PVP-SPIONs	PEG, PVP	18–22	0
PEG/PEI-SPIONs	PEG, PEI	19–24	25 ± 1.5

So our research team used “one-pot” thermal decomposition method, namely, improved polyol method, which had made the SPIO to be modified with surface coating such as PEG, PEI, and PVP during the synthesis procedures (Figure 1S, supplementary material), and the nanoparticles exhibited several advantages. First, the nanoparticle could be synthesized with inherent cation and consistent particle size (Figure 2S, supplementary material). Second, the nanoparticles could be easily dispersed in aqueous media and other polar solvents owing to the coating by hydrophilic polyol ligands. Finally, the relatively higher reaction temperature of this procedure favored particles with a higher crystallinity and therefore a stronger magnetism (Figure 3S, supplementary material) [12, 13]. We conjectured that this new type of SPIO with excellent characterization (inherent cation, consistent size, strong magnetism, etc.) might be more effective in the field of labeling and tracing stem cells which were negatively charged.

In this study, we present cationic SPIO (PEG/PEI-modified SPIO) labeled with SD rat-originated ADSCs, followed by the experiments of labeling efficiency, biocompatibility, neural differentiation, and in vitro MRI imaging, aiming to explore its feasibility towards stem cell labeling and make early preparations for its further in vivo MRI imaging of neurodegenerative disease. PEG/PVP-modified zero charge-coated SPIO, synthesized with the same method [12, 13], was also used for the comparison, aiming to explore the roles of cation(s) in cell labeling. Meanwhile, our study had used ICP-AES to quantify the lowest iron content that could be detected by MRI; to our knowledge, this is the first series study to explore this area.

2. Materials and Methods

2.1. Extraction, Purification, and Identification of SD Rat-Originated ADSCs. The inguinal adipose tissues were harvested from 4-week-old SD rats (purchased from Guangdong Medical Experimental Animal Center) under sterile conditions; type I collagenase (Sigma) was then added for 45-min agitating digestion at 37°C; the mixture was then repetitively centrifuged, and after discarding the supernatant, the cellular pellet (primary cells, P0) was resuspended in DMEM/F12 (Hyclone company) with 10% fetal bovine serum (Gibco) for consecutive passage and purification. The P3 cells were then detected in the surface antigens (CD29, CD45, CD44, and CD106, Biolegend) using FACScan flow cytometer (BD FASCanto™, USA).

2.2. ADSCs Labeling with SPIO. The PEG/PEI-modified SPIO (coated with positive charge(s)) and the PEG/PVP-modified SPIO (coated with zero charge), synthesized by the

improved polyol method, were used [12, 13], and the characteristics of these two types of functionalized nanoparticles are summarized in Table 1.

The stock solution of SPIO was firstly diluted with the cell culture medium to form the tracing agents with different concentrations (0 ug/ml, 6 ug/ml, 12 ug/ml, 25 ug/ml, 50 ug/ml, and 100 ug/ml), which were then used for direct coincubation for different periods (6 h, 12 h, 24 h, and 48 h); the pretest repetitively detected the effectiveness and safety of cell labeling using such assays as Prussian blue staining, cell viability (trypan blue staining), and cell proliferation (MTT).

Preexperiment had been carried out repetitively to detect the effectiveness and safety of cell labeling using such assays as Prussian blue staining (Figure 4S, supplementary material), cell viability (trypan blue staining), and cell proliferation (MTT) and then determined that the concentrations of PEG/PEI- and PEG/PVP-modified SPIO that could safely and effectively label ADSCs were 12 ug/ml, 25 ug/ml, and 25 ug/ml, and the incubation time was 12 h [14].

2.3. The Neural Induction Potential of Labeled Cells. 10^6 ADSCs were sampled, incubated with 25 ug/ml tracer for 12 h, and then set as the labeling group; 10^6 unlabeled ADSCs were set as the control group. Preinduction culture medium (DMEM + 20% FBS + 1 mM β -mercaptoethanol) was added to these two groups for 24-h before incubation; after that, induction culture medium (DMEM + 5 mM β -mercaptoethanol) was replaced and cultured for another 5 h~5 days, during which period the cells' morphological changes were observed, and the neural markers (nestin and NSE, Santa Cruz Inc.) were detected.

2.4. TEM Observation. After fixation, dehydration, infiltration, and embedding, the cell precipitate was prepared for embedding slice, followed by conventional ultrathin slicing (70 nm) and 2-h lead-uranium staining. The cellular ultrastructures in the slices were then observed using TEM (JEM1230, Japan), including the locations of the SPIO nanoparticles and the integrities of mitochondria, endoplasmic reticulum, or Golgi apparatus.

2.5. In Vitro MRI. The 10^6 ADSCs incubated with 12 ug/ml and 25 ug/ml PEG/PEI-modified SPIO and 25 ug/ml PEG/PVP-modified SPIO for 12 h were set as the labeling group, and another 10^6 ADSCs were set as the nonlabeling group; the cells in these two groups were digested into single cell suspension with trypsin and then transferred into 0.8 ml EP tubes for centrifugation. The supernatant was discarded, and then 200 μ l of 5% gelatin was added to resuspend the cell precipitate; their T2WI signals and T2 values were then repetitively detected for 18 times.

The single cell suspension of ADSCs incubated with 25 ug/ml tracer for 12 h was dispersed into 0.8 ml EP tubes with 10^6 cells/tube, 5×10^5 cells/tube, 10^5 cells/tube, 10^4 cells/tube, and 10^3 cells/tube, respectively; meanwhile, the non-labeling group were also set to determine the minimum number of the labeled cells that MRI scanning could display.

10^6 ADSCs incubated with 25 ug/ml tracer for 12 h were then washed with PBS, followed by continuous culture and passage. Each generation was then sampled with the same amount of cells for MRI scanning until no difference could be found with the nonlabeling group (10^6 ADSCs); another same experimental group was simultaneously set up for the detection of iron content in single cell using ICP-AES.

Simens Vrio Tim 3.0T MRI scanner was used with animal-specific coil (5-cm in diameter). T2WI sequences were as follows: TR 2000 ms, TE 85 ms, FOV 220 mm \times 220 mm, matrix 318 \times 448, and layer thickness 1.5 mm; T2-mapping: TR 1000 ms, TE 13.8~69.0 ms, FOV 85.2 mm \times 120 mm, matrix 318 \times 448, and layer thickness of 1.5 mm.

2.6. Detection of Iron Content in the Labeled Cells Using ICP-AES. 10^6 ADSCs incubated with 25 ug/ml tracer for 12 h were placed in one 15 ml glass tube, and then 500 ul of 65–68% concentrated nitric acid (Guangzhou Donghong Chemical industry) was added to each sample. All the samples were placed into one oil-pan for 3-h high-temperature high-pressure reaction (121°C) until all the samples fully dissolved and exhibited uniformly no colour or light yellow (depending on the sample concentration). The standard samples for the quantitative detection by ICP-AES (Thermo Fisher, USA) included blank, 0.1, 1, 10, 50, and 100 (PPm), and according to the quantitative results, the standard curve could be obtained for the further calculation of unicellular iron content.

2.7. Statistical Analysis. SPSS17.0 statistical software was used for statistical analysis; the signal comparison between the labeling and the nonlabeling group, as well as between the relaxation times, used the two-independent-sample *t*-test; the labeling longevity comparison between the labeling and nonlabeling group used ANOVA, with $P < 0.05$ considered as significant difference.

3. Results

3.1. Extraction, Purification, and Identification of SD Rat-Originated ADSCs. The passage 0 (P_0) cells began wall-adherent growth when cultured for 24–48 h, grew rapidly about 3–5 days later, and reached the peak on the 7th day. After that, the growth entered the plateau period, appearing as a reverse “S”-shaped growth curve (Figure 1(a)). The cells' morphologies became uniform when consecutively subcultured to passage 3 (P_3), and interconnection of spindle projections and fusion growth appeared (Figure 1(b)). Flow cytometric analysis showed that the P_3 ADSCs exhibited strongly positive expression of CD29 (reaching more than 95%), positive expression of CD44 (about 30%–40%), and negative expression of CD106 and CD45 (less than 5%) (Figure 1(c)).

3.2. The Neural Induction Potential of Labeled ADSCs. After neural induction, the labeled cells exhibited significant expressions of NSE and nestin; under a fluorescence microscope, cone and polygonal cells with green fluorescence could be seen, and projections with various lengths could be seen along the edge of the cell body, which tended towards the shape of pyramidal neurons (Figure 2).

3.3. TEM Observation. Electron microscope studies revealed that the absorbed nanoparticles dispersed inside lysosomes, vesicle-like aggregation appeared, and no nanoparticles were seen in nuclei. The chromatin was uniform, and the cell structures were basically intact, indicating that the absorbed nanoparticles did not significantly influence the morphology and structure of the cells (Figure 3).

3.4. In Vitro MRI

3.4.1. T2-Mapping Scanning of the Labeling Group and the Nonlabeling Group. After labeled with the PEG/PEI-modified SPIO (labeling group 1) and the PEG/PVP-modified SPIO (labeling group 2), T2 signal intensity and T2 relaxation time of the inter- and intragroup showed significant differences ($P < 0.01$). T2WI signal intensity was significantly reduced and the T2 relaxation time was significantly shortened between the labeling group and the nonlabeling group, between labeling groups 1 and 2, and between the 25 ug/ml-labeling group 1 and the 12 ug/ml-labeling group 1 (Figures 4(a) and 4(b)).

3.4.2. Labeling Rate of SPIO. It could be seen from the T2-mapping images that the signal was significantly reduced and the T2 relaxation time was gradually shortened along with the increasing of the cells. 10^3 labeled cells could be displayed in MRI scanning (Figures 5(a) and 5(b)).

3.4.3. Labeling Longevity of SPIO. On the T2-mapping images, the T2 signals and the relaxation time of the same amount of cells labeled with PEG/PEI-modified SPIO in different generation (25 ug/ml, passaged for 1 day, 3 days, 5 days, 7 days, 10 days, 15 days, and 20 days) were gradually increased with the extension of cell growth and proliferation time, and the T2 signal and relaxation time of passage 7 (P_7) ADSCs (20 d) showed no significant difference between the labeling group and the nonlabeling group ($F = 0.113$, $P = 0.740$; $F = 4.369$, $P = 0.051$). Meanwhile, the T2 signals and the relaxation time showed no significant difference between the labeling group with the PEG/PVP-modified SPIO and the nonlabeling group in passage 6 (P_6) ADSCs (15 d) ($F = 1.891$, $P = 0.186$; $F = 3.682$, $P = 0.071$, Figures 6(a)–6(d)).

3.4.4. Unicellular Iron Content in the Labeling Cells. With the extension of cell growth and proliferation, the unicellular iron content in the labeling cells was decreased. When the T2WI signal and the T2 value showed no significant difference, the intracellular iron content was 1.56~1.8 pg/cell by ICP-AES method (Table 2).

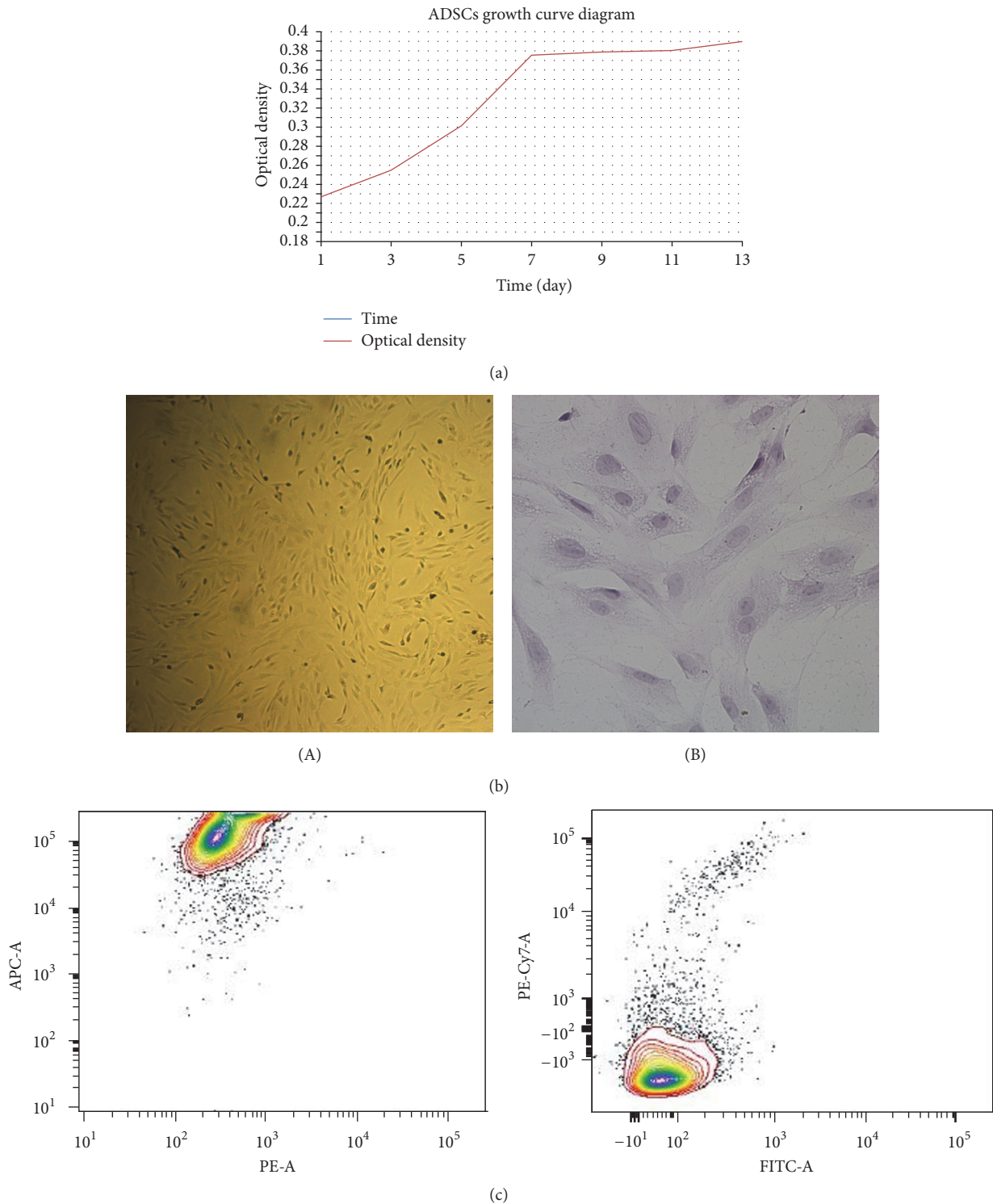


FIGURE 1: (a) The growth curve of ADSCs was appearing as a reverse “S”-shape. (b) The P₃ ADSCs ((A) ×100; (B) ×HE-400) were appearing fusiform and spindle growth, and the projections were interconnected and fused. (c) The expressions of ADSCs’ surface antigens: APC-CD29: strongly positively expressed, close to 100%; PE-CD44: positively expressed, approximately 30%–40%; PE/Cy-CD106 and FITC-CD45: negatively expressed, less than 5%.

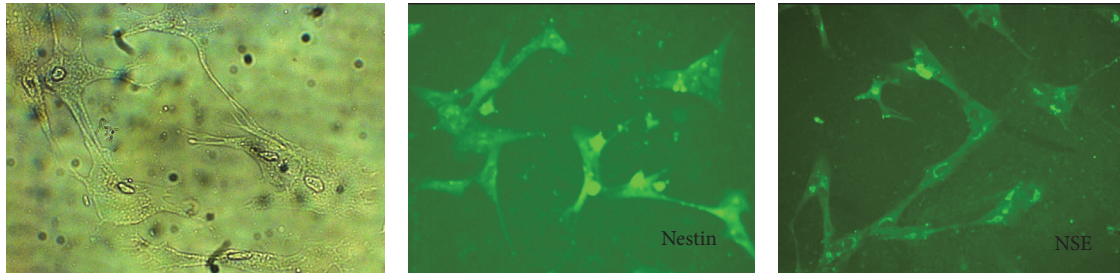


FIGURE 2: The microscopy revealed that the cell body turned round after induction, with several dendritic structures surrounded; the cells were similar to the pyramidal neurons, and the cellular immunofluorescence exhibited obvious expressions of NSE and nestin.

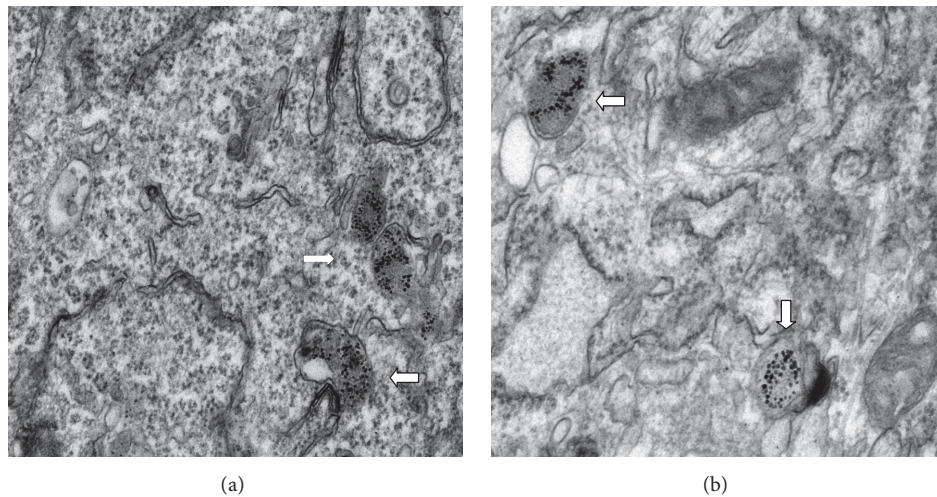


FIGURE 3: The absorbed SPIO nanoparticles mainly dispersed inside the perinuclear lysosomes (white arrows), and the phenomenon in the PEG/PEI-modified SPIO-labeling group (a) was more obvious than the PEG/PVP-modified SPIO-labeling group (b); the intracellular organelle structures were complete and not significantly damaged ($\times 30000$).

4. Discussion

It was reported that the commercial SPIO carried negative charge(s) on its surface, so commercial transfection agent which carried positive charge(s) must link to stem cells for effective labeling, but this strategy would result in inaccurate surface properties as well as inconsistent particle sizes, thus causing the discrepancy in labeling effects [15, 16]. Therefore, this study used coating-modified SPIO of positive or zero charge to label ADSCs directly, and the results showed that these two types of SPIO could safely and effectively label ADSCs without transfection agent, maintaining relatively stable status in labeling. Furthermore, the positive-charged SPIO could more effectively label ADSCs than the zero-charged groups, indicating that cation(s) on the surface of SPIO nanoparticle played an essential role in ADSCs' labeling.

In this study, 12 h incubation of ADSCs with the cationic PEG/PEI-modified SPIO (within the concentration range 12–25 $\mu\text{g}/\text{ml}$) could achieve more than 95% labeling rate of iron particles, and the intracellular iron content might reach as high as 35.4 pg/cell . Compared to this new type of SPIO, previous commercial SPIO required the concentration range as 25–50 $\mu\text{g}/\text{ml}$ and the incubation time as 18–24 h to achieve more than 95% labeling rate in mesenchymal stem

cells, and the intracellular iron content could only be up to 15 pg/cell or 17.9 pg/cell [17, 18]. These results suggested that this cationic SPIO could much more quickly and effectively label the stem cells than previous commercial SPIO, mainly due to the PEI coating. PEI is a typical water-soluble cationic polymer with high positive charge which can interact with the negatively charged cell membranes and facilitates better cell internalization through endocytosis. However, the high positive charges can disrupt the cell membrane, resulting in toxicity to the cells [19, 20]. So our research team grafted PEG to PEI, which provided colloidal stability and neutralized the toxic effects of the PEI [12, 14].

Safety is the primary premise of SPIO-labeling towards stem cells. In this study, the cytotoxicity of ADSCs caused by this cationic SPIO in the incubation concentration and time which could achieve labeling efficiency was investigated. The result showed that the concentrations of PEG/PEI-modified SPIO that could safely and effectively label ADSCs were 12–25 $\mu\text{g}/\text{ml}$, and the incubation time was 12 h, showing no significant change in cell viability and proliferation between labeling and nonlabeling group. TEM revealed that the labeled cells exhibited no obvious organelle damage. All these results indicated that this effective incubation concentration and time did not significantly inhibit the biological activities

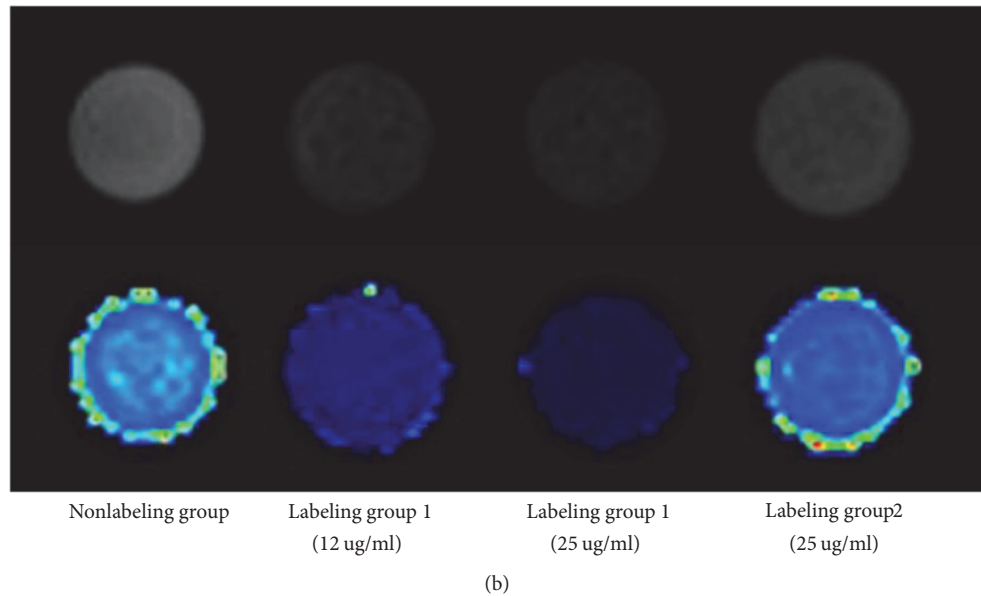
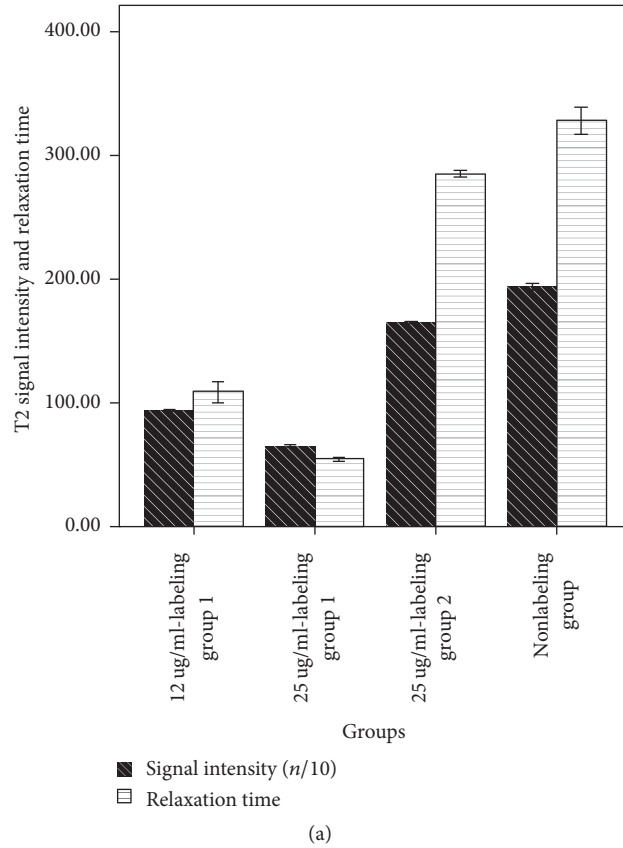
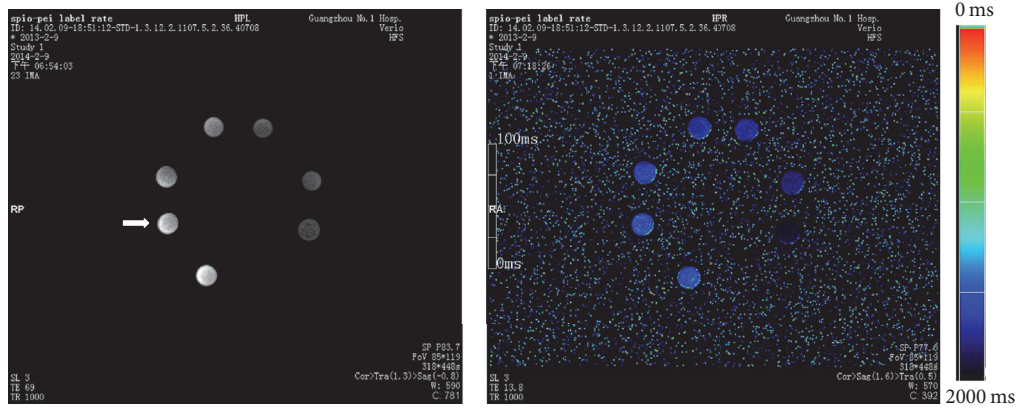


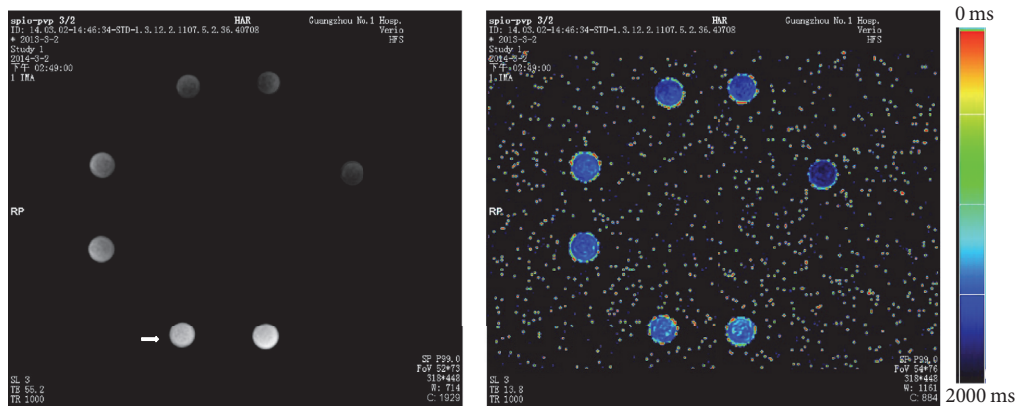
FIGURE 4: (a) The comparison of T2 signal intensity and relaxation time; (b) T2-mapping scanning among different groups.

of stem cells. The labeling safety should not only assess whether the tracer agent would inhibit the biological activities of the host cells but also consider whether the deposition area of the absorbed nano-iron particles could precipitate an effective metabolic degradation. Previous studies generally considered that the nanoparticles were transferred into the

stem cells via endocytosis, then the nanoparticles localized in the cytoplasm instead of entering the nuclei by forming the early stage of endosome-like vesicles [21, 22]. Some studies found that the nanoparticles positioned in the late endosomes or secondary lysosomes of the cytoplasm [23, 24]. Therefore, it was presumed that while the nanoparticles



(a) The labeling rate of PEG/PEI-modified SPIO: the signal was significantly reduced and the T2 relaxation time was gradually shortened along with the increasing of cells; 10^3 labeled cells could be displayed in MRI scanning (white arrow, the lower left one indicated the nonlabeling group, and the cells in each tube were increased clockwise)



(b) The labeling rate of PEG/PVP-modified SPIO: the signal was significantly reduced and the T2 relaxation time was gradually shortened along with the increasing of the cells; 10^3 labeled cells could be displayed in MRI scanning (white arrow, the left one indicated the nonlabeling group, and the cells in each tube were increased clockwise)

FIGURE 5

TABLE 2: The detection of iron content in labeling cells by ICP-AES (pg/cell).

	P1	P2	P3	P4	P5	P6	P7
<i>Labeling group 1</i>							
12 $\mu\text{g/ml}$	20.16	9.36	7.32	3.96	2.04	1.88	1.56
25 $\mu\text{g/ml}$	35.4	17.04	14.4	6.72	3.12	2.60	1.80
<i>Labeling group 2</i>							
25 $\mu\text{g/ml}$	5.52	3.36	3.12	2.64	2.64	1.56	

were internalized into the cytoplasm of the lysosomal compartment from early endosomes, then they might gradually be delivered to late endosomes and lysosomes around the nuclei with the release of the vesicles and the growth of the endosomes [25, 26]. In this study, the ultrastructural observation of labeled cells by TEM indicated that the internalized SPIO was located inside early endosomes and lysosomes at the region of cytoplasm, which was consistent with previous studies. Due to the existence of a large number of molecular proteins (ferritin, transferrin, and hemosiderin, etc.) in living tissues, the internalized iron in lysosomes might be stored or degraded by further hemoglobin synthesis, thus maintaining the iron metabolism balance in vivo [27, 28]. It might be more

beneficial in avoiding potential cytotoxicity as the absorbed SPIO could be metabolized and degraded in lysosomes.

All procedures, applied for this study, were to explore the feasibility of stem cell therapy towards CNS disorders. Therefore, it should make clear that whether this labeling strategy would impact the neural induction of ADSCs. Referring to the study of Zuk et al. [29] and Lin et al. [30], β -mercaptoethanol was coincubated with ADSCs in the labeling and nonlabeling group. The microscopic observation showed that both of them exhibited the similar morphologies of pyramidal neurons, and the expressions of neural markers (nestin and NSE) were positive, among which NSE was more obviously expressed. The expression of nestin proved

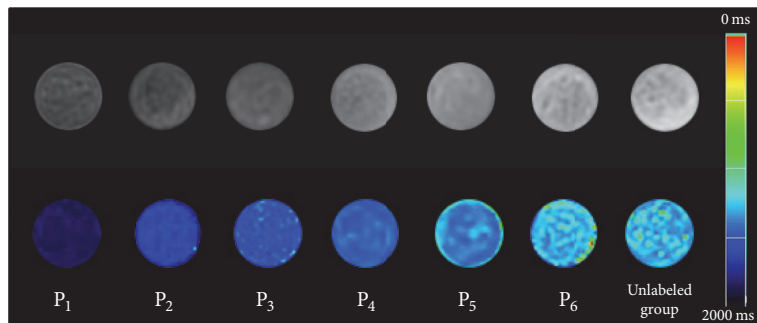
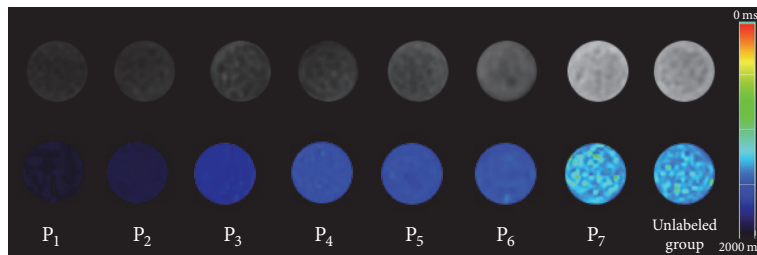
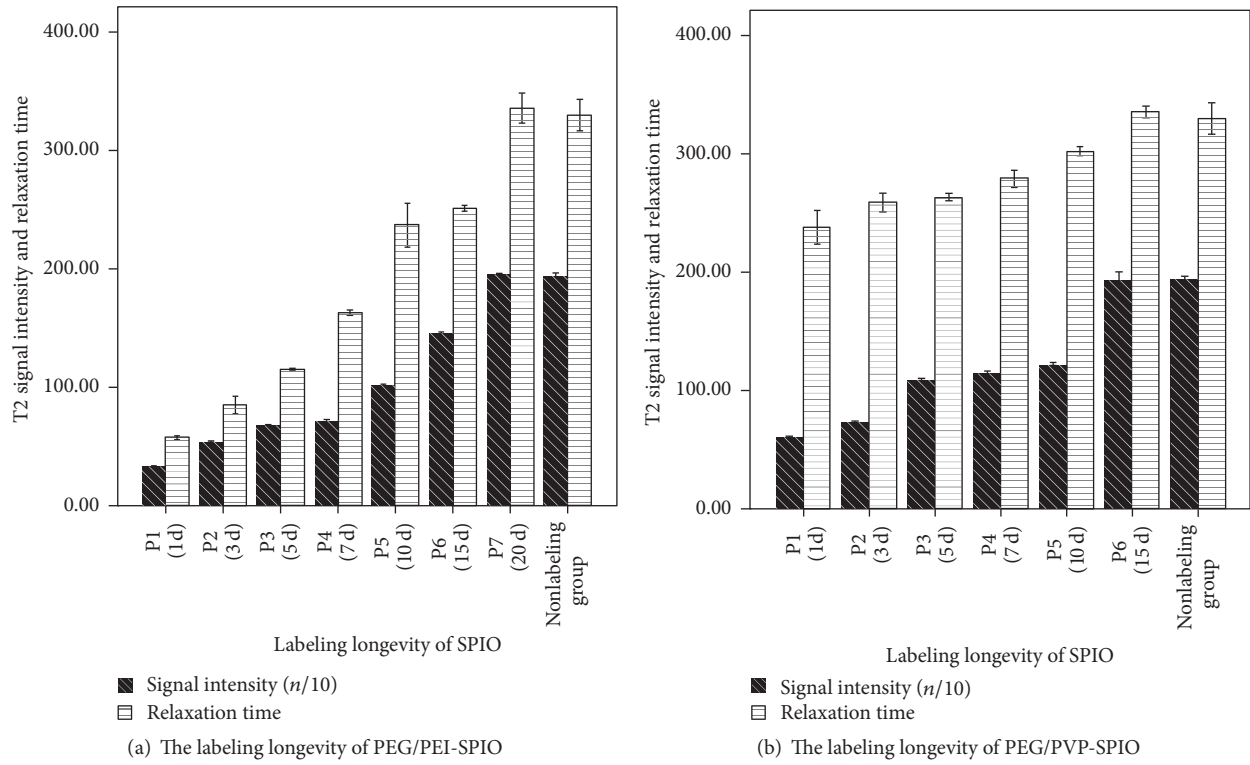


FIGURE 6

that ADSCs entered the key step of neural differentiation. Enolases include three homotypes (namely, α , β , and γ), and the γ -type enolase, namely, NSE, is expressed in the nervous tissues and secreted by the neurons. Therefore, the NSE expression proved that ADSCs differentiated and proliferated towards the neurons, and the feasibility of ADSCs differentiating towards the neurons was thus demonstrated. The neural induction potentials between the labeling and nonlabeling group showed no significant difference, indicating that SPIO-labeling would not significantly impact the neural induction potential of ADSCs, reflecting the safety of the SPIO-labeling indirectly.

Besides the labeling safety and effectiveness, effective relaxation and as-long-as-possible labeling durability should be required to achieve better dynamic visualization imaging of the transplanted stem cells. The SPIO-labeled ADSCs in this study showed sensitive and effective relaxation; 10^3 cells could cause the changes of the T2 signal and relaxation time. The T2 signal negative effects were also enhanced with the increasing of the incubation concentrations, which was consistent with previous studies using certain commercial SPIO [15, 31]. The other finding of this research was that the signal intensity and the relaxation time in the cationic PEG/PEI-modified SPIO group (12 ug/ml) were significantly lower and shorter than those in the PEG/PVP-modified SPIO group (25 ug/ml). Even more, the iron content detected with the ICP-AES could reach 20.16 pg/cell in the former group, but only 6.96 pg/cell in the latter group. Surmising that the stem cell surface is negatively charged, the surface charge would play an important role in the intracellular transportation of exogenous nanoparticles [32]. Therefore, cationic PEG/PEI-modified SPIO nanoparticles could be absorbed and lead to internalization more easily than zero charge-coated PEG/PVP-modified SPIO ones and then achieve greater relaxation performance.

Liu et al. [17] found the labeling longevity of Resovist-PLL complexes towards marrow mesenchymal stem cells (MSCs) could generally last up to 20 d, and even certain study found the detection of human marrow mesenchymal stem cells (hMSCs) with MRI was possible up to 35 d [33]. In this study, the labeling longevity of PEG/PEI-modified SPIO towards ADSCs could last up to 20 d, while the PEG/PVP-modified SPIO only last up to 15 d, showing no distinct advantage. Supposing that the proliferation of the cells inhibited the SPION from retaining inside the cells, some studies had shown that the proliferation of ADSCs was significantly greater than bone marrow mesenchymal stem cells (BMSCs) [34, 35], which might be the reason that the labeling longevity of PEG/PEI-modified SPIO towards ADSCs in this study was shorter than that of commercial SPIO towards hMSCs. In addition, the exocytosis of the cells which was enhanced as the decreasing of the particle size could also dilute the intracellular iron content. Xu et al. [36] added PLGA particles into SPIONs to change the diameter of the nanoparticles and found that these PLGA-SPIONs could significantly increase the labeling longevity towards MSCs because the particle diameters of Feridex and Resovist were bigger than SPIO synthesized by an improved polyol method, which would extend detection time with MRI at some degree. The

internalized iron would be evenly or unevenly dispersed into two daughter cells along with the cell proliferation, as passed through several cell cycles, and the iron content would be gradually diluted to the level lower than the MRI detectability. Previous studies did not specifically point out the detection limit of intracellular iron content by MRI. Our study had found that the T2 value showed no difference with the nonlabeling group when the iron content in labeling ADSCs cell was reduced to 1.56~1.8 pg/cell, quantifying the lowest iron content that could be detected by MRI.

ADSCs, which had wide source ranges and easy sampling procedures, were selected for the labeling in this study; the data from only one species were relatively limited. In further studies, different species of stem cells should be selected for the detection so as to better serve the field of stem cell labeling. Secondly, this study performed neural induction and MRI imaging in vitro towards the labeled stem cells, which belonged to one relatively early basic research. In order to achieve the integrity of the study, the next step should be focused on the biodistribution of the nanoparticles by using the accumulative dynamics of the nanoparticles in various animal model systems in vivo MRI.

5. Conclusions

The results of this study showed that the modified SPIO synthesized by an improved polyol method could be directly used to label ADSCs, safely and effectively. Labeling ADSCs could be inducted to differentiate into nerve and be imaged with MR in vitro. The surface charge(s) of nano-iron particles played an extremely important role in cell labeling. Meanwhile, the study also quantified the lowest iron content in labeling cell with MRI tracing imaging. Therefore, this cationic SPIO could be used for stem cell tractography, which would exhibit important guiding significance for the further in vivo MRI towards animal models with neurodegenerative disorders.

Abbreviation

ADSCs:	Adipose derived stem cells
CNS:	Central nervous system
MRI:	Magnetic resonance imaging
SPION:	Superparamagnetic iron oxide nanoparticles
PEG:	Polyethylene glycol
PVP:	Polyvinylpyrrolidone
ICP-AES:	Inductively coupled plasma-atomic emission spectrometry
NSE:	Neuron specific enolase
BMSCs:	Bone marrow mesenchymal stem cells
hMSCs:	Human marrow mesenchymal stem cells
SPIO:	Superparamagnetic iron oxide
PEI:	Polyethyleneimine
TEM:	Transmission electron microscopy.

Conflicts of Interest

The authors declare no conflicts of interest.

Authors' Contributions

All authors contributed equally to this work.

Acknowledgments

This work was funded by the science and technology projects of the people's livelihood, Bureau of Business-Economic Technology and Informationization, Nansha Dist., Guangzhou (no. 2014MS01); Special Projects of Guangzhou Science and Technology Plans (general project) (no. 1563000424); Technological Development Foundation of Guangdong Technological Projects (no. 2014A020212034); National Natural Science Foundation of China (no. 51162003, no. 51562007).

Supplementary Materials

Figure 1S: schematic representation of the synthesis and probable coating of the magnetite nanoparticles. Figure 2S: the magnetite nanoparticles coated with PEG/PVP or PEG/PEI dissolved in water: (a) hydrodynamic size analysis and (b) zeta potential measurements, showing inherent cation and consistent particle size. Figure 3S: M-H curve of the magnetite nanoparticles by the thermal decomposition of Fe(acac)₃ in PEG containing PEI and PVP, showing stronger magnetism. Figure 4S: the Prussian blue images of ADSCs incubated with 25 µg/ml PEG/PEI-SPIONs (a) and 25 µg/ml PEG/PVP-SPIONs (b). Prussian blue staining showed more iron content in PEG/PEI-SPIONs labeled groups than that in PEG/PVP-SPIONs labeled groups. (*Supplementary Materials*)

References

- [1] T. Lee, "Stem cell therapy independent of stemness," *World Journal of Stem Cells*, vol. 4, no. 12, pp. 120–124, 2012.
- [2] C. J. Taylor, D. J. Jhaveri, and P. F. Bartlett, "The therapeutic potential of endogenous hippocampal stem cells for the treatment of neurological disorders," *Frontiers in Cellular Neuroscience*, vol. 7, article 5, 2013.
- [3] H. E. Rice, E. W. Hsu, H. Sheng et al., "Superparamagnetic iron oxide labeling and transplantation of adipose-derived stem cells in middle cerebral artery occlusion-injured mice," *American Journal of Roentgenology*, vol. 188, no. 4, pp. 1101–1108, 2007.
- [4] E. Gu, W.-Y. Chen, J. Gu, P. Burrige, and J. C. Wu, "Molecular imaging of stem cells: Tracking Survival, biodistribution, tumorigenicity, and immunogenicity," *Theranostics*, vol. 2, no. 4, pp. 335–345, 2012.
- [5] K. von der Haar, A. Lavrentieva, F. Stahl, T. Scheper, and C. Blume, "Lost signature: progress and failures in in vivo tracking of implanted stem cells," *Applied Microbiology and Biotechnology*, vol. 99, no. 23, pp. 9907–9922, 2015.
- [6] P. Wang and A. Moore, "Molecular imaging of stem cell transplantation for neurodegenerative diseases," *Current Pharmaceutical Design*, vol. 18, no. 28, pp. 4426–4440, 2012.
- [7] D. Fayol, N. Luciani, L. Lartigue, F. Gazeau, and C. Wilhelm, "Managing Magnetic Nanoparticle Aggregation and Cellular Uptake: A Precondition for Efficient Stem-Cell Differentiation and MRI Tracking," *Advanced Healthcare Materials*, vol. 2, no. 2, pp. 313–325, 2013.
- [8] M. A. Busquets, R. Sabaté, and J. Estelrich, "Potential applications of magnetic particles to detect and treat Alzheimer's disease," *Nanoscale Research Letters*, vol. 9, no. 1, pp. 1–10, 2014.
- [9] H. Kalish, A. S. Arbab, B. R. Miller et al., "Combination of transfection agents and magnetic resonance contrast agents for cellular imaging: Relationship between relaxivities, electrostatic forces, and chemical composition," *Magnetic Resonance in Medicine*, vol. 50, no. 2, pp. 275–282, 2003.
- [10] B. Wang, C. Xu, J. Xie, Z. Yang, and S. Sun, "pH controlled release of chromone from chromone-Fe₃O₄ nanoparticles," *Journal of the American Chemical Society*, vol. 130, no. 44, pp. 14436–14437, 2008.
- [11] S. Laurent, D. Forge, M. Port et al., "ChemInform Abstract: Magnetic Iron Oxide Nanoparticles: Synthesis, Stabilization, Vectorization, Physicochemical Characterizations, and Biological Applications," *ChemInform*, vol. 39, no. 35, 2008.
- [12] F. Zhao, B. Zhang, J. Wang, and Z. Tu, "Synthesis and properties of magnetite nanoparticles coated with poly(ethylene glycol) and poly(ethylene imine)," *Journal of Nanoscience and Nanotechnology*, vol. 13, no. 10, pp. 6793–6797, 2013.
- [13] J. Wang, B. Zhang, L. Wang, M. Wang, and F. Gao, "One-pot synthesis of water-soluble superparamagnetic iron oxide nanoparticles and their MRI contrast effects in the mouse brains," *Materials Science and Engineering C: Materials for Biological Applications*, vol. 48, pp. 416–423, 2015.
- [14] G. Yang, W. Ma, B. Zhang, and Q. Xie, "The labeling of stem cells by superparamagnetic iron oxide nanoparticles modified with PEG/PVP or PEG/PEI," *Materials Science and Engineering C: Materials for Biological Applications*, vol. 62, pp. 384–390, 2016.
- [15] L. Matuszewski, T. Persigehl, A. Wall et al., "Cell tagging with clinically approved iron oxides: feasibility and effect of lipofection, particle size, and surface coating on labeling efficiency," *Radiology*, vol. 235, no. 1, pp. 155–161, 2005.
- [16] S. Metz, G. Bonaterra, M. Rudelius, M. Settles, E. J. Rummeny, and H. E. Daldrup-Link, "Capacity of human monocytes to phagocytose approved iron oxide MR contrast agents in vitro," *European Radiology*, vol. 14, no. 10, pp. 1851–1858, 2004.
- [17] G. Liu, H. Yang, X. M. Zhang, Y. Shao, and H. Jiang, "MR imaging for the longevity of mesenchymal stem cells labeled with poly-L-lysine-Resovist complexes," *Contrast Media & Molecular Imaging*, vol. 5, no. 2, pp. 53–58, 2010.
- [18] A. S. Arbab, L. A. Bashaw, B. R. Miller, E. K. Jordan, J. W. M. Bulte, and J. A. Frank, "Intracytoplasmic tagging of cells with ferumoxides and transfection agent for cellular magnetic resonance imaging after cell transplantation: methods and techniques," *Transplantation*, vol. 76, no. 7, pp. 1123–1130, 2003.
- [19] V. Cebrián, F. Martín-Saavedra, C. Yagüe, M. Arruebo, J. Santamaría, and N. Vilaboa, "Size-dependent transfection efficiency of PEI-coated gold nanoparticles," *Acta Biomaterialia*, vol. 7, no. 10, pp. 3645–3655, 2011.
- [20] A. Z. Rezvani, M. Rahimizadeh, H. Eshghi, A. Dehshahri, and M. Ramezani, "The effect of cationic charge density change on transfection efficiency of Polyethylenimine," *Iranian Journal of Basic Medical Sciences*, vol. 16, no. 2, pp. 150–156, 2013.
- [21] J.-H. Lee, M. J. Jung, Y. H. Hwang et al., "Heparin-coated superparamagnetic iron oxide for in vivo MR imaging of human MSCs," *Biomaterials*, vol. 33, no. 19, pp. 4861–4871, 2012.
- [22] G. Liu, Z. Wang, J. Lu et al., "Low molecular weight alkyl-polyacrylamide wrapped magnetite nanoparticle clusters as MRI probes for stem cell labeling and in vivo imaging," *Biomaterials*, vol. 32, no. 2, pp. 528–537, 2011.

- [23] C.-W. Lu, Y. Hung, J.-K. Hsiao et al., "Bifunctional magnetic silica nanoparticles for highly efficient human stem cell labeling," *Nano Letters*, vol. 7, no. 1, pp. 149–154, 2007.
- [24] N. Landázuri, S. Tong, J. Suo et al., "Magnetic targeting of human mesenchymal stem cells with internalized superparamagnetic iron oxide nanoparticles," *Small*, vol. 9, no. 23, pp. 4017–4026, 2013.
- [25] C. Corot, P. Robert, J.-M. Idée, and M. Port, "Recent advances in iron oxide nanocrystal technology for medical imaging," *Advanced Drug Delivery Reviews*, vol. 58, no. 14, pp. 1471–1504, 2006.
- [26] E. Schulze, J. T. Ferrucci, K. Poss, L. Lapointe, A. Bogdanova, and R. Weissleder, "Cellular uptake and trafficking of a prototypical magnetic iron oxide label in vitro," *Investigative Radiology*, vol. 30, no. 10, pp. 604–610, 1995.
- [27] Y.-W. Jun, J.-H. Lee, and J. Cheon, "Chemical design of nanoparticle probes for high-performance magnetic resonance imaging," *Angewandte Chemie International Edition*, vol. 47, no. 28, pp. 5122–5135, 2008.
- [28] J. Yang, J. Gunn, S. R. Dave, M. Zhang, Y. A. Wang, and X. Gao, "Ultrasensitive detection and molecular imaging with magnetic nanoparticles," *Analyst*, vol. 133, no. 2, pp. 154–160, 2008.
- [29] P. A. Zuk, M. Zhu, P. Ashjian et al., "Human adipose tissue is a source of multipotent stem cells," *Molecular Biology of the Cell (MBoC)*, vol. 13, no. 12, pp. 4279–4295, 2002.
- [30] Y. Lin, X. Chen, Z. Yan et al., "Multilineage differentiation of adipose-derived stromal cells from GFP transgenic mice," *Molecular and Cellular Biochemistry*, vol. 285, no. 1-2, pp. 69–78, 2006.
- [31] J. Jo, I. Aoki, and Y. Tabata, "Design of iron oxide nanoparticles with different sizes and surface charges for simple and efficient labeling of mesenchymal stem cells," *Journal of Controlled Release*, vol. 142, no. 3, pp. 465–473, 2010.
- [32] D. L. Thorek and A. Tsourkas, "Size, charge and concentration dependent uptake of iron oxide particles by non-phagocytic cells," *Biomaterials*, vol. 29, no. 26, pp. 3583–3590, 2008.
- [33] H. Itrich, C. Lange, H. Dahnke, A. R. Zander, G. Adam, and C. Nolte-Ernsting, "Labeling of mesenchymal stem cells with different superparamagnetic particles of iron oxide and detectability with MRI at 3T," *RöFo - Fortschritte auf dem Gebiet der Röntgenstrahlen und der bildgebenden Verfahren*, vol. 177, no. 8, pp. 1151–1163, 2005.
- [34] H. Ning, M. Albersen, G. Lin, T. F. Lue, and C.-S. Lin, "Effects of edu labeling on mesenchymal stem cells," *Cytotherapy*, vol. 15, no. 1, pp. 57–63, 2013.
- [35] M. A. Vidal, N. J. Walker, E. Napoli, and D. L. Borjesson, "Evaluation of senescence in mesenchymal stem cells isolated from equine bone marrow, adipose tissue, and umbilical cord tissue," *Stem Cells and Development*, vol. 21, no. 2, pp. 273–283, 2012.
- [36] C. Xu, D. Miranda-Nieves, J. A. Ankrum et al., "Tracking mesenchymal stem cells with iron oxide nanoparticle loaded poly(lactide-co-glycolide) microparticles," *Nano Letters*, vol. 12, no. 8, pp. 4131–4139, 2012.

Research Article

Carboxyl of Poly(D,L-lactide-co-glycolide) Nanoparticles of Perfluorooctyl Bromide for Ultrasonic Imaging of Tumor

Shengjuan Luo ¹, Jinsong Ding ², Peiqi Wang ³, Zheng Wang,⁴ Xiaoqian Ma ⁵,
Cejun Yang ⁵, Qi Liang,⁵ Pengfei Rong ⁵, and Wei Wang ⁵

¹Department of Ultrasound, The Third Xiangya Hospital, Central South University, Changsha 410013, China

²School of Pharmaceutical Sciences, Central South University, Changsha 410013, China

³Department of Pharmacy, Cancer Hospital of Henan Province, Zhengzhou 450008, China

⁴Department of Hepatobiliary Surgery, The Third Xiangya Hospital, Central South University, Changsha 410013, China

⁵Department of Radiology, The Third Xiangya Hospital, Central South University, Changsha 410013, China

Correspondence should be addressed to Wei Wang; cjr.wangwei@vip.163.com

Received 21 August 2017; Accepted 26 November 2017; Published 7 February 2018

Academic Editor: Rosalia Mendez-Otero

Copyright © 2018 Shengjuan Luo et al. This is an open access article distributed under the Creative Commons Attribution License, which permits unrestricted use, distribution, and reproduction in any medium, provided the original work is properly cited.

Perfluorooctyl bromide (PFOB) enclosed nanoparticles (NPs) as ultrasonic contrasts have shown promising results in the recent years. However, NPs display poor contrast enhancement in vivo. In this work, we used the copolymers poly(lactide-co-glycolide) carboxylic acid (PLGA-COOH) and poly(lactide-co-glycolide) poly(ethylene glycol) carboxylic acid (PLGA-PEG-COOH) as a shell to encapsulate PFOB to prepare a nanoultrasonic contrast agent. The NPs were small and uniform (210.6 ± 2.9 nm with a polydispersity index of 0.129 ± 0.016) with a complete shell nuclear structure under the transmission electron microscopy (TEM). In vitro, when concentration of NPs was ≥ 10 mg/ml and clinical diagnostic frequency was ≥ 9 MHz, NPs produced intensive enhancement of ultrasonic gray-scale signals. NPs could produce stable and obvious gray enhancement with high mechanical index (MI) ($MI > 0.6$). In vivo, the NPs offered good ultrasound enhancement in tumor after more than 24 h and optical imaging also indicated that NPs were mainly located at tumor site. Subsequent analysis confirmed that large accumulation of fluorescence was observed in the frozen section of the tumor tissue. All these results caused the conclusion that NPs encapsulated PFOB has achieved tumor-selective imaging in vivo.

1. Introduction

In recent years, ultrasonic molecular imaging has become a promising method for cancer diagnostics because it can image an intact living body at cellular and subcellular level with high spatial and temporal resolution, low cost, portability, and lack of ionizing irradiation [1]. Ultrasound contrast agents (UCAs) are necessary for ultrasound molecular imaging, and they can improve the accuracy and sensitivity of ultrasound diagnosis [2]. Currently, the contrast agents in the market consist of gas-encapsulated phospholipids or albumin (1 to 8 microns) [3]. However, most tumors have porous vasculature with fenestrations between 380 and 780 nm [4]. The micro-sized UCAs are often limited by their lack of efficient penetration. To overcome this limitation, decreasing

the UCA size to nanometer range would make UCA more likely to penetrate into tumor tissue.

Nanobubbles were used in most studies related to nanoscale UCAs because they produced good sound reflection [5–8]. However, in vitro nanobubbles would quickly break or fuse without pressure damage [8]; in vivo, nanobubbles could be removed by the reticuloendothelial system (RES) [9]; ultrasound also had some damage to them [10]. Therefore, the number of nanobubbles that went through the circulation to the tumor and inflammation was small, which would limit their ability of target diagnosis and treatment. Nanoparticles (NPs) with liquid perfluorocarbons as the core were more resistant to pressure changes and mechanical stresses. When bounding and gathering at a specific target, nanoparticles of liquid perfluorocarbons could produce

strong signals but negligible signals in circulation [11, 12]. Perfluorooctyl bromide (PFOB) is of low toxicity and stability. It is the most suitable liquid perfluorocarbon to be used in vivo [13]. Inferior vena cava of the nude mouse presented significant gray enhancement for a few seconds after being injected with nanoparticles of PLGA enclosed PFOB [14]. Because of the hydrophobic properties of PLGA, nanoparticles were quickly cleared by RES in vivo. At present, the most effective and widely used method is to use nonionized polymer polyethylene glycol (PEG) to modify the PLGA [9, 15]. DSPE-PEG was used to modify PLGA and it was found that the dosage of DSPE-PEG affected the core-shell structure of NPs. When the dosage of DSPE-PEG is >2.64 mg (100 mg PLGA), NPs could not maintain a complete core-shell structure, but when the dosage of DSPE-PEG is ≤ 2.64 mg, only 6% of DSPE-PEG in the shell, NPs with a complete core-shell structure could not prevent themselves from being cleared by RES and could not gather in the tumor for imaging [13]. In order to maintain the stability of the core-shell structured nanoparticles and have a good ultrasonic contrast enhancement, it is necessary to use the compatible material packaged PFOB to carry enough PEG to avoid RES.

Here, we would use hybrid membrane materials of PLGA-PEG-COOH and PLGA-COOH packaged PFOB to prepare nanoscale UCAs, which all had complete core-shell structure with a good gray enhancement in the aqueous solution in vitro. In in vivo experiments, the enhancement of ultrasound gray scales at the tumor site was analyzed after tail intravenous injection. Finally, tumor-selective imaging of NPs was assessed by both small animal optical imaging and fluorescence microscope.

2. Materials and Methods

2.1. Materials. Poly(D,L-lactide-co-glycolide) (50/50) with terminal carboxylate groups (PLGA-COOH, $M_w = 17000$) was purchased from Jinan Daigang Biotech Co., Ltd. (Jinan, Shandong, China). NH_2 -PEG-COOH ($M_w = 3400$) was purchased from Beijing Kaizheng Biotech Co., Ltd. (Beijing, China). Polyvinyl alcohol (M_w 13000–23000, 98% hydrolyzed), 4'-6-diamidino-2-phenylindole (DAPI), and coumarin-6 were provided by Sigma-Aldrich (St. Louis, MO). Perfluorooctyl bromide (PFOB) was purchased from Aladdin Industrial Corporation (Shanghai, China). HepG2 cells (human liver hepatocellular carcinoma cell line) were purchased from the Cell Institute of the Chinese Academy of Sciences (Shanghai, China). All other reagents were of analytical pure grade and were purchased from Sinopharm Chemical Reagent Co., Ltd. (Shanghai, China).

2.2. Synthesis of PLGA-PEG-COOH Copolymer. Carboxylate-functionalized copolymer PLGA-PEG was synthesized by conjugating COOH-PEG- NH_2 to PLGA-COOH according to a carbodiimide-N-hydroxysuccinimide (EDC/NHS)-mediated chemistry [16] (Figure 1(a)). The copolymer was dissolved in CDCl_3 and characterized by ^1H NMR at 400 Hz (AVANCE III 400 M, Bruker, Billerica, MA) to determine the modification ratio of PEG on PLGA.

2.3. Preparation of Nanoparticles/Microparticles Encapsulated PFOB. PFOB was encapsulated in nanoparticles by modifying the emulsion solvent evaporation method [17] (Figure 1(b)). Briefly, 50 mg PLGA blended membrane materials were dissolved in 2 ml methylene chloride along with 30 μl PFOB. The organic solution placed in a thermostatic bath was maintained at 20°C to ensure full miscibility of the PFOB. This was then emulsified into 10 ml 1.0% polyvinyl alcohol (PVA; w/v) aqueous solution to form a preemulsion. The preemulsion was sonicated at 300 W for 2 min over ice. Organic solvents were then evaporated for 3 h in a thermostatic bath (30°C) to remove the methylene chloride. To acquire microparticles encapsulated PFOB (MPs) as contrast, the organic solvents were evaporated immediately after the preemulsion's formation. NPs/MPs labeled coumarin-6/DiR were prepared by adding 50 μl coumarin-6/DiR to the organic solution prior to emulsification to label the polymer phase.

2.4. Measurement of NPs Characteristics. Particle diameter, size distribution, and zeta potential of the NPs/MPs were measured by a dynamic light-scattering system (DLS; Zetasizer Nano-ZS; Malvern Instruments, Worcestershire, England) at 25°C. The structure of the NPs was examined by transmission electron microscopy (TEM; Tecnai™ G2 Spirit TWIN, Netherlands). The morphology of microparticles was observed by optical microscope (Olympus, Japan).

2.5. Encapsulation Efficiency (EE). A weighed amount of NPs was dissolved into methanol following 5 min ultrasonic treatment and then centrifuged for 10 min. PFOB concentration of supernatant liquor was measured by gas chromatograph (GC) at 300°C, using flame ionization detector (FID). Percentages of encapsulation efficiency (% EE) were calculated based on the following equations:

$$\% \text{ EE} = \frac{\text{drug entrapped in NPs}}{\text{initial amount of drug added}} \times 100. \quad (1)$$

2.6. In Vitro Echogenicity of Contrast Agents Study. Each NP/MP suspension sample was filled in an Eppendorf tube. Ultrasound images were obtained in a nonlinear mode with a commercial ultrasound imaging system (L 74M probe, HI VISION Ascendus, Hitachi, Japan). All images were acquired using the same instrument parameters: frame rate (FR) 26, brightness (BG) 20, and dynamic range (DR) 65 db.

2.7. Tumor-Bearing Mouse Model. Nude male BALB/c mice (age of 5 weeks) were obtained from Hunan Slake Jingda Experimental Animal Co., Ltd. (Changsha, China). Approximately 1.0×10^7 HepG2 cells were inoculated subcutaneously into the right hind legs of the mice. All in vivo experiments began when the diameter of tumors reached 0.8–1.2 cm. The laboratory animal management committee and ethics committee at the Third Xiangya Hospital of Central South University approved all animal experiments.

2.8. In Vivo Echogenicity of Contrast Agents. Tumor-bearing nude mice were divided into two groups at random: the

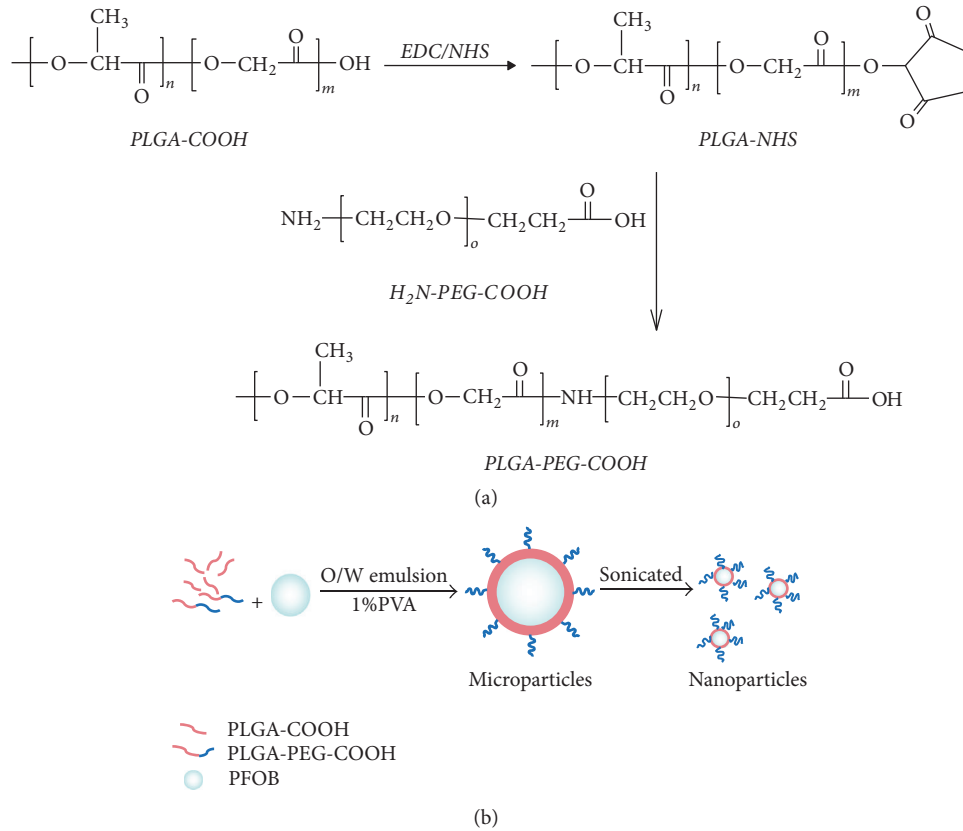


FIGURE 1: Synthesized PEG-PLGA-COOH copolymer in CDCl_3 (a). Schematic representation of the preparation process of nanoparticles for ultrasonic imaging (b).

control group (three mice injected with MPs) and the experimental group (six mice injected with NPs). No animal deaths occurred in the experimental process.

Mice were anesthetized with 1% pentobarbital sodium by abdominal injection (1 mg/100 g); 0.3 ml samples were injected into the body via the tail vein. Images were collected before and after injection: 0.5 h, 2 h, 12 h, 24 h, and 48 h, using a L74M transducer with 10 MHz and MI of 1.0. No instrument parameters changed during this experiment. All data and images were stored for offline analysis. Because of individual differences and tumor heterogeneity, gray-scale images were quite different. We defined the quantitative gray scale as follows.

$$\text{The increased rates} = \frac{\text{RGV}_x - \text{RGV}_0}{\text{RGV}_0}. \quad (2)$$

RGV_0 referred to image gray-scale intensity before the injection, and RGV_x referred to image gray-scale intensity after the injection [6].

2.9. Optical Imaging. IVIS Lumina II (Caliper, Alameda, CA, USA) was used for in vivo optical imaging. NPs and MPs containing DiR were injected into 2 groups of mice (3 mice per group). Then mice were put into an opaque black box. The excitation filter of DiR was 745 nm and emission filter of it was 810–875 nm. Images were obtained by the CCD camera at 0 h, 0.5 h, 2 h, 12 h, 24 h, and 48 h. All the data were analyzed by Living Image® Software 4.0 (Caliper, Alameda, CA, USA).

2.10. Histological Analysis. NPs or MPs labeled coumarin-6 was injected into two groups of mice (3 mice per group). After being injected for 24 h, tumor-bearing mice were killed, and collected tumors were sectioned into $5 \mu\text{m}$ slices. Frozen sections were stained with DAPI for labeling the nuclei of tumor cells. Images were obtained by using a fluorescence microscope (Olympus). DAPI and coumarin-6 were excited at 340 and 466 nm, respectively, and the emission was recorded at 488 and 504 nm, respectively.

2.11. Statistical Methods. All experiments were conducted in triplicate. All data were expressed as the mean \pm SD. Statistical analyses were performed using one-way analysis of variance (ANOVA) and *t* test.

3. Results

3.1. Synthesis and Characterization of PLGA-PEG. The chemical composition of the synthesized product was confirmed by $^1\text{H-NMR}$ (Figure 2). The characteristic peaks at 1.5, 4.8, and 5.2 ppm belonged to the methyl (d, $-\text{CH}_3$), methane (m, $-\text{CH}_2$), and methine (m, $-\text{CH}$) proton of the PLGA segment, respectively. The peak at 3.7 ppm was associated with the methene (s, $-\text{CH}_2$) proton of the PEG chain. By using the relative molecular weights and the integration of characteristic peaks at 5.20 and 3.7 ppm, the conjugation efficiency of NH_2 -PEG-COOH to PLGA-COOH was estimated to be 12.5%.

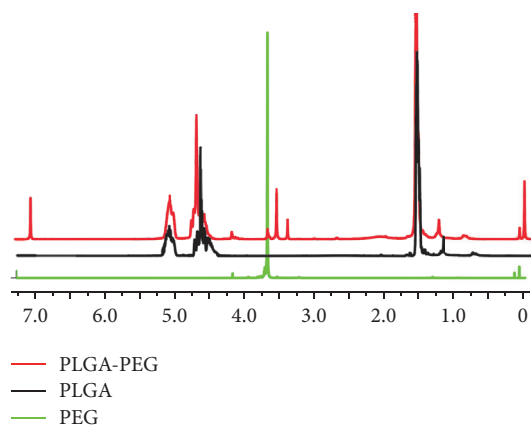


FIGURE 2: $^1\text{H-NMR}$ spectra of PLGA, PEG, and PLGA-PEG.

3.2. Characterization of NPs. The size distribution and zeta-potential of the NPs and MPs were assessed. The mean diameter of the NPs was 212.7 ± 2.76 nm (Figure 3(a)) with a polydispersity distribution (PDI) of 0.16 ± 0.03 . In contrast, the mean diameter of the MPs was 2480.4 ± 380.4 nm (Figure 3(b)) with a PDI of 0.32 ± 0.037 . The zeta-potential of the NPs was -32.7 ± 1.02 mV. MPs had a zeta-potential of -12.5 ± 2.03 mV. Under TEM, the NPs (Figure 3(c)) were spherical and had an intact and homogeneous shell. Because of the different electronic densities, the shell seemed darker than the gray core. MPs observed by optical microscopy were all core-shelled (Figure 3(d)). Encapsulation efficiency of the nanoparticles was $80.43 \pm 0.96\%$, and the concentration of PFOB in NPs solution was 10.09 mg/ml.

3.3. In Vitro Ultrasound Imaging. To compare the ultrasonic reflectance ability of NPs with that of MPs, in vitro ultrasound imaging was acquired by using diagnostic high-frequency ultrasound (10 MHz) (Figure 4(a)). The results showed that, with the same PFOB concentration of NPs and MPs (10 mg/ml), the ultrasonic signals of NPs were weaker, but there was no statistical difference between the two groups (Figure 4(b)).

We also studied the influence of concentration and probe frequency on ultrasonic signals produced by NPs. Enriched NPs were diluted with degassing deionized water (C6: 30 mg/ml; C5: 20 mg/ml; C4: 10 mg/ml; C3: 5 mg/ml; C2: 2.5 mg/ml; and C1: 1.25 mg/ml). Figure 5(a) showed ultrasonic reflection images of the NPs of six different concentrations at three different frequencies (5, 9, and 13 MHz). When the concentration and the frequency were the lowest, the echo reflection of the solution was the lowest (C1–5 MHz). The signal was weak at 5 MHz (C6–5 MHz) even if the concentration was high (>10 mg/ml). The signal obviously enhanced at 9 MHz or 13 MHz especially when the concentration of NPs was ≥ 10 mg/ml. The gray-scale concentration relationship was shown in Figure 5(b). The former part of steeper curves of 13 MHz and 9 MHz revealed a linear-like relationship when concentration was from 1.25 to 10 mg/ml, and the latter part of

the curves became even when concentration was ≥ 10 mg/ml. The curve at 5 MHz as a whole was comparatively flat.

We also separately studied the influence of mechanical index (MI) on NPs echo reflection. We selected a 10 mg/ml sample as the research object. Figure 5(c) showed that the image gray levels became higher with increasing MI. When the MI was 0.1, the echo reflection of the sample was close to the echo reflection of degassed deionized water. The contrast enhancement did not become weak at $\text{MI} > 0.6$ even if the contrast agent was exposed to ultrasound for 10 minutes.

3.4. Ultrasonic Imaging of Tumor-Burdened Mice. Tissue harmonic imaging- (THI-) mode imaging was carried out on two groups of tumor-bearing mice. The tumor images of the contrast enhancement were provided by NPs (Figure 6(a)) and MPs (Figure 6(b)). Tumor images showed obvious enhancement in the NP and MP groups at different time. Intensity-time diagrams of the tumors were illustrated in Figure 6(c). In the NP group, the increased rates (TIR) slowly rose after injection. The TIR was 30% 0.5 h after injection and two hours later, the TIR was 97%. The ultrasound enhancement effect produced by NPs was clearly distinguishable. After then, enhanced intensity strengthened continuously. 24 h after injection, contrast enhancement of NPs at the tumor site was still evident (TIR = 121%). This trend is different from that in MP group which had a rapid wash-in and washout. Time-intensity curve showed that ultrasound gray enhanced and reached the peak (TIR = 110%) at 0.5 h after being injected with MPs, and then it weakened quickly. In order to further compare the contrast enhancements in NP and MP groups, the area under the curve (AUC) plotted after injection from 0 to 48 h was created and statistically analyzed (Figure 6(d)). The results showed that the enhancement induced by NPs (AUC = 46.46 ± 5.92) was significantly stronger than the enhancement induced by the MPs (AUC = 8.24 ± 6.45 , $P = 0.001$).

In addition, the images of liver and kidney were also analyzed before and after injection of NPs. The results showed that there was no significant gray contrast enhancement in liver and spleen after injection of NPs (data not shown).

3.5. In Vivo Optical Imaging. We conducted small animals living optical imaging to further confirm that the NPs could gather in the tumor tissue. In NP group (Figure 7(a)), the red fluorescence was obviously distributed in the livers and spleens 0.5 h and 2 h after injection. 12 h after injection, significant fluorescence signals were detected at tumor site and they were still strong 48 h after injection. In the MP group, no fluorescence signals were detected in the tumor tissue (Figure 7(b)). We performed a region of interest (ROI) in the tumor tissue to analyze fluorescence enhancement which accessed the DiR uptake in each specimen (Figure 7(c)). Fluorescence signal intensity increased to the peak 24 h after injection. It slowly faded and only reduced 15% 48 h after injection. For fluorescence imaging of isolated tumors, the nude mice were sacrificed 48 h after intravenous injection. There was obvious fluorescence emission of isolated tumor tissues in NP group (left), while no fluorescence appeared in MP group (right) (Figure 7(d)).

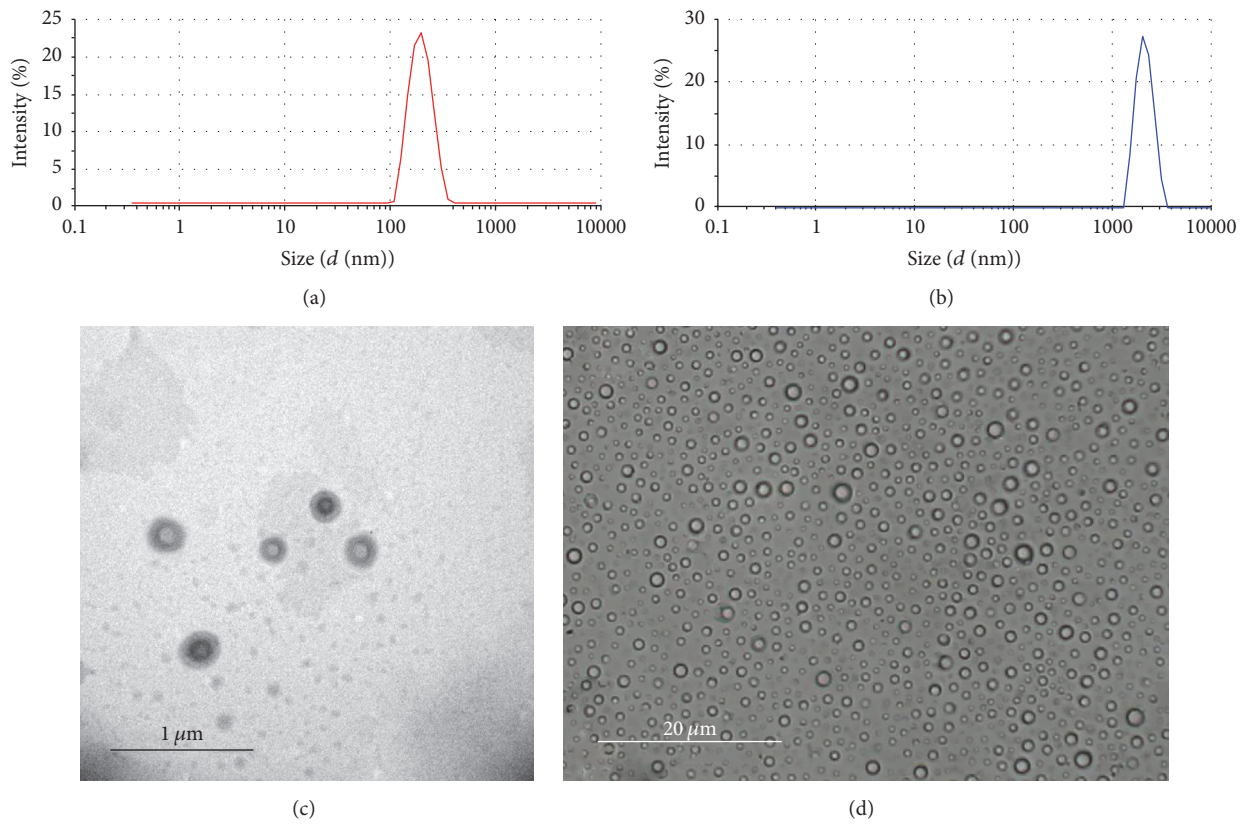


FIGURE 3: Particle size of the NPs and MPs. The size distribution was measured using dynamic light scattering in the NPs (a) and MPs (b). The morphologies of the NPs (c) and MPs (d) were determined by transmission electron micrographs and optical microscope, respectively.

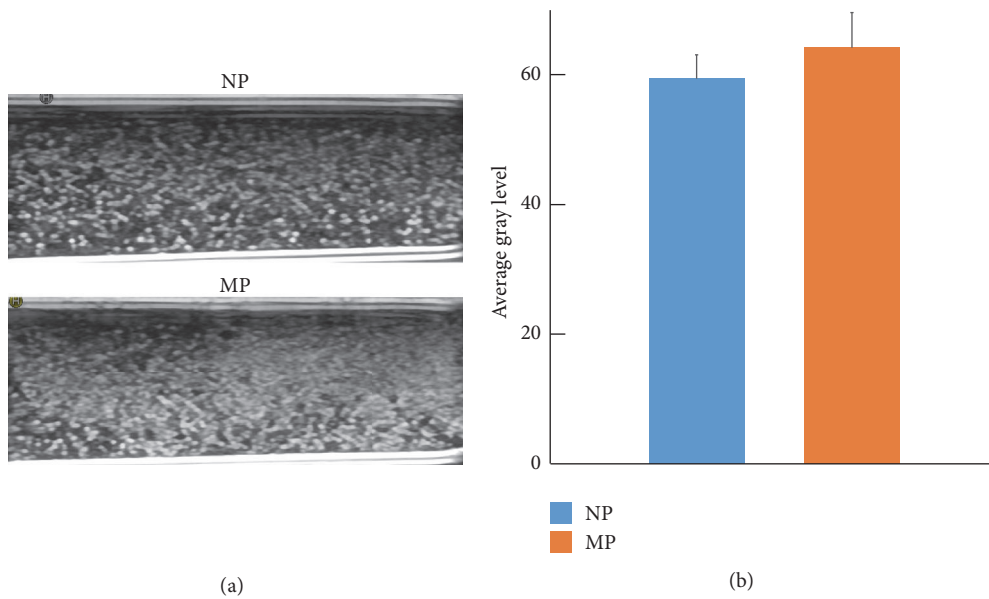


FIGURE 4: (a) Ultrasound imaging of NPs and MPs at 10 MHz in vitro. (b) Gray-scale ultrasonic intensity of NPs and MPs. NPs presented similar gray-scale intensity to MPs ($P = 0.361$).

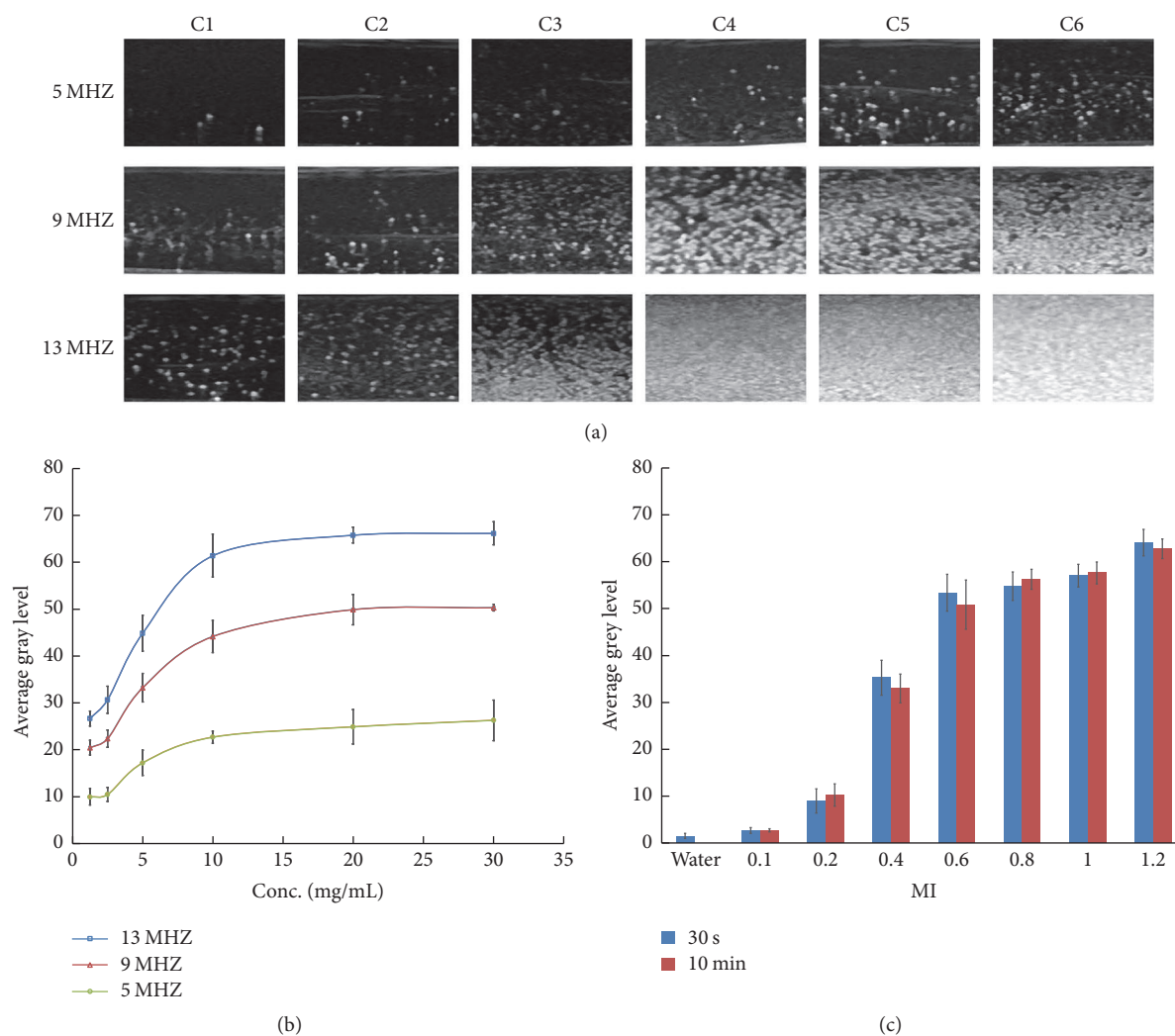


FIGURE 5: (a) Ultrasound images obtained in vitro in nonlinear mode at different concentration at 5, 9, and 13 MHz. C1: 1.25 mg/ml, C2: 2.5 mg/ml, C3: 5 mg/ml, C4: 10 mg/ml, C5: 20 mg/ml, and C6: 30 mg/ml. (b) Effect of nanoparticles concentration on echographic image brightness with different probe frequency at 5, 9, and 13 MHz. (c) Effect of mechanical index on echographic image brightness.

3.6. Histology. To further confirm the microscopic localization of NPs, the nude mice were sacrificed and frozen sections of the tumors were examined by fluorescence microscope. Tumor tissues of the nucleus were dyed blue by DAPI. NPs with green fluorescence appeared in areas beyond the nucleus in tumor tissue, but MPs with green fluorescence were not in tumor tissues (Figure 8).

4. Discussion

The purpose of this study is to use PFOB packaged PLGA-PEG-COOH and PLGA-COOH to prepare nanoscale UCA, which can generate contrast enhancement in vitro and in vivo. Regardless of the changes of the ratio of PLGA-PEG-COOH/PLGA-COOH, it is possible for a nanoparticle to maintain a complete shell structure by using such a mixture of membrane materials to package PFOB [18]. When the dose of PLGA-PEG was adjustable, NPs could carry enough PEG to avoid RES, so plasma half-life of NPs could be extended, and there was enough time for NPs to take advantage of EPR

effect to accumulate in the tumor [19, 20]. The combination between the end of PLGA-PEG containing active carboxyl group and the end of amino target ligand let NPs have the potential for active targeting [21, 22].

PEG molecular weight of 2000 or more can avoid the RES [9]. A PEG-3400 (25 nm) spacer was used in previous studies [22]. The PEG chain density is also important in achieving improved stealth. Both high and low surface coverage of PEG chains could not avoid RES [9]. In this experiment, the density of PEG is 2%, just within threshold values (between 2 and 5 wt %) for optimal protein resistance [23].

In the preparation of nanoscale UCA, particle size and size distribution are important parameters that determine the fate of UCA in vivo studies. To get through the tumor's endothelial pore (typically between 380 and 780 nm) and escape from the RES trapping effect (i.e., NPs whose diameters were bigger than 300 nm gradually start to be trapped significantly), the optimal diameter of NPs for clinical employment should be less than 300 nm [24]. In the process

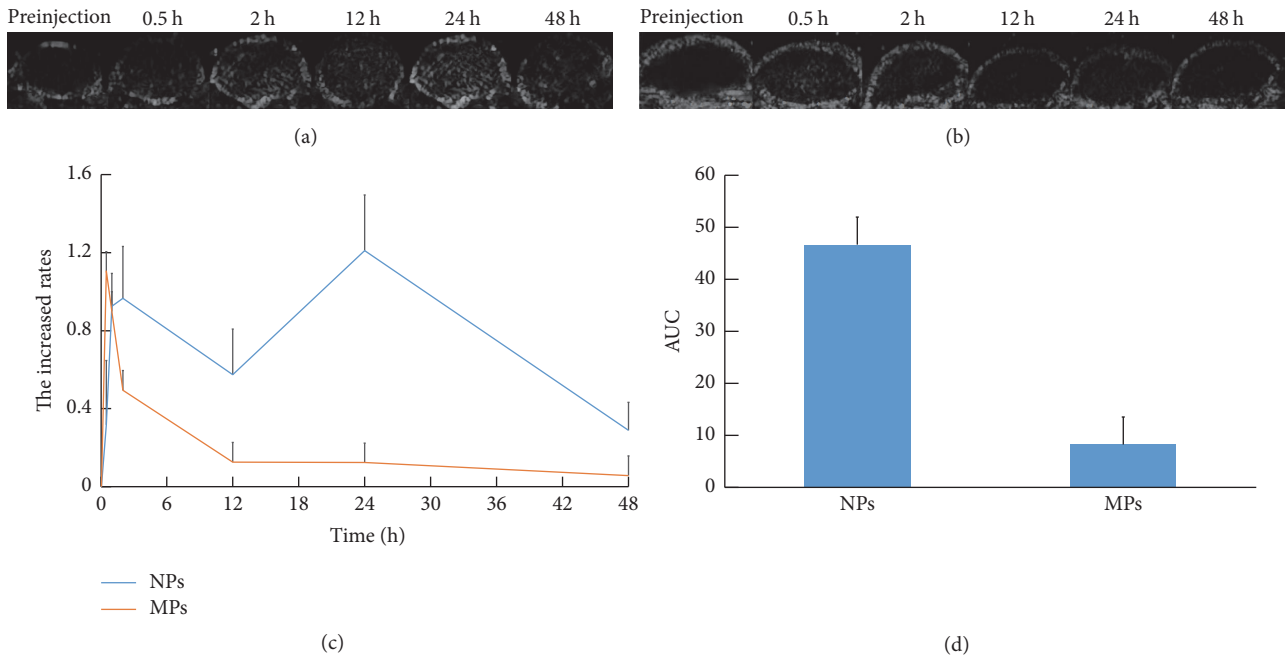


FIGURE 6: In vivo ultrasonic imaging of tumor-burdened mice. Representative subcutaneous tumor images before and after the injection of nanoparticles (NPs) (a) compared with MPs (b) at various time points (preinjection, 0.5 h, 2 h, 12 h, 24 h, and 48 h). Corresponding time-intensity curves of tumor enhancement after injection of the contrast agent (c). (d) AUC analysis with data was extracted from figure (c) ($P = 0.001$).

of preparation of nanoparticles, the shell thickness could influence the echogenicity of contrast agents. The T/R (the thickness-to-radius ratio) was used to evaluate the shell thickness of UCA. When PFOB was packaged by PLGA at maximum, the T/R was the largest, the shell of UCA was the thinnest, and the compressibility of UCA was best and it had the highest acoustic signal [14]. However, the T/R of UCA was only related to the proportion of PLGA and PFOB in the formulation. When PLGA was 100 mg and PFOB was 60 μl , the T/R was minimal. Therefore, when PFOB was $>60 \mu\text{l}$, free PFOB droplets appeared [17].

Ultrasound contrast agents have the ability to enhance echogenicity. Higher concentration could produce more echo reflection and stronger echo signal. The intensity of echo reflection was directly proportional to the concentration of the particles [25]. According to Rayleigh scattering, when the particle diameter was much smaller than the wavelength, the backscatter intensity produced by the particles was proportional to the incident wave frequency to the 4th power. The higher frequency was, the greater backscattering and the stronger ultrasound intensity were seen [26].

We separately studied the effect of the MI on echo reflection. The MI is a measure of the power of an ultrasound beam. The higher the MI was valued, the greater the energy of ultrasonic emission was and the greater echo reflection results were [27]. Echogenicity was brighter at a higher MI value than at a lower MI value. Our experiment showed that NPs were stable and produced sustained ultrasonic contrast enhancement at a high MI. While microbubbles produced ultrasonic contrast enhancement when $MI < 0.5$ and when $MI > 0.5$ for transient cavitation, the microbubbles burst

and produced instant and violent increases in ultrasonic reflection [28].

The ability of NPs to reflect ultrasound was almost the same as that of MPs but their time of contrast enhancement was longer than that of MPs in vivo due to the small size of NPs. The time of the contrast enhancement process was longer than 24 h, similar to Rapoport's research [29]. The time dependence of gray enhancement was based on the vascular permeability [30]. Tumor blood vessels with high permeability allowed nanoscale particles to permeate the tumor vasculature and remain in the tumor tissue. The gray contrast enhancement lasted for 24 hours after injection in tumor tissue which suggested that more NPs passed through the endothelial gaps and retained there with time going.

Target, distribution, and metabolism of contrast agents in vivo can be observed by small animals living optical imaging [31]. The tendency of the accumulated fluorescence at tumor site consistent with the tumor ultrasound imaging suggested that the NPs remained at the tumor tissue. 48 h after injection, the higher intensity of fluorescence was shown in the tumor since fluorescence agent DiR was not easy to quench in vivo [32]. Fluorescence signals were observed in livers and spleen in two groups due to reticuloendothelial system (RES) uptake. In the control group, the MPs were quickly cleared by RES, so no fluorescent signal was found in tumor tissues.

Histofluorescence imaging revealed the location of the NPs after intravenous injection. The tumors are heterogeneous. Endothelial monolayers and the cells lining of the tumor vessel are defective. This presented intercellular openings, transcellular holes, and endothelial fenestrae. The functional pore size of different tumors varied ranging from

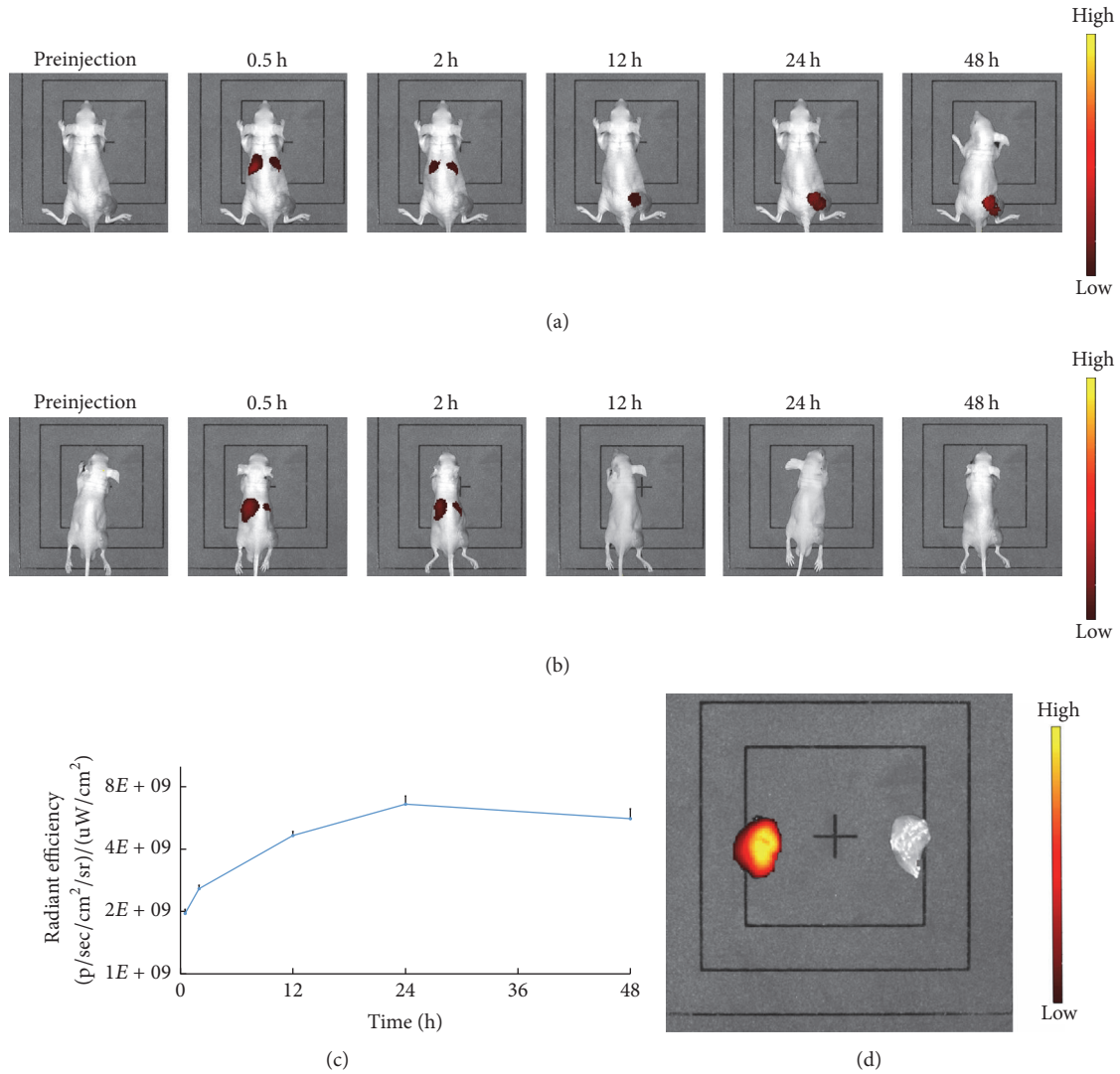


FIGURE 7: In vivo DiR fluorescence imaging results for NPs (a) group and MPs (b) group at preinjection, 0.5 h, 2 h, 12 h, 24 h, and 48 h. (c) Fluorescence intensity-time curve at tumor site after injection with NPs. (d) Comparison of DiR fluorescence in isolated tumor tissues of NP group (left) and MP group (right) at 48 h after intravenous injection.

200 nm to 2000 nm [4]. In the present research, NPs labeled Cou-6 accumulated in the tumor after penetrating through endothelial gaps, and we could observe green fluorescence in the images. However, in MP group, no green fluorescence was observed in the tumor, which meant that MPs labeled Cou-6 could not gather in the tumor by EPR. The ultrasonic imaging performance could be explained by these phenomena, where NPs penetrated tumor vessels and accumulated in the tumor at the later stage of ultrasound contrast-enhanced imaging. Thus, the time of the contrast enhancement would be much longer than that of using the MPs, which could not penetrate tumor vessels.

5. Conclusions

PFOB, with good echo enhancement ability, is the candidate of nanoultrasonic contrast agents. But PFOB is soluble neither in water nor in oil and it cannot be injected directly into the body, so usually it needs to be wrapped in a shell. The

membrane materials that make up the shell should be able to completely package PFOB within the nanometer range, and the generated NPs have a good echo enhancement in vitro. They also enable NPs to escape the removal of RES in vivo and image after gathering in tumor tissues.

In this work, we used membrane materials, PLGA-COOH and PLGA-PEG-COOH packaged PFOB, to produce nanometer UCA. Nanoparticles were all shell-core structures. We evaluated their echogenic ability in vitro and in vivo. In vivo fluorescence imaging and frozen section further confirmed that the NPs could accumulate in tumor tissues. Their characteristics suggested that NPs may be applicable to ultrasonic molecular imaging and targeting therapy/drug/gene delivery to tumor.

Conflicts of Interest

The authors report no conflicts of interest.

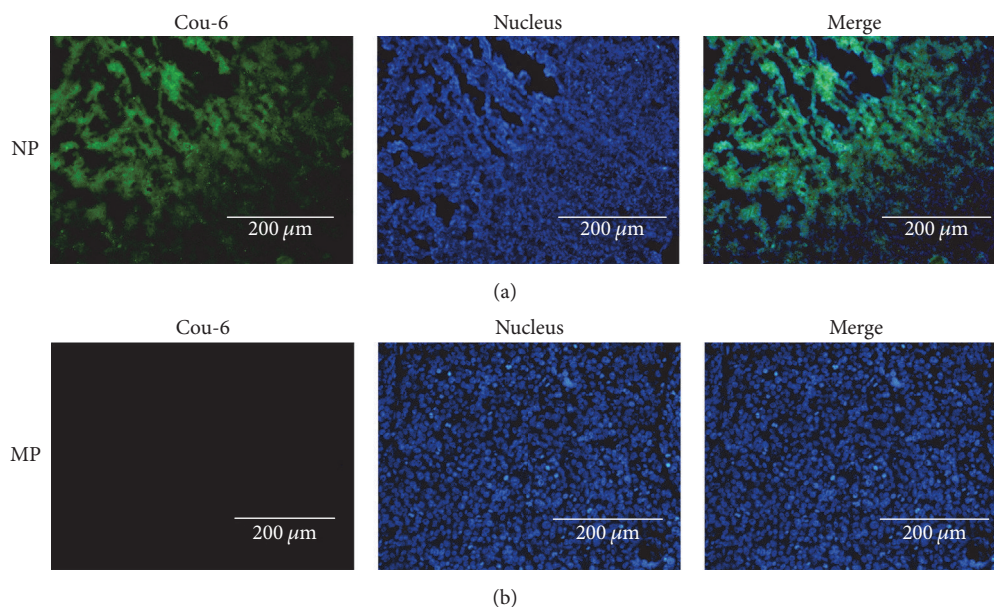


FIGURE 8: Histologic fluoroscopy images of frozen sections after nuclear labeling. Many coumarin-6-labeled NPs (green) were observed in the tumor intercellular space (a); coumarin-6-labeled MPs were hard to detect in the tumor intercellular space (b). Blue represents nuclear staining.

Acknowledgments

The authors thank Dr. Wuyang Zhu for his kind guidance and inspirational suggestions. This study is supported by the Hunan Province Science and Technology Fund (no. 2015JJ6112) and the National Natural Science Foundation of China (NSFC) (81202271, 81471715, 30900359, and 81771827).

References

- [1] K. H. Martin and P. A. Dayton, "Current status and prospects for microbubbles in ultrasound theranostics," *Wiley Interdisciplinary Reviews: Nanomedicine and Nanobiotechnology*, vol. 5, no. 4, pp. 329–345, 2013.
- [2] K. Seitz and D. Strobel, "A Milestone: Approval of CEUS for Diagnostic Liver Imaging in Adults and Children in the USA," *Ultraschall in der Medizin / European Journal of Ultrasound (UiM/EJU)*, vol. 37, no. 3, pp. 229–232, 2016.
- [3] T. Faez, M. Emmer, K. Kooiman, M. Versluis, A. Van Der Steen, and N. De Jong, "20 years of ultrasound contrast agent modeling," *IEEE Transactions on Ultrasonics, Ferroelectrics and Frequency Control*, vol. 60, no. 1, pp. 7–20, 2013.
- [4] S. K. Hobbs, W. L. Monsky, F. Yuan et al., "Regulation of transport pathways in tumor vessels: role of tumor type and microenvironment," *Proceedings of the National Academy of Sciences of the United States of America*, vol. 95, no. 8, pp. 4607–4612, 1998.
- [5] M. Néstor, N. E. Kei, N. M. Guadalupe, M. S. Elisa, G. Adriana, and Q. David, "Preparation and in vitro evaluation of poly(D,L-lactide-co-glycolide) air-filled nanocapsules as a contrast agent for ultrasound imaging," *Ultrasonics*, vol. 51, no. 7, pp. 839–845, 2011.
- [6] T. Yin, P. Wang, R. Zheng et al., "Nanobubbles for enhanced ultrasound imaging of tumors," *International Journal of Nanomedicine*, vol. 7, pp. 895–904, 2012.
- [7] H. Wu, N. G. Rognin, T. M. Krupka et al., "Acoustic characterization and pharmacokinetic analyses of new nanobubble ultrasound contrast agents," *Ultrasound in Medicine & Biology*, vol. 39, no. 11, pp. 2137–2146, 2013.
- [8] H. Yang, W. Cai, L. Xu et al., "Nanobubble-Affibody: Novel ultrasound contrast agents for targeted molecular ultrasound imaging of tumor," *Biomaterials*, vol. 37, pp. 279–288, 2015.
- [9] D. E. Owens III and N. A. Peppas, "Opsonization, biodistribution, and pharmacokinetics of polymeric nanoparticles," *International Journal of Pharmaceutics*, vol. 307, no. 1, pp. 93–102, 2006.
- [10] J. L. Raymond, Y. Luan, T. Peng et al., "Loss of gas from echogenic liposomes exposed to pulsed ultrasound," *Physics in Medicine and Biology*, vol. 61, no. 23, pp. 8321–8339, 2016.
- [11] G. M. Lanza, D. R. Abendschein, C. S. Hall et al., "In vivo molecular imaging of stretch-induced tissue factor in carotid arteries with ligand-targeted nanoparticles," *Journal of the American Society of Echocardiography*, vol. 13, no. 6, pp. 608–614, 2000.
- [12] J. N. Marsh, K. C. Partlow, D. R. Abendschein, M. J. Scott, G. M. Lanza, and S. A. Wickline, "Molecular Imaging With Targeted Perfluorocarbon Nanoparticles: Quantification of the Concentration Dependence of Contrast Enhancement for Binding to Sparse Cellular Epitopes," *Ultrasound in Medicine & Biology*, vol. 33, no. 6, pp. 950–958, 2007.
- [13] R. Díaz-López, N. Tsapis, M. Santin et al., "The performance of PEGylated nanocapsules of perfluorooctyl bromide as an ultrasound contrast agent," *Biomaterials*, vol. 31, no. 7, pp. 1723–1731, 2010.
- [14] E. Pisani, N. Tsapis, B. Galaz et al., "Perfluorooctyl bromide polymeric capsules as dual contrast agents for ultrasonography and magnetic resonance imaging," *Advanced Functional Materials*, vol. 18, no. 19, pp. 2963–2971, 2008.
- [15] J.-M. Rabanel, P. Hildgen, and X. Banquy, "Assessment of PEG on polymeric particles surface, a key step in drug carrier

- translation,” *Journal of Controlled Release*, vol. 185, no. 1, pp. 71–87, 2014.
- [16] V. Sanna, G. Pintus, P. Bandiera et al., “Development of polymeric microbubbles targeted to prostate-specific membrane antigen as prototype of novel ultrasound contrast agents,” *Molecular Pharmaceutics*, vol. 8, no. 3, pp. 748–757, 2011.
- [17] E. Pisani, N. Tsapis, J. Paris, V. Nicolas, L. Cattel, and E. Fattal, “Polymeric nano/microcapsules of liquid perfluorocarbons for ultrasonic imaging: Physical characterization,” *Langmuir*, vol. 22, no. 9, pp. 4397–4402, 2006.
- [18] E. Pisani, C. Ringard, V. Nicolas et al., “Tuning microcapsules surface morphology using blends of homo- and copolymers of PLGA and PLGA-PEG,” *Soft Matter*, vol. 5, no. 16, pp. 3054–3060, 2009.
- [19] H. Maeda, H. Nakamura, and J. Fang, “The EPR effect for macromolecular drug delivery to solid tumors: Improvement of tumor uptake, lowering of systemic toxicity, and distinct tumor imaging in vivo,” *Advanced Drug Delivery Reviews*, vol. 65, no. 1, pp. 71–79, 2013.
- [20] Y. Matsumura and H. Maeda, “A new concept for macromolecular therapeutics in cancer chemotherapy: mechanism of tumoritropic accumulation of proteins and the antitumor agent smancs,” *Cancer Research*, vol. 46, no. 12, pp. 6387–6392, 1986.
- [21] S. M. Taghdisi, N. M. Danesh, A. Sarreshtehdar Emrani et al., “Targeted delivery of Epirubicin to cancer cells by PEGylated A10 aptamer,” *Journal of Drug Targeting*, vol. 21, no. 8, pp. 739–744, 2013.
- [22] W. Zhou, Y. Zhou, J. Wu et al., “Aptamer-nanoparticle bioconjugates enhance intracellular delivery of vinorelbine to breast cancer cells,” *Journal of Drug Targeting*, vol. 22, no. 1, pp. 57–66, 2014.
- [23] R. Gref, M. Lück, P. Quellec et al., “‘Stealth’ corona-core nanoparticles surface modified by polyethylene glycol (PEG): Influences of the corona (PEG chain length and surface density) and of the core composition on phagocytic uptake and plasma protein adsorption,” *Colloids and Surfaces B: Biointerfaces*, vol. 18, no. 3–4, pp. 301–313, 2000.
- [24] S. Casciaro, F. Conversano, A. Ragusa et al., “Optimal enhancement configuration of silica nanoparticles for ultrasound imaging and automatic detection at conventional diagnostic frequencies,” *Investigative Radiology*, vol. 45, no. 11, pp. 715–724, 2010.
- [25] F. Calliada, R. Campani, O. Bottinelli, A. Bozzini, and M. G. Sommaruga, “Ultrasound contrast agents: Basic principles,” *European Journal of Radiology*, vol. 27, no. 2, pp. S157–S160, 1998.
- [26] K. A. Wear, T. A. Stiles, G. R. Frank et al., “Interlaboratory comparison of ultrasonic backscatter coefficient measurements from 2 to 9 MHz,” *Journal of Ultrasound in Medicine*, vol. 24, no. 9, pp. 1235–1250, 2005.
- [27] T. Şen, O. Tüfekçioğlu, and Y. Koza, “Mechanical index,” *Anadolu Kardiyoloji Dergisi*, vol. 15, no. 4, pp. 334–336, 2015.
- [28] R. E. Apfel and C. K. Holland, “Gauging the likelihood of cavitation from short-pulse, low-duty cycle diagnostic ultrasound,” *Ultrasound in Medicine & Biology*, vol. 17, no. 2, pp. 179–185, 1991.
- [29] N. Rapoport, Z. Gao, and A. Kennedy, “Multifunctional nanoparticles for combining ultrasonic tumor imaging and targeted chemotherapy,” *Journal of the National Cancer Institute*, vol. 99, no. 14, pp. 1095–1106, 2007.
- [30] T. Yamaoka, Y. Tabata, and Y. Ikada, “Distribution and tissue uptake of poly(ethylene glycol) with different molecular weights after intravenous administration to mice,” *Journal of Pharmaceutical Sciences*, vol. 83, no. 4, pp. 601–606, 1994.
- [31] S. Hak, Z. Garaiova, L. T. Olsen, A. M. Nilsen, and C. De Lange Davies, “The effects of oil-in-water nanoemulsion polyethylene glycol surface density on intracellular stability, pharmacokinetics, and biodistribution in tumor bearing mice,” *Pharmaceutical Research*, vol. 32, no. 4, pp. 1475–1485, 2015.
- [32] H. Cho, G. L. Indig, J. Weichert, H.-C. Shin, and G. S. Kwon, “In vivo cancer imaging by poly(ethylene glycol)-b-poly(ϵ -caprolactone) micelles containing a near-infrared probe,” *Nanomedicine: Nanotechnology, Biology and Medicine*, vol. 8, no. 2, pp. 228–236, 2012.

Research Article

Gallium-68 Labeled Iron Oxide Nanoparticles Coated with 2,3-Dicarboxypropane-1,1-diphosphonic Acid as a Potential PET/MR Imaging Agent: A Proof-of-Concept Study

Maria-Argyro Karageorgou,^{1,2} Sanja Vranješ-Djurić,³ Magdalena Radović,³ Anna Lyberopoulou,⁴ Bratislav Antić,³ Maritina Rouchota,⁵ Maria Gazouli,⁴ George Loudos,^{1,6} Stavros Xanthopoulos,¹ Zili Sideratou,⁷ Dimosthenis Stamopoulos,^{2,7} Penelope Bouziotis,¹ and Charalampos Tsoukalas¹

¹*Institute of Nuclear & Radiological Sciences & Technology, Energy & Safety, National Center for Scientific Research “Demokritos”, Aghia Paraskevi, 15310 Athens, Greece*

²*Department of Solid State Physics, NKUA, Athens, Greece*

³*“Vinča” Institute of Nuclear Sciences, University of Belgrade, Mike Petrovica Alasa 12-14, 11000 Belgrade, Serbia*

⁴*Department of Basic Medical Science, Laboratory of Biology, School of Medicine, NKUA, Athens, Greece*

⁵*Department of Medical Physics, School of Medicine, University of Patras, P.O. Box 132 73, 265 04 Rion, Greece*

⁶*Department of Medical Instruments Technology, Technological Educational Institute of Athens, 28 Ag. Spyridonos Street, 12210 Egaleo, Greece*

⁷*Institute of Nanoscience and Nanotechnology, National Center for Scientific Research “Demokritos”, Aghia Paraskevi, 15310 Athens, Greece*

Correspondence should be addressed to Charalampos Tsoukalas; ctsoukal@rrp.demokritos.gr

Received 21 July 2017; Revised 13 November 2017; Accepted 15 November 2017; Published 28 December 2017

Academic Editor: Fernando Herranz

Copyright © 2017 Maria-Argyro Karageorgou et al. This is an open access article distributed under the Creative Commons Attribution License, which permits unrestricted use, distribution, and reproduction in any medium, provided the original work is properly cited.

The aim of this study was to develop a dual-modality PET/MR imaging probe by radiolabeling iron oxide magnetic nanoparticles (IONPs), surface functionalized with water soluble stabilizer 2,3-dicarboxypropane-1,1-diphosphonic acid (DPD), with the positron emitter Gallium-68. Magnetite nanoparticles (Fe_3O_4 MNPs) were synthesized via coprecipitation method and were stabilized with DPD. The Fe_3O_4 -DPD MNPs were characterized based on their structure, morphology, size, surface charge, and magnetic properties. *In vitro* cytotoxicity studies showed reduced toxicity in normal cells, compared to cancer cells. Fe_3O_4 -DPD MNPs were successfully labeled with Gallium-68 at high radiochemical purity (>91%) and their stability in human serum and in PBS was demonstrated, along with their further characterization on size and magnetic properties. The *ex vivo* biodistribution studies in normal Swiss mice showed high uptake in the liver followed by spleen. The acquired PET images were in accordance with the *ex vivo* biodistribution results. Our findings indicate that $^{68}\text{Ga-Fe}_3\text{O}_4$ -DPD MNPs could serve as an important diagnostic tool for biomedical imaging.

1. Introduction

Iron oxide magnetic nanoparticles (IONPs) have been subjected to a variety of biomedical applications due to their remarkable nanoscale physicochemical properties. Their small size, high surface to volume ratio and size-dependent

[1] magnetic properties make them ideal candidates for clinical applications, including magnetic resonance imaging (MRI), in which they serve as T2-contrast enhancement agents [2–4], hyperthermia treatment of cancer [5–7], cell separation [8], tissue repair [9], and magnetic force guided drug delivery [10]. Magnetite (Fe_3O_4) and its oxidized form

maghemite (Fe_2O_3) are the most common IONPs, which compose the core in a typical core-shell nanoparticle structure. Among the unique magnetic properties that IONPs demonstrate upon reducing their magnetic core size above a critical diameter (less than 20 nm for spherical IONPs), superparamagnetism is worth noting. IONPs lose their magnetization after the removal of the magnetic field and thus can be controllable. Additionally, their surface can be modified with biocompatible coatings via various methods [11, 12], rendering them biocompatible and applicable for biological systems. Thanks to the ease of surface functionalization, IONPs are provided with colloidal stability via steric and electrostatic interactions and high loading capacity via functional (i.e., hydroxyl, carboxyl, amino, and thiol) groups, in order to be bound with many active targeting molecules (such as antibodies, aptamers, and peptides) [13–16], drugs, and detection elements (i.e., radionuclides for molecular imaging, fluorescent molecules) according to demand in biomedical applications.

Colloidal stability of IONPs is of great importance to be considered in order to develop an effective imaging agent able to circulate in the bloodstream for as long as it takes to be accumulated in the target-organ. However, uncoated nanoparticles are prone to opsonization and tend to agglomerate *in vivo* (i.e., via Van der Waals, magnetic dipole-dipole, and hydrophobic interactions), leading to the formation of micrometer-sized particles, which mostly accumulate in the organs of the Reticuloendothelial System (RES), resulting in rapid sequestration from blood circulation. On the other hand, surface coating with appropriate organic and inorganic [17, 18] coatings provides IONPs with stealth properties, increased stability, and reduced cytotoxicity, consequently improving their potential use for *in vivo* applications [19].

The need for early cancer diagnosis has led scientists to a tremendous effort of developing noninvasive multimodal imaging agents able to detect abnormalities *in vivo* more accurately. As a consequence, the necessity of synthesizing dual-modality imaging agents, such as radiolabeled IONPs, has emerged in the last years in biomedical sciences, due to their ability to circumvent the limitations of a single imaging modality. In fact, conventional imaging modalities, namely, X-ray computed tomography (CT), optical imaging (OI), and magnetic resonance imaging (MRI), as well as positron emission (PET) and single-photon emission (SPECT) tomography, widely used in nuclear medicine, possess their own advantages and disadvantages. Particularly, PET (and/or SPECT) provides qualitative images with high sensitivity and specificity; however the anatomical information via this modality is diminished. On the contrary, MRI provides necessary anatomical information due to its high spatial resolution and contrast in soft tissue, but it exhibits relatively poor sensitivity [20]. This is the case why radiolabeled IONPs surpass conventional imaging modalities, since the combination of these two modalities (PET/MRI and/or SPECT/MRI) in a dual-modality agent has a synergistic result, ultimately exhibiting a much improved potential for biomedical imaging. Several papers have been reported concerning radiolabeled IONPs developed for PET/SPECT-MRI imaging combined with other biomedical applications

like controlled drug delivery and hyperthermia treatment to achieve both diagnosis and therapy of cancer [21–24].

PET radionuclides such as Fluorine-18 and Carbon-11, commonly used in clinical practice, require time consuming and expensive facilities (i.e., on-site cyclotron) to be produced. On the other hand, radionuclides obtained from a generator-based system have received significant attention since they are inexpensive and easily available at any time for clinical use. Among them, Gallium-68 (^{68}Ga ; $T_{1/2} = 68$ min) is an attractive radioisotope for PET imaging due to its high proportion of positron decay (89%) of 1.9 MeV (maximum energy) and its availability from a $^{68}\text{Ge}/^{68}\text{Ga}$ generator permitting three elutions per day. Specifically, the long-lived radionuclide ^{68}Ge ($T_{1/2} = 270.8$ days) decays via electron capture, providing the ^{68}Ga radionuclide. It is worthy to be mentioned that few papers have been reported in the literature, concerning radiolabeling with ^{68}Ga radionuclide of IONPs, synthesized in various sizes and shapes, to create dual-modality conjugates able to detect malignancies [25–28].

The imaging agent described in this work consists of Fe_3O_4 MNPs, surface functionalized with the water soluble stabilizer 2,3-dicarboxypropane-1,1-diphosphonic acid (DPD) and radiolabeled directly with ^{68}Ga for PET imaging. The substance DPD was used because it is water soluble and biocompatible, providing the appropriate dispersing stability and minimizing the potential cytotoxicity of the naked Fe_3O_4 MNPs. Furthermore, as a tetradentate ligand (with two phosphonates and two carboxylate groups), DPD serves as an effective chelating agent, as has been shown for ^{90}Y , leading to the formation of a highly stable conjugate [29]. *In vitro* stability studies were performed with ^{68}Ga - Fe_3O_4 -DPD MNPs, to assess the stability of the complex in biological media, while *in vitro* cytotoxicity studies of the Fe_3O_4 -DPD MNPs were performed to evaluate their potential toxicity in both normal and cancer cell lines. To assess the *in vivo* behavior of the ^{68}Ga - Fe_3O_4 -DPD MNPs *ex vivo* biodistribution studies and dynamic and cumulative imaging studies were performed in normal animal models.

2. Materials and Methods

2.1. Chemicals. 2,3-Dicarboxypropane-1,1-diphosphonic acid (DPD) was synthesized at the Laboratory for Radioisotopes of the “Vinča” Institute of Nuclear Sciences, according to a previously reported procedure [30]. All other reagents and solvents used in these studies were obtained from commercial sources without further purification. Iron(II) sulfate hepta-hydrate ($\text{FeSO}_4 \times 7\text{H}_2\text{O}$), iron(III) sulfate hydrate ($\text{Fe}_2(\text{SO}_4)_3 \times \text{H}_2\text{O}$), sodium hydroxide (NaOH), and aqueous ammonia solution (25%) were obtained from Sigma-Aldrich. Purified deionized water was prepared by the Milli-Q system (Millipore Co., Billerica, MA, USA). A lower activity commercial $^{68}\text{Ge}/^{68}\text{Ga}$ generator was acquired from ITG Garching (Garching, Germany). 30% HCl Suprapur (Merck, Darmstadt, Germany), acetone (Sigma-Aldrich), 2,4-pentanedione 99% (Alfa Aesar, Karlsruhe, Germany), and 37% HCl (Riedel-de Haën) were commercially available and used as

received. Human serum was acquired from Sigma-Aldrich (St. Louis, MO, USA). The MTT tetrazolium salt, 3-(4,5-dimethylthiazol-2-yl)-2,5-diphenyltetrazolium bromide, was acquired from Thermo Fisher Scientific (Cat. number M6494).

2.2. Equipment. Radioactivity of the $^{68}\text{GaCl}_3$ eluent was measured using a dose calibrator (Capintec, Ramsey, NJ). Thin layer chromatography (TLC) silica gel 60 sheets (5×10 cm) were purchased from Merck (Darmstadt, Germany) and along with a Radio-TLC Scanner (Scan-Ram, LabLogic, Sheffield, UK) were used in the determination of radiolabeling yield/purity and *in vitro* stability studies. PD-10 columns (GE Healthcare), containing Sephadex G-25 resin, were used for the purification of radiolabeled samples. Water was deionized to 18 M Ω -cm using an easy-pure water filtration system (Barnstead International, Dubuque, Iowa). Gamma scintillation counter, Cobra II, Canberra, Packard, was used to measure the radioactivity of each organ and blood samples in *ex vivo* biodistribution studies. AXIOS-150/EX (Triton Hellas) dynamic light scattering (DLS) apparatus equipped with a 30 mW He-Ne laser emitting at 658 nm and an Avalanche photodiode detector at an angle of 90° was used for the determination of the size distributions of the particles. Atomic force microscopy (AFM) images were obtained by means of a scanning probe microscope [NT-MDT Solver PRO]. Magnetic measurements of liquid samples were performed by means of a SQUID magnetometer (5.5 T MPMS, Quantum Design). An ultrafast absorbance spectrophotometer (SPECTROstarNano, BMG LABTECH) for microplates and cuvettes was used in the MTT viability assay.

The imaging studies were performed on a custom-made trimodal system, incorporating a PET, a SPECT, and an X-ray subsystem [31]. For the current study the combination of PET coincidence imaging and X-rays was used. The dual head PET system is based on a pair of Position Sensitive Photo-Multiplier Tubes (PSPMTs), coupled to a 5×10 cm 2 bismuth germanium oxide (BGO) scintillator array, with a pixel size of $2 \times 2 \times 5$ mm 3 and readout based on programmable ADCs and FPGA. The two heads are placed at an 80 mm distance and predefined acquisition parameters are a timing window of 16 ns and an energy window between 350 and 700 keV. The system average spatial resolution in coincidence mode is 3.5 mm, the peak sensitivity is 13483 cps/MBq, and the energy resolution is 30%. The X-ray system consists of an X-ray tube and a CMOS detector, separated by a distance of 30 cm. The minimum pixel size is equal to 0.1 mm and the active area is approximately 12×12 cm 2 .

2.3. Synthesis of Fe_3O_4 -DPD MNPs. Magnetite nanoparticles were prepared by the alkali-mediated chemical coprecipitation of Fe^{2+} and Fe^{3+} ions (1:2 ratio), as described elsewhere [32]. In a typical experiment, ferrous sulfate heptahydrate (0.1 M) and ferric sulfate hydrate (0.2 M) were dissolved in deionized water. Subsequently 25% ammonia solution (ca. 20 ml) was injected into the flask and stirring was continued for 1 h at 50°C to allow the growth of the nanoparticles. The

solution was subjected to magnetic decantation followed by repeated washing with distilled water. After the magnetite synthesis, the coating reaction was carried out by the addition of 0.25 g/2 mL DPD water solution (Fe_3O_4 : DPD = 1:1). The pH of the resultant mixture was adjusted to 8-9 by addition of 6 M NaOH. Then, the mixture was stirred overnight at room temperature and further subjected to dialysis against deionized water (MWCO 12 kDa) for 1 d to remove the excess of unreacted DPD.

2.4. Physicochemical Characterization of MNPs. The phase analysis of the synthesized MNPs powder was performed on a Philips PW1710 X-ray diffractometer. The data were collected in the angular range 10 – 50° (2θ) with a step size of 0.06° and a counting time of 50 s per step. High resolution transmission electron microscopy (HRTEM) was employed to characterize the morphology, size and size distribution of the MNPs. The samples of MNPs were prepared by placing one drop of a dilute suspension of MNPs in water on a carbon-coated copper grid and allowing the solvent to evaporate at room temperature. The surface charge of the MNPs was investigated through zeta potential measurements (Zetasizer Nano, Malvern instruments, UK) at pH between 1 and 11. Fourier transform-infrared (FTIR) measurements were carried out at room temperature on a Nicolet 380 spectrometer (Thermo Fischer Scientific, USA) in the spectral range 4000 – 400 cm $^{-1}$, with 4 cm $^{-1}$ resolution. Thermogravimetric analysis (TGA) was carried out with a SDT Q600 TGA/DSC instrument (TA Instruments) up to 850°C , by heating the sample under a nitrogen flow at a heating rate of $10^\circ\text{C}/\text{min}$. The residual weight accounts for the mass of iron oxide nanoparticles in the ferrofluid. Magnetic measurements of powder samples were performed on a SQUID magnetometer. Magnetization versus temperature, $M(T)$, was measured in 2 – 300 K temperature range, under zero-field-cooled (ZFC) and field-cooled (FC) regimes, in 20 Oe. Hysteresis loops were measured at 300 K in ZFC regime.

2.5. In Vitro Cytotoxicity Study of Fe_3O_4 -DPD MNPs. Two epithelial cell lines were used for the evaluation of cytotoxicity of Fe_3O_4 -DPD MNPs, namely, HEK293T and 4T1. The normal cell line HEK293T is a highly transfectable derivative of human embryonic kidney 293 cell line that stably expresses the SV40 large T antigen. The 4T1 cell line is a highly breast metastatic tumorigenic 6-thioguanine resistant cell line derived from mouse that can metastasize to the lung, liver, lymph nodes, and brain, while the primary tumor is growing *in situ*. HEK293 are used as the control group (noncancerous cell line) in our experiments. Both cell lines were acquired from ATCC.

4T1 (ATCC CRL2539 $^{\text{TM}}$) and HEK293T (ATCC CRL-3216) cell lines were cultured in DMEM High Glucose Culture Medium (BioSera) containing 10% FBS, 2 mmol/L glutamine, 100 U/mL penicillin, and 0.1 mg/mL streptomycin at 37°C . The medium was changed every 48 h and cells were passaged once weekly using standard trypsin-EDTA concentrations. Beginning at passage 32 and 37, respectively, cells were

cultured continuously. Cells were frozen in freezing medium containing 10% FBS and 5% DMSO.

2.6. MTT Assay. The MTT tetrazolium salt is reduced by metabolically active cells, via the action of dehydrogenase enzymes. This leads to the generation of reducing equivalents such as nicotinamide adenine dinucleotide (NADH) and nicotinamide adenine dinucleotide phosphate (NADPH). The resulting intracellular purple formazan, from the initial yellow color of MTT, can be solubilized and quantified by spectrophotometry. The MTT cell viability assay measures alterations in cell viability thus; when metabolic events lead to apoptosis or necrosis, cell viability is decreased. As a general protocol, 5000 cells/well were seeded in 96-well plates (Corning-Costar, Corning, NY) and cultured overnight. Three different types of controls, namely, positive, negative, and background, were used throughout the study. Positive control had cells with culture medium but were not exposed to MNPs. Negative control had MNPs without cells. Background control had culture medium without cells. The two different cell lines were treated with various concentrations of MNPs for 24 h. Subsequently, the cells were rinsed once and incubated at 37°C with 100 μ L serum-free medium, containing 0.5 mg/mL MTT. After 1.5 to 2.5 h, 100 μ L of SDS-HCl was added to each well, mixed with the pipette and incubated for at least 1 h at 37°C. The optical densities were read at 570 nm (reference filter was set at 690 nm), using a microplate spectrophotometer (SPECTROstarNano, BMG LABTECH). Absorbances were normalized with respect to the untreated control cultures to calculate changes in cell viability.

2.7. Labeling of Fe_3O_4 -DPD MNPs with ^{68}Ga . For the radiolabeling experiment, ^{68}Ga was eluted from the $^{68}\text{Ge}/^{68}\text{Ga}$ generator [33]. A fraction containing $^{68}\text{GaCl}_3$ (~45 MBq) in a volume of 100 μ L was used. Radiolabeling was performed by mixing 50 μ L of Fe_3O_4 -DPD NPs suspension ($C = 3.2$ mg/mL dispersed in water), 350 μ L of sodium acetate buffer (0.2 M, pH 4), and 100 μ L of $^{68}\text{GaCl}_3$ and incubating at 90°C for 40 min. The radiolabeling yield was determined by thin layer chromatography analysis (TLC). The strip was developed using a 2:1 mixture of HCl/Acetone/deionized water and 2,4-Pentanedione as the mobile phase. With this system, $^{68}\text{Ga}-\text{Fe}_3\text{O}_4$ -DPD MNPs remained at the application point, while unbound $^{68}\text{Ga}^{3+}$ ions migrate with the solvent front. The radiolabeled sample was purified by centrifugation (12000 rpm, 10 min). After washing twice with deionized water, the supernatant was removed and the radiolabeled sample was redispersed in deionized water. The % radiochemical purity of $^{68}\text{Ga}-\text{Fe}_3\text{O}_4$ -DPD MNPs was determined by TLC, as previously described. A control test was also carried out, in the absence of Fe_3O_4 -DPD MNPs.

2.8. In Vitro Stability Studies of $^{68}\text{Ga}-\text{Fe}_3\text{O}_4$ -DPD MNPs. To evaluate the *in vitro* stability of $^{68}\text{Ga}-\text{Fe}_3\text{O}_4$ -DPD MNPs, a sample of 10 μ L $^{68}\text{Ga}-\text{Fe}_3\text{O}_4$ -DPD MNPs was incubated with 90 μ L phosphate buffer saline (PBS) pH 7.4 while shaking at room temperature. For serum stability studies, 20 μ L $^{68}\text{Ga}-\text{Fe}_3\text{O}_4$ -DPD MNPs were incubated with 180 μ L human serum

at 37°C. The *in vitro* stability was determined at three time points (30, 60, and 120 min) by TLC, as described above.

2.9. Determination of the Size of $^{68}\text{Ga}-\text{Fe}_3\text{O}_4$ -DPD MNPs. Atomic force microscopy (AFM) was used to assess the morphology and the size of $^{68}\text{Ga}-\text{Fe}_3\text{O}_4$ -DPD MNPs. All measurements concerning the ^{68}Ga -labeled MNPs were performed after the decay of ^{68}Ga to the nonradioactive isotope ^{68}Zn , in order to avoid any contamination due to the radioactive sample. Initially, the samples were spread onto cleaned standard microscope slides by means of an electronically rotating platform (rotation frequency 2000 rpm, rotation duration 10 sec) to prepare single layer films. Then, AFM images of the films were obtained by means of a scanning probe microscope [NT-MDT Solver PRO] set in noncontact tapping mode.

Dynamic light scattering (DLS) was also used to measure the size distributions of Fe_3O_4 -DPD MNPs and $^{68}\text{Ga}(\rightarrow^{68}\text{Zn})-\text{Fe}_3\text{O}_4$ -DPD MNPs in aqueous solutions using a DLS apparatus. In a typical DLS measurement, 60 μ L of Fe_3O_4 -DPD MNPs or 100 μ L of $^{68}\text{Ga}(\rightarrow^{68}\text{Zn})-\text{Fe}_3\text{O}_4$ -DPD MNPs diluted with 300 μ L ultrapure water was measured at 22°C. For each dispersion, at least ten light scattering measurements were collected and the results were averaged.

2.10. Magnetic Properties of Fe_3O_4 -DPD and $^{68}\text{Ga}-\text{Fe}_3\text{O}_4$ -DPD MNPs. The magnetic measurements of Fe_3O_4 -DPD and $^{68}\text{Ga}-\text{Fe}_3\text{O}_4$ -DPD samples were performed by means of a SQUID magnetometer (5.5 T MPMS, Quantum Design). As mentioned above, these measurements were performed after the decay of ^{68}Ga to the stable isotope ^{68}Zn . Each sample was measured at body temperature, $T = 36^\circ\text{C}$, and in liquid form, dispersed in bidistilled water. To this end, we employed a plastic cylindrical container of appropriate diameter (~5 mm) that fits the opening of the SQUID sample chamber. The container was filled with 190 μ L MNPs (0.608 mg, $C = 3.2$ mg/ml) and sealed carefully. Magnetization measurements versus magnetic field, $M(H)$, were performed both on the empty container and the sample-filled container under the exact same conditions. Thus, we were able to isolate the $M(H)$ data of the Fe_3O_4 -DPD and $^{68}\text{Ga}(\rightarrow^{68}\text{Zn})-\text{Fe}_3\text{O}_4$ -DPD MNPs samples by subtracting the signal of the empty container.

2.11. Ex Vivo Biodistribution Studies. Animal experiments were carried out according to European and national regulations. These studies have been further approved by the Ethics Committee of the NCSR "Demokritos" and animal care and procedures followed are in accordance with institutional guidelines and licenses issued by the Department of Agriculture and Veterinary Policies of the Prefecture of Attiki (Registration numbers: EL 25 BIO 022 and EL 25 BIO 021). Normal Swiss mice were obtained from the breeding facilities of the Institute of Biosciences and Applications, NCSR "Demokritos." The animals were housed in air-conditioned rooms under a 12 h light/dark cycle and allowed free access to food and water.

The sample of $^{68}\text{Ga}\text{-Fe}_3\text{O}_4\text{-DPD}$ MNPs was loaded onto a size exclusion PD-10 column, containing Sephadex G-25 resin and eluted with phosphate buffer saline (PBS), in order to eliminate aggregated $^{68}\text{Ga}\text{-Fe}_3\text{O}_4\text{-DPD}$ MNPs, which may cause venous thrombosis during tail injections of the sample in the animals. Ten 0.5 ml fractions were collected, and the radioactivity of each fraction was measured using a dose calibrator (Capintec). The fractions containing the highest radioactivity were pooled and used for the study.

The *in vivo* behavior of $^{68}\text{Ga}\text{-Fe}_3\text{O}_4\text{-DPD}$ MNPs was evaluated in 9 normal Swiss mice (weight 23–27 gr). Intravenous administration of 100 μl PBS suspension (11.11 $\mu\text{g}/100 \mu\text{l}$ $^{68}\text{Ga}\text{-Fe}_3\text{O}_4\text{-DPD}$ MNPs per mouse) of purified $^{68}\text{Ga}\text{-Fe}_3\text{O}_4\text{-DPD}$ MNPs was performed via the tail vein. The animals were sacrificed at 30, 60, and 120 min postinjection (3 mice per time-point). Then, samples of blood and organs were excised, weighed, and measured for radioactivity in a Gamma scintillation counter. The remaining radioactivity in the tail, as well as background counts was subtracted, and the radioactivity decay was autocorrected by the counter. Then, the accumulation of $^{68}\text{Ga}\text{-Fe}_3\text{O}_4\text{-DPD}$ MNPs in each organ was expressed as the percentage injected activity per gram of tissue (% IA/g \pm SD) and calculated compared to the activities of a standard dose of the injected solution.

2.12. In Vivo Imaging Studies. Dynamic coincidence images of the administered mice were obtained from 10 min up to 60 min p.i. Successive 2 min frames were collected, showing the gradual biodistribution of the studied substance. Frames were also summed, to achieve cumulative images of higher statistics. All functional images were planar, coincidence images and no tomographic reconstruction was performed. Upon completion of the coincidence imaging, X-ray images were also acquired at the exact same mouse positioning to act as an anatomical guide for the organs' exact location. The X-ray imaging parameters were set to 35 kVp, 500 μA , and 0.1 s exposure time. Fusion between coincidence and X-ray images was performed semiautomatically through an in-house standard procedure. The two heads were not rotated and no tomographic imaging was performed.

The images were stored in raw format and postprocessed with ImageJ open source software (version 1.49v; NIH). Then, they were linearly interpolated, to provide a smoother final image. No smoothing algorithm was used. ImageJ was also used to select the color map and enhance image contrast at a certain level where the organs/structures of interest can be distinguished.

3. Results and Discussion

In the present study, Fe_3O_4 nanoparticles have been coated with DPD. The primary idea behind the design and synthesis of these MNPs was to improve stability and biocompatibility, as well as provide a platform for the development of a theranostic agent. As was recently shown in a study by Djokić et al. [29], MNPs coated with DPD efficiently complexed Yttrium-90, leading to a radiolabeled species for therapeutic applications. Furthermore, DPD offers the capability to

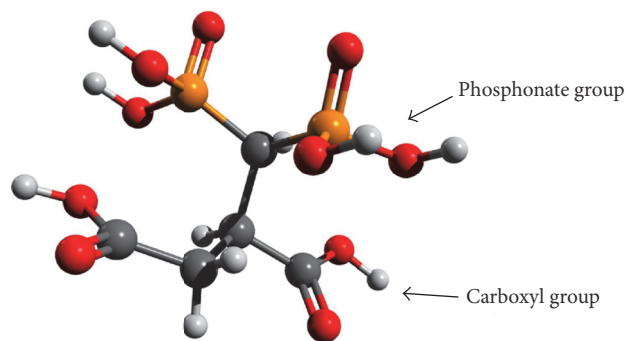


FIGURE 1: DPD ligand.

radiolabel the same MNPs with ^{68}Ga , for diagnostic applications.

3.1. Synthesis and Characterization of the $\text{Fe}_3\text{O}_4\text{-DPD}$ MNPs. In this study, MNPs were synthesized according to the coprecipitation method and stabilized with the tetradentate ligand DPD (Figure 1). The surface of MNPs was modified with hydrophilic carboxylate and phosphonate groups shortly after the particle formation, resulting in increased stability and dispersibility of the carrier in aqueous solution.

Transmission electron microscopy (TEM) was used in order to determine particle size and the distribution and morphology of $\text{Fe}_3\text{O}_4\text{-DPD}$ MNPs (Figure 2(a), (A) and (B)). From TEM micrographs, it is observed that the MNPs were pseudospherical or discrete squares with a diameter of around 6 nm. Particles were agglomerated due to magnetic interactions among them.

Crystal structures of the MNPs were checked by X-ray powder diffraction method. In the obtained diffraction patterns (Figure 2(b)) all reflections were indexed in the expected space group, $Fd\bar{3}m$, and spinel structure type. The mean crystallite diameter of 5.6 nm was estimated for the Fe_3O_4 using Scherer's equation and the peak half-height width of the (311) reflections. The same values were obtained using XRD data for pure Fe_3O_4 and $\text{Fe}_3\text{O}_4\text{-DPD}$ MNPs. The mean crystallite size calculated from the XRD patterns is consistent with particle size estimated from the relevant TEM micrographs. Hence, particles are composed from one crystallite.

DLS measurements were carried out on the $\text{Fe}_3\text{O}_4\text{-DPD}$ MNPs (Figure 3(a)). The sample was diluted with ultrapure water and measured at 22°C. A sharp monomodal size distribution of the MNPs was observed. Using CONTIN analysis of DLS measurements, it was found that the mean size distribution of intensity weighted hydrodynamic diameter of $\text{Fe}_3\text{O}_4\text{-DPD}$ MNPs was 96 nm. The polydispersity index (PDI) of $\text{Fe}_3\text{O}_4\text{-DPD}$ MNPs was calculated from the cumulants analysis and its value was less than 0.3, indicating that the nanoparticles have a considerably narrow size distribution and are essentially monodisperse. As PDI values are very sensitive to the presence of aggregates, it is obvious that the $\text{Fe}_3\text{O}_4\text{-DPD}$ MNPs are stable since PDI is not affected over time (Table 1). It should be noticed that the results obtained

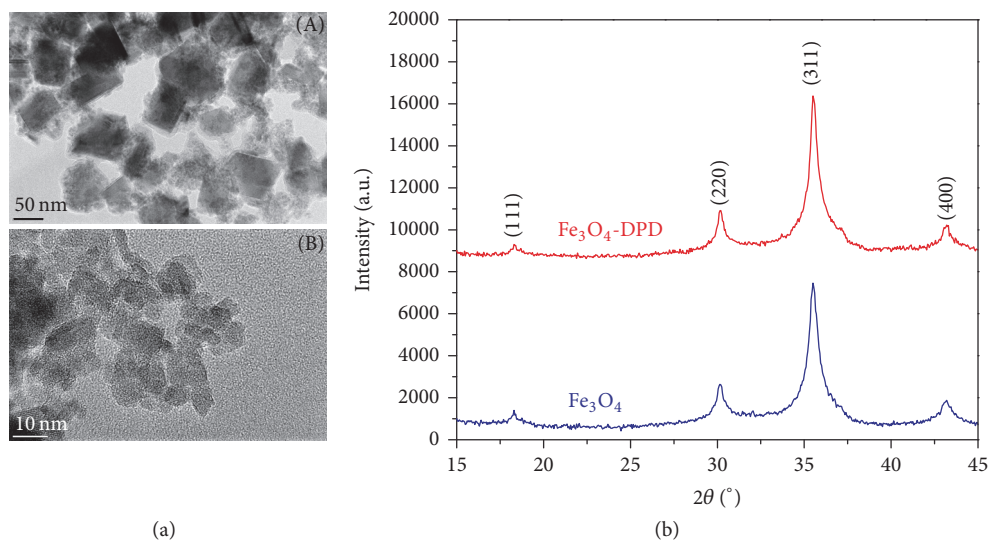


FIGURE 2: ((a), (A) and (B)) TEM images of DPD-coated MNPs; (b) XRD patterns of Fe_3O_4 and Fe_3O_4 -DPD MNPs.

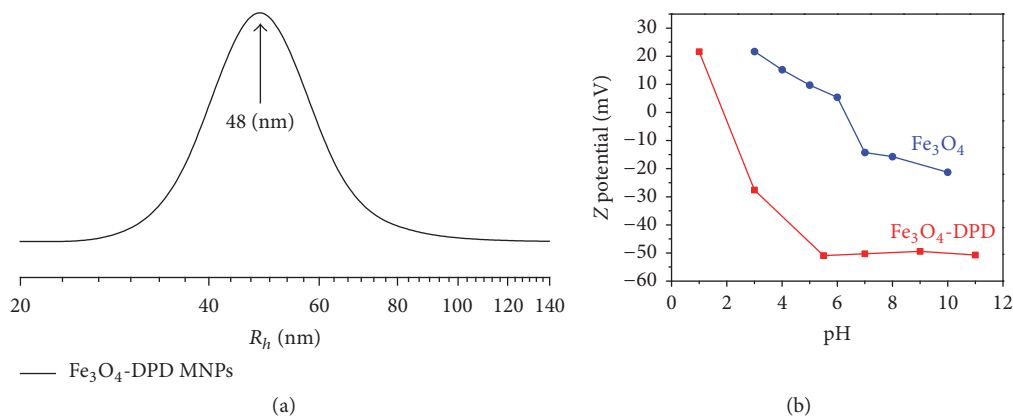


FIGURE 3: (a) Intensity weighted hydrodynamic radii size distribution of Fe_3O_4 -DPD MNPs; (b) dependence of zeta potential of Fe_3O_4 and Fe_3O_4 -DPD MNPs on the change of pH.

from DLS and TEM are different since the first obtained direct from solution and measured the hydrodynamic radii of the particles, while the second obtained from dried solution where the particles aggregated due to the removal of water. Zeta potential measurements as a function of pH for the Fe_3O_4 and Fe_3O_4 -DPD MNPs are shown in (Figure 3(b)). Due to the presence of carboxylate and phosphonate groups on the surface of Fe_3O_4 -DPD MNPs, the surface charge of the MNPs was observed to be highly negative (-50.4 mV at pH = 7) and shows high electrostatic repulsions between the charged nanoparticles, which ensures the colloidal stability. Again, this confirms the efficiency of coating since the IEP (1.9) has been shifted to lower pH values compared to naked MNPs (6.2). The correlation of zeta potential to pH is important to know so that one can predict how the pH inside the human body will affect the surface charge of the nanoparticles and therefore protein adsorption onto nanoparticles. Fe_3O_4 -DPD MNPs showed high stability in

TABLE 1: Stability analysis of Fe_3O_4 -DPD MNPs, variation in PDI and zeta potential against time.

Time (months)	1	2	3	4	5	6
PDI	0.255	0.241	0.267	0.287	0.263	0.271
Zeta potential (mV)	-49.8	-50.1	-48.6	-49.2	-50.3	-50.4

aqueous medium as their size and zeta potential remained unaffected over a long period of time (Table 1).

Further conformation of effective coating of the DPD ligand on the surface of MNPs came from FTIR spectroscopy and thermogravimetric analysis. The infrared spectra of the free ligand DPD, Fe_3O_4 MNPs, and Fe_3O_4 -DPD MNPs are shown for comparison (Figure 4(a)). DPD could coordinate the metal through the carboxylate and the phosphonate groups. In that case significant changes for the bands of

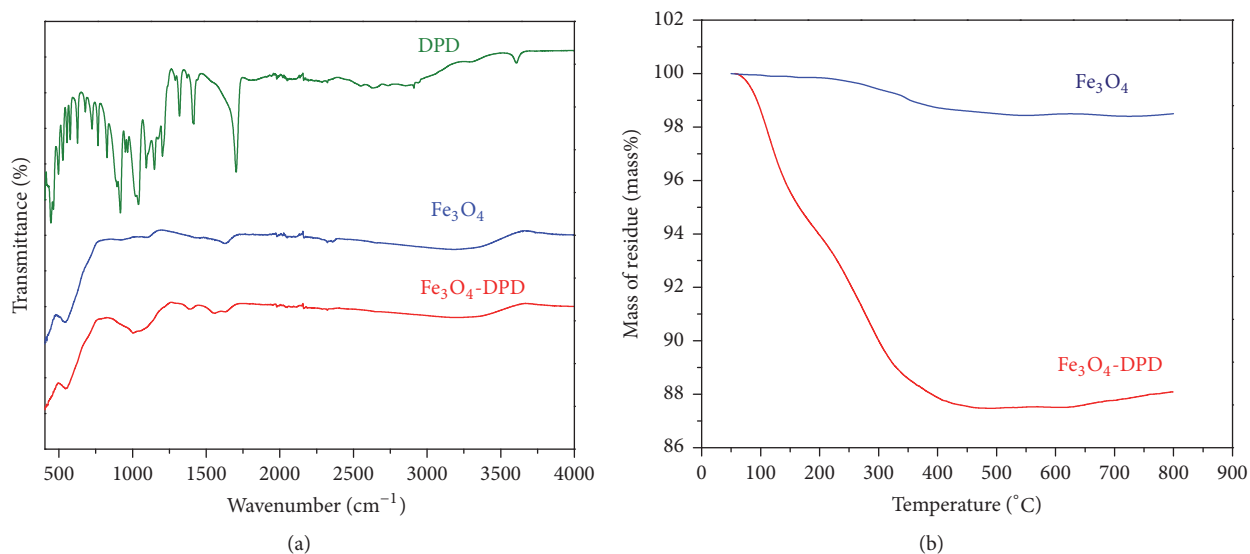


FIGURE 4: (a) ATR-FTIR spectra of DPD, Fe_3O_4 , and Fe_3O_4 -DPD MNPs; (b) TGA curves of Fe_3O_4 and Fe_3O_4 -DPD MNPs.

the carboxylate and the phosphonate groups of the Fe_3O_4 -DPD complex should be seen in its infrared spectra. The most important differences between DPD and Fe_3O_4 -DPD spectra are related to the phosphonate bands in the region $1200\text{--}800\text{ cm}^{-1}$.

Comparing the Fe_3O_4 -DPD MNPs (red curve) with the free DPD ligand (green curve) (Figure 4(a)), the large changes observed within the P–O stretching region ($1200\text{--}900\text{ cm}^{-1}$) show that a strong interaction between the phosphonate group and the Fe_3O_4 is present. The spectrum of the free DPD exhibits, within the P–O stretching region ($1200\text{--}900\text{ cm}^{-1}$), two sharp peaks at 1204 and 918 cm^{-1} , assigned to P=O and P–OH, respectively. The broadband at 1040 cm^{-1} in the spectrum of Fe_3O_4 -DPD MNPs is characteristic for the vibrational mode for the PO_3^{2-} group. Appearance of this broad phosphoryl band, as well as the disappearance of the P=O and P–O–H bands, indicates a mainly tridentate binding of DPD to the surface of Fe_3O_4 MNPs. For the DPD ligand, the carboxylate ions present two characteristic bands at 1704 and 1414 cm^{-1} due to the asymmetric and symmetric carboxylate stretches, respectively. Comparing the Fe_3O_4 -DPD MNPs with the free DPD, the characteristic carboxylate stretches were shifted to lower frequencies at 1635 and 1396 cm^{-1} , respectively, which suggests that DPD molecules are bound to the particle surface also via $-\text{COO}^-$ groups. The ATR-FTIR spectrum of Fe_3O_4 -DPD MNPs exhibited a strong band at 540 cm^{-1} , characteristic of the Fe–O vibration related to the magnetite core. Thermogravimetric analysis (TGA) of naked MNPs detected no significant peaks (Figure 4(b)). There was a 3% weight loss as the temperature increased from 100°C to 800°C , which might be due to a loss of absorbed water. In contrast, the functionalized MNPs lost weight in two steps. The first step occurred over the range $25\text{--}200^\circ\text{C}$ and might also be due to the loss of absorbed water. The second step consisted of a weight loss of about 12.5% over the range $200\text{--}450^\circ\text{C}$ and might be due to the burning of

bonded ionic liquids. At higher temperatures of $450\text{--}900^\circ\text{C}$, the weight remained constant, implying the presence of only Fe_3O_4 left within the temperature range.

Magnetic properties of Fe_3O_4 and Fe_3O_4 -DPD MNPs were investigated by magnetization measurements versus field, $M(H)$ at 290 K as well as by ZFC-FC magnetization from $2\text{--}300\text{ K}$ in applied field of 100 Oe . Magnetization versus field, $M(H)$, curves are shown in Figure 5(a). It can be observed that the magnetization does not fully saturate up to 50 kOe , reflecting the hard magnetic behavior of the particle surface. The saturation magnetization, M_s , as determined by extrapolating $M(1/H)$ to $H = 0$, was $M_s = 47$ and 42 emu/g , for Fe_3O_4 and Fe_3O_4 -DPD, respectively. Remanent magnetization, M_R , and coercivity, H_C , values are nearly zero, in agreement with the superparamagnetic behavior expected for these nanoparticles on the time scale of magnetization measurement time $\tau_M \sim 100\text{ s}$. Temperature dependencies of ZFC and FC magnetization for Fe_3O_4 and Fe_3O_4 -DPD MNPs are shown in Figure 5(b). The ZFC and FC magnetization curves furcate at the maximum temperature of measurements, 300 K . A broad maximum in ZFC branch around 200 K is a consequence of a broad particle size distribution, as was shown by TEM examinations (Figure 2(a), (B)). In the FC branches magnetization increases a little bit from room temperature to 100 K , and below it shows a tendency to be saturated. The found FC behavior indicates the interparticle interactions and probably a spins glass state.

3.2. In Vitro Cytotoxicity Study of Fe_3O_4 -DPD MNPs. Although the chemical characterization of the synthesized Fe_3O_4 -DPD MNPs is crucial in order to further characterize their diagnostic utility as a PET radiotracer, quantitative assays of the metabolic activity of cancer cell lines could grant a better knowledge of the mechanisms implied in the toxicity caused by those MNPs. The assays based on the measurement of the metabolic activity of the cells are

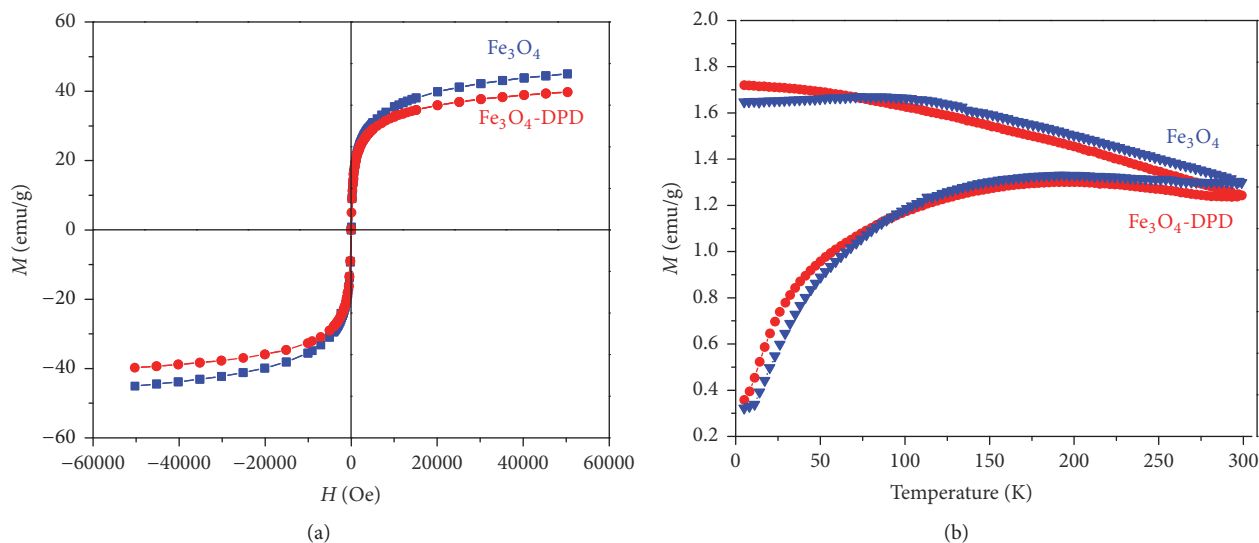


FIGURE 5: (a) Hysteresis loop for Fe_3O_4 and Fe_3O_4 -DPD MNPs at 300 K; (b) temperature dependence on magnetization of the Fe_3O_4 and Fe_3O_4 -DPD MNPs taken in zero-field (lower branch) and field-cooling (upper branch) modes.

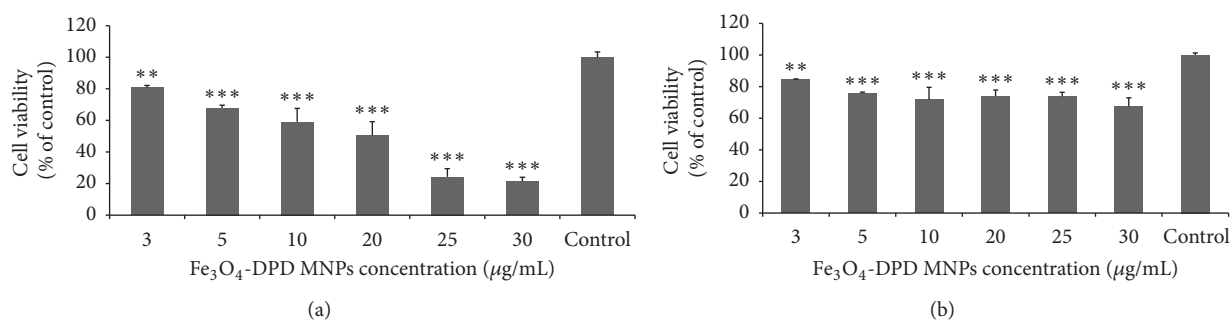


FIGURE 6: MTT cell viability assay after 24 h treatment of (a) 4T1 cells and (b) HEK293T cells with Fe_3O_4 -DPD MNPs. Positive control shows cells without exposure to MNPs. Cell viability is expressed as % cell viability \pm SD between two experiments. The symbols ** and *** show statistical significance using one-way ANOVA ($p < 0.01$ and $p < 0.005$, resp.), compared to positive control.

the most common methods in order to designate the cell viability under nanoparticle treatment. The MTT viability assay intends to track the activity of reductase enzymes in order to measure the cell viability of 4T1 and HEK293 cell lines and thus the cytotoxicity caused by treatment with various concentrations of Fe_3O_4 -DPD MNPs (3, 5, 10, 20, 25, and 30 $\mu\text{g/mL}$) for 24 h, an appropriate incubation time for Fe_3O_4 -DPD MNPs internalization from the cells [34].

According to our results, the viability of cancer 4T1 cells shows a 50% reduction ($p < 0.005$) when treated with 20 $\mu\text{g/mL}$, while the viability of the cells falls to 20% under treatment with 30 $\mu\text{g/mL}$ ($p < 0.005$) of Fe_3O_4 -DPD MNPs (Figure 6(a)). Thus, the cytotoxicity results demonstrate a dose-dependent cytotoxicity effect of Fe_3O_4 -DPD MNPs in 4T1 cancer cell line. Recently, several *in vitro* experiments in eukaryotic cells show that internalized MNPs, depending on their size and modification, can induce mitochondrial dysfunction, increase the level of ROS, and subsequently cause DNA damage, chromosomal aberrations, apoptosis, impairment of the cell membrane, and cell cycle rest. The

later effects are probably caused by the ions released (ROS generation) by magnetic MNPs that lead to the ignition of oxidative stress responses into the cell and at the end to cytotoxicity. Moreover, although iron MNPs degraded in the cell, they can change the cellular iron pool, leading to aberrant expression of transferrin receptor, cyclins, and induction of apoptotic responses [35–37]. Regarding cytotoxicity, the choice of the cell line tested under MNPs treatment is of great importance, since it is demonstrated that MNPs toxicity is highly cell-type dependent [38, 39]. Therefore, the cytotoxicity of Fe_3O_4 -DPD MNPs against a noncancerous cell line (HEK293) was also tested and it was shown that toxicity against this cell line is greatly reduced, compared to the 4T1 cell line (Figure 6(b)). Even at a concentration of 30 $\mu\text{g/mL}$ the viability is $>60\%$ ($p < 0.005$). These results indicate selective cytotoxic effects of Fe_3O_4 -DPD MNPs in cancer cells with regard to normal cells. Further experiments are needed in order to elucidate the mechanism by which Fe_3O_4 -DPD MNPs cause higher cytotoxicity in cancer cells, thus highlighting their potential use as therapeutic agents.

3.3. Radiolabeling of Fe_3O_4 -DPD MNPs with ^{68}Ga . Fe_3O_4 -DPD MNPs were radiolabeled with ^{68}Ga radionuclide without the presence of a chelator. In our study DPD, a tetradentate ligand with two phosphonates and two carboxylates serves as an effective ligand that coordinates with $^{68}\text{Ga}^{3+}$. The radiolabeling yield of the sample was found to be $\sim 70\%$, as determined by radio-TLC analysis. Moreover, the radiolabeled sample was purified via centrifugation and afforded a radiochemical purity of $>91\%$. The radiolabeling results are in agreement with the literature [21, 40–44].

3.4. In Vitro Stability Studies of ^{68}Ga - Fe_3O_4 -DPD MNPs. A significant factor to be considered when developing a new radiolabeled nanoparticle is that the radionuclide must be bound to the nanoparticle to form a stable conjugate under physiological conditions to avoid their separation and nonspecific deposition of free ions in tissues. Otherwise, biodistribution and imaging data will not indicate the fate of nanoparticles, as the radionuclide distribution will not reflect that of the nanoparticles.

With the aim of assessing the *in vitro* stability of ^{68}Ga - Fe_3O_4 -DPD MNPs in biological media, the radiolabeled sample was incubated with PBS and human serum. The results exhibited satisfactory *in vitro* stability in PBS ($\sim 80\%$ stable ^{68}Ga - Fe_3O_4 -DPD MNPs) and high *in vitro* stability in human serum ($>92\%$ stable ^{68}Ga - Fe_3O_4 -DPD MNPs), as evaluated by TLC analysis, at three time points (30, 60, and 120 min) after incubation. Our results are in accordance with work reported by other groups [18, 21, 26, 28, 40, 41].

3.5. Determination of the Morphology and Size of ^{68}Ga - Fe_3O_4 -DPD MNPs. The size of radiolabeled magnetic nanoparticles highly affects their pharmacokinetics and *in vivo* behavior. Nanoparticles larger than 200 nm are sequestered by macrophages of liver and spleen, while nanoparticles smaller than 10 nm are rapidly removed through renal clearance. Also, nanoparticles bigger than $4\ \mu\text{m}$ in diameter are mainly captured in the lungs and may lead to the risk of embolism. Thus, nanoparticles with a mean size in the range of 10–200 nm escape opsonization exhibit longer blood circulation times and are most effective for biological applications. In our study, AFM measurements were performed to assess the size of the ^{68}Ga - Fe_3O_4 -DPD MNPs as described elsewhere [45]. These measurements were performed after the decay of ^{68}Ga to the stable isotope ^{68}Zn , as mentioned in Materials and Methods.

The acquired AFM images showed that the size of ^{68}Ga ($\rightarrow^{68}\text{Zn}$)- Fe_3O_4 -DPD MNPs ranged from 30 to 180 nm ($N = 87$ nanoparticles measured from several AFM images). As shown in Figure 7(a) the nanoparticles are homogenous and spherical, while the majority of the nanoparticles are less than 50 nm (Figure 7(b)). Some aggregates of varying sizes may be created in the radiolabeled sample during the radiolabeling process. It has also been reported that PEG-coated superparamagnetic iron oxide nanoparticles subjected to high salt concentration (0.2 M ammonium acetate buffer) during radiolabeling procedure with ^{68}Ga exhibit larger size compared to their size before the radiolabeling [27].

DLS measurements were also carried out on the radiolabeled sample following the procedure described above. Also in this case, a sharp monomodal size distribution of ^{68}Ga ($\rightarrow^{68}\text{Zn}$)- Fe_3O_4 -DPD MNPs with average intensity weighted hydrodynamic diameters of about 400–500 nm was observed (Figure 8). The value of mean diameter is higher than that of the nonradiolabeled sample due to the radiolabeling process as mentioned before.

3.6. Magnetic Properties of Fe_3O_4 -DPD and ^{68}Ga ($\rightarrow^{68}\text{Zn}$)- Fe_3O_4 -DPD MNPs. Figure 9 shows representative magnetization measurements of Fe_3O_4 -DPD and ^{68}Ga ($\rightarrow^{68}\text{Zn}$)- Fe_3O_4 -DPD MNPs as they were measured by means of a SQUID magnetometer at conditions of body temperature ($T = 36^\circ\text{C}$) and in liquid form (dispersed in bidistilled water) since we wanted to simulate, at least at the laboratory level, the conditions that these conjugates will ultimately be used in subsequent studies on animal models. As shown in this figure, the saturation magnetization of Fe_3O_4 -DPD MNPs is $M_s = 44$ emu/g, while that of ^{68}Ga ($\rightarrow^{68}\text{Zn}$)- Fe_3O_4 -DPD MNPs is $M_s = 8$ emu/g. The observed reduction of M_s is attributed to two unavoidable factors: first, the reduction of the effective concentration of the Fe_3O_4 content during the radiolabeling process of the Fe_3O_4 -DPD MNPs sample (mass loss of Fe_3O_4 during centrifugation/washing cycles needed to remove free ^{68}Ga that possibly exists in the supernatant and inability to completely remove all supernatant before the final dilution to the specified final liquid volume); second, to the change in the chemical composition of Fe_3O_4 to Fe_2O_3 due to oxidization (the radiolabeling process is performed in atmosphere, at relatively high temperature conditions, $T = 90^\circ\text{C}$). Finally, we should note that neither the Fe_3O_4 -DPD nor the ^{68}Ga ($\rightarrow^{68}\text{Zn}$)- Fe_3O_4 -DPD MNPs were aggregated even under the application of a magnetic field as high as 20 kOe.

3.7. Ex Vivo Biodistribution Studies. The *ex vivo* biodistribution of ^{68}Ga - Fe_3O_4 -DPD MNPs was performed to assess their *in vivo* behavior as potential PET/MRI imaging agents. The ^{68}Ga - Fe_3O_4 -DPD MNPs were administered via tail vein injection in normal Swiss mice. In general, the accumulation of ^{68}Ga - Fe_3O_4 -DPD MNPs in the organs at all time points examined is presented in Figure 10, as percentage of injected activity per gram tissue (% IA/gr \pm SD). ^{68}Ga - Fe_3O_4 -DPD MNPs were distributed throughout the organs, while in liver and spleen the uptake was the highest. Specifically, the blood retention of the nanoparticles was $2.19 \pm 0.42\%$ IA/g up to 60 min postinjection (p.i.) and showed a decrease to $1.49 \pm 0.92\%$ IA/g at 120 min p.i. The accumulation of ^{68}Ga - Fe_3O_4 -DPD MNPs in the heart was increased with time ($1.41 \pm 0.42\%$ IA/g at 30 min, $1.87 \pm 0.20\%$ IA/g at 60 min, and $1.99 \pm 0.35\%$ IA/g at 120 min p.i.). On the contrary, in the lungs the uptake showed opposite behavior ($2.10 \pm 0.49\%$ IA/g at 30 min, $1.57 \pm 0.43\%$ IA/g at 60 min, and $1.32 \pm 0.69\%$ IA/g at 120 min p.i.). The small percentage of the uptake in lungs can be attributed to possible embolization caused by postinjection aggregation.

The organs of the reticuloendothelial system (RES) exhibit the highest accumulation of ^{68}Ga - Fe_3O_4 -DPD MNPs,

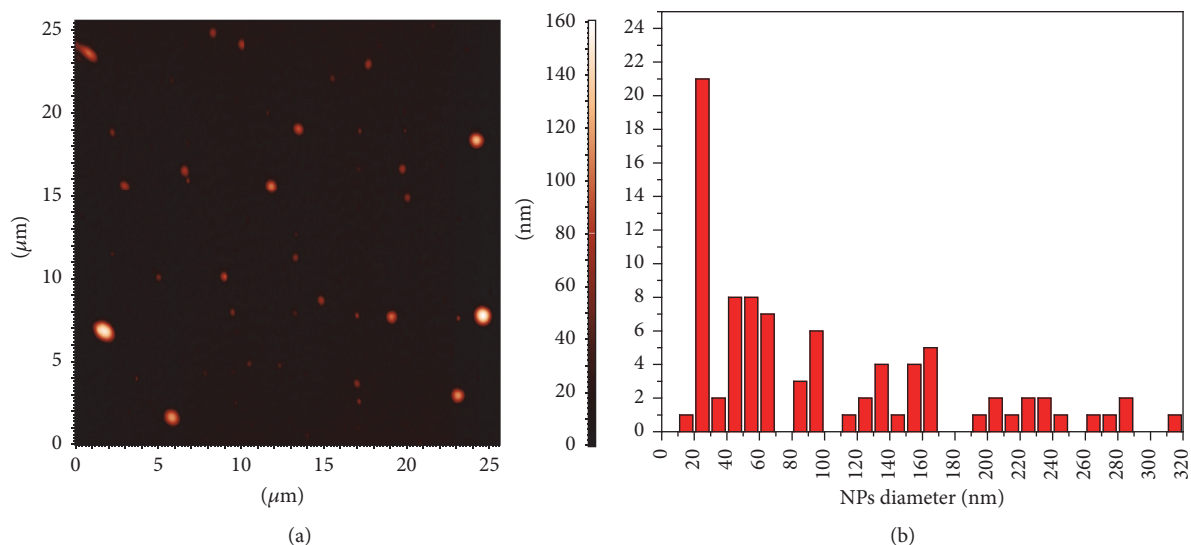


FIGURE 7: (a) Typical AFM image showing the morphology of $^{68}\text{Ga}(\rightarrow^{68}\text{Zn})\text{-Fe}_3\text{O}_4\text{-DPD MNPs}$; (b) size distribution of $^{68}\text{Ga}(\rightarrow^{68}\text{Zn})\text{-Fe}_3\text{O}_4\text{-DPD MNPs}$ measured from several AFM images.

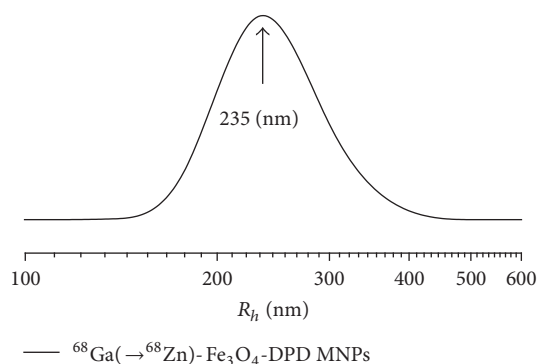


FIGURE 8: Intensity weighted hydrodynamic radii size distribution of $^{68}\text{Ga}(\rightarrow^{68}\text{Zn})\text{-Fe}_3\text{O}_4\text{-DPD MNPs}$.

compared to the other organs. In the liver, there were 32.42 ± 16.12 , 42.52 ± 1.95 , and $44.66 \pm 22.86\%$ IA/g at 30, 60, and 120 min p.i., while in the spleen the uptake reached the $16.48 \pm 3.58\%$ IA/g at 60 min p.i. and remained relatively constant ($16.21 \pm 1.74\%$ IA/g) up to 120 min p.i. These organs are rich in macrophages (i.e., liver's Kupffer cells), which are able to recognize and engulf $^{68}\text{Ga}\text{-Fe}_3\text{O}_4\text{-DPD MNPs}$ through phagocytosis. The kidney uptake was relatively low at all time points. All other organs studied showed low or negligible uptake.

It is well known that following intravenous injection of radiolabeled magnetic nanoparticles in the bloodstream, plasma proteins, namely, opsonins, are adsorbed onto the surface of the nanoparticles [46]. These plasma proteins are recognized by the macrophages mostly found in the liver and spleen, resulting in rapid clearance of the nanoparticles from the bloodstream. The opsonization process and therefore the

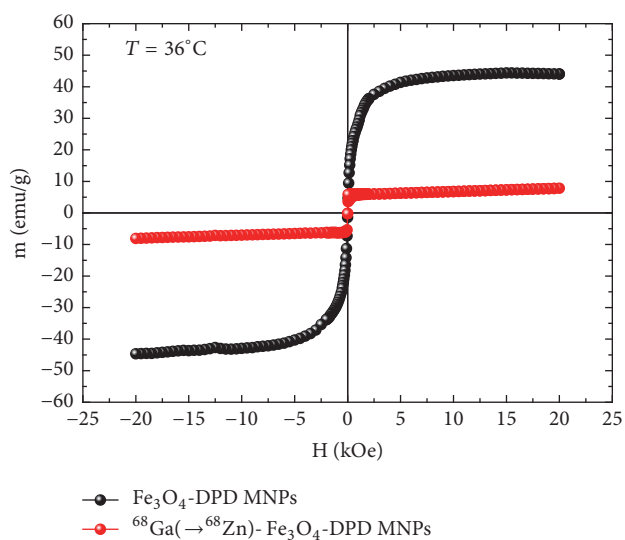


FIGURE 9: Magnetization versus magnetic field at $T = 36^\circ\text{C}$ for $\text{Fe}_3\text{O}_4\text{-DPD}$ and $^{68}\text{Ga}(\rightarrow^{68}\text{Zn})\text{-Fe}_3\text{O}_4\text{-DPD MNPs}$. Both samples were in liquid form, dispersed in bidistilled water.

in vivo behavior of the radiolabeled magnetic nanoparticles are highly affected by their physicochemical properties, such as their coating, size and surface charge.

Despite the coating with DPD, a biocompatible and hydrophilic coating, the $^{68}\text{Ga}\text{-Fe}_3\text{O}_4\text{-DPD MNPs}$ displayed long-term retention in the liver, as discussed above. This behavior was similar to ^{90}Y -labeled Fe_3O_4 MNPs coated with PEG600 diacid, with a size of $46 \pm 0.6 \text{ nm}$ [18]. This behavior may be attributed to the size of the $^{68}\text{Ga}\text{-Fe}_3\text{O}_4\text{-DPD MNPs}$ as measured with AFM [46, 47]. As discussed by

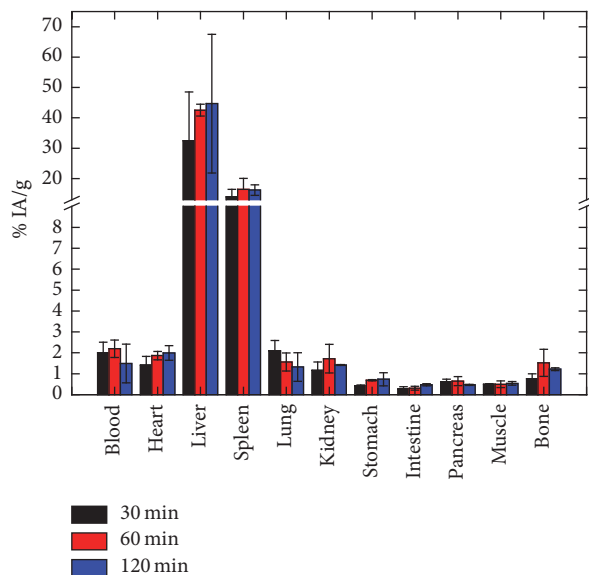


FIGURE 10: *Ex vivo* biodistribution study of $^{68}\text{Ga-Fe}_3\text{O}_4$ -DPD MNPs in normal Swiss mice performed at 30, 60, and 120 min postinjection.

Chouly et al. [48], a similar behavior was observed for ^{59}Fe -labeled dextran-coated Fe_3O_4 MNPs with different diameters (30 nm–100 nm). When injected in Swiss mice, they showed decreased blood retention with increasing size, while the liver accumulation was increased following the increasing size of the nanoparticles.

Another fact to be considered is the surface charge of Fe_3O_4 -DPD MNPs. It has been shown that a neutral charge interacts minimally with the plasma proteins and thus contributes to the extended circulation time of the MNPs, whereas a high surface charge enhances the phagocytosis process [46]. Positively charged nanoparticles show nonspecific internalization rate, plasma protein binding, aggregation, and short blood circulation half-life [47]. In a study carried out using dextran-coated Fe_3O_4 MNPs with different surface charges (neutral, negative -30 mV, positive $+20$ mV) [48], the accumulation of nanoparticles in the liver was 3 times lower for the neutral nanoparticles than the charged ones, while the negatively charged nanoparticles exhibited increased liver uptake. In our study, the highly negative surface charge of Fe_3O_4 -DPD MNPs (-50.4 mV at $\text{pH} = 7$) led to high electrostatic repulsions between the charged nanoparticles, thus ensuring the colloidal stability of the nanoparticles, while their high liver uptake can be attributed to their negative surface charge.

3.8. In Vivo Imaging Studies. Dynamic and cumulative imaging studies of anesthetized healthy Swiss mice were performed on a dedicated small animal PET/X-ray system, up to 1 hour p.i. (Figure 11). Imaging and biodistribution studies were found to be in good agreement. Kidney uptake is not discernable in the PET images, due to the significant concentration in the liver and the partial overlapping of kidneys with liver and intestines.

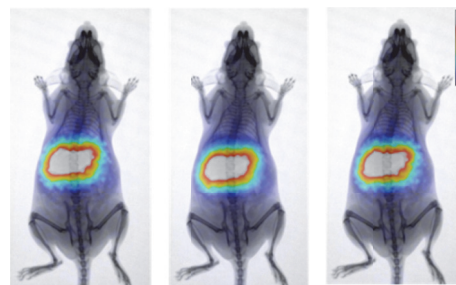


FIGURE 11: Cumulative PET/X-ray images of a normal Swiss mouse injected with $^{68}\text{Ga-Fe}_3\text{O}_4$ -DPD MNPs at 20, 30, and 60 min p.i. The gradual alteration in color indicates a lower to higher number of recorded counts.

4. Conclusions

Iron oxide nanoparticles were successfully synthesized and surface functionalized with the biocompatible and water soluble stabilizer DPD, providing the bare Fe_3O_4 MNPs with the appropriate dispersing stability, minimizing their potential cytotoxicity and exhibiting chelating properties. Fe_3O_4 -DPD MNPs showed reduced toxicity in the normal cells, compared to cancer cells and efficient labeling with the positron emitter Ga-68 to form stable constructs. Although *ex vivo* biodistribution and *in vivo* PET imaging studies of $^{68}\text{Ga-Fe}_3\text{O}_4$ -DPD MNPs showed high accumulation in the RES organs, they indicated satisfactory blood retention at 30, 60, and 120 min p.i. As a result, $^{68}\text{Ga-Fe}_3\text{O}_4$ -DPD MNPs exhibit great potential as a PET/MR imaging agent. We are currently working on the assessment of $^{68}\text{Ga-Fe}_3\text{O}_4$ -DPD MNPs in tumor bearing animal models to evaluate their application in cancer imaging.

Conflicts of Interest

The authors declare that they have no conflicts of interest.

Acknowledgments

The research work was financially supported by Ministry of Education and Science of the Republic of Serbia (Grant no. III 45015) and COST ACTION TD 1402-Multifunctional Nanoparticles for Magnetic Hyperthermia and Indirect Radiation Therapy (RADIOMAG). The authors gratefully acknowledge Dr. K. Zhernosekov for provision of the $^{68}\text{Ge}/^{68}\text{Ga}$ generator utilized in this work and for helpful discussions.

References

- [1] B. Issa, I. M. Obaidat, B. A. Albiss, and Y. Haik, "Magnetic nanoparticles: Surface effects and properties related to biomedicine applications," *International Journal of Molecular Sciences*, vol. 14, no. 11, pp. 21266–21305, 2013.
- [2] Z. Zhao, Z. Zhou, J. Bao et al., "Octapod iron oxide nanoparticles as high-performance T 2 contrast agents for magnetic

- resonance imaging,” *Nature Communications*, vol. 4, article no. 2266, 2013.
- [3] H. B. Na, I. C. Song, and T. Hyeon, “Inorganic nanoparticles for MRI contrast agents,” *Advanced Materials*, vol. 21, no. 21, pp. 2133–2148, 2009.
 - [4] J. Estelrich, M. J. Sánchez-Martín, and M. A. Busquets, “Nanoparticles in magnetic resonance imaging: from simple to dual contrast agents,” *International Journal of Nanomedicine*, vol. 10, pp. 1727–1741, 2015.
 - [5] A. C. Silva, T. R. Oliveira, J. B. Mamani et al., “Application of hyperthermia induced by superparamagnetic iron oxide nanoparticles in glioma treatment,” *International Journal of Nanomedicine*, vol. 6, pp. 591–603, 2011.
 - [6] C. L. Dennis, A. J. Jackson, J. A. Borchers et al., “The influence of magnetic and physiological behaviour on the effectiveness of iron oxide nanoparticles for hyperthermia,” *Journal of Physics D: Applied Physics*, vol. 41, no. 13, Article ID 134020, 2008.
 - [7] S. Laurent, S. Dutz, U. O. Häfeli, and M. Mahmoudi, “Magnetic fluid hyperthermia: focus on superparamagnetic iron oxide nanoparticles,” *Advances in Colloid and Interface Science*, vol. 166, no. 1–2, pp. 8–23, 2011.
 - [8] B. D. Plouffe, S. K. Murthy, and L. H. Lewis, “Fundamentals and application of magnetic particles in cell isolation and enrichment: A review,” *Reports on Progress in Physics*, vol. 78, no. 1, Article ID 016601, pp. 1–38, 2015.
 - [9] Q. Wang, B. Chen, M. Cao et al., “Response of MAPK pathway to iron oxide nanoparticles in vitro treatment promotes osteogenic differentiation of hBMSCs,” *Biomaterials*, vol. 86, pp. 11–20, 2016.
 - [10] J. Estelrich, E. Escribano, J. Queralt, and M. Busquets, “Iron oxide nanoparticles for magnetically-guided and magnetically-responsive drug delivery,” *International Journal of Molecular Sciences*, vol. 16, no. 4, pp. 8070–8101, 2015.
 - [11] J. Xie, J. Huang, X. Li, S. Sun, and X. Chen, “Iron oxide nanoparticle platform for biomedical applications,” *Current Medicinal Chemistry*, vol. 16, no. 10, pp. 1278–1294, 2009.
 - [12] N. T. K. Thanh and L. A. W. Green, “Functionalisation of nanoparticles for biomedical applications,” *Nano Today*, vol. 5, no. 3, pp. 213–230, 2010.
 - [13] K. Zarschler, L. Rocks, N. Licciardello et al., “Ultrasmall inorganic nanoparticles: state-of-the-art and perspectives for biomedical applications,” *Nanomedicine: Nanotechnology, Biology and Medicine*, vol. 12, no. 6, pp. 1663–1701, 2016.
 - [14] R. Bazak, M. Hourri, S. El Achy, S. Kamel, and T. Refaat, “Cancer active targeting by nanoparticles: a comprehensive review of literature,” *Journal of Cancer Research and Clinical Oncology*, vol. 141, no. 5, pp. 769–784, 2015.
 - [15] O. Veiseh, J. W. Gunn, and M. Zhang, “Design and fabrication of magnetic nanoparticles for targeted drug delivery and imaging,” *Advanced Drug Delivery Reviews*, vol. 62, no. 3, pp. 284–304, 2010.
 - [16] R. Subbiah, M. Veerapandian, and K. S. Yun, “Nanoparticles: Functionalization and multifunctional applications in biomedical sciences,” *Current Medicinal Chemistry*, vol. 17, no. 36, pp. 4559–4577, 2010.
 - [17] W. Wu, Q. He, and C. Jiang, “Magnetic iron oxide nanoparticles: synthesis and surface functionalization strategies,” *Nanoscale Research Letters*, vol. 3, no. 11, pp. 397–415, 2008.
 - [18] M. Radović, M. P. Calatayud, G. F. Goya et al., “Preparation and *in vivo* evaluation of multifunctional ^{90}Y -labeled magnetic nanoparticles designed for cancer therapy,” *Journal of Biomedical Materials Research Part A*, vol. 103, no. 1, pp. 126–134, 2015.
 - [19] Z. Shaterabadi, G. Nabyouni, and M. Soleymani, “High impact of in situ dextran coating on biocompatibility, stability and magnetic properties of iron oxide nanoparticles,” *Materials Science and Engineering C: Materials for Biological Applications*, vol. 75, pp. 947–956, 2017.
 - [20] R. Thomas, I.-K. Park, and Y. Y. Jeong, “Magnetic iron oxide nanoparticles for multimodal imaging and therapy of cancer,” *International Journal of Molecular Sciences*, vol. 14, no. 8, pp. 15910–15930, 2013.
 - [21] L. Sandiford, A. Phinikaridou, A. Protti et al., “Bisphosphonate-anchored pegylation and radiolabeling of superparamagnetic iron oxide: Long-circulating nanoparticles for in vivo multimodal (T1 MRI-SPECT) imaging,” *ACS Nano*, vol. 7, no. 1, pp. 500–512, 2013.
 - [22] H. Zolata, F. Abbasi Davani, and H. Afarideh, “Synthesis, characterization and theranostic evaluation of Indium-111 labeled multifunctional superparamagnetic iron oxide nanoparticles,” *Nuclear Medicine and Biology*, vol. 42, no. 2, pp. 164–170, 2015.
 - [23] I. Tsiapa, E. K. Efthimiadou, and E. Fragoageorgi, “ $^{99\text{m}}\text{Tc}$ -labeled aminosilane-coated iron oxide nanoparticles for molecular imaging of $\alpha_v\beta_3$ -mediated tumor expression and feasibility for hyperthermia treatment,” *Journal of Colloid and Interface Science*, vol. 433, pp. 163–175, 2014.
 - [24] S. Deng, W. Zhang, B. Zhang et al., “Radiolabeled cyclic arginine-glycine-aspartic (RGD)-conjugated iron oxide nanoparticles as single-photon emission computed tomography (SPECT) and magnetic resonance imaging (MRI) dual-modality agents for imaging of breast cancer,” *Journal of Nanoparticle Research*, vol. 17, no. 1, 2015.
 - [25] J. Pellico, J. Ruiz-Cabello, M. Saiz-Alía et al., “Fast synthesis and bioconjugation of ^{68}Ga core-doped extremely small iron oxide nanoparticles for PET/MR imaging,” *Contrast Media & Molecular Imaging*, vol. 11, no. 3, pp. 203–210, 2016.
 - [26] B. P. Burke, N. Baghdadi, A. E. Kownacka et al., “Chelator free gallium-68 radiolabelling of silica coated iron oxide nanorods via surface interactions,” *Nanoscale*, vol. 7, no. 36, pp. 14889–14896, 2015.
 - [27] B. P. Burke, N. Baghdadi, G. S. Clemente et al., “Final step gallium-68 radiolabelling of silica-coated iron oxide nanorods as potential PET/MR multimodal imaging agents,” *Faraday Discussions*, vol. 175, pp. 59–71, 2014.
 - [28] R. Madru, T. A. Tran, J. Axelsson et al., “ ^{68}Ga -labeled superparamagnetic iron oxide nanoparticles (SPIONs) for multimodality PET/MR/Cherenkov luminescence imaging of sentinel lymph nodes,” *American Journal of Nuclear Medicine and Molecular Imaging*, vol. 4, no. 1, pp. 60–69, 2014.
 - [29] D. D. Djokić, D. L. Janković, and N. S. Nikolić, “Labeling, characterization, and in vivo localization of a new ^{90}Y -based phosphonate chelate 2,3-dicarboxypropane-1,1-diphosphonic acid for the treatment of bone metastases: Comparison with $^{99\text{m}}\text{Tc}$ -DPD complex,” *Bioorganic & Medicinal Chemistry*, vol. 16, no. 8, pp. 4457–4465, 2008.
 - [30] N. Vanlić-Razumenić and N. Vukićević, “The synthesis and physico-chemical properties of 2, 3-dicarboxypropane-1, 1-diphosphonic acid, a ligand for preparing the $^{99\text{m}}\text{Tc}$ -labeled skeletal imaging agent,” *Journal of the Serbian Chemical Society*, pp. 5163–5166, 1986.
 - [31] M. Rouchota, M. Georgiou, E. Fysikopoulos et al., “A prototype PET/SPECT/X-rays scanner dedicated for whole body small animal studies,” *Hellenic Journal of Nuclear Medicine*, vol. 20, no. 2, pp. 146–153, 2017.

- [32] R. Massart, "Preparation of aqueous magnetic liquids in alkaline and acidic media," *IEEE Transactions on Magnetics*, vol. 17, no. 2, pp. 1247–1248, 1981.
- [33] K. P. Zhernosekov, D. V. Filosofov, R. P. Baum et al., "Processing of generator-produced ^{68}Ga for medical application," *Journal of Nuclear Medicine*, vol. 48, no. 10, pp. 1741–1748, 2007.
- [34] G. Jarockyte, E. Daugelaite, M. Stasys et al., "Accumulation and toxicity of superparamagnetic iron oxide nanoparticles in cells and experimental animals," *International Journal of Molecular Sciences*, vol. 17, no. 8, article no. 1193, 2016.
- [35] W. Zhang, I. Qiao, X. Wang, R. Senthilkumar, F. Wang, and B. Chen, "Inducing cell cycle arrest and apoptosis by dimercaptosuccinic acid modified Fe_3O_4 magnetic nanoparticles combined with nontoxic concentration of bortezomib and gambogic acid in rpmi-8226 cells," *International Journal of Nanomedicine*, vol. 10, pp. 3275–3289, 2015.
- [36] C. Xu and S. Sun, "New forms of superparamagnetic nanoparticles for biomedical applications," *Advanced Drug Delivery Reviews*, vol. 65, no. 5, pp. 732–743, 2013.
- [37] G. Xia, B. Chen, J. Ding et al., "Effect of magnetic Fe_3O_4 nanoparticles with 2-methoxyestradiol on the cell-cycle progression and apoptosis of myelodysplastic syndrome cells," *International Journal of Nanomedicine*, vol. 6, pp. 1921–1927, 2011.
- [38] W. Kai, X. Xiaojun, P. Ximing, H. Zhenqing, and Z. Qiqing, "Cytotoxic effects and the mechanism of three types of magnetic nanoparticles on human hepatoma BEL-7402 cells," *Nanoscale Research Letters*, vol. 6, article no. 480, pp. 1–10, 2011.
- [39] S. K. Sohaebuddin, P. T. Thevenot, D. Baker, J. W. Eaton, and L. Tang, "Nanomaterial cytotoxicity is composition, size, and cell type dependent," *Particle and Fibre Toxicology*, vol. 7, article 22, 2010.
- [40] R. T. M. De Rosales, R. Tavaré, A. Glaria, G. Varma, A. Protti, and P. J. Blower, " ^{99m}Tc -bisphosphonate-iron oxide nanoparticle conjugates for dual-modality biomedical imaging," *Bioconjugate Chemistry*, vol. 22, no. 3, pp. 455–465, 2011.
- [41] M. Evertsson, P. Kjellman, M. Cinthio et al., "Combined Magnetomotive ultrasound, PET/CT, and MR imaging of ^{68}Ga -labelled superparamagnetic iron oxide nanoparticles in rat sentinel lymph nodes in vivo," *Scientific Reports*, vol. 7, article 4824, 2017.
- [42] H. Wang, R. Kumar, D. Nagesha, R. I. Duclos, S. Sridhar, and S. J. Gatley, "Integrity of ^{111}In -radiolabeled superparamagnetic iron oxide nanoparticles in the mouse," *Nuclear Medicine and Biology*, vol. 42, no. 1, pp. 65–70, 2015.
- [43] A. Lahooti, S. Sarkar, H. Saligheh Rad et al., "PEGylated superparamagnetic iron oxide nanoparticles labeled with ^{68}Ga as a PET/MRI contrast agent: a biodistribution study," *Journal of Radioanalytical and Nuclear Chemistry*, vol. 311, no. 1, pp. 769–774, 2017.
- [44] Ç. İçhedef, S. Teksöz, P. Ünak, E. İ. Medine, T. Ertay, and R. Bekiş, "Preparation and characterization of radiolabeled magnetic nanoparticles as an imaging agent," *Journal of Nanoparticle Research*, vol. 14, no. 8, article 1077, 2012.
- [45] D. Stamopoulos, E. Manios, V. Gogola, D. Niarchos, and M. Pissas, "On the biocompatibility of Fe_3O_4 ferromagnetic nanoparticles with human blood cells," *Journal of Nanoscience and Nanotechnology*, vol. 10, no. 9, pp. 6110–6115, 2010.
- [46] L. H. Reddy, J. L. Arias, J. Nicolas, and P. Couvreur, "Magnetic nanoparticles: design and characterization, toxicity and biocompatibility, pharmaceutical and biomedical applications," *Chemical Reviews*, vol. 112, no. 11, pp. 5818–5878, 2012.
- [47] F. Alexis, E. Pridgen, L. K. Molnar, and O. C. Farokhzad, "Factors affecting the clearance and biodistribution of polymeric nanoparticles," *Molecular Pharmaceutics*, vol. 5, no. 4, pp. 505–515, 2008.
- [48] C. Chouly, D. Pouliquen, I. Lucet, J. J. Jeune, and P. Jallet, "Development of superparamagnetic nanoparticles for MRI: effect of particle size, charge and surface nature on biodistribution," *Journal of Microencapsulation*, vol. 13, no. 3, pp. 245–255, 1996.

Review Article

Brain Tumor Diagnostics and Therapeutics with Superparamagnetic Ferrite Nanoparticles

Fahmeed Hyder^{1,2,3} and S. Manjura Hoque^{1,3,4}

¹Magnetic Resonance Research Center, Yale University, New Haven, CT, USA

²Department of Biomedical Engineering, Yale University, New Haven, CT, USA

³Department of Radiology and Biomedical Imaging, Yale University, New Haven, CT, USA

⁴Materials Science Division, Bangladesh Atomic Energy Commission, Dhaka, Bangladesh

Correspondence should be addressed to Fahmeed Hyder; fahmeed.hyder@yale.edu

Received 21 July 2017; Accepted 24 September 2017; Published 11 December 2017

Academic Editor: Paulo H. Rosado-de-Castro

Copyright © 2017 Fahmeed Hyder and S. Manjura Hoque. This is an open access article distributed under the Creative Commons Attribution License, which permits unrestricted use, distribution, and reproduction in any medium, provided the original work is properly cited.

Ferrite nanoparticles (F-NPs) can transform *both* cancer diagnostics and therapeutics. Superparamagnetic F-NPs exhibit high magnetic moment and susceptibility such that in presence of a static magnetic field transverse relaxation rate of water protons for MRI contrast is augmented to locate F-NPs (i.e., diagnostics) and exposed to an alternating magnetic field local temperature is increased to induce tissue necrosis (i.e., thermotherapy). F-NPs are modified by chemical synthesis of mixed spinel ferrites as well as their size, shape, and coating. Purposely designed drug-containing nanoparticles (D-NPs) can slowly deliver drugs (i.e., chemotherapy). Convection-enhanced delivery (CED) of D-NPs with MRI guidance improves glioblastoma multiforme (GBM) treatment. MRI monitors the location of chemotherapy when D-NPs and F-NPs are coadministered with CED. However superparamagnetic field gradients produced by F-NPs complicate MRI readouts (spatial distortions) and MRS (extensive line broadening). Since extracellular pH (pH_e) is a cancer hallmark, pH_e imaging is needed to screen cancer treatments. Biosensor imaging of redundant deviation in shifts (BIRDS) extrapolates pH_e from paramagnetically shifted signals and the pH_e accuracy remains unaffected by F-NPs. Hence effect of *both* chemotherapy and thermotherapy can be monitored (by BIRDS), whereas location of F-NPs is revealed (by MRI). Smarter tethering of nanoparticles and agents will impact GBM theranostics.

1. Introduction

The prognosis for patients with brain tumors remains poor despite surgical advances [1]. Thousands of intracranial malignancies are reported in United States each year, and, moreover, the incidence rates worldwide are rising faster [2]. The survival rate for patients with glioblastoma multiforme (GBM)—the most common malignant glioma in adults—is a little more than a year [3]. Although surgeries and survival rate improve, most GBMs remain difficult to treat [1]. Therefore novel approaches are needed for improved management of patients with malignant brain tumors, in terms of early diagnosis, tracking therapeutic response, and, of course, improved therapies.

1.1. Bypassing the Blood-Brain Barrier to Treat Brain Tumors. Most GBM patients undergoing chemotherapy usually

receive drugs systemically. However drugs injected into the body in this manner do not reach the tumor cells in pharmacologically relevant levels [4], which in part could be the reason for tumor recurrence while receiving chemotherapy [5]. An impediment to management of patients with malignant brain tumors is that the blood-brain barrier (BBB) obstructs efficient drug delivery for a vast majority of small- and large-molecule drugs [6]. Compared to vasculature in normal tissue, GBM tumors consist of abnormal vasculature comprised of proliferative, leaky, and unorganized blood vessels with necrotic cores [7]. Various approaches are being utilized to bypass the BBB, for example, implantation of biodegradable wafers [8]. However the most promising methods are based on bioengineered nanomaterials [9], in part, because their sizes are biologically relevant to cells, viruses, proteins, and genes.

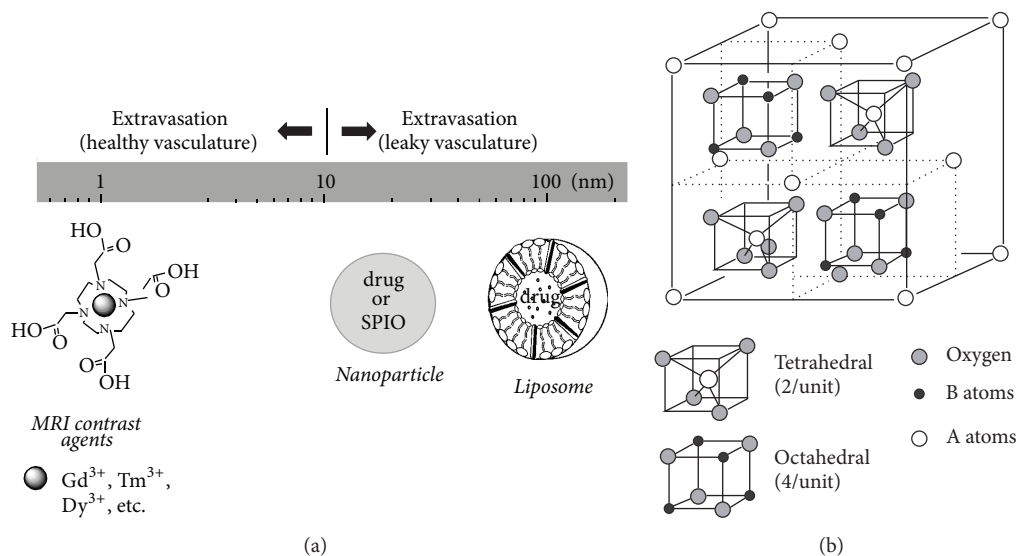


FIGURE 1: Nanomaterials and MRI contrast agents for cancer theranostics. (a) Size scaling of nanomaterials (e.g., liposomes, nanoparticles) and MRI contrast agents in relation to their extravasation when injected systemically. It is generally believed that in cancer the vasculature is more leaky [7]. Drug and/or SPIO can be encapsulated into nanomaterials. (b) Spinel ferrite structure showing tetrahedral and octahedral sites. There are 64 tetrahedral and 32 octahedral positions that are available for cations in one ferrite unit cell. However 12.5% and 75% of the tetrahedral and octahedral sites, respectively, are occupied by cations. See [14] for details.

A method for drug delivery across the BBB—approved in 1996 by the Federal Drug Agency (FDA)—is to insert drug-eluting materials into the brain, for example, either by direct implantation or by specific molecular targeting [4]. If sufficiently biocompatible nanomaterials are used to load the drugs, then the drug can be slowly released for treating diseases, for example, from neurodegeneration [11] to neurooncology [12]. This method is believed to provide the highest drug concentrations within a specific region of interest (ROI) that are most in need of the treatment, and thus, reduce many systemic side effects. The first nanomedicines were based on liposomes, and today there are several liposomal formulations for clinical therapy [13]. Liposomes are vesicles composed of lipid bilayers with an aqueous inner core, which is ideal for hydrophilic drugs. Nanoparticles are ideal for encapsulating hydrophobic drugs and their structure can be varied according to the design, synthesis, composition, and functionalization. Because many small- and large-molecule chemotherapy drugs are hydrophobic [6], drug-containing nanoparticles (D-NPs) will have significance in treatment of GBM patients [4]. By controlling the size of D-NPs, they maintain long retention times and they are not rapidly eliminated via the reticuloendothelial system (Figure 1(a)). When this feature is combined with the slow delivery of drugs in an ROI, the therapeutic effect can be quite significant [12].

It is believed that most treatments for malignant brain tumor fail because the cancer cells are infiltrative and invade beyond the site of origin [1], BBB blocks intravenous drugs from adequate distribution to regions of cell infiltration [6], and systemic toxicity significantly reduces effectiveness of current therapies [5]. These reasons have been the motivation for extensive developments of improved drug delivery methods. A promising strategy is bypassing the BBB and infusing

drugs directly into the tumor with intracranial catheters using a method called convection-enhanced delivery (CED) [23]. Although clinical studies show that CED is safe [24], most CED trials for GBM fail for two reasons: while small- or large-molecule drugs penetrate tissue, they disappear almost as soon as CED infusion stops [25]; infused drugs cannot be precisely delivered to tumor sites without intraprocedural visualization during the CED method itself (i.e., inability to track the location of chemotherapy) [4]. New technologies for D-NPs can meet these challenges. While D-NPs can be engineered for targeted delivery and controlled over long-term for slow drug release [12], loading drugs into nanocarriers like liposomes and nanoparticles (Figure 1(a)) can protect drugs from rapid clearance [26]. Thus use of D-NPs with CED shows some promise for GBM therapies [4].

1.2. Magnetic Nanoparticles in Treatment of Cancer. Magnetic nanoparticles (M-NPs) can be manipulated by external magnetic fields to provide a range of biomedical applications, that is, from providing novel cancer therapies to generating contrast for magnetic resonance imaging (MRI) [27]. M-NPs consist of the magnetic (e.g., inner core consisting of specific metal oxides) and chemical (i.e., outer core designed for functionality) components. M-NPs less than 30 nm in diameter become superparamagnetic to exhibit high magnetic moment and susceptibility—behavior that appears in both ferromagnetic or ferrimagnetic materials—but superparamagnetic properties are also controlled by how they are composed. Ferromagnetism occurs in several metallic elements because the magnetic moments align parallel to produce strong permanent magnets. Ferrimagnetism is similar to ferromagnetism (e.g., spontaneous magnetization, Curie temperatures, and magnetic hysteresis), but this

biocompatible family is based on superparamagnetic iron oxide nanoparticles (SPIO-NPs) and occurs in magnetite (Fe_3O_4) or its oxidized form, maghemite ($\gamma\text{-Fe}_2\text{O}_3$). Net magnetic moment arises when these nanomaterials are exposed to external magnetic fields, static or alternating.

SPIO-NPs combined with one or more additional metallic elements (e.g., Fe, Ni, Co, and Zn) are called ferrites and like M-NPs they have applications across a range of disciplines, from biomedical to industrial [14]. F-NPs are metal oxides with spinel structure with an AB_2O_4 formula, where A and B are cations located tetrahedrally (A atom; smaller and two per unit) and octahedrally (B atom; larger and four per unit) coordinated to oxygen atoms, respectively (Figure 1(b)). Recent studies show that F-NPs have novel applications in different areas of biomedical engineering [28, 29], for example, drug delivery [30], MRI contrast generation [31], and hyperthermia treatments [32]. One of the ways targeted cancer cells are killed is by heat induced by F-NPs on its immediate environment, which is achieved by exposing them to an alternating magnetic field (AMF) [14].

1.3. Magnetic Resonance Methods in Treatment of Cancer. Tissue contrast with MRI relies on relaxation of water protons (i.e., transverse (T_2^* or T_2) and longitudinal (T_1) time constants). Thus contrast depends on varying degrees of intrinsic values of transverse ($R_2^* = 1/T_2^*$ by gradient-echo or $R_2 = 1/T_2$ by spin-echo methods) and longitudinal ($R_1 = 1/T_1$ by inversion recovery or saturation recovery methods) relaxation rates of tissue water protons across tissues. However to generate additional distinction between tissues (e.g., tumor versus normal tissue) MRI contrast agents are used to enhance the relaxation rates, where the ROI darkens and brightens with R_2^* (or R_2) and R_1 agents, respectively. Gd^{3+} is a widely used R_1 agent, and it is the most efficient of all paramagnetic lanthanide ions at relaxing water protons because of its seven unpaired electrons. The FDA-approved Gd^{3+} -based agents, to reduce systemic toxicity, are complexed with macrocyclics, e.g., DOTA^{4-} (1,4,7,10-tetraazacyclododecane-1,4,7,10-tetraacetic acid) (Figure 1(a)) or variants like DOTMA^{4-} (1,4,7,10-tetramethyl 1,4,7,10-tetraazacyclododecane-1,4,7,10-tetraacetate), DOTP^{8-} (1,4,7,10-tetraazacyclododecane-1,4,7,10-tetrakis methylene phosphonate), and DTPA^{5-} (diethylenetriaminopentaacetic acid). Feridex is an FDA-approved version of SPIO-NPs, which is a strong R_2^* (or R_2) agent (Figure 1(a)). While the above-mentioned MRI methods are widely used to measure the tumor location and size, other MRI and MRS methods are used to measure the metabolic dysfunction of cancer cells (Figure 2).

A new MRI contrast called chemical exchange saturation transfer (CEST) is generated when a radio frequency (RF) pulse saturates a pool of exchangeable protons (e.g., amide/amine ($-\text{NH}_x$) or hydroxyl ($-\text{OH}$) protons) to decrease the steady-state proton signal arising from bulk water [33]. The amide proton transfer (APT) version of CEST, generated from proton exchange between protons of water and protons of endogenous mobile proteins and peptides, is enabled by saturation at 3.5 ppm downfield water. Given that such exchangeable protons (assumed to be arising from

endogenous mobile proteins and peptides in the cytoplasm) are abundant in tumor tissues compared to healthy tissues, generally 3-4% APT contrast increase is observed in intratumoral region compared to peritumoral region. The APT contrast increase suggests a rise in intracellular pH (pH_i). While further validation is needed for APT contrast, this has been shown to be responsive to temozolomide treatment in GBM [34]. The amine and amide concentration-independent detection (AACID) is another CEST contrast that combines influences from *both* amine and amide protons in a ratiometric manner such that the need to know the concentration of the exchangeable pool is removed [35]. The AACID contrast, enabled by independent saturations at both 2.75 ppm (amine) and 3.5 ppm (amide) downfield of water, has been validated to pH_i measured by ^{31}P MRS, which can measure pH_i from endogenous inorganic phosphate (P_i) shift and extracellular pH (pH_e) from exogenous 3-aminopropyl phosphonate (3-APP) shift, where 3-APP is nontoxic and does not cross the cell membrane [36]. The pH_e can also be measured by CEST methods, where the exchangeable proton group resides on the injected agent, which may or may not consist of a paramagnetic cation (i.e., diamagnetic CEST or paramagnetic CEST) [37, 38].

Recently a chemical shift imaging (CSI) based molecular imaging method called biosensor imaging of redundant deviation in shifts (BIRDS) was developed [39, 40], which uses the nonexchangeable protons on agents like TmDOTP^{5-} (i.e., not the effect of the agent on water proton relaxation) as the physiological readout. BIRDS agents demonstrate high signal-to-noise ratio (SNR) and specificity from the paramagnetically shifted proton signals, and this has been used for metabolic imaging (e.g., pH_e) in a wide range of brain tumors [20, 21, 41].

1.4. Metabolic Markers of Cancer. Metabolic studies describe the amount of energy needed for cellular building blocks versus cellular functional activity [42]. While these metabolic distinctions are fundamental for quantitative functional brain imaging [42], they are also very pertinent to cancer imaging because it is a disease that reflects out of control cell growth [15]. It is well known that rapidly growing cancer cells have high glycolytic rate (CMR_{glc}) in relation to rate of oxidative demand (CMR_{O_2}) [43]. All gliomas, specifically malignant brain tumors that progress to GBM, demonstrate uncoupling between CMR_{glc} and CMR_{O_2} even in presence of sufficient oxygen and thus generate excess lactate and H^+ in the intracellular space [15]. This process is known as aerobic glycolysis or the Warburg effect [43]. If these acidic constituents are not extruded out appropriately, their presence can radically perturb intracellular function (Figure 2(a)). Thus measuring the acidification of the extracellular milieu is very important for cancer research [15, 44], as extracellular acidosis affects many pathways linked to tumor growth (Figure 2(b)). However tumor cells have alkaline (or near neutral) pH_i compared to pH_e [16]. Figure 3 shows the pH_i - pH_e gradients measured in a variety of tumors versus normal tissue [16, 45, 46], indicating that pH_e is more acidic in tumors whereas pH_i in tumors is near neutral to alkaline. Thus measuring both pH_e and pH_i could be very important for brain cancer

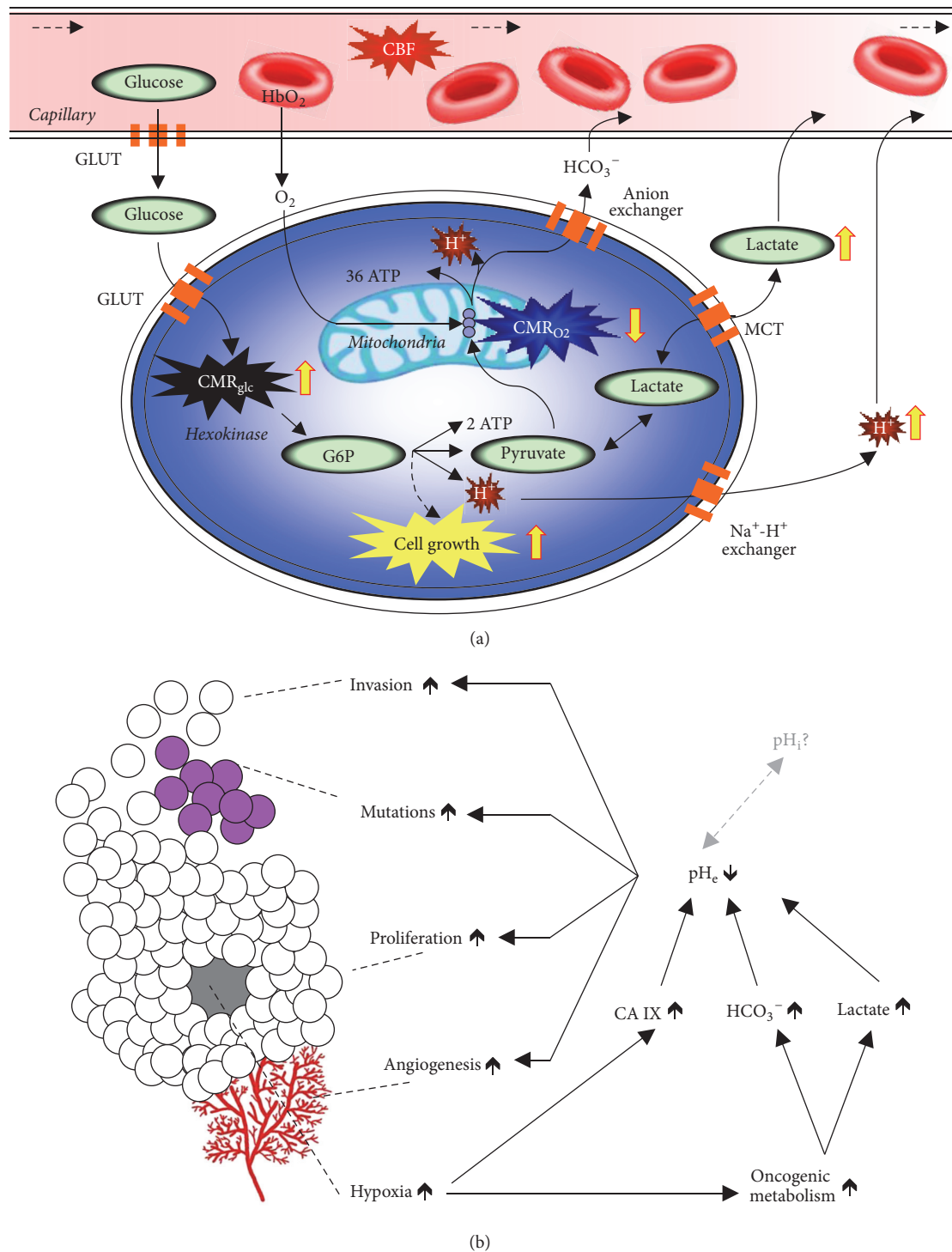


FIGURE 2: Relationship between tumor metabolism and tumor biology. (a) The tumor microenvironment, compared to the normal neuropil, is characterized by aerobic glycolysis and endothelial dysfunction [15]. CBF, cerebral blood flow; GLUT, glucose transporter; HbO₂, oxyhemoglobin; G6P, glucose-6-phosphate; H⁺, hydrogen ions; CMR_{glc}, glycolysis; CMR_{O₂}, oxidative phosphorylation; MCT, monocarboxylic acid transporters. To maintain intracellular pH homeostasis acidic constituents are extruded out to acidify the extracellular space. (b) Tumor biology is intricately linked to cancer metabolism. Tumor growth (i.e., invasion, mutation, and proliferation) has been linked to acidic pH_e arising from aerobic glycolysis [15]. The altered metabolic pathways, to support cell growth, create byproducts that are actively exported out of tumor cells to help maintain neutral intracellular pH (pH_i), but this comes at the cost of acidification of the extracellular milieu (pH_e). These multifaceted processes all decrease pH_e while maintaining near normal pH_i, which lead to tumor invasion, mutations, proliferation, and even angiogenesis.

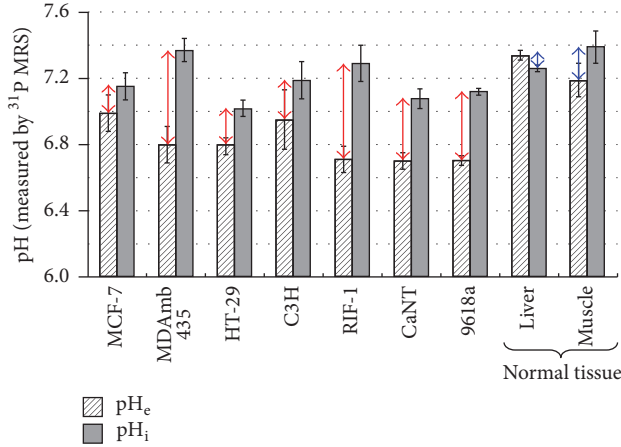


FIGURE 3: ³¹P MRS detection of 3-aminopropyl phosphonate (3-APP) and inorganic phosphate (P_i) for extracellular pH (pH_e) and intracellular pH (pH_i), respectively. The pH_i-pH_e gradient for different types of tumor (red arrows) and normal tissue (blue arrows). From [16] with permission.

research [15]. The superparamagnetic field gradients formed by F-NPs (i.e., >5 mg/kg Fe³⁺) hinder molecular readouts, specifically at high static magnetic field (B_0), due to spatial distortions from severe relaxation enhancement for MRI contrast [47] and extensive line broadening reducing MRS specificity/sensitivity [48]. Thus novel imaging methods are needed that are compatible with F-NPs so that *both* their physical location and therapeutic impact could be assessed, because these types of information will greatly benefit subsequent applications to GBM patients.

1.5. Outline. This review examines the value of F-NPs to impact *both* diagnostics and therapeutics for GBM treatment in preclinical translational research. The narrative begins with synthesis and characterization of F-NPs, because these procedures affect their magnetic properties and hence their ability to function as MRI contrast agents and provide AMF-induced heat therapy (Section 2). While MRI spots the location of F-NPs, the location of D-NPs is only monitored (by MRI) when D-NPs and F-NPs are coadministered with CED (Section 3). Since F-NPs generate large superparamagnetic fields specifically when delivered by CED, they obscure molecular readouts from *both* MRI (i.e., spatial distortions [47]) and MRS (i.e., extensive line broadening [48]). Given that pH_e is a biomarker of cancer progression and treatment, recent developments with a novel pH_e mapping method called BIRDS shows that readout capability remains unaffected by presence of F-NPs. In essence these results suggest that effects of *both* impact and location of therapy (i.e., chemotherapy from D-NPs and thermotherapy from F-NPs) can be monitored simultaneously (Section 4). Finally, smarter designs for nanoparticles and agents (i.e., better targeting, reduced toxicity, and higher SNR) in conjunction with the aforementioned bioengineering and bioimaging advances can considerably advance GBM theranostics in the near future (Section 5).

2. Synthesis and Characterization of Ferrite Nanoparticles

The effectiveness of M-NPs as mediators for hyperthermia has been studied since 1957 by Gilchrist and coworkers [49] who first conducted the heat induction experiments on M-NPs. Since the early hyperthermia studies with M-NPs, knowledge about heating mechanisms of M-NPs has advanced [50]. The magnetic heating of M-NPs originates from magnetic losses associated with the magnetization-demagnetization cycling, a process known as specific loss power (SLP), which is the ability for nanoparticles to dissipate energy in terms of heat. The SLP depends on eddy current loss, hysteresis loss, and residual loss, where the latter two are more critical for F-NPs.

Eddy current loss is induced by the AMF and thus depends on electrical resistivity. Magnetic heating is initiated by hysteresis loss and residual loss during AMF. Hysteresis loss is due to reversing the magnetization in the alternating current of the magnetic field, which is proportional to the area of the hysteresis loop. The residual loss is due to relaxation effects. When the alternating field is applied to M-NPs, their magnetic moments rotate following the magnetic field with an effective relaxation time (τ):

$$\frac{1}{\tau} = \frac{1}{\tau_N} + \frac{1}{\tau_B}, \quad (1a)$$

where τ_N is the Néel relaxation time:

$$\tau_N = \tau_o e^{KV/kT} \quad (1b)$$

and τ_B is the Brownian relaxation time:

$$\tau_B = \frac{3\eta V_H}{kT} \quad (1c)$$

and τ_o is the time constant with the value of 10^{-9} s, k is the Boltzmann constant, T is the temperature, η is the viscosity of the carrier fluid, K is the anisotropy constant of the nanoparticle, V is the volume of the nanoparticle, and V_H is the hydrodynamic volume of the nanoparticle. These indicate that the anisotropy, hydrodynamic volume, and physical size of the nanoparticle all greatly influence the effective relaxation time. Since the magnetic (i.e., magnetic moment and susceptibility) and physical (i.e., size, shape, and distributions) properties of the M-NPs dictate their behavior upon AMF induction (see [14] for details), thus SLP has to be measured per nanomaterial:

$$\text{SLP} = \frac{C}{m} \frac{\Delta T}{\Delta t} V_s, \quad (2)$$

where C is the sample heat capacity (i.e., the mass weighted mean value of the nanoparticle and water), m is mass of the magnetic materials, V_s is the sample volume, and $\Delta T/\Delta t$ is evaluated from the initial temperature rise (ΔT) over time (Δt). Since the nanoparticle C is small (i.e., tiny samples), water heat capacity ($4.18 \text{ Jg}^{-1}\text{K}^{-1}$) is considered instead for SLP estimation.

Since F-NPs are superparamagnetic (i.e., high magnetic moment and susceptibility), they provide strong enhancement of the observed transverse relaxation rate (R_2):

$$R_2 = R_2^0 + r_2 C_{\text{NP}}, \quad (3a)$$

where r_2 is the contrast agent's relaxivity, R_2^0 is the intrinsic relaxation rate, and C_{NP} is the nanoparticle concentration. Advanced MRI relaxation theories [51, 52] show that r_2 increases in the motional averaging regime (also known as the other sphere model), r_2 reaches maximum in the static dephasing regime, and r_2 decreases in the echo-limited regime. The diffusional motion is very fast in motional averaging regime and it follows that

$$R_2 = \frac{16}{45} f \tau_D (\Delta\omega)^2, \quad (3b)$$

where f is the volume fraction occupied by the nanoparticles in the suspension, $\Delta\omega (= \gamma\mu_0 M_v/3)$ is the angular frequency shift experienced by a proton at the equator of the nanoparticle, γ is the proton gyromagnetic ratio, M_v is the volume saturation magnetization, μ_0 is the magnetic permeability of vacuum, and $\tau_D (= d_{\text{NP}}^2/4D; D$ is the water diffusion constant and d_{NP} is the particle diameter) is the translational diffusion time of protons in magnetic field inhomogeneity created by nanoparticles. When water protons surround a small space compared to the outer shell (or hydrodynamic diameter) around the nanoparticle, the static dephasing regime is invoked and it follows that

$$R_2 = \frac{2\pi}{3\sqrt{3}} f \Delta\omega. \quad (3c)$$

For larger nanoparticles or agglomeration of smaller nanoparticles, R_2 is governed by the echo-limited regime where neither the motional averaging nor static dephasing regimes are effective. Overall, the factors that mediate R_2 are

$$R_2 = \frac{A}{d_{\text{NP}}} \frac{1}{D} \gamma^2 \mu^2 C_{\text{NP}} J(\omega, \tau_D), \quad (3d)$$

where A is a constant, μ is the magnetic moment of the nanoparticle, and $J(\omega, \tau_D)$ is the spectral density function. Since R_2 decreases directly with μ and inversely with d_{NP} , nanoparticles with higher moment and smaller size would reduce the amount of particles necessary to obtain efficient MRI contrast enhancement.

Physical properties of F-NPs can be tailored by controlling their size, morphology, and composition, whereas surface chemistry could be achieved by varying pH of solution, ionic strength, capping agent, reaction temperature, and ambient atmosphere [30–32]. Significant variations in anisotropy can be introduced by changing the shape of the nanoparticles [53], but this must happen in conjunction with the physicochemical characteristics of the nanoparticles that exert enhanced permeability and retention within the ROI to avoid nonspecific interactions [54]. F-NPs are not colloidally stable in aqueous media near neutral pH because the surface of the metal oxide is not electrostatically charged. Thus to

provide electrostatic or steric repulsion, the nanoparticles can be stabilized by biocompatible ligands, e.g., polyethylene glycol (PEG), poly(lactic-co-glycolic acid) (PLGA), dextran, or chitosan.

Lee and coworkers [50] developed highly anisotropic F-NPs with compositions of $\text{CoFe}_2\text{O}_4@ \text{MnFe}_2\text{O}_4$, $\text{CoFe}_2\text{O}_4@ \text{Fe}_3\text{O}_4$, $\text{MnFe}_2\text{O}_4@ \text{CoFe}_2\text{O}_4$, and $\text{Fe}_3\text{O}_4@ \text{CoFe}_2\text{O}_4$, where SLP was enhanced by one order of magnitude by coating compared to the bare components. They also compared the therapeutic effect of their anisotropic F-NPs and doxorubicin versus the isotropic Feridex and doxorubicin on cancer cells. Feridex is an FDA-approved version of SPIO-NPs, whereas doxorubicin is an anticancer chemotherapeutic drug. The F-NPs provided only thermotherapy upon AMF induction, whereas Feridex could provide AMF-induced thermotherapy and doxorubicin could provide continuous chemotherapy. The thermotherapy of F-NPs was shown to be more effective than Feridex (thermotherapy) and doxorubicin (chemotherapy) together. While this study showed that anisotropic F-NPs are far more effective in heat-induced mortality of cancer cells compared to isotropic SPIO-NPs, mechanisms relating anisotropy to SLP are still under debate.

Nándori and Rácz [55] studied hyperthermia with anisotropic M-NPs focusing on SLP under circularly polarized field. They found that below a critical anisotropy level the SLP remained unaltered, while above that critical limit SLP diminished with increasing anisotropy. Fortin and coworkers [56] studied a variety of different anisotropic maghemite and cobalt ferrite dispersed in aqueous suspension by electrostatic stabilization. They reported that the most important factors for heat are particle size, solvent viscosity, magnetic anisotropy, and the AMF frequency and amplitude. Prado and coworkers [57] demonstrated that enhancing anisotropy of maghemite by surface coordination enhanced the magnetic properties; that is, anisotropy increased from 26 to 65 kJ/m³, the blocking temperature (i.e., below this temperature magnetization is lost) increased from 11 to 30 K, and coercivity (i.e., resistance of a material to magnetization changes) increased from 62 to 839 Oe.

Poperechny and coworkers [58] performed experiments with single domain nanoparticles to show that with a uniaxial anisotropy low AMF frequency magnetic hyperthermia can be achieved. Habib and coworkers [59] showed that while the heating rate of Fe-Co nanoparticles increased with nanoparticle size, the heating rate increased/decreased with low/high anisotropy, that is, in the range of 5–25 kJ/m³ and 50–400 kJ/m³, respectively. These suggest that larger nanoparticle size with lower anisotropy may be more favorable for hyperthermia, but at the same time access of larger nanoparticles can provide delivery challenges. Given that Tackett and coworkers [60] showed a significant magnetocrystalline anisotropy difference between Fe_3O_4 and CoFe_2O_4 nanoparticles (i.e., 14 and 380 kJ/m³), Hoque and coworkers [10] hypothesized that the Fe-Co mixed spinel system will allow for effective tuning of the anisotropy.

Hoque and coworkers [10] synthesized Fe-Co mixed spinel ferrites by chemical coprecipitation (i.e., $\text{Fe}_x\text{Co}_{1-x}\text{Fe}_2\text{O}_4$, where $x = 0.8, 0.6, 0.4, 0.2$) using NH_4OH or NaOH , which required molar ratio of $[\text{M}^{2+}]/[\text{Fe}^{3+}]$ at

1:2 where M^{2+} is the salt of divalent Fe and Co dissolved in distilled water. To avoid Fe^{2+} oxidation, all reactions were carried out in N_2 at normal room temperature. Highly concentrated coprecipitating agents were quickly added under basic conditions ($pH = 11$) and the precipitate was collected through high centrifugation. The magnetic properties were analyzed by superconducting quantum interference device magnetometer at room temperature. Structural characterizations were performed by X-ray diffraction (XRD) and transmission electron microscopy (TEM). The grain size was determined from the width of the 311 peak in the XRD spectrum, whereas the lattice parameter was measured from the d values and the peak positions of respective XRD spectra. Mössbauer spectroscopy examined the Fe valence. The blocking temperature was measured by zero-field cooled measurements of bare nanoparticles with an applied field lower than the coercive field. The hydrodynamic diameter was measured by dynamic light scattering. MRI relaxivity was measured at B_0 of 11.7 T. AMF-induced heat induction heating was carried out on a solid-state induction power supply with a field of 400 kHz and amplitude of 76 mT. Toxicity profile of coated Fe-Co mixed spinel ferrites was examined on 9L tumor cell cultures.

The $Fe_xCo_{1-x}Fe_2O_4$ characterization data are shown in Figure 4 and Table 1. Although the shapes of the nanoparticles were slightly nonspherical in the bare and coated states, the TEM bright field images of the bare nanoparticles showed some agglomeration, but upon coating the nanoparticles were well dispersed (Figure 4(a)). The average size of the nanoparticle from TEM in the bare state (~ 7 nm) was different from the XRD data (3–5 nm) (Table 1). The XRD patterns were representative of high crystallinity with well-indexed peaks associated with single-phase ferrites. The grain sizes ranged from 3 to 5 nm. The lattice parameters were slightly larger (~ 8.5 nm) than the TEM depicted size (~ 7 nm), whereas the hydrodynamic diameter was about an order of magnitude larger with chitosan or PEG coatings (100–150 nm). The bulk size parameters remained relatively constant with increasing Co content and no significant difference was found with the coprecipitation techniques. However with increasing Co content the blocking temperature and maximum magnetization both increased significantly. The maximum magnetization increased with coating versus bare nanoparticles, and these patterns were also observed for coercivity and MRI relaxivity.

The Mössbauer spectra (Figure 4(b)) demonstrated slow relaxation for $Fe_{0.8}Co_{0.2}Fe_2O_4$ and $Fe_{0.2}Co_{0.8}Fe_2O_4$ synthesized by chemical coprecipitation using NH_4OH and $NaOH$, respectively, whereas a mixture of slow/fast relaxation was observed for all other compositions. These spectra were best fitted with 4–6 components corresponding to Fe^{3+} situated on the tetrahedral A sites of the spinel structure, while the remaining Fe^{2+} and Fe^{3+} were on the nonequivalent octahedral B sites (see Figure 1(b)). AMF-induced heating for the nanoensembles was quite comparable with either coating except for PEG-coated $Fe_{0.2}Co_{0.8}Fe_2O_4$, which was twice as less efficient as the others (Figure 4(c)). AMF-induced cell death of 9L tumor cells showed no significant differences with either coating using a dose of 4 mg/mL (Figure 4(c)). This study with Fe-Co mixed spinel ferrites suggests that chitosan

and PEG coating of most compositions will have good potential for cancer therapy. While another study by Hoque and coworkers [61] on the Fe-Zn mixed spinel system with regard to chitosan and PEG coatings arrives at a very similar conclusion, other biocompatible coatings for nanoparticles like PLGA [19] and dextran [62] could also be considered for future considerations. However it is crucial to assess the toxicity of any nanoparticle, either bare or in conjunction with its coating [63].

3. Monitoring the Location of Chemotherapy from Drug-Containing Nanoparticles

If D-NPs are deposited into a specific ROI, then, designing F-NPs in the same fashion as the D-NPs, the location of chemotherapy delivered by the nanoparticles can also be observed with MRI. CED is a strategy to facilitate targeted delivery of drugs into specific brain ROIs [23]. The insertion of microcatheters directly towards the brain tumor, as guided by MRI, is considered to be a minimally invasive surgical procedure. While CED of various types of drugs has been shown to be clinically safe [24], monitoring the actual convective process or the volume of injected drug has proven to be vital in the optimization of the CED procedure [64].

Theoretical considerations [17] suggest that the effective delivery volume by a CED injection is much larger than an intraparenchymal injection (Figure 5(a)). Contrasting CED with diffusion-based methods clarifies the difference. The drug injected directly into the parenchyma usually requires a larger cannula (up to 2 mm, e.g., for microdialysis), and thus this process typically displaces the parenchyma at the tip of the cannula to form a cavity-like bulb from which diffusion of the drug occurs only within that small tissue volume. Hence the primary mechanism of drug spread with intraparenchymal injection is diffusion and the distance is usually a few mm around the cannula tip. The typical CED cannula is much narrower (150–200 μm) and is intricately attached to a finely controlled pump that provides very slow infusion rates (0.2–5.0 $\mu L/min$). This allows pressurized extracellular bulk flow in addition to diffusion (i.e., convection plus diffusion) so that the homogenous distribution of materials in the infusate can spread across significant distances (estimated to be up to several cm in the human brain) from the infusion cannula tip. Moreover, typically the infusion cannula extends beyond the outer guide to minimize reflux or backflow along the cannula. When these effective volume advantages of CED (versus intraparenchymal injection methods) are combined with nanoparticles (which provide slow delivery over extended durations), the impact for treatment can be quite significant.

Practical considerations need to accurately image the convective volume of the infusate [64]. Previously Zhou and coworkers [12] conjugated N-(4-[^{18}F]fluorobenzyl)propanamido—a positron emission tomography (PET) tracer—to the surface of D-NPs and injected them by CED into rat brain to demonstrate the effective volume of D-NPs by PET. While PET was useful in this diagnostic purpose of the tracking the D-NPs, due to the short half-life of PET isotopes and high cost of PET scans, recent investigations

TABLE I: Physical characterization of $\text{Fe}_x\text{Co}_{1-x}\text{Fe}_2\text{O}_4$ (where $x = 0.8, 0.6, 0.4, 0.2$) for bare and coated (chitosan, PEG) nanoparticles using different coprecipitating agents (NH_4OH , NaOH) for chemical synthesis. See Figure 4 for other details [10].

x	Method used	Grain size (nm)	Lattice (\AA)	Blocking temperature ($^\circ\text{C}$)	Hydrodynamic diameter (nm)		Maximum magnetization (emu/g)				Coercivity (Oe)		Relaxivity ($\text{mM}^{-1}\text{s}^{-1}$)	
					Chitosan	PEG	Bare	Chitosan	PEG	Bare	Chitosan	PEG	Chitosan	PEG
0.8	NH_4OH	4.0 (± 0.6)	8.48 (± 0.06)	-100	97.5	158.3	59.3	37.2	26.0	3.5	2.08	1.4	528 (± 26)	314 (± 25)
0.6	NH_4OH	4.5 (± 0.1)	8.52 (± 0.26)	25	135.5	154.5	55.3	28.0	20	20	7.5	8.6	509 (± 45)	441 (± 12)
0.4	NH_4OH	2.8 (± 0.1)	8.45 (± 0.20)	65	140.6	159.1	43.6	25.2	16.9	157	4.2	4.8	326 (± 37)	310 (± 5)
0.2	NH_4OH	—	—	100	110.0	155.5	32.3	—	—	506	—	—	—	—
0.2	NaOH	4.9 (± 0.1)	8.43 (± 0.05)	—	—	—	73.1	54.5	46.6	673	11.5	7.8	769 (± 92)	377 (± 14)

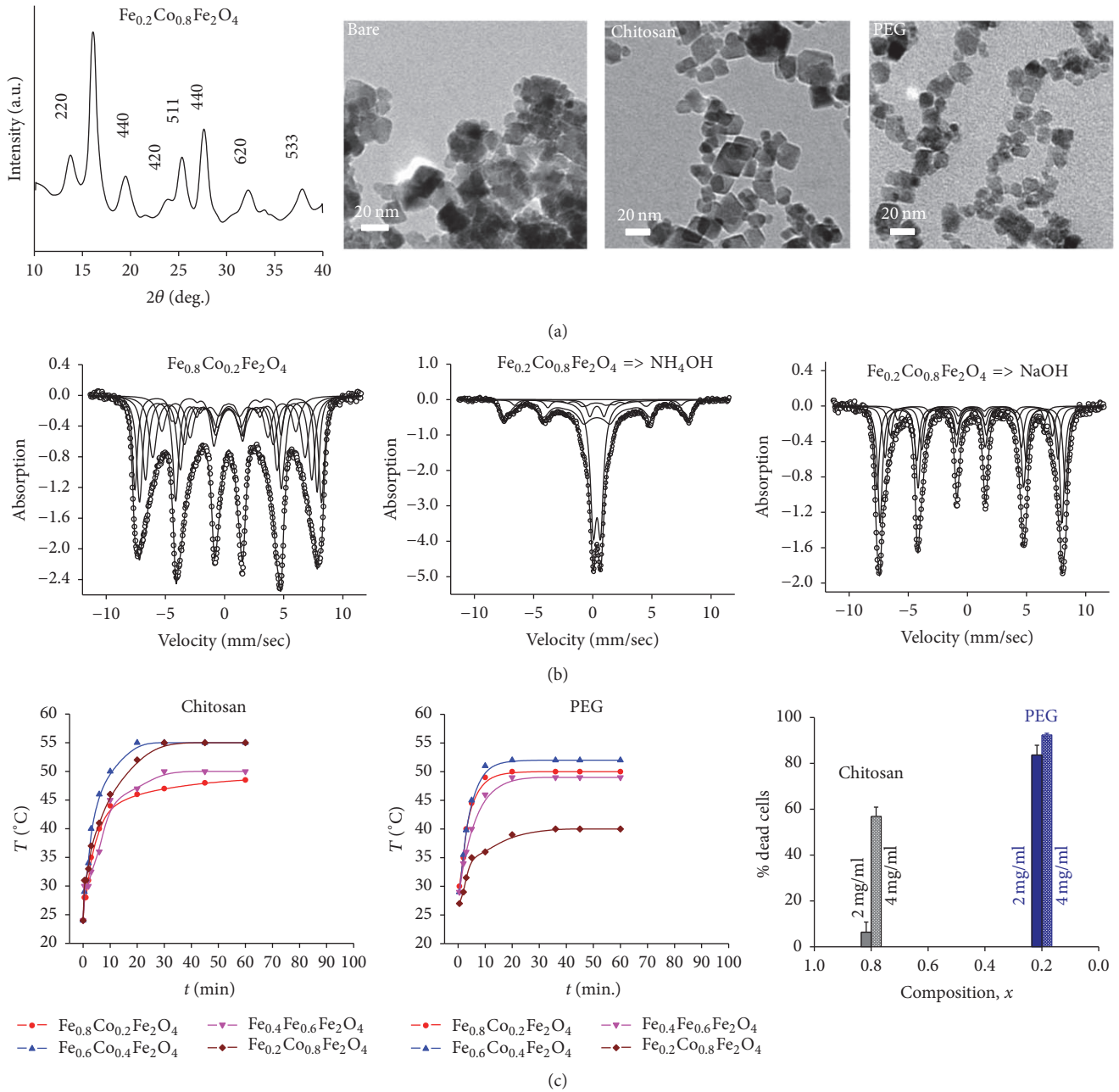


FIGURE 4: Characterization of $\text{Fe}_x\text{Co}_{1-x}\text{Fe}_2\text{O}_4$ nanoparticles. (a) XRD (left) and TEM (from left to right) data of $\text{Fe}_{0.2}\text{Co}_{0.8}\text{Fe}_2\text{O}_4$ with bare nanoparticles as well as chitosan and PEG-coated nanoparticles, respectively. (b) Mössbauer spectra at room temperature for the compositions $\text{Fe}_{0.8}\text{Co}_{0.2}\text{Fe}_2\text{O}_4$ with NH_4OH coprecipitating agent (left), $\text{Fe}_{0.2}\text{Co}_{0.8}\text{Fe}_2\text{O}_4$ with NH_4OH coprecipitating agent (middle), and $\text{Fe}_{0.2}\text{Co}_{0.8}\text{Fe}_2\text{O}_4$ with NaOH coprecipitating agent (right). Slow relaxation is observed for $x = 0.8$ and $x = 0.2$ synthesized by NH_4OH and NaOH , respectively, as the coprecipitating agent, while other compositions showed mixture of slow/fast relaxation. (c) Heating profiles of Fe-Co mixed spinel ferrites at a concentration of 2 mg/mL of the nanoparticles in water for different compositions coated with chitosan (left) and PEG (middle). The right panel shows the concentration dependence of the nanoparticles in solution for mortality of 9L cells exposed to AMF-induced heating for 30 minutes with chitosan (gray) and PEG (blue) coating. From [10] with permission. See Table 1 for other details [10].

have attempted to measure the effective CED volume by both T_1 -weighted [18] and T_2 -weighted [19] MRI methods so that continuous monitoring of the infusate volume in relation to the tumor itself can be obtained.

Mardor and coworkers [18] used T_1 -weighted MRI in normal rat brain (cannula in striatum) to show differences

between poor, moderate, and efficient CED experiments. They determined the effective volume of CED by mixing GdDTPA^{2-} and Evans blue in the infusate prior to infusion, where the latter ex vivo test validated the former in vivo test. High correlation between the GdDTPA^{2-} (Figure 5(b)) and Evans blue (Figure 5(c)) data was observed, suggesting that

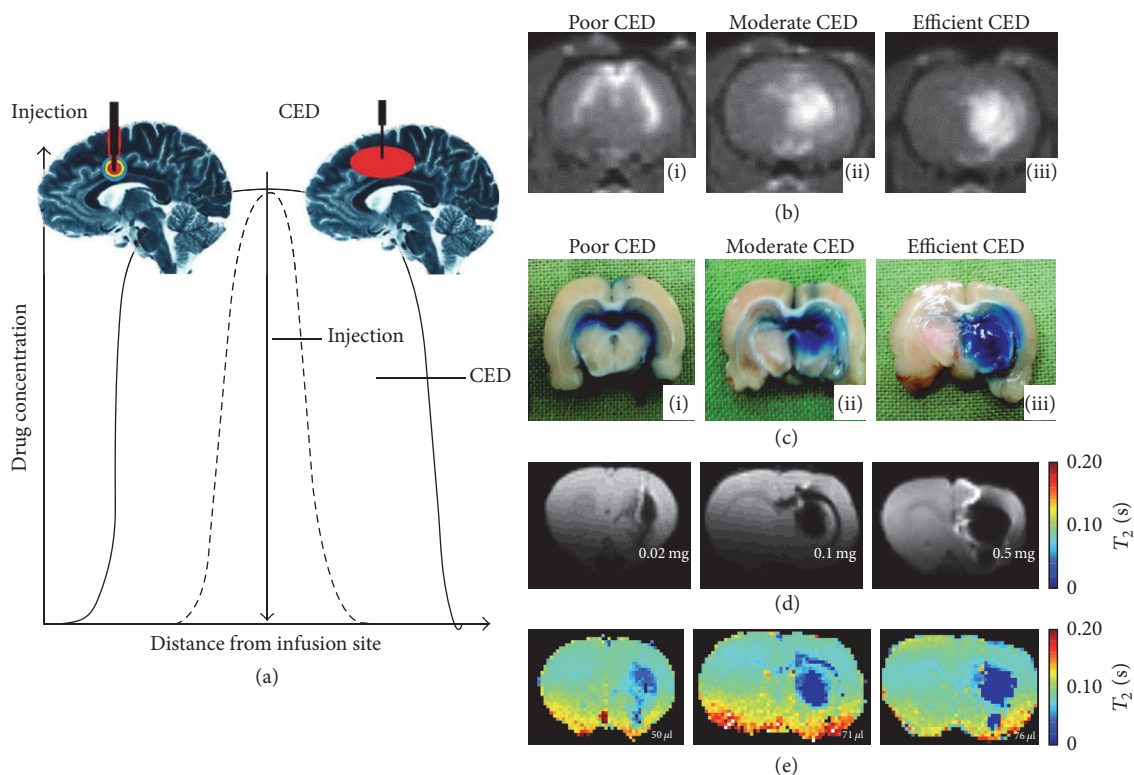


FIGURE 5: Theoretical and experimental considerations of CED for effective drug delivery. (a) 2D representation of effective convection-enhanced region with intraparenchymal drug injection (small red circle; black dashed line) and CED injected drug (large red oval; black solid line). From [17] with permission. CED in normal rat brain, where the infusate contained GdDTPA²⁻ and Evans blue together, showing examples from three separate rats with different effective convection-enhanced region as depicted by (b) T_1 -weighted MRI at B_0 of 3.0 T and (c) Evans blue staining for poor, moderate, and efficient CED conditions. From [18] with permission. CED demonstrated with T_2 -weighted MRI at B_0 of 4.0 T, where the 20 μL infusate contained 0.02 mg, 0.1 mg, and 0.5 mg of SPIO-NPs injected into three normal rats resulting in doses of 1, 5, and 25 mg/kg Fe^{3+} , respectively. These respective Fe^{3+} doses were represented as either (d) spin-echo images with an echo time of less than 80 ms and (e) absolute T_2 images. The effective volumes were 50 μL , 71 μL , and 76 μL , respectively, based on either the spin-echo images in (d) or T_2 images in (e). From [19] with permission.

T_1 -weighted MRI can accurately represent the CED volume. In these experiments the CED conditions were purposely varied so that poor, moderate, and efficient CED volumes were achieved. For example, poor CED was characterized by significant backflow along the catheter and into the ventricles with almost no enhancement in the striatum, whereas efficient CED was represented by even spread in the striatum with minimal backflow into the ventricles. Similarly, Strohhahn and coworkers [19] used T_2 -weighted MRI in normal rat brain (cannula in striatum) to measure effective volumes for different amounts of D-NPs injected by CED (Figures 5(d) and 5(e)). Using SPIO-NPs (1–25 mg/kg Fe^{3+}), they tracked the D-NPs injected with both spin-echo and T_2 images over several weeks. Given that the SNR of T_2 -weighted MRI is higher, this method is preferred over the T_1 -weighted MRI method.

4. Monitoring the Therapeutic Response in Presence of Ferrite Nanoparticles

Recently a ^1H MRS method called BIRDS was introduced [39, 40, 65] to meet the challenge of providing absolute

pH_e readout in presence of large superparamagnetic field gradients created by F-NPs, specifically when delivered by CED. It is based on detecting the paramagnetic agent itself (e.g., TmDOTP⁵⁻), and it combines high molecular specificity/sensitivity in the same 3D-CSI platform, where the pH_e readout even at 1 μL resolution provides insights into metabolism of the tumor versus the neighboring healthy/nontumor tissue.

The essence of the method is as follows. While a ^1H spectrum of the chelating agent (e.g., without the Tm³⁺ ion) shows conventional diamagnetic shifts spread over a narrow range (~ 5 ppm), a ^1H spectrum of the complexed agent (e.g., with the Tm³⁺ ion) shows unusual paramagnetic shifts spread much farther apart (>100 ppm). These extremely wide paramagnetically shifted signals also have unusual relaxation properties (i.e., T_1 and T_2 of the paramagnetic protons are in the ms range, instead of hundreds to thousands of ms for typical diamagnetic protons) because the protons are proximal to the unpaired electrons [66]. Because of the extremely short relaxation times of these widely shifted signals, ultrashort excitation RF pulses are used (i.e., μs range), and by using the Shinnar-Le Roux algorithm for

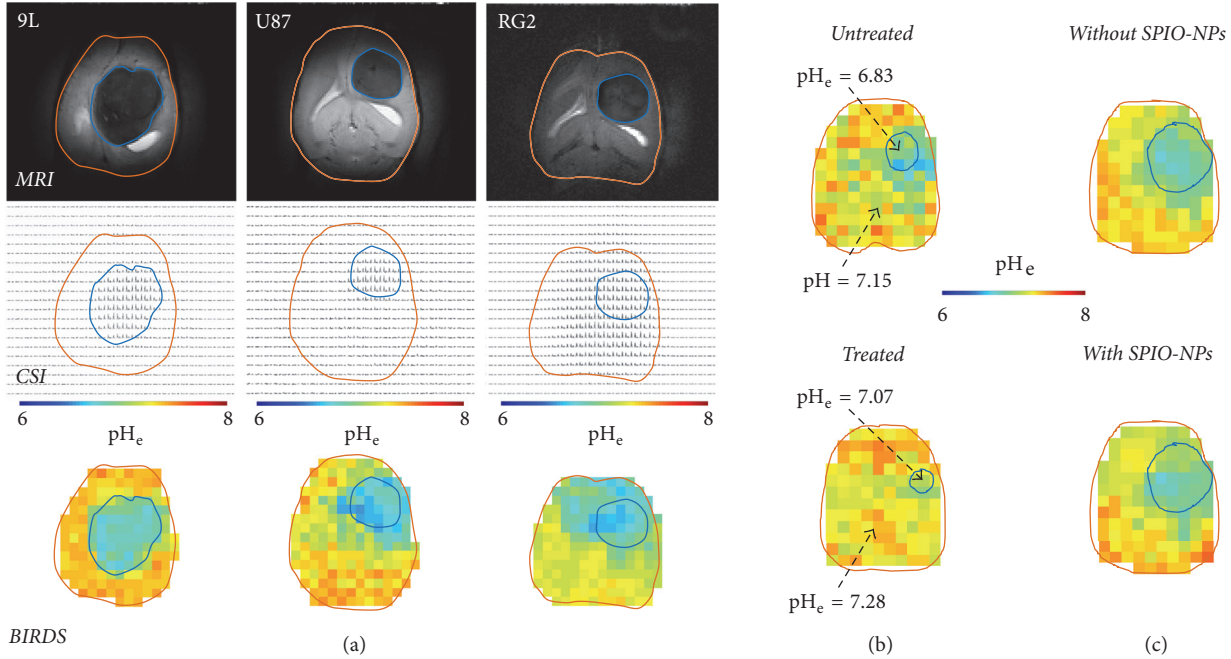


FIGURE 6: BIRDS-based pH_e mapping of different brain tumors at B_0 of 11.7 T. (a) Representative T_2 -weighted MRI with TmDOTP^{5-} (top row), CSI of protons on TmDOTP^{5-} (middle row), and pH_e map by BIRDS (bottom row) of rats bearing 9L, U87, and RG2 tumors during probenecid- TmDOTP^{5-} coinjection. The tumor boundaries in CSI and BIRDS data (blue line) are from the MRI-defined region outlined by contrast enhancement arising from TmDOTP^{5-} . From [20] with permission. (b) Representative pH_e maps from BIRDS in untreated (top) and temozolamide-treated (bottom) different rats bearing U251 tumors. The tumor boundary in BIRDS data (blue line) are from the MRI-defined region outlined by contrast enhancement arising from TmDOTP^{5-} . From [21] with permission. (c) Representative pH_e maps from BIRDS before (top) and after (bottom) injection of SPIO-NPs in the same rat bearing an RG2 tumor. A SPIO-NPs dose of 7.3 mg/kg Fe^{3+} was injected systemically. The tumor boundaries in BIRDS data (blue line) are from the MRI-defined region outlined by contrast enhancement arising from SPIO-NPs dose of 1.7 mg/kg Fe^{3+} in the tumor. From [22] with permission.

the RF pulses, the signals on both sides of water can be simultaneously excited without exceeding FDA safety limits for in vivo MRI/MRS experiments.

These relaxation/shift properties of the probe (e.g., TmDOTP^{5-}) enable high-resolution and high speed CSI, and, furthermore, the signals are impervious to poor B_0 shim conditions. Because the T_2/T_1 ratio remains high (i.e., ~ 1 for paramagnetic protons versus ~ 0.1 for diamagnetic protons), the molecular readout is largely unaffected across different B_0 . While all of these features of paramagnetic agents combined into one imaging platform for BIRDS are distinctive [20–22, 39–41, 67, 68], there are other studies using these types of agents for bioimaging [69–97]. Since the chemical shift depends on vector L between the proton and the unpaired electrons, factors like temperature and protonation can alter the geometry and thus change the relative shift. The total shift term, $\Delta\delta_O$, is modeled as

$$\Delta\delta_O = C_T\Delta T + C_{\text{pH}}\Delta\text{pH} + C_X\Delta[X], \quad (4)$$

where both temperature (T) and pH can change simultaneously, $C_T = (\Delta\delta_O/\Delta T)_{\text{pH}}$ is the temperature dependence at a given pH, $C_{\text{pH}} = (\Delta\delta_O/\Delta\text{pH})_T$ is the pH dependence at a given temperature, and the much weaker C_X term is for effects arising from cation X . Because the molecular readout by BIRDS is based on shifts, the method is independent of

agent dose, diffusion, blood flow, and vessel permeability. However ROIs with high vessel permeability (e.g., tumor tissue) reveal higher peaks.

Recent BIRDS studies by Coman and coworkers [41] and Huang and coworkers [20], both at B_0 of 11.7 T using a pH-sensitive TmDOTP^{5-} probe, measured pH_e in rat brain containing various types of gliomas, that is, 9L, RG2, and U87 [20, 41]. The agent's clearance was perturbed to build up the agent concentration in the circulation, either by injecting the agent alone upon renal ligation [41] or by coinjecting the agent with probenecid (i.e., an organic anion transporter inhibitor) to enable longitudinal scans [20]. Generally a higher agent concentration and thus higher SNR for BIRDS was achieved with the former method, but the pH_e mapping was shown to be independent of the agent dose using the latter method.

Upon BIRDS agent infusion, MRI identified the tumor boundary by enhanced relaxation because of TmDOTP^{5-} (i.e., its paramagnetic effect on R_2 of water protons) and BIRDS allowed pH_e mapping of brains with different gliomas (Figure 6(a)). While the intratumoral pH_e was acidic for all glioma types, the peritumoral pH_e varied with the tumor type. For example, in RG2 (and U87) tumors acidic pH_e was found in distal peritumoral regions beyond the RG2 (and U87) tumor border which corresponded to increased

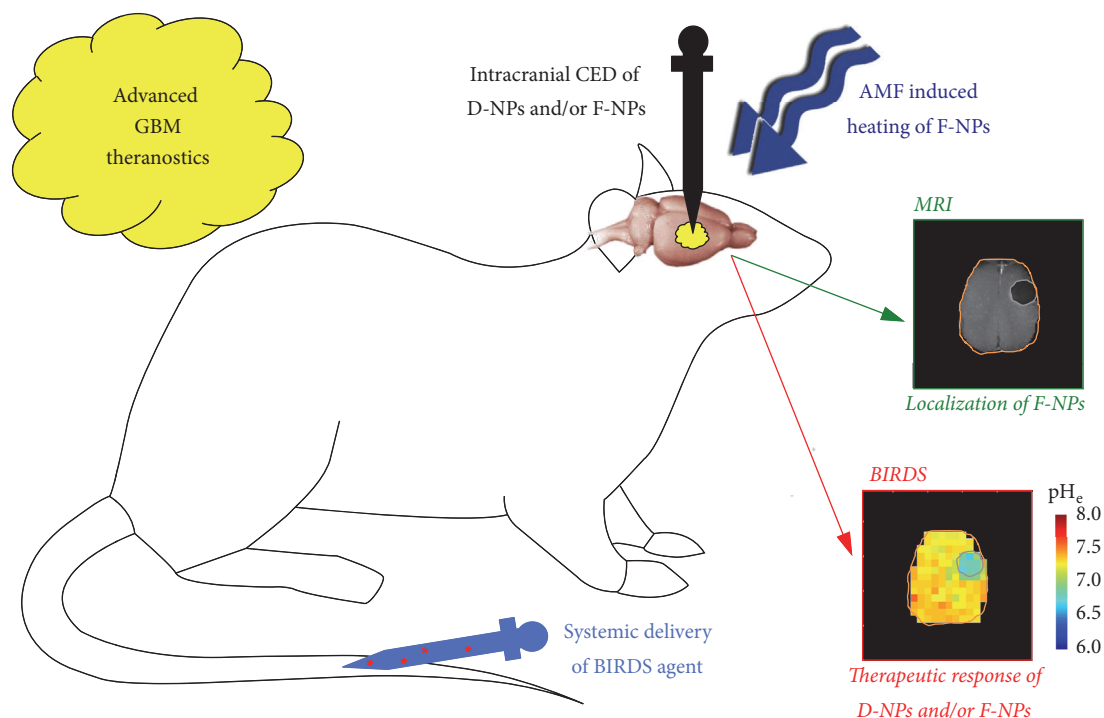


FIGURE 7: Advanced GBM theranostics. Intracranial CED of D-NPs is used to deliver high concentration chemotherapy over prolonged periods directly into the tumor. However when intracranial CED of D-NPs is combined with F-NPs, MRI can be used to monitor the location of the chemotherapy. Alternatively, intracranial CED of F-NPs alone can be used to provide thermotherapy by AMF-induced heating. BIRDS, which requires systemic injection of an imaging agent, can measure responses to chemotherapy from D-NPs and thermotherapy from F-NPs, because BIRDS is unaffected by the superparamagnetic field gradients generated by F-NPs. The MRI and BIRDS data shown are from [22] with permission.

presence of Ki-67 positive cells, and this was not the case with 9L tumor which is a far less aggressive tumor [41].

Given these exciting pH_e results with BIRDS, Rao and coworkers measured U251 tumors with and without temozolomide, a DNA alkylating agent [21]. Treated rats had reduced tumor volume and higher pH_e compared to untreated rats (Figure 6(b)), and these findings were supported by reduced proliferation (Ki-67 staining) and apoptosis induction (cleaved caspase-3 staining) examined within the tumor boundaries of treated rats. Since GBM treatment is hampered by a lack of bioimaging methodologies that can simultaneously and noninvasively measure location of F-NPs and response to therapeutic benefits of F-NPs, Maritim and coworkers [22] demonstrated that quantitative pH_e imaging using BIRDS in different gliomas is compatible with MRI contrast from SPIO-NPs for tumor delineation. It was found that the pH_e inside and outside the MRI-defined tumor boundary remained unaffected after the infusion of 7.3 mg/kg Fe³⁺ SPIO-NPs (Figure 6(c)), regardless of whether the tumor was aggressive or not (9L versus RG2) or the agent injection method was terminal or not (renal ligation versus coinjection with probenecid).

5. Future Theranostics for Brain Tumors

The aforementioned advances show great potential for GBM theranostics with current technologies to impact both

chemotherapy from D-NPs and thermotherapy from F-NPs. The therapeutic response can be measured by BIRDS, and this can be achieved at the same time as determining the location of F-NPs by MRI (Figure 7). But new imaging methods could provide greater metabolic insights. Unlike BIRDS, which allows pH_e mapping, CEST-based imaging of pH_i is incompatible with F-NPs at doses greater than 5 mg/kg Fe³⁺ because superparamagnetic field gradients create challenges for MRI contrast (due to extensive spatial distortions) [47] and MRS specificity (due to extreme line broadening) [48] needed for molecular imaging. Although in vivo pH_e mapping by BIRDS has been shown to be unaffected with SPIO-NPs dose of ~7 mg/kg Fe³⁺ [22], in vitro studies suggest that the pH_e mapping limit can extend up to 3 times higher doses of SPIO-NPs [68]. However, whenever D-NPs alone are used, CEST and BIRDS can be combined to obtain both pH_i and pH_e information together. While FDA-approved versions of F-NPs are already available, further research and approvals are needed to translate novel imaging methods that require infusion of exogenous imaging probes. Regardless of this, these novel imaging methods are valuable for preclinical research and have significant clinical relevance because xenografted human GBM cells directly injected into an animal brain represent an accurate GBM model [98–100].

Nanoparticles can be bioengineered for drug delivery into the brain [101] using endogenous methods like transcytosis

(e.g., adsorptive-mediated [102], carrier-mediated [103], and receptor-mediated [104]) or targeting the disease itself [105] to transient disruption of the BBB by ultrasound [106]. Future designs of F-NPs (or D-NPs) could incorporate these modifications to their surfaces for improved cancer targeting, which may even alleviate the need for intraoperative CED. However these surface modifications of F-NPs should be attentive to anisotropy, hydrodynamic volume, and physical size, which all greatly influence the effective relaxation enhancement. Since F-NPs are not colloiddally stable in aqueous media, the biocompatible coatings should allow for some electrostatic charge build-up. The imaging advances in conjunction with smarter designs of agents could be even greater for GBM theranostics. Compatibility of BIRDS with various nanoensembles such as SPIO-NPs, GdDTPA²⁻, liposomes, and even dendrimers [68, 107] may create exciting opportunities for multimodal imaging of drug response. Therefore, development of next generation imaging agents along with surface modification of nanoparticles will allow simultaneous detection of therapy response and location will greatly impact GBM theranostics.

Abbreviations

AACID:	Amine and amide concentration-independent detection
AMF:	Alternating magnetic field
3-APP:	3-Aminopropyl phosphonate
APT:	Amide proton transfer
B_0 :	Static magnetic field
BBB:	Blood-brain barrier
BIRDS:	Biosensor imaging of redundant deviation in shifts
CED:	Convection-enhanced delivery
CEST:	Chemical exchange saturation transfer
CSI:	Chemical shift imaging
DOTA ⁴⁻ :	1,4,7,10-Tetraazacyclododecane-1,4,7,10-tetraacetic acid
DOTMA ⁴⁻ :	1,4,7,10-Tetramethyl 1,4,7,10-tetraazacyclododecane-1,4,7,10-tetraacetate
DOTP ⁸⁻ :	1,4,7,10-Tetraazacyclododecane-1,4,7,10-tetrakis methylene phosphonate
DTPA ⁵⁻ :	Diethylenetriamine pentaacetic acid
D-NPs:	Drug-containing nanoparticles
F-NPs:	Ferrite nanoparticles
FDA:	Federal Drug Agency
GBM:	Glioblastoma multiforme
M-NPs:	Magnetic nanoparticles
MRI:	Magnetic resonance imaging
MRS:	Magnetic resonance spectroscopy
pH _e :	Extracellular pH
pH _i :	Intracellular pH
P _i :	Inorganic phosphate
RF:	Radio frequency
ROI:	Region of interest
SLP:	Specific loss power
SNR:	Signal-to-noise ratio
SPIO-NPs:	Superparamagnetic iron oxide nanoparticles

TEM: Transmission electron microscopy
XRD: X-ray diffraction.

Conflicts of Interest

The authors declare no conflicts of interest.

Authors' Contributions

Fahmeed Hyder and S. Manjura Hoque wrote the paper.

Acknowledgments

This work is supported by NIH Grants (R01 EB-023366 and P30 NS-052519).

References

- [1] A. R. Asthagiri, N. Pouratian, J. Sherman, G. Ahmed, and M. E. Shaffrey, "Advances in Brain Tumor Surgery," *Neurologic Clinics*, vol. 25, no. 4, pp. 975–1003, 2007.
- [2] <http://www.cancer.gov/>, 2014.
- [3] C. B. Scott, C. Scarantino, R. Urtasun et al., "Validation and predictive power of Radiation Therapy Oncology Group (RTOG) recursive partitioning analysis classes for malignant glioma patients: a report using RTOG 90-06," *International Journal of Radiation Oncology, Biology, Physics*, vol. 40, pp. 51–55.
- [4] J. Zhou, K.-B. Atsina, B. T. Himes, G. W. Strohhahn, and W. M. Saltzman, "Novel delivery strategies for glioblastoma," *Cancer Journal*, vol. 18, no. 1, pp. 89–99, 2012.
- [5] S. Sathornsumetee and J. N. Rich, "New treatment strategies for malignant gliomas," *Expert Review of Anticancer Therapy*, vol. 6, no. 7, pp. 1087–1104, 2006.
- [6] W. M. Pardridge, "Blood-brain barrier delivery," *Drug Discovery Therapy*, vol. 12, no. 1-2, pp. 54–61, 2007.
- [7] J. Blakeley, "Drug delivery to brain tumors," *Current Neurology and Neuroscience Reports*, vol. 8, no. 3, pp. 235–241, 2008.
- [8] A. Gutenberg, C. B. Lumenta, W. E. K. Braunsdorf et al., "The combination of carmustine wafers and temozolomide for the treatment of malignant gliomas. a comprehensive review of the rationale and clinical experience," *Journal of Neuro-Oncology*, vol. 113, no. 2, pp. 163–174, 2013.
- [9] F. Re, M. Gregori, and M. Masserini, "Nanotechnology for neurodegenerative disorders," *Nanomedicine: Nanotechnology, Biology and Medicine*, vol. 8, no. 1, pp. S51–S58, 2012.
- [10] S. M. Hoque, Y. Huang, E. Cocco et al., "Improved specific loss power on cancer cells by hyperthermia and MRI contrast of hydrophilic FexCoI-xFe2O4 nanoensembles," *Contrast Media & Molecular Imaging*, vol. 11, no. 6, pp. 514–526, 2016.
- [11] G. Modi, V. Pillay, Y. E. Choonara, V. M. K. Ndesendo, L. C. du Toit, and D. Naidoo, "Nanotechnological applications for the treatment of neurodegenerative disorders," *Progress in Neurobiology*, vol. 88, no. 4, pp. 272–285, 2009.
- [12] J. Zhou, T. R. Patel, R. W. Sirianni et al., "Highly penetrative, drug-loaded nanocarriers improve treatment of glioblastoma," *Proceedings of the National Academy of Sciences of the United States of America*, vol. 110, no. 29, pp. 11751–11756, 2013.
- [13] A. Z. Wang, R. Langer, and O. C. Farokhzad, "Nanoparticle delivery of cancer drugs," *Annual Review of Medicine*, vol. 63, pp. 185–198, 2012.

- [14] K. K. Kefeni, T. A. M. Msagati, and B. B. Mamba, "Ferri-rite nanoparticles: Synthesis, characterisation and applications in electronic device," *Materials Science and Engineering: B Advanced Functional Solid-State Materials*, vol. 215, pp. 37–55, 2017.
- [15] R. A. Gatenby and R. J. Gillies, "Why do cancers have high aerobic glycolysis?" *Nature Reviews Cancer*, vol. 4, no. 11, pp. 891–899, 2004.
- [16] A. I. Hashim, X. Zhang, J. W. Wojtkowiak, G. V. Martinez, and R. J. Gillies, "Imaging pH and metastasis," *NMR in Biomedicine*, vol. 24, no. 6, pp. 582–591, 2011.
- [17] S. J. Allen, J. J. Watson, D. K. Shoemark, N. U. Barua, and N. K. Patel, "GDNF, NGF and BDNF as therapeutic options for neurodegeneration," *Pharmacology & Therapeutics*, vol. 138, no. 2, pp. 155–175, 2013.
- [18] Y. Mardor, O. Zahav, Y. Zauberman et al., "Convection-enhanced drug delivery: Increased efficacy and magnetic resonance image monitoring," *Cancer Research*, vol. 65, no. 15, pp. 6858–6863, 2005.
- [19] G. Strohbehn, D. Coman, L. Han et al., "Imaging the delivery of brain-penetrating PLGA nanoparticles in the brain using magnetic resonance," *Journal of Neuro-Oncology*, vol. 121, no. 3, pp. 441–449, 2015.
- [20] Y. Huang, D. Coman, P. Herman, J. U. Rao, S. Maritim, and F. Hyder, "Towards longitudinal mapping of extracellular pH in gliomas," *NMR in Biomedicine*, vol. 29, no. 10, pp. 1364–1372, 2016.
- [21] J. U. Rao, D. Coman, J. J. Walsh, M. M. Ali, Y. Huang, and F. Hyder, "Temozolomide arrests glioma growth and normalizes intratumoral extracellular pH," *Scientific Reports*, vol. 7, no. 1, article no. 7865, 2017.
- [22] S. Maritim, D. Coman, Y. Huang, J. U. Rao, J. J. Walsh, and F. Hyder, "Mapping extracellular pH of gliomas in presence of superparamagnetic nanoparticles: towards imaging the distribution of drug-containing nanoparticles and their curative effect on the tumor microenvironment," *Contrast Media and Molecular Imaging*, Article ID 3849373.
- [23] R. Hunt Bobo, D. W. Laske, A. Akbasak, P. F. Morrison, R. L. Dedrick, and E. H. Oldfield, "Convection-enhanced delivery of macromolecules in the brain," *Proceedings of the National Academy of Sciences of the United States of America*, vol. 91, no. 6, pp. 2076–2080, 1994.
- [24] S. Kunwar, S. Chang, M. Westphal et al., "Phase III randomized trial of CED of IL13-PE38QQR vs Gliadel wafers for recurrent glioblastoma," *Neuro-Oncology*, vol. 12, no. 8, pp. 871–881, 2010.
- [25] J. H. Sampson, G. Archer, C. Pedain et al., "Poor drug distribution as a possible explanation for the results of the PRECISE trial," *Journal of Neurosurgery*, vol. 113, no. 2, pp. 301–309, 2010.
- [26] H. Sarin, "On the future development of optimally-sized lipid-insoluble systemic therapies for CNS solid tumors and other neuropathologies," *Recent Patents on CNS Drug Discovery*, vol. 5, no. 3, pp. 239–252, 2010.
- [27] Q. A. Pankhurst, J. Connolly, S. K. Jones, and J. Dobson, "Applications of magnetic nanoparticles in biomedicine," *Journal of Physics D: Applied Physics*, vol. 36, no. 13, pp. R167–R181, 2003.
- [28] J. Lee, Y. Huh, Y. Jun et al., "Artificially engineered magnetic nanoparticles for ultra-sensitive molecular imaging," *Nature Medicine*, vol. 13, no. 1, pp. 95–99, 2007.
- [29] M. S. Thu, L. H. Bryant, T. Coppola et al., "Self-assembling nanocomplexes by combining ferumoxytol, heparin and protamine for cell tracking by magnetic resonance imaging," *Nature Medicine*, vol. 18, no. 3, pp. 463–467, 2012.
- [30] Y. Okuhata, "Delivery of diagnostic agents for magnetic resonance imaging," *Advanced Drug Delivery Reviews*, vol. 37, no. 1–3, pp. 121–137, 1999.
- [31] H. B. Na, I. C. Song, and T. Hyeon, "Inorganic nanoparticles for MRI contrast agents," *Advanced Materials*, vol. 21, no. 21, pp. 2133–2148, 2009.
- [32] R. Ghosh, L. Pradhan, Y. P. Devi et al., "Induction heating studies of Fe₃O₄ magnetic nanoparticles capped with oleic acid and polyethylene glycol for hyperthermia," *Journal of Materials Chemistry*, vol. 21, no. 35, pp. 13388–13398, 2011.
- [33] K. M. Ward and R. S. Balaban, "Determination of pH using water protons and chemical exchange dependent saturation transfer (CEST)," *Magnetic Resonance in Medicine*, vol. 44, no. 5, pp. 799–802, 2000.
- [34] K. Sagiya, T. Mashimo, O. Togao et al., "In vivo chemical exchange saturation transfer imaging allows early detection of a therapeutic response in glioblastoma," *Proceedings of the National Academy of Sciences of the United States of America*, vol. 111, no. 12, pp. 4542–4547, 2014.
- [35] N. McVicar, A. X. Li, D. F. Gonçalves et al., "Quantitative tissue pH measurement during cerebral ischemia using amine and amide concentration-independent detection (AACID) with MRI," *Journal of Cerebral Blood Flow & Metabolism*, vol. 34, no. 4, pp. 690–698, 2014.
- [36] R. J. Gillies, Z. Liu, and Z. Bhujwala, "31P-MRS measurements of extracellular pH of tumors using 3-aminopropylphosphonate," *American Journal of Physiology-Cell Physiology*, vol. 267, no. 1, pp. C195–C203, 1994.
- [37] L. Q. Chen, E. A. Randtke, K. M. Jones, B. F. Moon, C. M. Howison, and M. D. Pagel, "Evaluations of tumor acidosis within in vivo tumor models using parametric maps generated with AcidoCEST MRI," *Molecular Imaging and Biology*, vol. 17, no. 4, pp. 488–496, 2015.
- [38] B. Yoo and M. D. Pagel, "An overview of responsive MRI contrast agents for molecular imaging," *Frontiers in Bioscience*, vol. 13, no. 5, pp. 1733–1752, 2008.
- [39] D. Coman, H. K. Trubel, R. E. Rycyna, and F. Hyder, "Brain temperature and pH measured by ¹H chemical shift imaging of a thulium agent," *NMR in Biomedicine*, vol. 22, no. 2, pp. 229–239, 2009.
- [40] D. Coman, R. A. De Graaf, D. L. Rothman, and F. Hyder, "In vivo three-dimensional molecular imaging with Biosensor Imaging of Redundant Deviation in Shifts (BIRDS) at high spatiotemporal resolution," *NMR in Biomedicine*, vol. 26, no. 11, pp. 1589–1595, 2013.
- [41] D. Coman, Y. Huang, J. U. Rao et al., "Imaging the intratumoral-peritumoral extracellular pH gradient of gliomas," *NMR in Biomedicine*, vol. 29, no. 3, pp. 309–319, 2016.
- [42] F. Hyder and D. L. Rothman, "Advances in Imaging Brain Metabolism," *Annual Review of Biomedical Engineering*, vol. 19, no. 1, pp. 485–515, 2017.
- [43] O. Warburg, "On the origin of cancer cells," *Science*, vol. 123, no. 3191, pp. 309–314, 1956.
- [44] R. J. Harris, T. F. Cloughesy, L. M. Liau et al., "pH-weighted molecular imaging of gliomas using amine chemical exchange saturation transfer MRI," *Neuro-Oncology*, vol. 17, no. 11, pp. 1514–1524, 2015.
- [45] Z. M. Bhujwala, D. Artemov, P. Ballesteros, S. Cerdan, R. J. Gillies, and M. Solaiyappan, "Combined vascular and extracellular pH imaging of solid tumors," *NMR in Biomedicine*, vol. 15, no. 2, pp. 114–119, 2002.

- [46] N. Raghunand, M. I. Altbach, R. Van Sluis et al., "Plasmalemmal pH-gradients in drug-sensitive and drug-resistant MCF-7 human breast carcinoma xenografts measured by 31P magnetic resonance spectroscopy," *Biochemical Pharmacology*, vol. 57, no. 3, pp. 309–312, 1999.
- [47] T. P. Murillo, C. Sandquist, P. M. Jacobs, G. Nesbit, S. Manninger, and E. A. Neuwelt, "Imaging brain tumors with ferumoxtran-10, a nanoparticle magnetic resonance contrast agent," *Thérapie*, vol. 2, no. 6, pp. 871–882, 2005.
- [48] G. Le Duc, L. V. Elst, J. M. Colet et al., "Ultrasmall particulate iron oxides as contrast agents for magnetic resonance spectroscopy: A dose-effect study," *Journal of Magnetic Resonance Imaging*, vol. 13, no. 4, pp. 619–626, 2001.
- [49] R. K. Gilchrist, R. Medal, W. D. Shorey, R. C. Hanselman, J. C. Parrott, and C. B. Taylor, "Selective inductive heating of lymph nodes," *Annals of Surgery*, vol. 146, pp. 596–606, 1957.
- [50] J.-H. Lee, J.-T. Jang, J.-S. Choi et al., "Exchange-coupled magnetic nanoparticles for efficient heat induction," *Nature Nanotechnology*, vol. 6, no. 7, pp. 418–422, 2011.
- [51] B. Issa, I. M. Obaidat, B. A. Albiss, and Y. Haik, "Magnetic nanoparticles: Surface effects and properties related to biomedicine applications," *International Journal of Molecular Sciences*, vol. 14, no. 11, pp. 21266–21305, 2013.
- [52] A. Roch, R. N. Muller, and P. Gillis, "Theory of proton relaxation induced by superparamagnetic particles," *The Journal of Chemical Physics*, vol. 110, no. 11, pp. 5403–5411, 1999.
- [53] H. M. Joshi, Y. P. Lin, M. Aslam et al., "Effects of shape and size of cobalt ferrite nanostructures on their MRI contrast and thermal activation," *The Journal of Physical Chemistry C*, vol. 113, no. 41, pp. 17761–17767, 2009.
- [54] X. Duan and Y. Li, "Physicochemical characteristics of nanoparticles affect circulation, biodistribution, cellular internalization, and trafficking," *Small*, vol. 9, no. 9–10, pp. 1521–1532, 2013.
- [55] I. Nándori and J. Rácz, "Magnetic particle hyperthermia: Power losses under circularly polarized field in anisotropic nanoparticles," *Physical Review E: Statistical, Nonlinear, and Soft Matter Physics*, vol. 86, Article ID 061404, 2012.
- [56] J.-P. Fortin, C. Wilhelm, J. Servais, C. Ménager, J.-C. Bacri, and F. Gazeau, "Size-sorted anionic iron oxide nanomagnets as colloidal mediators for magnetic hyperthermia," *Journal of the American Chemical Society*, vol. 129, no. 9, pp. 2628–2635, 2007.
- [57] Y. Prado, N. Daffé, A. Michel et al., "Enhancing the magnetic anisotropy of maghemite nanoparticles via the surface coordination of molecular complexes," *Nature Communications*, vol. 6, Article ID 10139, 2015.
- [58] I. S. Poperechny, Y. L. Raikher, and V. I. Stepanov, "Dynamic magnetic hysteresis in single-domain particles with uniaxial anisotropy," *Physical Review B: Condensed Matter and Materials Physics*, vol. 82, no. 17, Article ID 174423, 2010.
- [59] A. H. Habib, C. L. Ondeck, P. Chaudhary, M. R. Bockstaller, and M. E. McHenry, "Evaluation of iron-cobalt/ferrite core-shell nanoparticles for cancer radiotherapy," *Journal of Applied Physics*, vol. 103, no. 7, Article ID 07A307, 2008.
- [60] R. Tackett, C. Sudakar, R. Naik, G. Lawes, C. Rablau, and P. P. Vaishnava, "Magnetic and optical response of tuning the magnetocrystalline anisotropy in Fe₃O₄ nanoparticle ferrofluids by Co doping," *Journal of Magnetism and Magnetic Materials*, vol. 320, no. 21, pp. 2755–2759, 2008.
- [61] S. M. Hoque, M. S. Hossain, S. Choudhury, S. Akhter, and F. Hyder, "Synthesis and characterization of ZnFe₂O₄ nanoparticles and its biomedical applications," *Materials Letters*, vol. 162, pp. 60–63, 2016.
- [62] S. Palchoudhury, F. Hyder, T. K. Vanderlick, and N. Geerts, "Water-soluble anisotropic iron oxide nanoparticles: Dextran-coated crystalline nanoplates and nanoflowers," *Particulate Science and Technology*, vol. 32, no. 3, pp. 224–233, 2014.
- [63] N. Singh, G. J. Jenkins, R. Asadi, and S. H. Doak, "Potential toxicity of superparamagnetic iron oxide nanoparticles (SPION)," *Nano Reviews*, vol. 1, article 5358, 2010.
- [64] N. J. Szerlip, S. Walbridge, L. Yang et al., "Real-time imaging of convection-enhanced delivery of viruses and virus-sized particles," *Journal of Neurosurgery*, vol. 107, no. 3, pp. 560–567, 2007.
- [65] D. Coman, H. K. Trubel, and F. Hyder, "Brain temperature by Biosensor Imaging of Redundant Deviation in Shifts (BIRDS): Comparison between TmDOTP5- and TmDOTMA-," *NMR in Biomedicine*, vol. 23, no. 3, pp. 277–285, 2010.
- [66] A. Abragam, *Principles of Nuclear Magnetism*, Oxford University Press, Oxford, UK, 1961.
- [67] H. K. F. Trübel, P. K. Maciejewski, J. H. Farber, and F. Hyder, "Brain temperature measured by 1H-NMR in conjunction with a lanthanide complex," *Journal of Applied Physiology*, vol. 94, no. 4, pp. 1641–1649, 2003.
- [68] S. Maritim, Y. Huang, D. Coman, and F. Hyder, "Characterization of a lanthanide complex encapsulated with MRI contrast agents into liposomes for biosensor imaging of redundant deviation in shifts (BIRDS)," *Journal of Biological Inorganic Chemistry*, vol. 19, no. 8, pp. 1385–1398, 2014.
- [69] D. C. Buster, M. M. C. A. Castro, C. F. G. C. Geraldles, C. R. Malloy, A. D. Sherry, and T. C. Siemers, "Tm(DOTP)5-: A 23Na+ shift agent for perfused rat hearts," *Magnetic Resonance in Medicine*, vol. 15, no. 1, pp. 25–32, 1990.
- [70] N. Bansal, M. J. Germann, I. Lazar, C. R. Malloy, and A. D. Sherry, "In vivo Na-23 MR imaging and spectroscopy of rat brain during TmDOTP5- infusion," *Journal of Magnetic Resonance Imaging*, vol. 2, no. 4, pp. 385–391, 1992.
- [71] N. Bansal, M. J. Germann, V. Seshan, G. T. Shires III, C. R. Malloy, and A. D. Sherry, "Thulium 1,4,7,10-tetraazacyclododecane-1,4,7,10-tetrakis(methylene phosphonate) as a 23Na shift reagent for the in vivo rat liver," *Biochemistry*, vol. 32, no. 21, pp. 5638–5643, 1993.
- [72] C. F. G. C. Geraldles, A. D. Sherry, I. Lázár et al., "Relaxometry, animal biodistribution, and magnetic resonance imaging studies of some new gadolinium (III) macrocyclic phosphinate and phosphonate monoester complexes," *Magnetic Resonance in Medicine*, vol. 30, no. 6, pp. 696–703, 1993.
- [73] Z. F. Xia, J. W. Horton, P. Y. Zhao et al., "In vivo studies of cellular energy state, pH, and sodium in rat liver after thermal injury," *J Appl Physiol*, vol. 76, pp. 1507–1511, 1994.
- [74] V. Seshan, M. J. Germann, P. Preisig, C. R. Malloy, A. Dean Sherry, and N. Bansal, "Tmdotp5- as a 23na shift reagent for the in vivo rat kidney," *Magnetic Resonance in Medicine*, vol. 34, no. 1, pp. 25–31, 1995.
- [75] A. D. Sherry, J. Ren, J. Huskens et al., "Characterization of Lanthanide(III) DOTP complexes: thermodynamics, protonation, and coordination to alkali metal ions," *Inorganic Chemistry*, vol. 35, no. 16, pp. 4604–4612, 1996.
- [76] C. S. Zuo, J. L. Bowers, K. R. Metz, T. Nosaka, A. D. Sherry, and M. E. Clouse, "TmDOTP5-: A substance for NMR temperature measurements in vivo," *Magnetic Resonance in Medicine*, vol. 36, no. 6, pp. 955–959, 1996.
- [77] W. D. Kim, G. E. Kiefer, J. Huskens, and A. Dean Sherry, "NMR Studies of the Lanthanide(III) Complexes of 1,4,7,10-Tetraazacyclododecane-1,4,7,10-tetrakis(methanephosphonic acid

- mono(2',2'-trifluoroethyl) ester)," *Inorganic Chemistry*, vol. 36, no. 18, pp. 4128–4134, 1997.
- [78] P. M. Winter, V. Seshan, J. D. Makos, A. D. Sherry, C. R. Malloy, and N. Bansal, "Quantitation of intracellular [Na⁺] in vivo by using TmDOTP⁵⁻ as an NMR shift reagent and extracellular marker," *Journal of Applied Physiology*, vol. 85, no. 5, pp. 1806–1812, 1998.
- [79] C. S. Zuo, K. R. Metz, Y. Sun, and A. D. Sherry, "NMR temperature measurements using a paramagnetic lanthanide complex," *Journal of Magnetic Resonance*, vol. 133, no. 1, pp. 53–60, 1998.
- [80] J.-M. Colet, N. Bansal, C. R. Malloy, and A. D. Sherry, "Multiple quantum filtered ²³Na NMR spectroscopy of the isolated, perfused rat liver," *Magnetic Resonance in Medicine*, vol. 41, no. 6, pp. 1127–1135, 1999.
- [81] P. M. Winter and N. Bansal, "Triple-quantum-filtered (²³Na) NMR spectroscopy of subcutaneously implanted 9L gliosarcoma in the rat in the presence of TmDOTP(5-1)," *Journal of Magnetic Resonance*, vol. 152, no. 1, pp. 70–78, 2001.
- [82] P. M. Winter and N. Bansal, "TmDOTP⁵⁻ as a ²³Na shift reagent for the subcutaneously implanted 9L gliosarcoma in rats," *Magnetic Resonance in Medicine*, vol. 45, no. 3, pp. 436–442, 2001.
- [83] R. Zhou, N. Bansal, D. B. Leeper, S. Pickup, and J. D. Glickson, "Enhancement of hyperglycemia-induced acidification of human melanoma xenografts with inhibitors of respiration and ion transport," *Academic Radiology*, vol. 8, no. 7, pp. 571–582, 2001.
- [84] S. K. Hekmatyar, H. Poptani, A. Babsky, D. B. Leeper, and N. Bansal, "Non-invasive magnetic resonance thermometry using thulium-1,4,7,10-tetraazacyclododecane-1,4,7,10-tetraacetate (TmDOTA(-)), " *International Journal of Hyperthermia*, vol. 18, no. 3, pp. 165–179, 2002.
- [85] A. Babsky, S. K. Hekmatyar, S. Wehrli, D. Nelson, and N. Bansal, "Effects of temperature on intracellular sodium, pH and cellular energy status in RIF-1 tumor cells," *NMR in Biomedicine*, vol. 17, no. 1, pp. 33–42, 2004.
- [86] A. Babsky, S. K. Hekmatyar, T. Gorski, D. S. Nelson, and N. Bansal, "Heat-induced changes in intracellular Na⁺, pH and bioenergetic status in superfused RIF-1 tumour cells determined by ²³Na and ³¹P magnetic resonance spectroscopy," *International Journal of Hyperthermia*, vol. 21, no. 2, pp. 141–158, 2005.
- [87] A. M. Babsky, S. K. Hekmatyar, H. Zhang, J. L. Solomon, and N. Bansal, "Application of ²³Na MRI to monitor chemotherapeutic response in RIF-1 tumors," *Neoplasia*, vol. 7, no. 7, pp. 658–666, 2005.
- [88] S. K. Hekmatyar, P. Hopewell, S. K. Pakin, A. Babsky, and N. Bansal, "Noninvasive MR thermometry using paramagnetic lanthanide complexes of 1,4,7,10-tetraazacyclododecane- $\alpha, \alpha, \alpha, \alpha$ -tetramethyl-1, 4,7,10-tetraacetic acid (DOTMA4-)," *Magnetic Resonance in Medicine*, vol. 53, no. 2, pp. 294–303, 2005.
- [89] S. K. Hekmatyar, R. M. Kerkhoff, S. K. Pakin, P. Hopewell, and N. Bansal, "Noninvasive thermometry using hyperfine-shifted MR signals from paramagnetic lanthanide complexes," *International Journal of Hyperthermia*, vol. 21, no. 6, pp. 561–574, 2005.
- [90] S. K. Pakin, S. K. Hekmatyar, P. Hopewell, A. Babsky, and N. Bansal, "Non-invasive temperature imaging with thulium 1,4,7, 10-tetraazacyclododecane- 1,4,7, 10-tetramethyl-1,4,7, 10-tetraacetic acid (TmDOTMA-)," *NMR in Biomedicine*, vol. 19, no. 1, pp. 116–124, 2006.
- [91] M. Hentschel, P. Wust, W. Wlodarczyk et al., "Non-invasive MR thermometry by 2D spectroscopic imaging of the Pr[MOE-DO3A] complex," *International Journal of Hyperthermia*, vol. 14, no. 5, pp. 479–493, 1998.
- [92] W. Wlodarczyk, R. Boroschewski, M. Hentschel, P. Wust, G. Mönich, and R. Felix, "Three-dimensional monitoring of small temperature changes for therapeutic hyperthermia using MR," *Journal of Magnetic Resonance Imaging*, vol. 8, no. 1, pp. 165–174, 1998.
- [93] M. Hentschel, W. Dreher, P. Wust, S. Röhl, D. Leibfritz, and R. Felix, "Fast spectroscopic imaging for non-invasive thermometry using the Pr[MOE-DO3A] complex," *Physics in Medicine and Biology*, vol. 44, no. 10, pp. 2397–2408, 1999.
- [94] W. Wlodarczyk, M. Hentschel, P. Wust et al., "Comparison of four magnetic resonance methods for mapping small temperature changes," *Physics in Medicine and Biology*, vol. 44, no. 2, pp. 607–624, 1999.
- [95] K. H. Chalmers, E. De Luca, N. H. M. Hogg et al., "Design principles and theory of paramagnetic fluorine-labelled lanthanide complexes as probes for (¹⁹F) magnetic resonance: a proof-of-concept study," *Chemistry - A European Journal*, vol. 16, no. 1, pp. 134–148, 2010.
- [96] P. K. Senanayake, N. J. Rogers, K.-L. N. A. Finney et al., "A new paramagnetically shifted imaging probe for MRI," *Magnetic Resonance in Medicine*, vol. 77, no. 3, pp. 1307–1317, 2017.
- [97] K. N. Finney, A. C. Harnden, N. J. Rogers et al., "Simultaneous Triple Imaging with Two PARASHIFT Probes: Encoding Anatomical, pH and Temperature Information using Magnetic Resonance Shift Imaging," *Chemistry - A European Journal*, vol. 23, no. 33, pp. 7976–7989, 2017.
- [98] K. M. Hulse, T. Mashimo, A. Banerjee et al., "(¹H) MRS characterization of neurochemical profiles in orthotopic mouse models of human brain tumors," *NMR in Biomedicine*, vol. 28, no. 1, pp. 108–115, 2015.
- [99] T. Ozawa and C. D. James, "Establishing intracranial brain tumor xenografts with subsequent analysis of tumor growth and response to therapy using bioluminescence imaging," *Journal of visualized experiments : JoVE*, no. 41, 2010.
- [100] R. El Meskini, A. J. Iacovelli, A. Kulaga et al., "A preclinical orthotopic model for glioblastoma recapitulates key features of human tumors and demonstrates sensitivity to a combination of MEK and PI3K pathway inhibitors," *Disease Models & Mechanisms*, vol. 8, no. 1, pp. 45–56, 2015.
- [101] J. F. Deeken and W. Löscher, "The blood-brain barrier and cancer: transporters, treatment, and trojan horses," *Clinical Cancer Research*, vol. 13, no. 6, pp. 1663–1674, 2007.
- [102] L. Liu, S. S. Venkatraman, Y.-Y. Yang et al., "Polymeric micelles anchored with TAT for delivery of antibiotics across the blood-brain barrier," *Biopolymers - Peptide Science Section*, vol. 90, no. 5, pp. 617–623, 2008.
- [103] J. Li, Y. Guo, Y. Kuang, S. An, H. Ma, and C. Jiang, "Choline transporter-targeting and co-delivery system for glioma therapy," *Biomaterials*, vol. 34, no. 36, pp. 9142–9148, 2013.
- [104] R. Qiao, Q. Jia, S. Hüwel et al., "Receptor-mediated delivery of magnetic nanoparticles across the blood-brain barrier," *ACS Nano*, vol. 6, no. 4, pp. 3304–3310, 2012.
- [105] F. M. Kievit, O. Veiseh, C. Fang et al., "Chlorotoxin labeled magnetic nanovectors for targeted gene delivery to glioma," *ACS Nano*, vol. 4, no. 8, pp. 4587–4594, 2010.

- [106] E. Nance, K. Timbie, G. W. Miller et al., "Non-invasive delivery of stealth, brain-penetrating nanoparticles across the blood - Brain barrier using MRI-guided focused ultrasound," *Journal of Controlled Release*, vol. 189, pp. 123–132, 2014.
- [107] Y. Huang, D. Coman, F. Hyder, and M. M. Ali, "Dendrimer-Based Responsive MRI Contrast Agents (G1-G4) for Biosensor Imaging of Redundant Deviation in Shifts (BIRDS)," *Bioconjugate Chemistry*, vol. 26, no. 12, pp. 2315–2323, 2015.

Research Article

Key Parameters on the Microwave Assisted Synthesis of Magnetic Nanoparticles for MRI Contrast Agents

Maria Eugênia Fortes Brollo,¹ Sabino Veintemillas-Verdaguer,¹
Cesar Menor Salván,^{2,3} and Maria del Puerto Morales¹

¹*Institute of Material Science of Madrid, ICMM-CSIC, Sor Juana Inés de la Cruz 3, 28049 Madrid, Spain*

²*School of Chemistry and Biochemistry, Georgia Institute of Technology, 315 Ferst Drive NW, Atlanta, GA 30332, USA*

³*IMIDRA, Finca El Encín, Autovía del Noreste A-2, Km. 38.200, Alcalá de Henares, 28805 Madrid, Spain*

Correspondence should be addressed to Maria Eugênia Fortes Brollo; brollo@icmm.csic.es

Received 14 July 2017; Revised 20 October 2017; Accepted 5 November 2017; Published 4 December 2017

Academic Editor: Ralf Schirmacher

Copyright © 2017 Maria Eugênia Fortes Brollo et al. This is an open access article distributed under the Creative Commons Attribution License, which permits unrestricted use, distribution, and reproduction in any medium, provided the original work is properly cited.

Uniform iron oxide magnetic nanoparticles have been synthesized using a microwave assisted synthesis method in organic media and their colloidal, magnetic, and relaxometric properties have been analyzed after its transference to water and compared with those nanoparticles prepared by thermal decomposition in organic media. The novelty of this synthesis relies on the use of a solid iron oleate as precursor, which assures the reproducibility and scalability of the synthesis, and the microwave heating that resulted in being faster and more efficient than traditional heating methods, and therefore it has a great potential for nanoparticle industrial production. The effect of different experimental conditions such as the solvent, precursor, and surfactant concentration and reaction time as well as the transference to water is analyzed and optimized to obtain magnetic iron oxide nanoparticles with sizes between 8 and 15 nm and finally colloids suitable for their use as contrast agents on Magnetic Resonance Imaging (MRI). The r_2 relaxivity values normalized to the square of the saturation magnetization were shown to be constant and independent of the particle size, which means that the saturation magnetization is the main parameter controlling the efficiency of these magnetic nanoparticles as MRI T_2 -contrast agents.

1. Introduction

In the last decade a new synthesis approach of nanoparticles based on the use of microwave dielectric heating has gained a lot of attention because of its versatility in different application areas, such as polymer chemistry, biomedicine, material science, and nanotechnology [1]. This nonclassical heating has shown an impressive reduction in synthesis time, from hours to minutes, increased product yield, and improved material properties, when compared to the conventional heating (by convective heat transfer), improving its reproducibility [1–3]. This synthesis approach seems to be especially interesting for the synthesis of nanoparticles for biomedical applications such as magnetic iron oxide [4], particularly in relation to the transference of the technology to the clinic and the need for standardization to avoid batch to batch inhomogeneity [5].

The traditional heating, transferring energy from the reaction vessel to the reactant mixture by forced convection depends on viscosity and thermal conductivity of the fluid to be heated; temperature gradients are unavoidable in such a system. In contrast, microwave irradiation triggers heating of the overall system by two mechanisms: ionic conduction and dipolar polarization. The charged particles in the mixture contribute with the first one while the dipoles (like a polar solvent) contribute with the second one. The heating is produced by direct coupling of the energy from the microwave with the molecules in the mixture. Thus, the more polar a reaction mixture is, the greater its ability to couple with the microwave energy will be [6] so either the substrate or reagents have to be polar in order to allow sufficient heating by microwaves.

Up to now, microwave synthesis of iron oxide nanoparticles has been carried out mainly for the preparation of ultrasmall nanoparticles in water or alcohol resulting in

extremely interesting positive contrast agents for diagnosis [7–10] in Magnetic Resonance Imaging (MRI). On the contrary, uniform flower-like Fe_3O_4 clusters of a few μm were fabricated in ethylene glycol with FeCl_3 , sodium acetate and a surfactant, under microwave irradiation for 15 to 60 minutes [11]. An organic solvent like benzyl ether has also been used with microwave heating, but, in that case, addition of a small proportion of ionic liquid was required to obtain magnetite nanoparticles up to 10 nm [12]. The control of the nanoparticle size by this route deserves further investigation in order to use microwave heating for the preparation of nanoparticles not only as T_1 but also as T_2 MRI contrast agents.

With the aim to produce a T_2 MRI contrast agent, iron oxide nanoparticles were prepared in organic media using a microwave assisted synthesis method; then their colloidal and magnetic properties are explored before and after its transference to water and compared with those nanoparticles prepared by thermal decomposition in organic media. The effect of different experimental conditions such as the solvent, Fe concentration, oleic acid/Fe ratio, the heating ramp, and the reaction time is analyzed. For standardization purpose, a unique precursor that is a solid iron oleate, easy to prepare in large quantities, modified from Patent US number 20130089740 [13], easy to handle, and stable for long storage times was used for the first time and properly characterized in comparison to the liquid oleate, traditionally used in the thermal decomposition process [14]. Finally, the colloids are evaluated for MRI imaging measuring r_1 and r_2 relaxivities. The results were related to the particle and hydrodynamic size and magnetic moment per particle using the universal scaling law to predict the efficiency of magnetic nanoparticles as MRI T_2 -contrast agents recently reported [15].

2. Materials and Methods

2.1. Solid Oleate Synthesis. The sodium oleate was synthesized by adding sodium hydroxide (5.91 g) and oleic acid 90% (43.6 g) to 140 ml of hexane and heating the mixture up to 60°C in an oil bath, with magnetic stirring at 400 rpm. After one day at 60°C , a white precipitate of sodium oleate that is dissolved by adding 80 ml of ethanol at the same temperature appears. Then 10.8 g of FeCl_3 in 80 ml of distilled water is added and the solution boils violently at 57°C . The system is heated for 2 hours more, and then it is chilled with a cold water bath. The denser aqueous phase was eliminated by decantation using a separating funnel; the upper organic phase was filtered with filter paper prior to the precipitation of the solid iron oleate by the addition of an equal volume of methanol. The orange solid iron oleate was redissolved in hexane and reprecipitated with methanol three times. Finally it was dried over P_2O_5 , milled gently, and stored at room temperature in a desiccator over silica gel. For comparison, a liquid oleate was prepared following a methodology previously reported [14, 16, 17].

2.2. Microwave Synthesis. The synthesis of magnetic nanoparticles was carried out using a microwave oven Monowave 300®. This instrument has built-in magnetic stirrer, temperature control by internal fiber-optics probe surface temperature

by infrared sensor, and pressure measurement produced by Anton Paar GmbH, Austria, working on 2.45 GHz. Different parameters were explored in the synthesis of oleic acid coated iron oxide nanoparticles by microwave heating such as the nature of the solvents with different dielectric constant (octadecene, dibenzyl ether, benzyl alcohol, phenyl ether, and dimethyl sulfoxide (DMSO)), the Fe concentration, and the heating ramps ($2\text{--}4^\circ\text{C}/\text{min}$). The reaction mechanism was also explored fixing all the experimental conditions and varying the reaction time from 1/2 h up to 4 hours. Finally, two microwave samples were prepared under selected conditions as follows: a mixture containing 0.15 g of solid iron oleate, 0.76 g of oleic acid, and 8.32 ml of dibenzyl ether (MwE8) or benzyl alcohol (MwA8) was stirred at 600 rpm, while the temperature increases at $3.75^\circ\text{C}/\text{min}$ until 250°C and then was maintained at this temperature for 1 hour. For comparison, two samples were prepared by standard thermal decomposition [14, 18] under similar conditions of Fe concentration, oleic acid content, and temperature ramp. In brief, a mixture containing 0.9 g of solid iron oleate, 4.5 g of oleic acid, and 50 ml of dibenzyl ether (TdE12) or octadecene (TdO15) was added on a three-neck round-bottom flask mounted on a temperature-controlled N_2 reflux system, overhead stirred at 100 rpm until reach 100°C . The temperature was increased in a controlled way, with a heating ramp of $3.75^\circ\text{C}/\text{min}$ until reflux temperature, given by boiling point of the solvent, 290°C or 320°C , and this temperature was maintained for 1 hour.

2.3. Nanoparticle Coating. Nanoparticles were transferred to an aqueous medium by exchanging the oleic acid at the surface by dimercaptosuccinic acid (DMSA) [19]. For that purpose a solution of 20 ml of toluene containing 50 mg of carefully washed nanoparticles was added to a solution of 90 mg of DMSA in 5 ml of DMSO. The resulting suspension was then gently stirred by rotation for at least 2 days, until 2 phases appear. The resulting nanoparticles were washed with ethanol and centrifuged at 7500 rcf, at least 3 times. The final black solid was air dried and redispersed in distilled water. Diluted sodium hydroxide was added to increase the pH up to 10. The dispersion was then placed in a cellulose membrane tube molecular weight cut-off (MWCO) 10000 Da and dialyzed for 3 days in front of distilled water, to remove any excess of unreacted DMSA. Finally the pH of the dispersion was adjusted to 7 and the dispersion filtered through a polyethylene oxide filter with a pore size of $0.22\ \mu\text{m}$ in order to check its capability for being sterilized by this procedure.

2.4. Characterization. The core size and shape of nanoparticles were measured by transmission electron microscopy, where a drop of toluene, in the case of the oleate precursor, or water, in the case of the nanoparticles, was placed on a carbon coated copper grid, allowing all the solvent to evaporate at room temperature. The images were captured at a 100 keV JEOL-JEM 1010 microscope, equipped with a digital camera Gatan model Orius 200 SC, at the Universidad Autónoma de Madrid. Size and size distributions were obtained with the open source software ImageJ, using TEM images and

counting at least 300 nanoparticles [ISO13322-1]. A log-normal fit was performed to obtain mean sizes and deviation in number (TEM diameter in number $d = \sum x dN / \sum dN$), which can be transformed to a volume distribution in order to compare the values with XRD mean size (TEM diameter in volume = $\sum x^4 dN / \sum x^3 dN$, where x = particle size and N = number of particles) [20].

The iron oxide phase was determined by X-ray diffraction on a Powder Diffractometer Bruker D8 Advance with Cu K α radiation with energy-discriminator, in 2θ ranging from 10 to 90 degrees, with acquisition time of 5 seconds using 0.05-degree step. Crystal sizes were calculated by the width of the peak with the greatest intensity (311), using the Scherrer equation [21]. Fourier transform infrared spectroscopy (FTIR) spectra were recorded using a Bruker IFS 66VS to confirm the iron oxide phase, the presence, and nature of the coating and its surface bonding. IR spectra were recorded between 4000 and 250 cm^{-1} and the samples were prepared by diluting 2% wt iron oxide powder in KBr and pressing it into a pellet. Quantification of the coating was carried out by simultaneous thermogravimetric (TGA) and differential thermal analysis (DTA) of the samples on a Seiko Exstar 6300 instrument. Samples were heated from room temperature to 900°C at 10°C/min under an air flow of 100 ml/min.

Magnetic characterization was performed on dried powder samples after transference to water using a vibrating sample magnetometer (VSM; MLVSM9 MagLab 9 T, Oxford Instrument). Magnetization temperature dependence was recorded following a ZFC-FC standard protocol: ZFC curve, the sample is cooled down from 290 K to 5 K without any applied magnetic field and then, a small DC magnetic field is applied and the magnetization is recorded as temperature increases up to 290 K; FC curve, the sample is cooled down to 5 K under an applied magnetic field and the magnetization is recorded as temperature increases up to 290 K. To obtain the hysteresis loops, the samples were first demagnetized at fixed temperature and DC magnetization was measured in discrete constant fields during the field sweep. The initial susceptibility (χ) was measured in the field range ± 100 Oe and the saturation magnetization (M_s) was achieved by fitting the magnetization curves at room temperature to the Langevin function.

The hydrodynamic size of the nanoparticle aqueous suspensions at pH 7 was measured by dynamic light scattering (DLS) in a standard cuvette, using a Zetasizer NanoZS device (Malvern Instruments). A laser emitting red light is the energy source with an angle of 173° between the sample and detector. The hydrodynamic size of the particles was measured by photon correlation spectroscopy and expressed in terms of intensity, which reflects better the quality of the sample and number [22]. Zeta Potential was measured as a function of the pH, at room temperature, using KNO_3 0.01 M as the electrolyte and HNO_3 and KOH to adjust the pH.

Finally, MRI relaxometric properties were investigated by measuring the longitudinal (T_1) (sequence t1_ir_mb) and transversal (T_2) (sequence t2_ir_mb) protons relaxation times at different dilutions between 0 and 0.07 mM of Fe in a MINISPEC MQ60 (Bruker) at 37°C and a magnetic field of 1.5 T. The sequences used are original from Bruker.

3. Results and Discussion

The microwave assisted synthesis of magnetic nanoparticles in organic media was carried out starting from a solid oleate-Fe precursor, being one of the achievements of this work, the precursor itself. The advantages of having a solid precursor in comparison to a liquid oleate are numerous: first of all, its reproducibility, scalability, easy purification by precipitation, high stability over time, and finally its ease to weight in comparison to the standard liquid oleate, which is a highly viscous plastic fluid; secondly, the solid oleate presents distinctive characteristics in comparison to the liquid oleate such as a higher Fe content as determined by TG (33 wt% Fe in the solid oleate-Fe against 6 wt% in the liquid iron oleate, Figure 1(c)) and different iron-oleic acid coordination. This means that the reaction using the solid oleate-Fe requires the addition of a larger amount of extra oleic acid to preserve the oleic acid/Fe ratio of 3-4 that has been described as ideal for the synthesis of uniform magnetic nanoparticles by thermal decomposition [16, 23]. The use of a liquid oleate with a composition that changes with time makes the control of the amount of oleic acid in the reaction media difficult, which is critical to control the particle growth and consequently the particle size [23, 24]. Slight differences in composition and oxidation degree of the iron oleates have been further analyzed by gas chromatography coupled with mass spectrometry GC-MS and are included in the supporting information (Figures S1 and Table S1).

On the other hand, solid and liquid oleates have different Fe coordination to the carboxylic groups of the oleic acid as shown by IR spectroscopy (Figures 1(a) and 1(b)), being bidentate in the case of the solid oleate instead of monodentate. This is reflected in the distance between the carboxyl bands at 1600 and 1455 cm^{-1} [25], which is 145 cm^{-1} for the liquid oleate and for the solid oleate is 86 cm^{-1} . Solid iron oleate is in fact an iron hydroxide as demonstrated by X-ray diffraction (Figure 1(d)). This oleic coated hydroxide is expected to be less reactive than liquid oleate that present also X-ray diffraction pattern but with low crystallinity (Figure S2). Therefore, the temperature ramp becomes a key parameter to control the solid oleate precursor decomposition and consequently the particle nucleation. Moreover, the solid oleate consists of tiny anisometric nanoparticles (around 10 by 2 nm as shown by TEM Figure S3) that resemble those for Fe hydroxides such as goethite or lepidocrocite [26]. In contrast to that, liquid oleate having monodentate coordination and amorphous structure decomposes easily and is less sensible to the temperature ramp resulting in similar particle sizes for temperature ramps between 3 and 6°C/min [27].

3.1. Effect of Key Microwave Synthesis Parameters on Particle Size and Size Distribution. The effect of different key parameters such as solvent, heating ramp, and iron concentration on the microwave assisted synthesis of magnetic nanoparticles has been evaluated. For some selected conditions, the effect of the heating source has also been analyzed in comparison to the thermal heating.

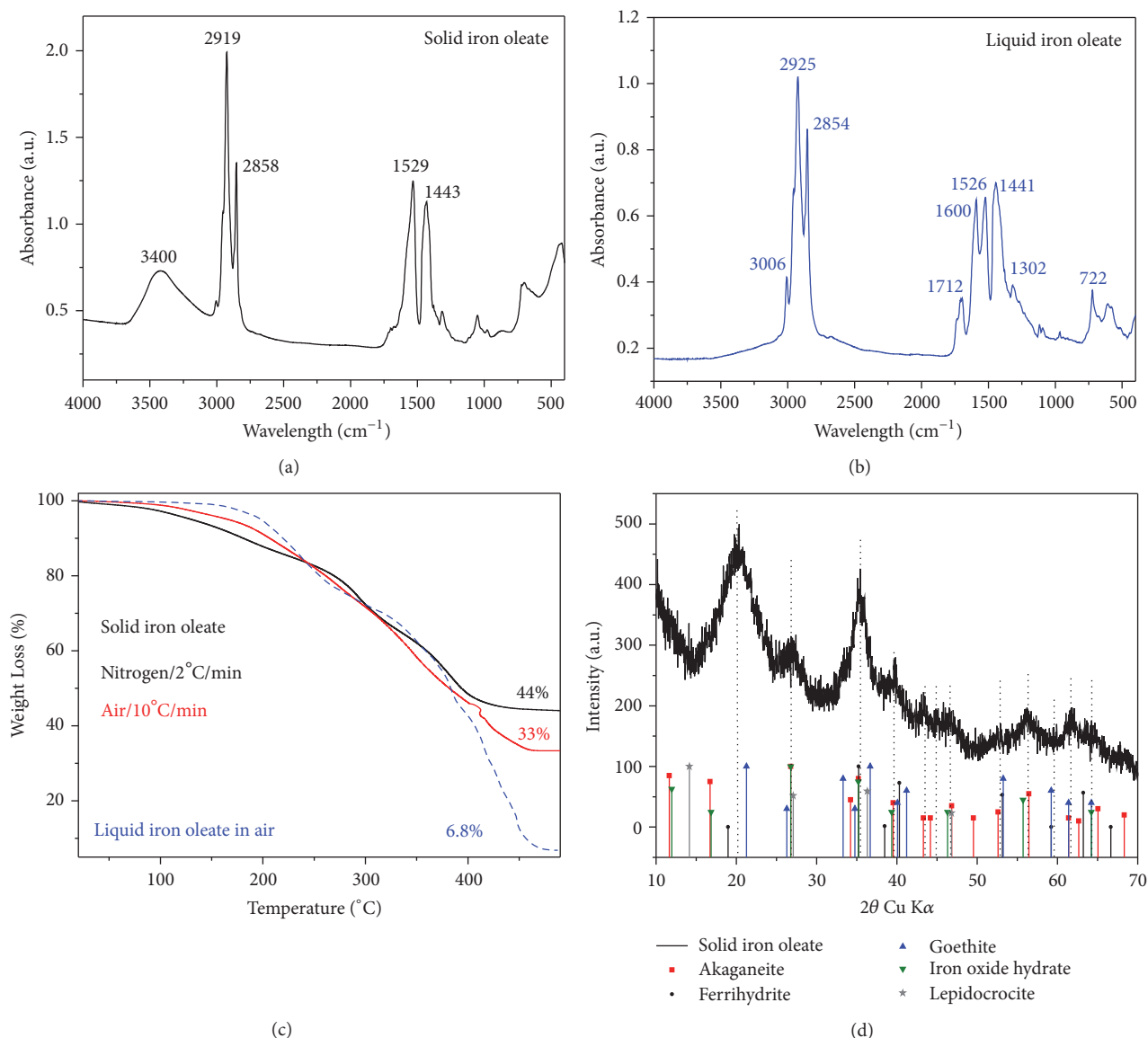


FIGURE 1: Infrared spectroscopy absorbance of solid (a) and liquid oleate (b) [14, 28]; (c) Thermogravimetric analysis of the Fe oleates (solid and liquid) under different conditions; (d) X-ray diffraction pattern for solid iron oleate.

3.1.1. Solvent. When considering solvents for the microwave reaction in a pressurized vessel, boiling points become less important than the efficiency of the reactant mixture to couple with an applied microwave field. Among the different solvents with dielectric constants between 1 (vacuum) and 88 (water), solvents with dielectric constants from above 2 (octadecene) to 47 (DMSO) were chosen. It was observed that too polar solvents with relatively high vapor pressure, like DMSO, generate a fast built up pressure in the system and the equipment shuts down, as a safety precaution. On the other side, solvents with low dielectric constant, such as octadecene, generate paramagnetic nanoparticles (Figure S4). Dibenzyl ether, with a dielectric constant of 3.86, was chosen as the best one in this case, given the magnetic properties of synthesized nanoparticles, and the price that is 10 times lower than benzyl alcohol, solvent utilized by the majorities of research groups using microwave heating [4, 7–9, 30].

3.1.2. Heating Ramps. Basically three heating ramps were tested as shown in Figures 2(b), 2(e), and 2(f), that is, $3.75^{\circ}\text{C}/\text{min}$, $7.5^{\circ}\text{C}/\text{min}$, and $1.8^{\circ}\text{C}/\text{min}$. The optimal ramp is $3.75^{\circ}\text{C}/\text{min}$ that gives rise to uniform nanoparticles of around 5 nm (Figures 2(a) and 2(b)). Faster heating ramps result in smaller nanoparticles, 3.3 nm (Figure 2(e)), while slower heating ramps result in larger particles with heterogeneous geometry, 6.5 nm, main diameter (Figure 2(f)). Prolonging the reaction time from 1 up to 4 hours it is possible to get larger uniform particles up to a limit of around 8 nm, which is given by the exhaustion of iron precursor (Figures 2(c) and 2(d)) [24].

3.1.3. Iron Concentration. Other important parameters to consider in iron oxide nanoparticle synthesis is the iron concentration. Different tests were carried out as presented in Figure S5 and summarized on Table 1. From Figure S5 (A) to (D), four samples with different iron concentration are

TABLE 1: Comparison of nanoparticle sizes when changing the iron concentration and the oleic acid/Fe molar ratio.

[Fe] mg/ml	[Fe] mg/ml	2	3	4	5
Molar ratio 5 (Oleic/Fe)	d (σ) nm	8.2 (± 2.2)	9.7 (± 2.7)	6.9 (± 1.5)	6.7 (± 1.7)
[Fe] = 4 mg/ml	Molar ratio (oleic/Fe)	2	3.5	5	6.5
	d (σ) nm	6.5 (± 1.3)	7.1 (± 2.2)	6.9 (± 1.5)	5.7 (± 1.2)

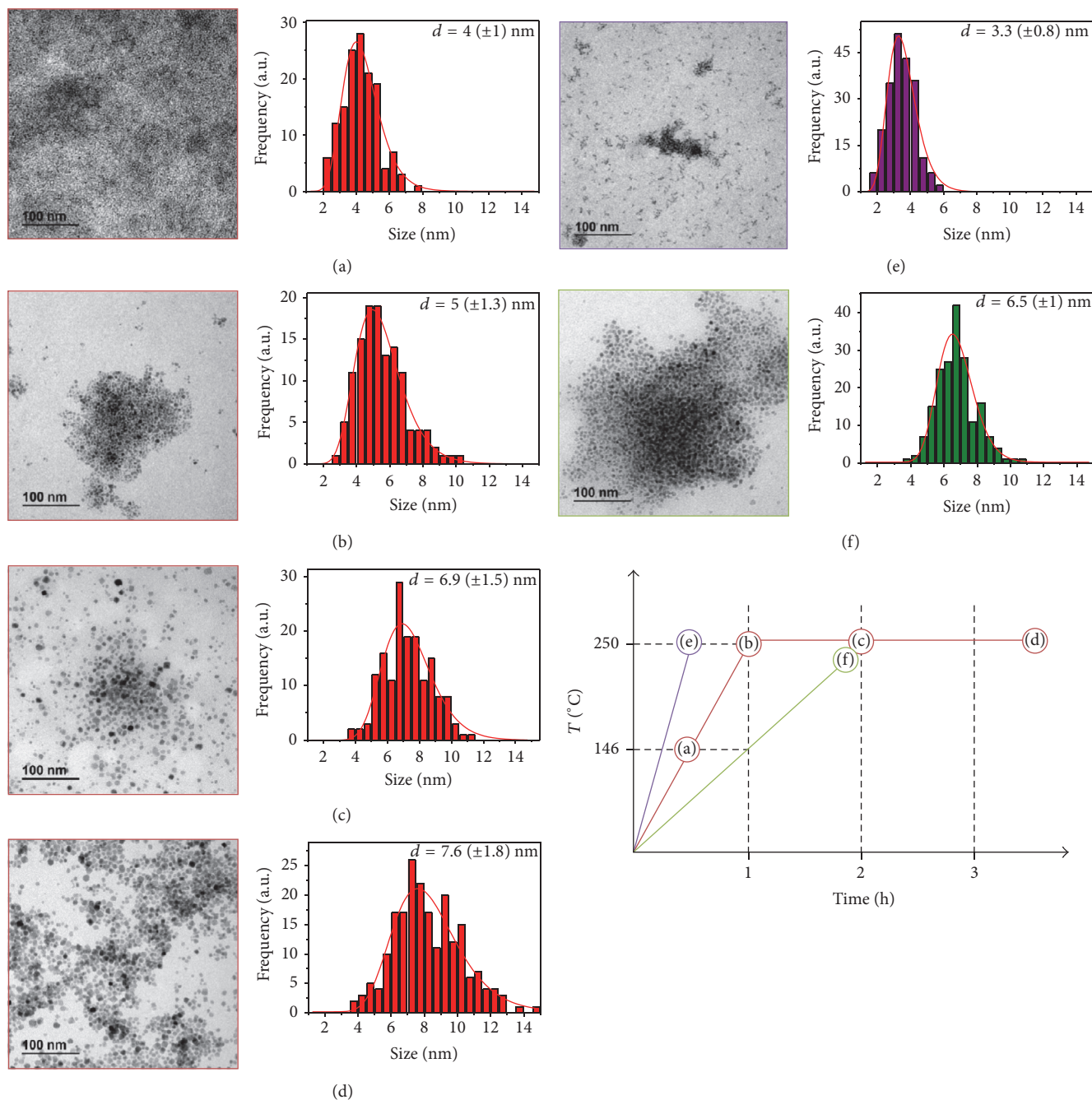


FIGURE 2: TEM images of the nanoparticles, with its respective size distribution, obtained with different heating ramps and total synthesis time, with a schematic figure of these ramps. (a) 146°C in 30 minutes, (b) 250°C in 1 hour, (c) 250°C in 1 hour and maintained for 1 hour, (d) 250°C in 1 hour and maintained for 2 hours and 30 minutes, (e) 250°C in 30 minutes, and (f) 250°C in 2 hours.

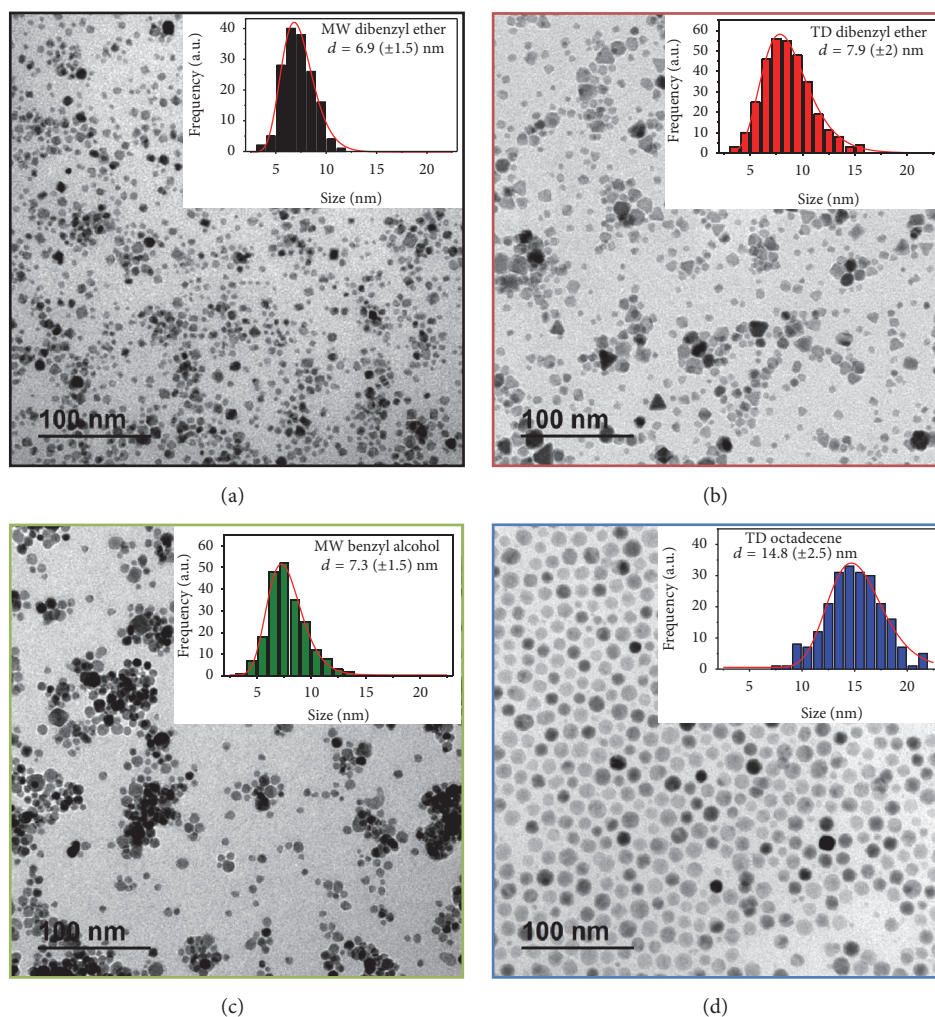


FIGURE 3: TEM images of magnetite nanoparticles obtained by microwave (MW) and thermal decomposition (TD), using different solvents (dibenzyl ether (a and b), octadecene (d), and benzyl alcohol (c)). Nanoparticles coated with DMSA. Descriptions of the samples are included in Table 2.

shown while the heating ramp and the oleic acid/Fe molar ratio were kept constant. It can be observed that the higher the iron concentration (from 2 to 5 mg Fe/ml), the smaller the particles and the size distribution, always below 25%. Similar results were found for thermal decomposition [31]. However, at 4 mg Fe/ml concentration, particle size is not affected by the addition of three times more oleic acid to the reaction mixture (Figure S5, from E to H) (slight reduction in size from 6.5 to 5.7 nm and narrower distribution, 20%) in contrast with the strong oleic acid effect when using other iron precursors such as iron acetylacetonate [32]. In that case, $\text{Fe}(\text{acac})_3$ decomposes forming an intermediate iron-oleate complex at 200°C and nucleation takes place at higher temperatures as the concentration of oleic acid increases leading to an important reduction in particle size.

3.1.4. Heating Source. Heating method is expected to play an important role on the final size and distribution of the nanoparticles. To analyze this the same reaction mixture was decomposed with microwave and thermal heating. The

parameters chosen as default are iron concentration of 4 mg Fe/ml, molar ratio (oleic/Fe) of 5, heating ramp of 3.75°C/min until 250°C, kept for 1 hour at this temperature, and solid iron oleate as iron precursor. Microwave samples were synthesized using dibenzyl ether (Figure 3(a)) and benzyl alcohol (Figure 3(c)) as solvents (MwE8 and MwA8), while the samples prepared by thermal decomposition were obtained using dibenzyl ether (Figure 3(b)) and octadecene (Figure 3(d)) as solvents (TdE12 and TdO15). Figure 3 shows their respective TEM images, with the same magnification for ease comparison. Insets show their size distribution fitted by Log-normal. Mean size and distribution are included in Table 2. For sample MwE8 the mean size is 6.9 nm ($\sigma = 0.21$), while MwA8 has a size of 7.3 nm ($\sigma = 0.21$). On the other side, TdE12 has a mean size of 7.9 nm ($\sigma = 0.26$) while TdO15 has a size of 14.8 nm ($\sigma = 0.17$).

First, it should be noted that the largest size is always obtained for the particles prepared in the solvent with the highest boiling point (dibenzyl ether = 160°C, benzyl alcohol = 205°C, and octadecene = 315°C) [14, 24, 33]. In

TABLE 2: Comparison of structural and magnetic properties^a for all samples described on the manuscript.

	MwE8	MwA8	TdE12	TdO15
Diameter TEM (nm) number	6.9 (0.21)	7.3 (0.21)	7.9 (0.26)	14.8 (0.17)
Diameter TEM (nm) volume	8.1	9	10.5	16.3
Diameter XRD (nm)	7.9	8.5	12.2	15.5
Diameter DLS (nm)	23 (0.2)	68 (0.5)	37 (0.3)	173 (0.3)
Diameter VSM (nm)	6.4 (0.33)	7.1 (0.4)	8.5 (0.29)	8.8 (0.27)
Volume XRD (10 ³ nm ³)	2.1	2.5	7.6	15.6
M_S at 5 K (Am ² /kgFe)	60	114	105	128
M_S at RT (Am ² /kgFe)	55	100	93	115
H_C at 5 K (10 ⁴ A/m)	2.4	2.2	2.8	3.2
H_C at RT (10 ⁴ A/m)	0.47	0.21	0.18	0.63
Zeta potential (mV) at pH 7	-34.4	-27.6	-28.3	-32.2
r_2/r_1	8	28.1	6.8	72
r_2 (mM ⁻¹ s ⁻¹)	85.2	222	143	165.6
r_1 (mM ⁻¹ s ⁻¹)	10.6	7.9	20.9	2.3

^aDiameter DLS is $Z_{average}$ and the number between brackets is the polydispersity index; M_S = saturation magnetization; H_C = coercive field; r_2 = MRI transversal relaxivity; r_1 = MRI longitudinal relaxivity.

addition, nanoparticles synthesized by heat transfer tend to be larger than the ones produced by microwave heating. This difference in sizes between both synthesis methods can be explained by their different nucleation and growth processes, as seen in Figure 4. Using conventional heating, nanocrystals tend to nucleate on the vessel walls first, given its inhomogeneous heating profile [34]. When a sample is irradiated with microwave frequencies, the dipoles tend to align in the direction of the applied electric field; in such a way energy is lost in the form of heat, through dielectric loss and molecular friction [6]. Given that, microwave produces efficient internal heating, creating numerous “hot spots,” which could trigger multiple nucleation events throughout the solution, increasing the product yield [1, 35] but decreasing the average size due to the enhanced competitive growth.

3.2. *Effect of the Heating Source on the Structural, Colloidal, and Magnetic Properties of the Nanoparticles.* Structural characterization of the nanoparticles prepared in this work was carried out by X-ray diffraction. Figure 5(a) shows the X-ray patterns for nanoparticles obtained by microwave (MW) and thermal decomposition (TD) using different solvents. All peaks correspond to crystallographic magnetite or maghemite planes discarding the presence of secondary phases. Crystal sizes calculated from the broadening of 311 peak vary from 7.9 nm to 8.5 nm for MW samples and from 12.2 nm to 15.5 nm for TD samples. The values differ only slightly from the size distribution obtained by TEM images indicating the single-core character of the particles.

Nanoparticles were transferred to an aqueous medium by exchanging the oleic acid of the surface by dimercaptosuccinic acid (DMSA) [36]. DMSA coating on nanoparticles is responsible for the high negative charge (between -27 and -34 mV) in a wide pH range, between pH 2 and 11 (Figure 5(b)). Hydrodynamic sizes in intensity are between 30 and 170 nm (Figure S6), increasing as the amount of coating on the nanoparticle surface increases, as it can be seen

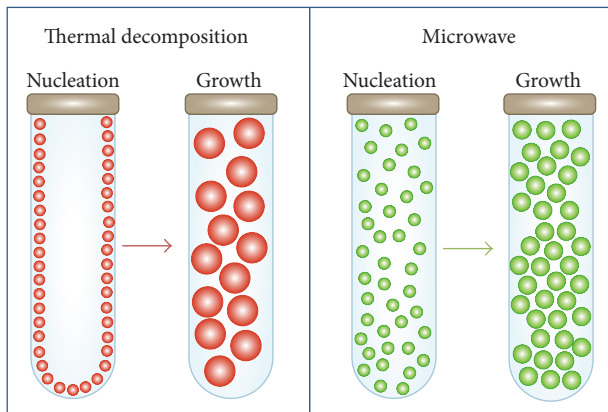


FIGURE 4: Comparison between thermal decomposition and microwave heating showing the effect on nanoparticles sizes. Nanocrystals tend to nucleate on the vessel wall first for thermal decomposition; on the contrary for microwave nanocrystals tend to form rapidly, creating more seeds that grow less.

from the thermogravimetric analysis (Figure S7 and S8). For example, sample TdO15, which has the larger hydrodynamic size, has a larger amount of DMSA on the nanoparticle surface, but the presence of aggregates cannot be completely discarded. Hydrodynamic sizes in number are adjusted to a monomodal distribution with mean values around 6–9 nm for the smallest particles and 58 nm for the largest ones, that is, TDO15 (Figure 5(c)). This means that most of the particles are well dispersed forming a stable colloid and only a small fraction are aggregated leading to a broadening of the peak in the DLS intensity distribution or a bimodal distribution, as it is the case of sample MwA8 (Figure S6). No significant differences were found for particles prepared by MW or by TD in relation to the colloidal properties. Hydrodynamic sizes are important depending on the application since it may limit its use. For example, for hydrodynamic sizes

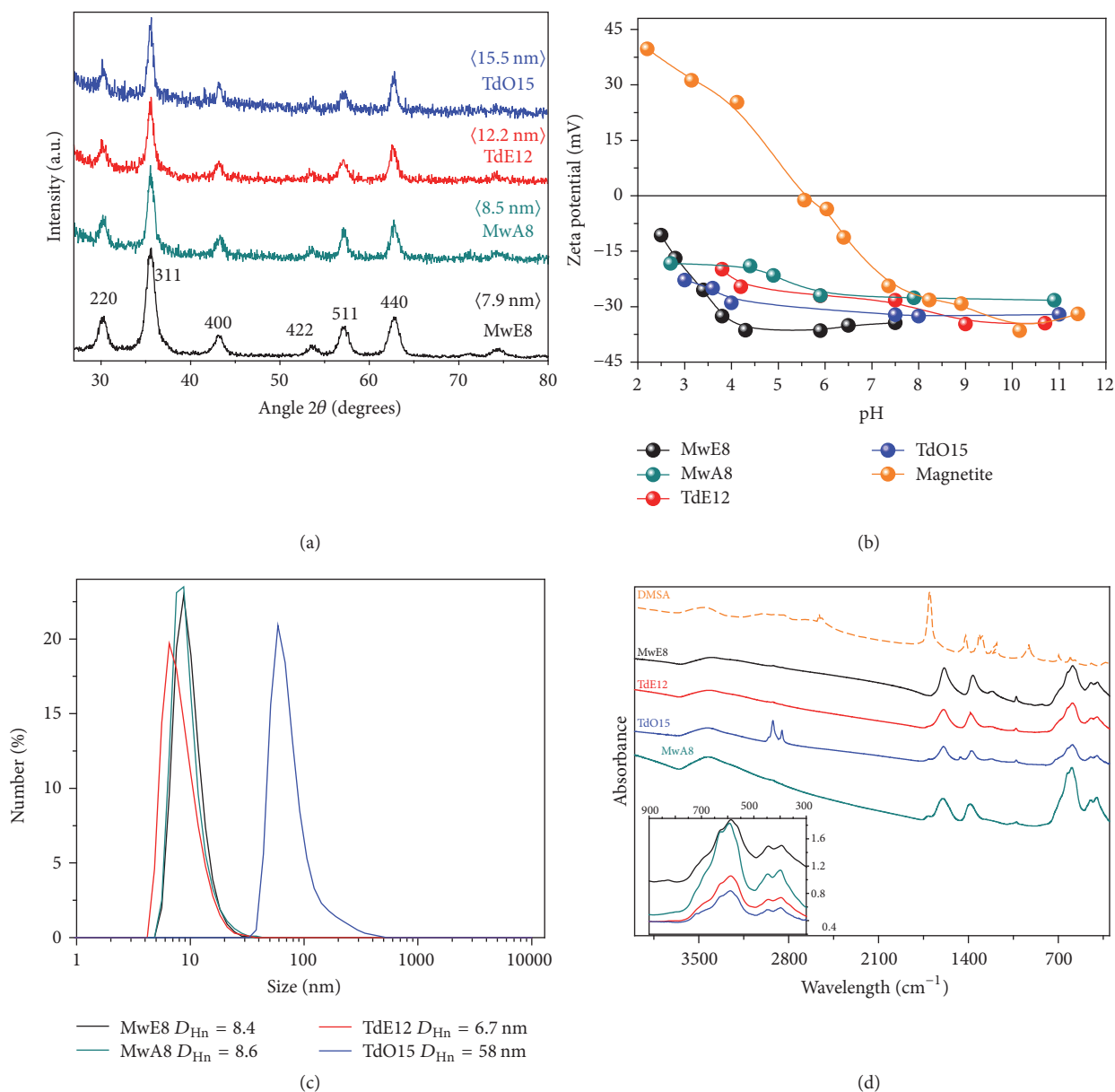


FIGURE 5: (a) X-ray diffraction patterns with calculated mean size of crystal for magnetite nanoparticles obtained by microwave (MW) and thermal decomposition (TD) using different solvents; (b) zeta potential measurements as a function of pH for DMSA coated nanoparticles and uncoated magnetite for comparison; (c) hydrodynamic size in number distribution; (d) infrared spectra for DMSA coated nanoparticles and DMSA for comparison. Inset shows the IR low frequency range.

larger than 200 nm, particles are rapidly captured by the Reticuloendothelial System (RES) or cell uptake is interfered [36].

Infrared spectra of these nanoparticles show the typical bands for water above 3100 cm^{-1} , at 3000 cm^{-1} for C-H vibration, between 1000 and 1700 cm^{-1} for the coating signature and bands below 1000 cm^{-1} associated with the vibration modes of the iron oxide, Fe-O stretching [37] (Figure 5(d)). Infrared spectra of the nanoparticles coated with oleic acid are presented on Figure S9.

Magnetic properties were analyzed for DMSA coated nanoparticles at room temperature and 5 K (Figure 6). The

saturation magnetization values and nanoparticle magnetic size were achieved by fitting the magnetization curves at room temperature to the Langevin function taking into account the particle size log normal distribution (Table 2). The hysteresis loops show that the larger the particle, the larger their saturation magnetization due to the decrease in surface area/volume ratio, and therefore the lower the surface effects such as spin canting [16, 38]. The higher saturation magnetization values for TdO15 are close to those reported for bulk magnetite (115 – 130 emu/gFe at RT and 5 K) [21]. The smallest values (55 – 60 emu/gFe) correspond to MwE8 sample with the smallest crystal size (Figure 5(a)). However,

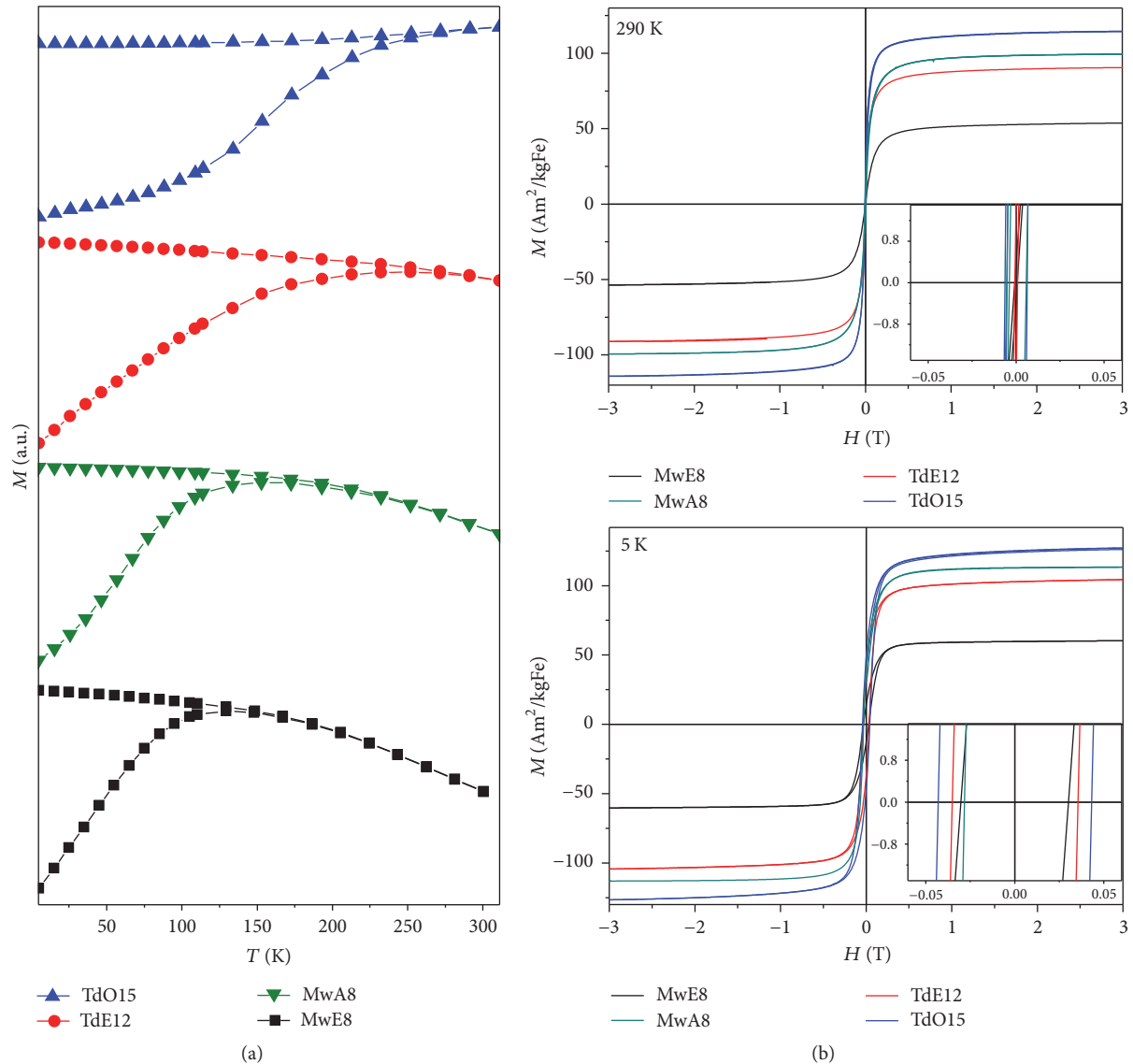


FIGURE 6: Hysteresis loops at room temperature and 5 K (b) and zero field cooled (ZFC)/field cooled (FC) magnetization curves measured at 100 Oe (a) for DMSA coated magnetite nanoparticles obtained by microwave (MW) and thermal decomposition (TD) using different solvents. The loops were fitted by Langevin function.

sample MwA8 with smaller crystal size than TdE12 has higher saturation magnetization suggesting less spin canting due to internal or surface disorder for the sample prepared by the microwave assisted route. At room temperature these nanoparticles are close to the superparamagnetic regime, showing rather low coercive fields, while at 5 K the systems are magnetically blocked, showing higher coercivity for larger particles [38, 39]. The initial susceptibility values increase as the particle size increases, given that the number of magnetic moments that align with the field grows. Magnetic particle sizes calculated from the Langevin function vary from 6.4 nm ($\sigma = 0.33$) for MwE8 up to 8.8 nm for TdO15 ($\sigma = 0.27$) (Table 2). The differences between TEM and magnetic size for TD samples suggest a strong influence of magnetic interactions on the M/H curves for these samples with larger particle sizes.

Figure 6 shows the ZFC-FC curve for all samples; they are measured from 20 K to room temperature. Where the blocking at low temperature is evident for smaller nanoparticles (MW), bigger particles are still blocked at room temperature (TD) [16].

Measurements of the MRI relaxation times (T_1 and T_2) were made at different iron concentrations from 0 to 0.07 mM Fe to obtain the relaxivity value (r_1 and r_2), as seen in Figure 7. The maximum r_1 value ($20.9 \text{ mM}^{-1} \text{ s}^{-1}$) was found for a TD sample, while the maximum r_2 value ($222 \text{ mM}^{-1} \text{ s}^{-1}$) was found for a MW sample. Samples obtained by thermal decomposition with the largest particle size (TdO15) present extremely low r_1 , and consequently much higher r_2/r_1 ratio probably as a consequence of the larger hydrodynamic size (Figure 5(c)). On the other hand, samples synthesized by microwave assisted route have similar r_1 values but sample

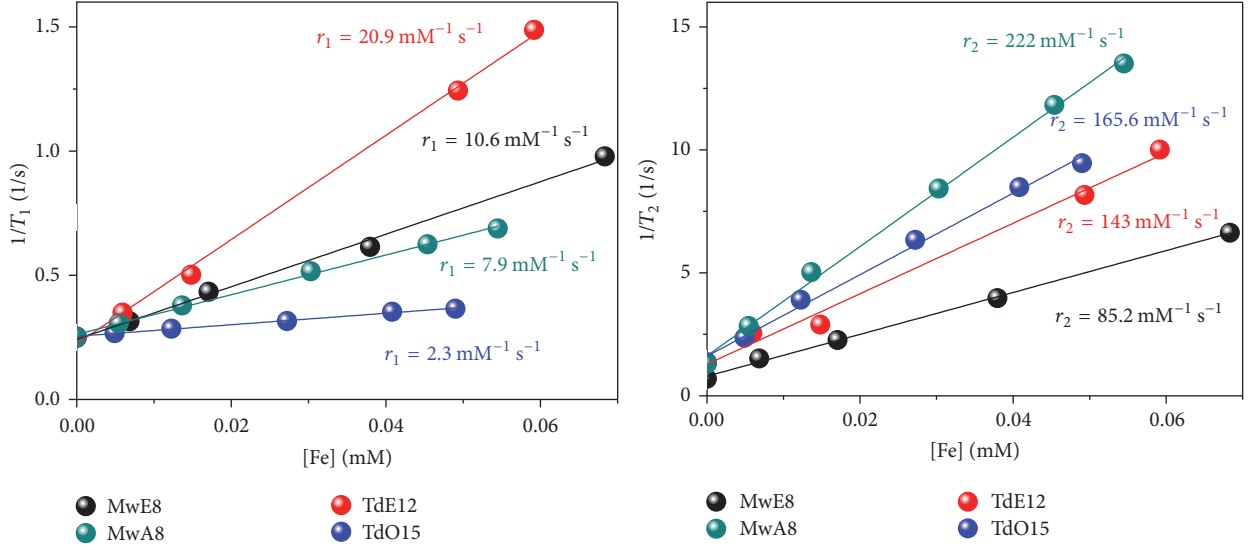


FIGURE 7: MRI T_1 and T_2 relaxation times as a function of the Fe concentration for DMSA coated magnetite nanoparticle suspensions obtained by microwave (MW) and thermal decomposition (TD) using different solvents.

MwA8 presents more than double r_2 value, indicating higher efficiency as negative contrast agent. In the literature, the maximum experimental value reported for r_2 is around $500 \text{ mM}^{-1} \text{ s}^{-1}$ for iron oxide nanoparticles, while the theoretical maximum value is $750 \text{ mM}^{-1} \text{ s}^{-1}$, not yet reached [15]. Commercial formulations using magnetic nanoparticles used for pathology diagnosis in the liver and spleen, as Feridex[®], produced by Berlex Laboratories and Resovist, produced by Bayer Healthcare have r_1 and r_2 values between 24 and $150 \text{ mM}^{-1} \text{ s}^{-1}$ and r_2/r_1 of around 4–6 [40]. Looking at the relation between r_2 and r_1 for our samples it can be seen that samples MwA8 and TdO15 have high possibility to become T_2 contrast agents, with a quotient of 28.1 and 72, respectively.

The relaxivity at high magnetic fields for the particles synthesized in this work is expected to follow the motional average regime (MAR) that describes the interaction of the nanoparticles with water protons taking into account the nanoparticle size (TEM) and the magnetic field distribution around it [41]. Therefore, the relaxivity r_2 is given by

$$r_2 = \frac{4\gamma^2\mu_0^2\nu_{\text{mat}}M_v^2d^2}{405D}, \quad (1)$$

where $\gamma = 2.67513 \times 10^8 \text{ rad}\cdot\text{s}^{-1}\cdot\text{T}^{-1}$ is the gyromagnetic factor of the proton, $\mu_0 = 4\pi 10^{-7} \text{ T}\cdot\text{m}\cdot\text{A}^{-1}$ is the magnetic permeability of vacuum, D is the water translational diffusion constant, d is the particle diameter, ν_{mat} is the molar volume of the material ($1.5 \times 10^{-5} \text{ m}^3/\text{mol}$ for magnetite), and M_v is the saturation magnetization expressed in SI units, $\text{A}\cdot\text{m}^{-1}$ [15, 41].

Figure 8 shows theoretical (straight line) and experimental (symbols) r_2 values for magnetic nanoparticles of different sizes (iron oxide core measured by TEM) normalized by the square of the saturation magnetization [15]. Experimental values obtained in this work together with other reported data for particles of similar core size prepared by microwave

synthesis (Figure 8 star [4]), thermal decomposition (Figure 8 purple square [29]), Massart's procedure [42] (Figure 8 orange triangles [15]), or the commercial one Resovist (Figure 8, purple circle) are included. Deviation from the theoretical curve may be due to differences in intra-aggregate volume fraction, that is, the number of cores per aggregate. In the case of the nanoparticles obtained in this work $\psi_{\text{intra}} = 1$ was used given the single-core character supported by TEM and DLS measurements. It should be noted that r_2/M_v^2 is almost constant with particle size for all samples studied in this work. Saturation magnetization seems to be the main parameter controlling the efficiency of these nanoparticles as MRI T_2 -contrast agents independently of the particle size.

4. Conclusions

The microwave assisted synthesis has been explored for the preparation of magnetic iron oxide nanoparticles showing the critical effect of different experimental parameters such as the solvent, the precursor, and the surfactant on the nucleation and growth processes that determine particle size and uniformity. Dibenzyl ether was chosen as the best solvent for this synthesis given its dielectric constant, the optimal ramp was set at $3.75^\circ\text{C}/\text{min}$, the iron concentration was $4 \text{ mgFe}/\text{ml}$, and (oleic/Fe) molar ratio was 5 giving rise to the most uniform nanoparticles. In comparison to conventional heating where nanocrystals tend to nucleate on the vessel walls first given its inhomogeneous heating profile, microwave produces efficient internal heating promoting nucleation everywhere and reducing the growth possibilities of the numerous nuclei generated.

Magnetic iron oxide nanoparticles with sizes between 8 and 15 nm synthesized by microwave and thermal decomposition in organic media present nearly superparamagnetic behavior at RT and relaxivity values that make them good candidates for MRI negative contrast agents. Given the low

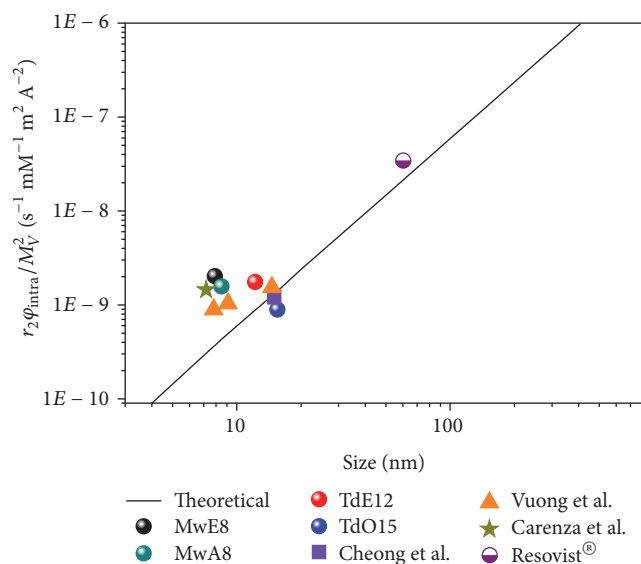


FIGURE 8: Influence of the core size calculated by TEM on r_2 relaxivity normalized by the square of the saturation magnetization. Colorful dots correspond to the nanoparticles studied on this work and compared to others works (orange triangles [15], purple square [29], and star [4]) and compared to commercial one Resovist® (purple circle); the solid line corresponds to the theoretical values for the motional averaging regime (MAR). For the calculations $\psi_{\text{intra}} = 1$ was used for all samples but the Resovist, which used $\psi_{\text{intra}} = 8.4E - 2$.

hydrodynamic size of these suspensions, saturation magnetization seems to be the main parameter controlling the efficiency of these magnetic nanoparticles as MRI T_2 -contrast agents.

Conflicts of Interest

The authors declare no competing financial interest.

Authors' Contributions

All authors have given approval to the final version of the manuscript and have contributed equally.

Acknowledgments

This work was supported by the Spanish Ministry of Economy and Competitiveness (MAGO project MAT2014-52069R) and by the Brazilian agency CNPq grant [232947/2014-7]. X-ray diffraction, FTIR spectroscopy, and thermogravimetric and chemical analysis were carried out in the support laboratories of Instituto de Ciencia de Materiales de Madrid (CSIC). MRI relaxivity data were carried out at the CNIC, Madrid. The authors would like to acknowledge Lucia Gutierrez for the ZFC/FC curves using the SQUID at the Servicio General de Apoyo a la Investigación-SAI, Universidad de Zaragoza, and the TEM facilities at the SIDI of the Madrid Autonomous University. Finally, M. E. F. Brollo acknowledges the Brazilian

agency CNPq for her grant within the Science Without Borders Program.

Supplementary Materials

Figure S1. GC-MS trace (total ion chromatogram) of the methylated fatty acid composition of the solid iron oleate (A) and liquid iron oleate (B). Table S1. Fatty acid composition of synthesized iron oleates. Figure S2. X-ray diffraction pattern for liquid iron oleate. Figure S3. TEM image of solid iron oleate, where a hydrophobized hydroxide nano-material can be seen. Figure S4. Hysteresis loops at room temperature for nanoparticles obtained by microwave using different solvents. Solvents with low dielectric constant such as octadecene and phenyl ether generate paramagnetic nanoparticles while solvents with higher dielectric constant generate nanoparticles with high saturation magnetization values. Figure S5. TEM images and size distribution of the nanoparticles obtained when changing the iron concentration from 2 to 5 mg Fe/ml (35.8 mM to 89.5 mM), shown on images A to D. On the other hand, changing the molar ratio oleic acid/Fe (MR) from 2 to 6.5, images E to H. Red lines represent a Log-normal fit. Figure S6. Hydrodynamic size in intensity distribution is between 30 and 170 nm for all samples. Figure S7. Thermogravimetric analysis showing the amount of DMSA coating on nanoparticles obtained by microwave (MW) and thermal decomposition (TD), using different solvents. DMSA weight loss is included for comparison. Figure S8. Thermogravimetric analysis showing the amount of oleic acid coating on nanoparticles obtained by microwave (MW) and thermal decomposition (TD) using different solvents. Figure S9. Infrared spectra for oleic acid coated nanoparticles obtained by microwave (MW) and thermal decomposition (TD) using different solvents. The inset shows the IR low frequency range. (*Supplementary Materials*)

References

- [1] M. Baghbanzadeh, L. Carbone, P. D. Cozzoli, and C. O. Kappe, "Microwave-assisted synthesis of colloidal inorganic nanocrystals," *Angewandte Chemie International Edition*, vol. 50, no. 48, pp. 11312–11359, 2011.
- [2] R. J. Giguere, T. L. Bray, S. M. Duncan, and G. Majetich, "Application of commercial microwave ovens to organic synthesis," *Tetrahedron Letters*, vol. 27, no. 41, pp. 4945–4948, 1986.
- [3] R. Gedye, F. Smith, K. Westaway et al., "The use of microwave ovens for rapid organic synthesis," *Tetrahedron Letters*, vol. 27, no. 3, pp. 279–282, 1986.
- [4] E. Carena, V. Barceló, A. Morancho, J. Montaner, A. Rosell, and A. Roig, "Rapid synthesis of water-dispersible superparamagnetic iron oxide nanoparticles by a microwave-assisted route for safe labeling of endothelial progenitor cells," *Acta Biomaterialia*, vol. 10, no. 8, pp. 3775–3785, 2014.
- [5] P. Mulvaney, W. J. Parak, F. Caruso, and P. S. Weiss, "Standardizing nanomaterials," *ACS Nano*, vol. 10, no. 11, pp. 9763–9764, 2016.
- [6] K. K. Rana and S. Rana, "Microwave reactors: a brief review on its fundamental aspects and applications," *Open Access Library Journal*, vol. 1, article e686, pp. 1–20, 2014.

- [7] J. Pellico, A. V. Lechuga-Vieco, M. Benito et al., "Microwave-driven synthesis of bisphosphonate nanoparticles allows in vivo visualisation of atherosclerotic plaque," *RSC Advances*, vol. 5, no. 3, pp. 1661–1665, 2015.
- [8] L. Gonzalez-Moragas, S.-M. Yu, N. Murillo-Cremaes, A. Laro-main, and A. Roig, "Scale-up synthesis of iron oxide nanoparticles by microwave-assisted thermal decomposition," *Chemical Engineering Journal*, vol. 281, pp. 87–95, 2015.
- [9] I. Bilecka, I. Djerdj, and M. Niederberger, "One-minute synthesis of crystalline binary and ternary metal oxide nanoparticles," *Chemical Communications*, no. 7, pp. 886–888, 2008.
- [10] J. Pellico, J. Ruiz-Cabello, M. Saiz-Alía et al., "Fast synthesis and bioconjugation of ^{68}Ga core-doped extremely small iron oxide nanoparticles for PET/MR imaging," *Contrast Media & Molecular Imaging*, vol. 11, no. 3, pp. 203–210, 2016.
- [11] Z. Ai, K. Deng, Q. Wan, L. Zhang, and S. Lee, "Facile microwave-assisted synthesis and magnetic and gas sensing properties of Fe_3O_4 nanoroses," *The Journal of Physical Chemistry C*, vol. 114, no. 14, pp. 6237–6242, 2010.
- [12] H. Hu, H. Yang, P. Huang et al., "Unique role of ionic liquid in microwave-assisted synthesis of monodisperse magnetite nanoparticles," *Chemical Communications*, vol. 46, no. 22, pp. 3866–3868, 2010.
- [13] D. Burdinski and C. Bohlender, *Synthesis and use of iron oleate*, Patent US, 2013.
- [14] J. Park, K. An, Y. Hwang et al., "Ultra-large-scale syntheses of monodisperse nanocrystals," *Nature Materials*, vol. 3, no. 12, pp. 891–895, 2004.
- [15] Q. L. Vuong, J.-F. Berret, J. Fresnais, Y. Gossuin, and O. Sandre, "A universal scaling law to predict the efficiency of magnetic nanoparticles as MRI T2-contrast agents," *Advanced Healthcare Materials*, vol. 1, no. 4, pp. 502–512, 2012.
- [16] A. G. Roca, M. P. Morales, K. O'Grady, and C. J. Serna, "Structural and magnetic properties of uniform magnetite nanoparticles prepared by high temperature decomposition of organic precursors," *Nanotechnology*, vol. 17, no. 11, pp. 2783–2788, 2006.
- [17] G. Salas, C. Casado, F. J. Teran, R. Miranda, C. J. Serna, and M. P. Morales, "Controlled synthesis of uniform magnetite nanocrystals with high-quality properties for biomedical applications," *Journal of Materials Chemistry*, vol. 22, no. 39, pp. 21065–21075, 2012.
- [18] S. Sun and H. Zeng, "Size-controlled synthesis of magnetite nanoparticles," *Journal of the American Chemical Society*, vol. 124, no. 28, pp. 8204–8205, 2002.
- [19] A. G. Roca, S. Veintemillas-Verdaguer, M. Port, C. Robic, C. J. Serna, and M. P. Morales, "Effect of nanoparticle and aggregate size on the relaxometric properties of MR contrast agents based on high quality magnetite nanoparticles," *The Journal of Physical Chemistry B*, vol. 113, no. 19, pp. 7033–7039, 2009.
- [20] T. Allen, *Particle Size Measurement*, vol. 151 of *Powder Technology*, Springer, Dordrecht, Netherlands, 4th edition, 1990.
- [21] B. D. Cullity and S. R. Stock, *Elements of X-Ray Diffraction*, Pearson, 3rd edition, 2001.
- [22] R. Finsy, N. de Jaeger, R. Sneyers, and E. Geladé, "Particle sizing by photon correlation spectroscopy. Part III: mono and bimodal distributions and data analysis," *Particle & Particle Systems Characterization*, vol. 9, no. 1–4, pp. 125–137, 1992.
- [23] L. M. Bronstein, X. Huang, J. Retrum et al., "Influence of iron oleate complex structure on iron oxide nanoparticle formation," *Chemistry of Materials*, vol. 19, no. 15, pp. 3624–3632, 2007.
- [24] W. Baaziz, B. P. Pichon, S. Fleutot et al., "Magnetic iron oxide nanoparticles: reproducible tuning of the size and nanosized-dependent composition, defects, and spin canting," *The Journal of Physical Chemistry C*, vol. 118, no. 7, pp. 3795–3810, 2014.
- [25] V. Robert and G. Lemerrier, "A combined experimental and theoretical study of carboxylate coordination modes: a structural probe," *Journal of the American Chemical Society*, vol. 128, no. 4, pp. 1183–1187, 2006.
- [26] R. M. Cornell and U. Schwertmann, *The Iron Oxides: Structure, Properties, Reactions, Occurrences and Uses*, John Wiley & Sons, 2003.
- [27] W. W. Yu, J. C. Falkner, C. T. Yavuz, and V. L. Colvin, "Synthesis of monodisperse iron oxide nanocrystals by thermal decomposition of iron carboxylate salts," *Chemical Communications*, vol. 10, no. 20, pp. 2306–2307, 2004.
- [28] A. K. Peacock, S. I. Cauët, A. Taylor et al., "Poly[2-(methacryloyloxy)ethylphosphorylcholine]-coated iron oxide nanoparticles: synthesis, colloidal stability and evaluation for stem cell labelling," *Chemical Communications*, vol. 48, no. 75, pp. 9373–9375, 2012.
- [29] S. Cheong, P. Ferguson, K. W. Feindel et al., "Simple synthesis and functionalization of iron nanoparticles for magnetic resonance imaging," *Angewandte Chemie International Edition*, vol. 50, no. 18, pp. 4206–4209, 2011.
- [30] O. Pascu, E. Carenza, M. Gich et al., "Surface reactivity of iron oxide nanoparticles by microwave-assisted synthesis; comparison with the thermal decomposition route," *The Journal of Physical Chemistry C*, vol. 116, no. 28, pp. 15108–15116, 2012.
- [31] N. R. Jana, Y. Chen, and X. Peng, "Size- and shape-controlled magnetic (Cr, Mn, Fe, Co, Ni) oxide nanocrystals via a simple and general approach," *Chemistry of Materials*, vol. 16, no. 20, pp. 3931–3935, 2004.
- [32] C. Moya, X. Batlle, and A. Labarta, "The effect of oleic acid on the synthesis of $\text{Fe}_{3-x}\text{O}_4$ nanoparticles over a wide size range," *Physical Chemistry Chemical Physics*, vol. 17, no. 41, pp. 27373–27379, 2015.
- [33] S. Sun, H. Zeng, D. B. Robinson et al., "Monodisperse MF_2O_4 (M = Fe, Co, Mn) nanoparticles," *Journal of the American Chemical Society*, vol. 126, no. 1, pp. 273–279, 2004.
- [34] Y. Yin and A. P. Alivisatos, "Colloidal nanocrystal synthesis and the organic-inorganic interface," *Nature*, vol. 437, no. 7059, pp. 664–670, 2005.
- [35] D. Obermayer and C. O. Kappe, "On the importance of simultaneous infrared/fiber-optic temperature monitoring in the microwave-assisted synthesis of ionic liquids," *Organic & Biomolecular Chemistry*, vol. 8, no. 1, pp. 114–121, 2010.
- [36] A. Ruiz, P. C. Morais, R. Bentes de Azevedo, Z. G. M. Lacava, A. Villanueva, and M. del Puerto Morales, "Magnetic nanoparticles coated with dimercaptosuccinic acid: development, characterization, and application in biomedicine," *Journal of Nanoparticle Research*, vol. 16, no. 11, 2014.
- [37] B. Gillot, F. Jemmali, and A. Rousset, "Infrared studies on the behavior in oxygen of cobalt-substituted magnetites: comparison with zinc-substituted magnetites," *Journal of Solid State Chemistry*, vol. 50, no. 2, pp. 138–145, 1983.
- [38] M. Blanco-Mantecon and K. Ógrady, "Interaction and size effects in magnetic nanoparticles," *Journal of Magnetism and Magnetic Materials*, vol. 296, no. 2, pp. 124–133, 2006.
- [39] C. Blanco-Andujar, D. Ortega, P. Southern, Q. A. Pankhurst, and N. T. K. Thanh, "High performance multi-core iron oxide nanoparticles for magnetic hyperthermia: microwave synthesis,

- and the role of core-to-core interactions,” *Nanoscale*, vol. 7, no. 5, pp. 1768–1775, 2015.
- [40] Y.-X. J. Wang, “Superparamagnetic iron oxide based MRI contrast agents: Current status of clinical application,” *Quantitative Imaging in Medicine and Surgery*, vol. 1, no. 1, pp. 35–40, 2011.
- [41] A. Merbach, L. Helm, and É. Tóth, *The Chemistry of Contrast Agents in Medical Magnetic Resonance Imaging*, Wiley Online Library, 2nd edition, 2013.
- [42] A. Bee, R. Massart, and S. Neveu, “Synthesis of very fine maghemite particles,” *Journal of Magnetism and Magnetic Materials*, vol. 149, no. 1-2, pp. 6–9, 1995.

Research Article

Mapping Extracellular pH of Gliomas in Presence of Superparamagnetic Nanoparticles: Towards Imaging the Distribution of Drug-Containing Nanoparticles and Their Curative Effect on the Tumor Microenvironment

Samuel Maritim,^{1,2} Daniel Coman,^{1,3} Yuegao Huang,^{1,3} Jyotsna U. Rao,^{1,3}
John J. Walsh,^{1,2} and Fahmeed Hyder^{1,2,3}

¹Magnetic Resonance Research Center, Yale University, New Haven, CT, USA

²Department of Biomedical Engineering, Yale University, New Haven, CT, USA

³Department of Radiology and Biomedical Imaging, Yale University, New Haven, CT, USA

Correspondence should be addressed to Samuel Maritim; samuel.maritim@yale.edu and Fahmeed Hyder; fahmeed.hyder@yale.edu

Received 11 July 2017; Revised 25 September 2017; Accepted 3 October 2017; Published 22 November 2017

Academic Editor: Maria P. Morales

Copyright © 2017 Samuel Maritim et al. This is an open access article distributed under the Creative Commons Attribution License, which permits unrestricted use, distribution, and reproduction in any medium, provided the original work is properly cited.

Since brain's microvasculature is compromised in gliomas, intravenous injection of tumor-targeting nanoparticles containing drugs (D-NPs) and superparamagnetic iron oxide (SPIO-NPs) can deliver high payloads of drugs while allowing MRI to track drug distribution. However, therapeutic effect of D-NPs remains poorly investigated because superparamagnetic fields generated by SPIO-NPs perturb conventional MRI readouts. Because extracellular pH (pH_e) is a tumor hallmark, mapping pH_e is critical. Brain pH_e is measured by biosensor imaging of redundant deviation in shifts (BIRDS) with lanthanide agents, by detecting paramagnetically shifted resonances of nonexchangeable protons on the agent. To test the hypothesis that BIRDS-based pH_e readout remains uncompromised by presence of SPIO-NPs, we mapped pH_e in glioma-bearing rats before and after SPIO-NPs infusion. While SPIO-NPs accumulation in the tumor enhanced MRI contrast, the pH_e inside and outside the MRI-defined tumor boundary remained unchanged after SPIO-NPs infusion, regardless of the tumor type (9L versus RG2) or agent injection method (renal ligation versus coinjection with probenecid). These results demonstrate that we can simultaneously and noninvasively image the specific location and the healing efficacy of D-NPs, where MRI contrast from SPIO-NPs can track their distribution and BIRDS-based pH_e can map their therapeutic impact.

1. Introduction

Treatment and management of glioblastoma, the most common and malignant form of primary brain tumors, represent an unmet clinical challenge [1]. While gliomas are relatively rare compared to other forms of cancer malignancies [1], they are characterized by the worst prognosis, with a 5-year survival of less than 10% [2]. Treatments fail because gliomas are highly invasive, the blood brain barrier (BBB) prevents drugs from reaching the tumor at therapeutic doses, and systemic toxicity limits benefits from therapy [3–5]. In addition, there is a lack of reliable in vivo methods that can

simultaneously and noninvasively measure the delivery and therapeutic benefits of cancer drugs. Therapy can be greatly improved by delivering high drug doses specifically to the tumor (while minimizing systemic toxicities) and by timely and quantitative monitoring of the delivery and efficacy of these drugs.

The transport and delivery of therapeutic agents into the brain parenchyma are impeded by a dense network of capillary endothelial cells, pericytes, and perivascular macrophages, which together form the BBB [6]. In the healthy brain, the BBB allows a highly selective transport of endogenous substances (e.g., nutrients) that are critical to brain function

while keeping out potentially harmful toxins and drugs that are circulating in the blood [7, 8]. However, the BBB is disrupted in several pathologies including high-grade gliomas leading to increased leakiness (i.e., hyperpermeability) [9, 10]. Breakthroughs in glioma imaging and chemotherapy exploit the fact that nanoparticles (NPs) loaded with drugs (D-NPs) and MRI contrast agents like superparamagnetic iron oxide (SPIO-NPs) can extravasate from the blood through the large vascular fenestrations into the tumor [11, 12]. The combination of increased vascular permeability and poor lymphatic clearance in tumors leads to accumulation of NPs in tumors through enhanced permeation and retention (EPR) [13]. While tumors, including gliomas, generally possess larger vascular fenestrations (and hence higher permeability) compared to healthy tissue, these fenestrations are highly dependent on the location of the vessels in the tumor (i.e., fewer abnormalities in vessels on tumor periphery and higher in the tumor core), and moreover the fenestrations depend on the age/size of the tumor (i.e., larger tumors tend to have more abnormalities) [14, 15]. The pores on tumor vasculature include caveolae, vesiculo-vacuolar organelles, and fenestrations that are on the order of 10–20 nm along with larger but sporadic interendothelial cell gaps, which are significantly larger than 200 nm in diameter [16–20]. Thus NPs like the Molday ION (or SPIO-NPs; 30–50 nm hydrodynamic diameter) can extravasate passively across the BBB of the tumor niche more effectively compared to the normal neuropil. Therefore extravasation and accumulation of NPs will vary between the tumor core, tumor boundary, and healthy tissue [21–25].

Tumor-specific delivery of D-NPs can be further enhanced by coating the D-NPs with ligands that target overexpressed receptors and/or transporters in tumors [26–29]. Despite these advances in targeting of D-NPs for delivering high drug payloads to tumors, the effect of these D-NPs on the tumor microenvironment remains largely unknown. SPIO-NPs have been evaluated and approved for clinical use as MRI contrast agents [30–37]. Because the MRI contrast generated by SPIO-NPs persists for a long time, SPIO-NPs have recently been combined with D-NPs and used to simultaneously image drug delivery and biodistribution with MRI [12, 38–41]. However, the large superparamagnetic fields generated by SPIO-NPs disturb most MRI molecular readouts.

Because low extracellular pH (pH_e) is a hallmark of cancer pathogenesis and promotes tumor invasion and resistance to therapy [42–48], there is need for advanced pH_e mapping methods to enable monitoring of glioma invasion. Since some drugs only work in certain pH ranges, precise knowledge of pH_e can aid in choosing and tailoring therapeutic regimens [49–51]. Additionally, their therapeutic efficacy may be assessed by measuring their ability to raise and normalize pH_e , for example, by drugs that alter pH_e directly or affect tumor's aerobic glycolysis. Many MRI methods exist for measuring and mapping pH_e . Relaxation-based methods (e.g., with Gd^{3+}) are highly dependent on the degree of tissue perfusion and local agent concentration thus making quantification of pH_e difficult [52]. pH_e -sensitive MRI methods based

on proton exchange (i.e., between water protons and protons of amide/amine and hydroxyl moieties) such as chemical exchange saturation transfer (CEST) are also dependent on agent concentration and may additionally be complicated by magnetization transfer effects [53]. Spectroscopic methods, for example, ^{31}P MRS with 3-aminopropyl phosphonate (3-APP), which have pH_e -sensitive exchangeable protons [54, 55], suffer from low spatial resolution and significant line broadening in the presence of SPIO-NPs [56].

We previously obtained pH_e maps in glioma-bearing rats with biosensor imaging of redundant deviation in shifts (BIRDS) using lanthanide agents, for example, thulium 1,4,7,10-tetraazacyclododecane-1,4,7,10-tetrakis(methylene phosphonate), TmDOTP $^{5-}$ [57, 58]. Since the BIRDS platform is based on direct detection of the paramagnetically shifted resonances of the nonexchangeable protons on the agents (rather than their peak amplitude or effect on water relaxation rate), the pH_e readout with BIRDS is independent of agent concentration [59, 60]. The functional part of the pH sensitivity stems from the pH-sensitive exchangeable protons of the phosphonate groups on the agents. With advanced k-space sampling of ultra-fast chemical shift imaging (CSI), the spatiotemporal resolution of BIRDS has improved [61]. Previously we observed in vitro that the pH sensitivities and readout with BIRDS agents are not compromised by the presence of SPIO-NPs [62]. Here we hypothesized that BIRDS-based pH_e readout in glioma-bearing rats remains uncompromised by the presence of SPIO-NPs. We compared pH_e measured with TmDOTP $^{5-}$ by BIRDS before and after infusion of SPIO-NPs in rats bearing 9L gliosarcomas and RG2 gliomas. We used different agent administration methods (renal ligation versus coinjection with probenecid) to inhibit the rapid clearance of the agent by the renal system. In addition, we compared the transverse relaxation rate enhancement from SPIO-NPs across brain regions. Our results suggest that we can use the MRI contrast from SPIO-NPs to track the distribution of D-NPs and then use the BIRDS-based pH_e readout to map their therapeutic impact.

2. Materials and Methods

TmDOTP $^{5-}$ for BIRDS was purchased from Macrocyclics Inc. (Plano, TX, USA), while SPIO-NPs (Molday ION) were purchased from BioPAL Inc. (Worcester, MA, USA). The Molday ION (10 mg Fe/mL, dextran-coated, hydrodynamic diameter 30 nm, zeta potential -4.8 mV) were used without further modification or dilution to avoid altering their physical properties. Probenecid (used for temporary inhibition of renal clearance) was purchased from Sigma-Aldrich (St. Louis, MO, USA). Fischer 344 rats (male, 200–250 g) were obtained from Yale University vendors. RG2 and 9L tumor cell lines were purchased from American Type Culture Collections (Manassas, VA, USA). All animal experiments were conducted in accordance with Yale University's approved institutional animal care and use committee (IACUC) protocols. Tumor inoculation, animal preparation, and handling were conducted as described in our previous work [57, 58]. In vivo magnetic resonance (MR) scans were conducted on

a 9.4T Agilent (Santa Clara, CA, USA) or Bruker (Billerica, MA, USA) horizontal-bore spectrometer with a 1.4-cm ^1H surface RF coil.

2.1. Tumor Inoculation. The RG2 and 9L tumor cell lines were cultured and grown at 37°C and 5% CO_2 in DMEM media containing 10% heat-activated fetal bovine serum and 1% penicillin-streptomycin. The cells were harvested when they reached 80% confluence and suspended in serum-free media for inoculation. Rats were anesthetized with 3% isoflurane and placed on a stereotactic holder. A heating pad was used to maintain the rat at physiological temperature ($36\text{--}37^\circ\text{C}$). An aliquot volume of $5\ \mu\text{L}$ with RG2 cells (1,250 cells) or 9L cells (100,000 cells) was injected into the right striatum 3 mm laterally to the right of bregma and 3 mm below the dura using a $10\ \mu\text{L}$ Hamilton syringe fitted with a 26-gauge beveled needle. The $5\ \mu\text{L}$ volume was injected over the course of 5 minutes and the needle was left in place for an additional 5 minutes after the infusion stopped. The needle was then withdrawn slowly to prevent backflow of the cells. The cranial burr hole was sealed with bone wax. The scalp was sutured and treated with antibiotics to prevent infection. Meloxicam (1 mg/kg) was administered to prevent pain and inflammation.

2.2. Animal Preparation and Scanning. The tumor-bearing rats were scanned ~ 3 weeks after tumor inoculation when the tumor diameter was at least ~ 3 mm. The rats were anesthetized with 2% isoflurane, tracheotomized, and artificially ventilated (70% $\text{N}_2\text{O}/30\% \text{O}_2$). The rats were placed on a heating pad to keep them warm during surgery. A femoral vein was cannulated with a PE-10 line for contrast agent administration (1 mmol/kg for TmDOTP^{5-} and 14 mg Fe/kg for SPIO-NPs). A femoral artery was cannulated with a PE-50 line for monitoring animal physiology (pCO_2 , pO_2 , pH, blood pressure) throughout the experiment. The rat was then anesthetized with α -chloralose using an intraperitoneal line. To inhibit renal clearance and enhance contrast agent extravasation into the extracellular space and accumulation in the tumor, rats either received a coinfusion of TmDOTP^{5-} and probenecid ($n = 5$) or underwent renal ligation and infusion of TmDOTP^{5-} alone ($n = 3$). While renal ligation inhibits clearance efficiently, it is not suitable for longitudinal studies. Previously, we demonstrated that probenecid temporarily inhibited renal clearance when coinjected with the agent, thus enabling longitudinal studies and obviating the need for invasive renal surgeries [58]. Probenecid (100 mg/kg) was infused for 10 minutes ($24.5\ \mu\text{L}/\text{min}$), followed by a waiting period of 20 minutes, and then coinfused slowly with TmDOTP^{5-} over a period of 90 minutes. A water-heating blanket was used to maintain body temperature of the animals between 36 and 37°C over the course of the experiment. A rectally placed fiber optic probe was used to monitor the body temperature during the scans.

2.3. MRI and BIRDS. In vivo transverse relaxation rate (R_2) maps were obtained using a standard spin-echo sequence with 11 slices, 128×128 in-plane resolution, 1 mm slice

thickness, field of view (FOV) $25 \times 25\ \text{mm}^2$, recycle time (TR) 6 s, and 12 different values of echo time (TE) from 10–120 ms. The transverse relaxivity (r_2) of Molday ION (SPIO-NPs) was measured in vitro using the same pulse sequence using samples of varying concentrations of Molday ION (1 mg/kg to 15 mg/kg). The relaxivity was calculated from the slope of the linear fit of R_2 versus concentration. Although extreme pH changes can significantly alter properties of NPs, Liu et al. showed that the zeta potentials and hydrodynamic diameters of dextran-coated SPIO-NPs are fairly stable at physiologically relevant pH and ionic concentrations [63]. They showed that, between pH 4–8 and media of different ionic strength (0–140 mM), there was no aggregation of SPIO-NPs and that the change in hydrodynamic diameter of SPIO-NPs was less than 10 nm, while the change in zeta potential was less than 10%. Nevertheless, extreme pH changes could affect the physical features of SPIO-NPs. For example, a pH less than 4 could degrade the SPIO-NPs altogether, while a pH greater than 10 could lead to significant aggregation. Because we did not modify the SPIO-NPs or change their media and pH, we do not expect property changes within the pH_e range of tumors, normal tissue, and blood.

The rats were infused with TmDOTP^{5-} and the 3D CSI acquisition was started 40 minutes after TmDOTP^{5-} infusion in both the probenecid coinfused and renal-ligated rats. TmDOTP^{5-} and similar lanthanide agents have previously been shown to cross the BBB and have been used to map whole brain pH_e and temperature by BIRDS in healthy rodents [60, 64, 65]. We previously proposed that these agents slowly diffuse in the brain through the fenestrated vessels of circumventricular organs [66, 67]. Moreover, diffusion of these agents from blood vessels into the extracellular space is enhanced by the high concentration gradient achieved by inhibition of renal clearance using renal ligation or coinfusion of the agent with probenecid [58, 60, 64].

The 3D CSI datasets were acquired with a reduced spherical encoding of k-space, as previously described [57], with a TR of 5 ms, FOV of $25 \times 25 \times 25\ \text{mm}^3$, and a nominal voxel resolution of $1\ \mu\text{L}$. A dual-banded refocused 90° Shinnar-Le Roux (SLR) pulse of 35 kHz bandwidth, 90 kHz separation, and 205 μs duration was used to selectively excite the H2/H3 and H6 protons of TmDOTP^{5-} (i.e., on either side of water). The phase encoded gradient duration was 160 μs , the spectral width was 250 kHz, and the acquisition time was 4.1 ms. The total acquisition time for each 3D CSI dataset scan was 12 minutes. First a pH_e map was acquired before the SPIO-NPs injection. Then a spin-echo dataset was obtained to determine the R_2 enhancement induced by TmDOTP^{5-} . Next, the TmDOTP^{5-} infusion was stopped and SPIO-NPs were injected slowly (over 5 minutes). Then another spin-echo dataset was obtained 15 minutes after the infusion of SPIO-NPs to determine the additional R_2 enhancement due to SPIO-NPs. Finally, infusion of remaining TmDOTP^{5-} dose was then resumed and another pH_e map was obtained after infusion of SPIO-NPs.

R_2 maps were obtained by fitting the absolute MRI intensity at different TEs to a single exponential function using Matlab (Mathworks Inc., Natick, MA, USA). R_2 values from

the 3 conditions (i.e., no contrast agent, after TmDOTP⁵⁻ infusion, and after SPIO-NPs infusion) were compared to determine the relaxation enhancement of each contrast agent. Average R_2 values were measured in regions of interest (ROIs), where 1 mm circular rings were taken from the center of mass of the tumor. The tumor edge was defined as regions 1 mm immediately outside the MRI-defined tumor core. Comparing the measured R_2 against the relaxivity of Molday ION allowed the amount of SPIO-NPs in each region to be approximated.

The 3D CSI datasets were used to create maps of the H2, H3, and H6 resonances of TmDOTP⁵⁻ before and after infusion of SPIO-NPs. The linewidth (LW) of the H6 resonance was measured to generate LW maps and create histograms before and after infusion of SPIO-NPs. While any of the three resonances could have been used to make the LW maps, H6 was chosen because it had the highest signal-to-noise ratio (SNR). BIRDS-based pH_e maps of the brain obtained with TmDOTP⁵⁻ were calculated as previously described [57, 58, 60, 62]. Briefly, the 3D CSI datasets were reconstructed to a $25 \times 25 \times 25$ matrix using an in-house Matlab script. pH_e was calculated by fitting the H2, H3, and H6 resonances (i.e., δ_2 , δ_3 , and δ_6 , respectively) to

$$\text{pH}_e = a_0 + \sum_{k=2,3,6} a_1^k \delta_k + \sum_{k=2,3,6} \sum_{j=2,3,6} a_2^{kj} \delta_k \delta_j, \quad (1)$$

where the coefficients a_0 , a_1^k , and a_2^{kj} were calculated from linear least-squares fit of pH_e as a function of the resonances δ_2 , δ_3 , and δ_6 [60]. Average pH_e values before and after infusion of SPIO-NPs were determined as a function of distance from the center of mass of the tumor, similar to the procedure described above for the R_2 maps.

2.4. Prussian Blue Iron Staining. Rats were sacrificed at the end of the experiments and brains were perfusion-fixed in 4% paraformaldehyde for Prussian blue iron staining to assess the distribution of SPIO-NPs. 10 μm thick coronal sections of the fixed tissue were incubated in a solution of 4% potassium ferrocyanide and 4% hydrochloric acid twice for 10 minutes and then counterstained with nuclear fast red. Regions with Fe^{3+} (from SPIO-NPs) were expected to stain blue due to formation of ferric ferrocyanide.

3. Results

The R_2 maps before any contrast agent infusion (Figure 1(a)), after TmDOTP⁵⁻ infusion (Figure 1(b)), and after the infusion of SPIO-NPs (Figure 1(c)) are shown for a renal-ligated rat bearing an RG2 tumor. While tumor localization was obtained in all three MRI cases, much better delineation was observed upon enhancements by TmDOTP⁵⁻ alone or TmDOTP⁵⁻ + SPIO-NPs. While R_2 increases were observed after infusion of TmDOTP⁵⁻ (relative to the intrinsic contrast), a superior MRI contrast was observed after the infusion of SPIO-NPs. The circular ROIs that were drawn from the tumor center are shown in Figure 1(d). The R_2 relaxation enhancement was ROI-dependent with higher R_2 values inside the tumor and lower R_2 outside the tumor

(Figure 1(e)). Since R_2 enhancement was dependent on the concentration of the paramagnetic agents, the observed ROI-specific R_2 enhancement suggests that the extravasation (and accumulation) of both TmDOTP⁵⁻ and SPIO-NPs was highest in the tumor core and lower in regions farthest from the tumor's center of mass.

The R_2 values in the tumor (boundary marked by black outlines in Figures 1(a)–1(c)) were 22.5, 43.4, and 61.2 s^{-1} before contrast agent infusion, after infusion of TmDOTP⁵⁻, and after infusion of SPIO-NPs, respectively. For the healthy/nontumor tissue (contralateral side), the R_2 values were 25.8, 27.3, and 31.5 s^{-1} before contrast agent administration, after infusion of TmDOTP⁵⁻, and after infusion of SPIO-NPs, respectively. The measured R_2 relaxivity of Molday ION at 9.4 T in vitro was $2.45 \text{ s}^{-1} \text{ mg}^{-1} \text{ Fe/kg}$. By comparing the R_2 enhancement by SPIO-NPs against the relaxivity of the Molday ION, the average concentration of SPIO-NPs in the tumor (ROIs 1–3 mm) was determined to be 7.27 mg Fe/kg . In healthy/nontumor tissue (ROIs 4–9 mm), there was a 4.1 s^{-1} change in R_2 with SPIO-NPs, which corresponds to 1.69 mg Fe/kg . Thus, the concentration of SPIO-NPs in the tumor was 4.3 times greater than in healthy/nontumor tissue, suggesting a fourfold enhanced extravasation/accumulation in the tumor.

Given the physical characteristics of Molday ION, we anticipate that the induced MRI effect is from SPIO-NPs within the extracellular milieu and calculating the concentration of SPIO-NPs in vivo should not be significantly affected by using the relaxivity measured in vitro. Girard et al. showed that the relaxivity of SPIO-NPs internalized in cells was lower than that of freely dispersed (in vitro) SPIO-NPs by as much as up to 4 times [68]. Taylor et al. also showed that the relaxivity of Molday ION internalized in cells was 4 times lower than the relaxivity in solution [69]. If we assume the relaxivity of Molday ION in vivo is 4 times lower than what was measured in vitro, then the calculated concentration of SPIO-NPs in both the tumor and healthy brain would be 4 times higher, but the relative distribution in tumor versus healthy/nontumor tissue would remain the same. For example, if we assume a 4x lower in vivo relaxivity ($0.61 \text{ mg}^{-1} \text{ s}^{-1}$ in vivo versus $2.45 \text{ mg}^{-1} \text{ s}^{-1}$ in vitro), the concentration of SPIO-NPs in the tumor would be 29.16 mg Fe/kg while the concentration in the healthy tissue would be 6.72 mg Fe/kg (4.3 times lower than in the tumor). However, we expect that most of the SPIO-NPs will accumulate in the extracellular space where the microenvironment is more similar to the in vitro situation than that of SPIO-NPs internalized in cells. Moreover, we do not expect the relaxation of SPIO-NPs to change significantly over the pH range of our in vivo studies (i.e., pH_e 6.8 in tumors to 7.3 in healthy/nontumor tissue). Liu et al. and others have shown that the R_2 of dextran-coated SPIO-NPs was not significantly different over this pH range [63, 70]. Using different concentrations of Molday ION, Shu et al. showed that the R_2 increase with increasing Molday ION dose was uniform across different brain regions [71]. Thus we expect the relaxivity of SPIO-NPs calculated in vitro to be a good approximation of the in vivo situation. Although we expect our concentration estimation to be

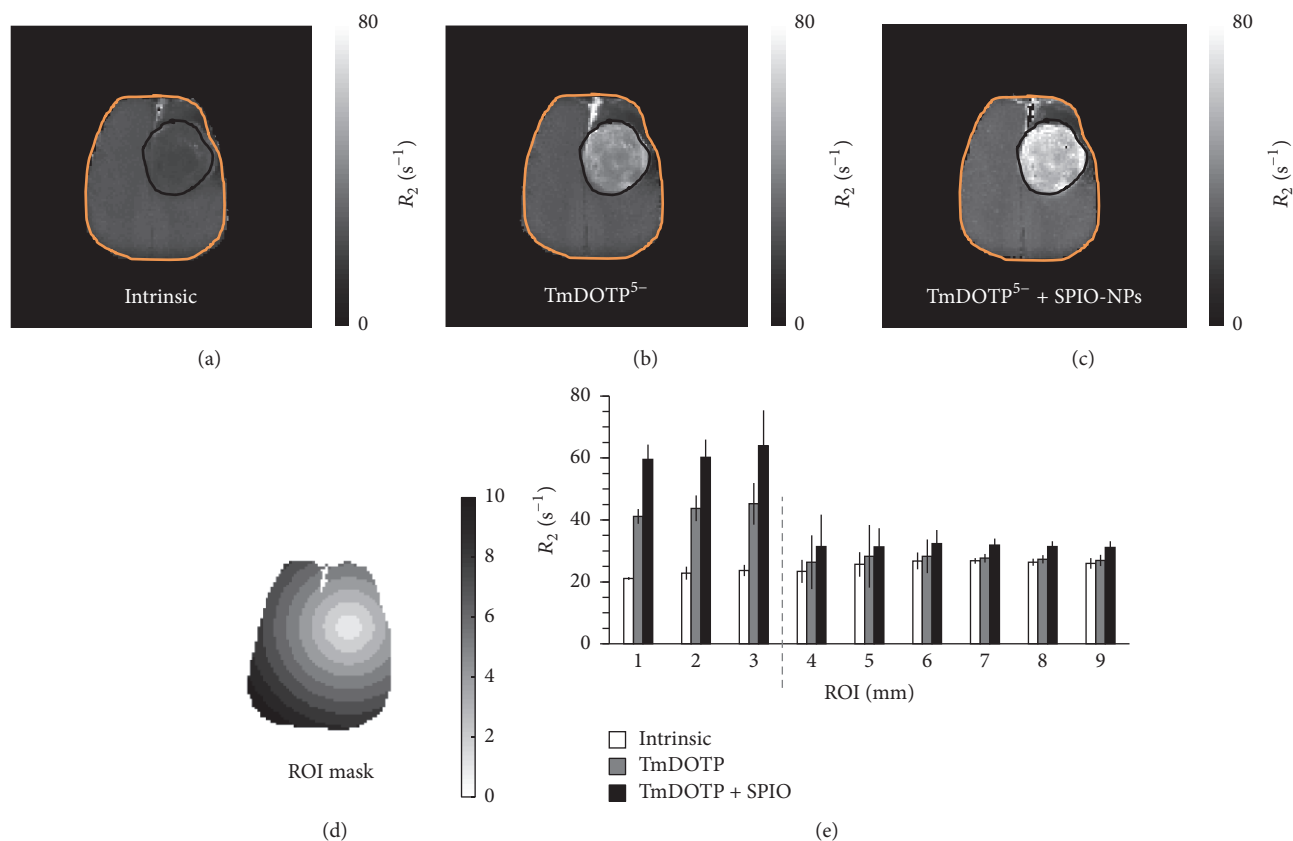


FIGURE 1: Transverse relaxation rate (R_2) maps of an RG2 glioma-bearing rat that underwent renal ligation for TmDOTP⁵⁻ infusion, (a) without any contrast agent, (b) after infusion of TmDOTP⁵⁻, and (c) after infusion of SPIO-NPs. The scale bar in (a–c) denotes R_2 values from 0 to 80 s⁻¹. Compared to the R_2 map before TmDOTP⁵⁻ infusion (a), the R_2 enhancement was observed throughout the brain after TmDOTP⁵⁻ infusion (b), but superior R_2 enhancement and tumor delineation were observed following infusion of SPIO-NPs which also had cumulative effects from infusion of TmDOTP⁵⁻ (c). The contrast enhancement from both TmDOTP⁵⁻ and TmDOTP⁵⁻ with SPIO-NPs was region-specific, with highest enhancement in the tumor core and limited enhancement outside the tumor (relative to the intrinsic contrast, (a)). The black outline in (a–c) denotes the tumor boundary, which is based on the superior MRI contrast after infusion of SPIO-NPs. The region of interest (ROI) mask based on 1 mm circular rings from the tumor center (d) was used to generate the radial R_2 distribution histogram of these ROIs (e). Scale bar in (d) denotes 0 to 10 mm diameter circular ROIs (portrayed on a representative rat brain slice). The gray dashed line in (e) denotes the demarcation between tumor and nontumor regions. The amount of SPIO-NPs in the tumor was 4.3 times greater than in the healthy tissue suggesting a preferential extravasation and accumulation of SPIO-NPs in the tumor. See Figure S1 for examples of Prussian blue staining for SPIO-NPs of an RG2 glioma-bearing rat that underwent renal ligation for TmDOTP⁵⁻ infusion. See Figure S2 for examples of R_2 maps of an RG2 glioma-bearing rat that underwent coinfusion of probenecid and TmDOTP⁵⁻.

only minimally affected, nevertheless these values should be considered “apparent” concentrations.

The preferential distribution of SPIO-NPs in tumors over healthy/nontumor tissues was tested with Prussian blue staining for Fe³⁺. Although the results from Prussian blue staining are not quantitative, regions that showed higher levels of SPIO-NPs were stained blue, indicating presence of Fe³⁺ (see Figure S1 in the Supplementary Material available online at <https://doi.org/10.1155/2017/3849373>). The Prussian blue stained images show an abundance of SPIO-NPs in the tumor, but very little staining on the healthy/nontumor contralateral side of the brain, supporting the enhanced accumulation of SPIO-NPs in the tumors observed with R_2 mapping.

Since the R_2 data shown in Figure 1 is from a renal-ligated rat, we obtained similar data from a rat that underwent

coinfusion of TmDOTP⁵⁻ and probenecid (Figure S2). The amount of SPIO-NPs in the tumor was 2 times higher than in nontumor tissue (i.e., 4.5 versus 2.2 mg Fe/kg). In this case, the R_2 enhancement (Figure S2) was slightly lower than that observed in a renal-ligated rat (Figure 1), which is possibly due to higher TmDOTP⁵⁻/SPIO-NPs concentration buildup in a renal-ligated rat.

Because acidic pH_e is a hallmark of tumor pathology [72, 73], we obtained brain pH_e maps in glioma-bearing rat brains with BIRDS using TmDOTP⁵⁻ before and after infusion of SPIO-NPs. We previously demonstrated that high concentrations of SPIO-NPs increase the LW of the TmDOTP⁵⁻ proton resonances in vitro [62]. In the current work, in addition to pH_e maps, we also calculated the LW of the H6 proton of TmDOTP⁵⁻ in each voxel in the brain, before and after infusion of SPIO-NPs. Multimodal data

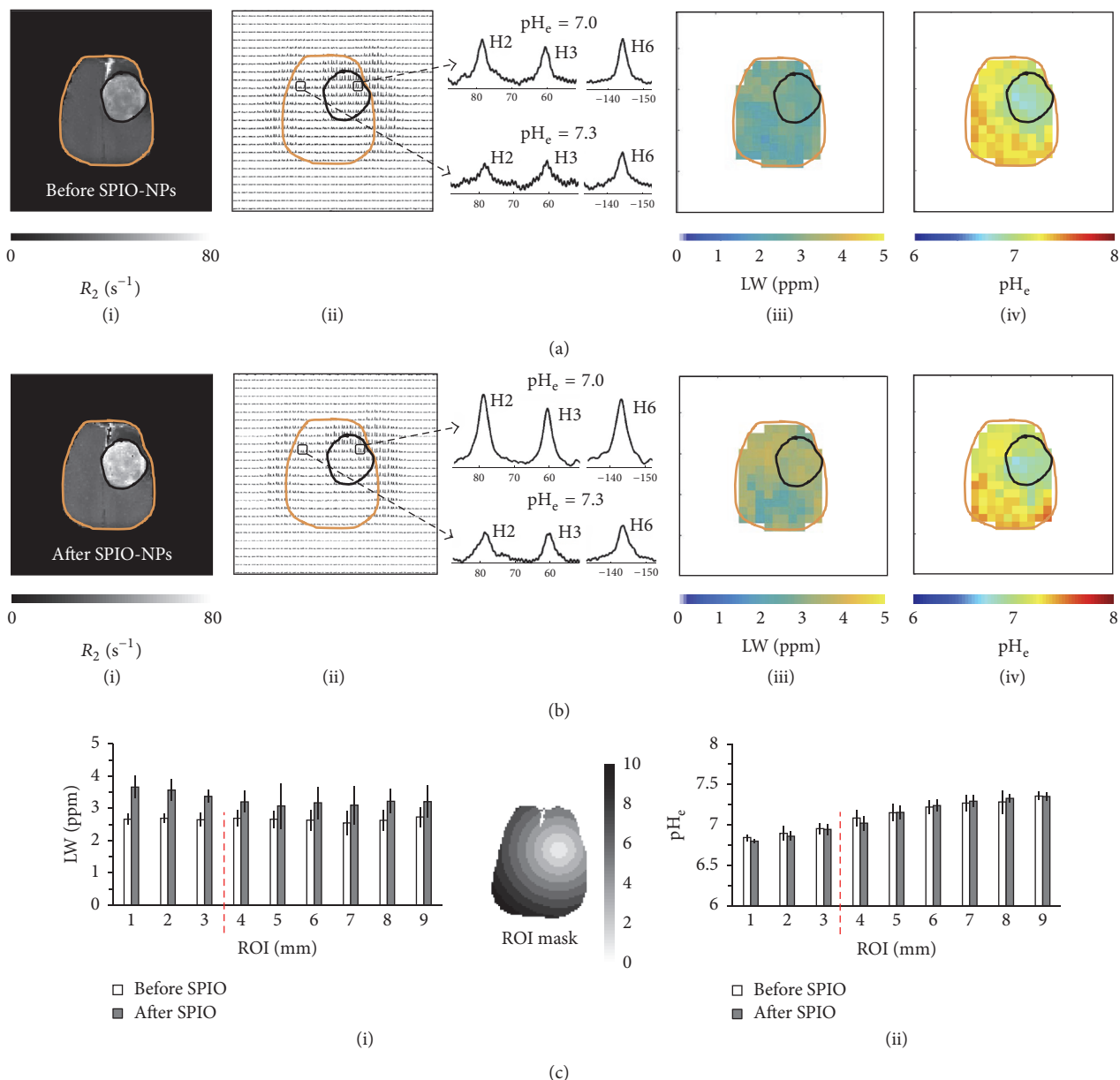


FIGURE 2: Multimodal data of relaxation rate (R_2), chemical shift imaging (CSI), linewidth (LW), and extracellular pH (pH_e) maps obtained for the same RG2 tumor-bearing rat in Figure 1, which had undergone renal ligation. ((a)(i)–(iv)) represent maps before the SPIO-NPs infusion while ((b)(i)–(iv)) represent the maps after the SPIO-NPs infusion. The R_2 maps were used to delineate and localize the tumor (black outline) and brain (orange outline) boundaries on the CSI, LW, and pH_e maps. R_2 values inside the tumor increased significantly after infusion of SPIO-NPs. The CSI maps were used to create the LW maps and pH_e maps. The LW increased after SPIO-NPs infusion especially in the tumor. The pH_e values within the tumor core and also on the tumor margin were lower than in the healthy/nontumor regions. The panels between the CSI and the LW maps show examples of 1H spectra of TmDOTP $^{5-}$ protons from voxels inside and outside the tumor, revealing a significant intratumoral and peritumoral LW and pH_e difference. A more detailed comparison was done using a region of interest (ROI) analysis of LW ((c)(i)) and pH_e ((c)(ii)) maps before and after the infusion of SPIO-NPs, using the ROI mask shown. The scale bar in the mask denotes 0 to 10 mm diameter circular ROIs (portrayed on a representative rat brain slice). The red dashed line denotes the demarcation between tumor (ROIs 1–3) and tumor edge (ROI 4)/nontumor regions (ROIs 5–9). See Figure S3 for an example of multimodal data of an RG2 tumor rat that underwent coinfusion of probenecid and TmDOTP $^{5-}$.

(R_2 maps (i), CSI maps (ii), LW maps (iii), and pH_e maps (iv)) before (Figure 2(a)) and after (Figure 2(b)) infusion of SPIO-NPs for the same RG2 tumor-bearing rat shown in Figure 1, which had undergone renal ligation, were obtained.

The R_2 maps (Figures 2(a)(i) and 2(b)(i)) were used to delineate and localize the tumor (black outline) and brain (orange outline) boundaries on the CSI, LW, and pH_e maps. The CSI maps (Figures 2(a)(ii) and 2(b)(ii)) were used to

TABLE 1: Regional analysis for relaxation rate (R_2) for all RG2 tumor-bearing rats that underwent coinfusion of TmDOTP⁵⁻ and probenecid ($n = 5$). See Figure 3(a) for details. R_2 was measured inside the MRI-defined tumor core (see Figure S2), at the tumor edge (regions 1 mm outside the tumor boundary), and in the healthy/nontumor tissue before and after the infusion of SPIO-NPs. Data shown are mean and standard deviation (SD).

R_2	Intrinsic		TmDOTP ⁵⁻		TmDOTP ⁵⁻ + SPIO-NPs	
	Mean	SD	Mean	SD	Mean	SD
Tumor core	22.5	2.1	24.7	2.5	32.7	5.2
Tumor's edge	22.7	4.0	23.7	4.4	28.6	7.9
Nontumor tissue	23.8	3.8	23.2	3.4	27.3	3.7

create the LW maps (Figures 2(a)(iii) and 2(b)(iii)) and pH_e maps (Figures 2(a)(iv) and 2(b)(iv)). Examples of ¹H spectra of TmDOTP⁵⁻ protons from voxels inside and outside the tumor—illustrated in the panel between the CSI maps and LW maps—show that there is a significant intratumoral and peritumoral LW and pH_e differences. The SNR was higher in the spectra after infusion of SPIO-NPs than before because TmDOTP⁵⁻ infusion was resumed 15 minutes after the end of SPIO-NPs infusion. While the CSI maps (Figures 2(a)(ii) and 2(b)(ii)) show regionally varying TmDOTP⁵⁻ intensities, after infusion of SPIO-NPs, there is a clear variation in the LW maps, increasing from ~ 2.5 ppm globally before the infusion (Figure 2(a)(iii)) to ~ 3.7 ppm inside the tumor and ~ 3.4 ppm in the healthy/nontumor contralateral side of the brain (Figure 2(b)(iii)). A detailed ROI analysis of the average LWs shows similar LWs inside and outside the tumor before infusion of SPIO-NPs (Figure 2(c)(i), white bars). However, upon infusion of SPIO-NPs (Figure 2(c)(i), gray bars), the average LW increased (from 2.6 to 3.5 ppm) in the tumor (ROIs # 1–3) and to a lesser extent (from 2.6 to 3.1 ppm) outside the tumor (ROIs # 4–9). The LW broadening in the tumor correlated with the R_2 enhancement suggesting that the LW broadening was due to higher concentration of SPIO-NPs in the tumor.

The pH_e maps (Figures 2(a)(iv) and 2(b)(iv)) were obtained by fitting the chemical shifts of the H2, H3, and H6 protons of TmDOTP⁵⁻ to equation (1) as previously described [60]. Although the CSI maps show regional variation of TmDOTP⁵⁻ proton intensities, both before and after infusion of SPIO-NPs (Figures 2(a)(ii) and 2(b)(ii)), the pH_e calculation depends only on the chemical shifts of the nonexchangeable TmDOTP⁵⁻ protons and is independent of their concentration (or peak intensity) [59, 60]. The pH_e maps of RG2 tumors show lower pH_e within the tumor core, but also beyond the tumor boundary, which is in good agreement with previous observations of this aggressive tumor type [57, 58]. Before injection of SPIO-NPs the average pH_e was 7.0 ± 0.1 within the tumor and 7.3 ± 0.1 in the healthy/nontumor tissue on the contralateral side for the RG2 tumor-bearing brain (Figure 2(a)(iv)). After injection of SPIO-NPs similar average pH_e values were observed in these regions (i.e., 7.0 ± 0.1 in the tumor and 7.3 ± 0.1 in healthy/nontumor tissue; Figure 2(b)(iv)). These in vivo results are consistent with our earlier in vitro report which showed that the pH readout and sensitivities of TmDOTP⁵⁻ are unaffected by the presence of paramagnetic agents like SPIO-NPs and Gd³⁺

agents [62]. Moreover, a detailed ROI analysis of the spatial pH_e distribution shows that the average pH_e increased as the ROI is positioned farther from the center of mass of the tumor (Figure 2(c)(ii)). However, no significant differences were observed between the average pH_e values in each ROI before and after the SPIO-NPs infusion, indicating that BIRDS-based pH_e mapping is not affected by the presence of SPIO-NPs.

Similar R_2 , CSI, LW, and pH_e maps as those shown in Figure 2 were obtained from rats, bearing RG2 tumors, that underwent coinfusion of TmDOTP⁵⁻ and probenecid (Figure S3). The results show that these distributions were similar to those observed in renal-ligated rats. Generally, the LWs increased after infusion of SPIO-NPs in all regions of the brain, but higher LW increases were observed inside the tumor. Before infusion of SPIO-NPs, the pH_e was 6.85 ± 0.03 in the tumor and the pH_e was 7.15 ± 0.06 in healthy/nontumor tissue (Figure S3 (A)(iv)). After infusion of SPIO-NPs, the pH_e was 6.86 ± 0.07 in the tumor and the pH_e was 7.17 ± 0.06 in healthy/nontumor tissue (Figure S3 (B)(iv)). The pH_e of the tumor edge (ROI 4) was also relatively acidified (pH 6.98 ± 0.13 before and 6.90 ± 0.09 after infusion of SPIO-NPs) compared to healthy/nontumor tissue farthest from the tumor core (ROIs 5–9).

Figure 3 shows the ROI analysis for R_2 and pH_e before and after infusion of SPIO-NPs for all RG2 tumor-bearing rats that underwent coinfusion of TmDOTP⁵⁻ and probenecid ($n = 5$). The R_2 enhancement was region-dependent (Figure 3(a); Table 1). Small R_2 enhancement was observed after infusion of TmDOTP⁵⁻, where R_2 increased by 2.2 s^{-1} in the tumor, 1.1 s^{-1} in the tumor edge, and no significant increase in the healthy/nontumor tissue. The tumor edge was defined as a circular ROI just 1 mm outside of the MRI defined tumor core. It is important to identify and analyze the tumor edge because after radiation therapy, it becomes edematous and harbors most therapy-resistant cells. Additionally, greater R_2 enhancement was observed upon infusion of SPIO-NPs (i.e., R_2 increase of 10.2 s^{-1} in tumor, 5.9 s^{-1} in tumor edge, and 4.1 s^{-1} in healthy/nontumor tissue). In contrast to the R_2 measurements, the average pH_e values were not affected by the SPIO-NPs infusion (Figure 3(b); Table 2). However, pH_e varied across regions; pH_e was lowest (6.9 ± 0.1) in the tumor and highest (7.2 ± 0.1) in the healthy/nontumor tissue farthest from the tumor. Low pH_e (6.9 ± 0.1) was also measured on the tumor edge. While the pH_e of the tumor edge in RG2 gliomas was acidic

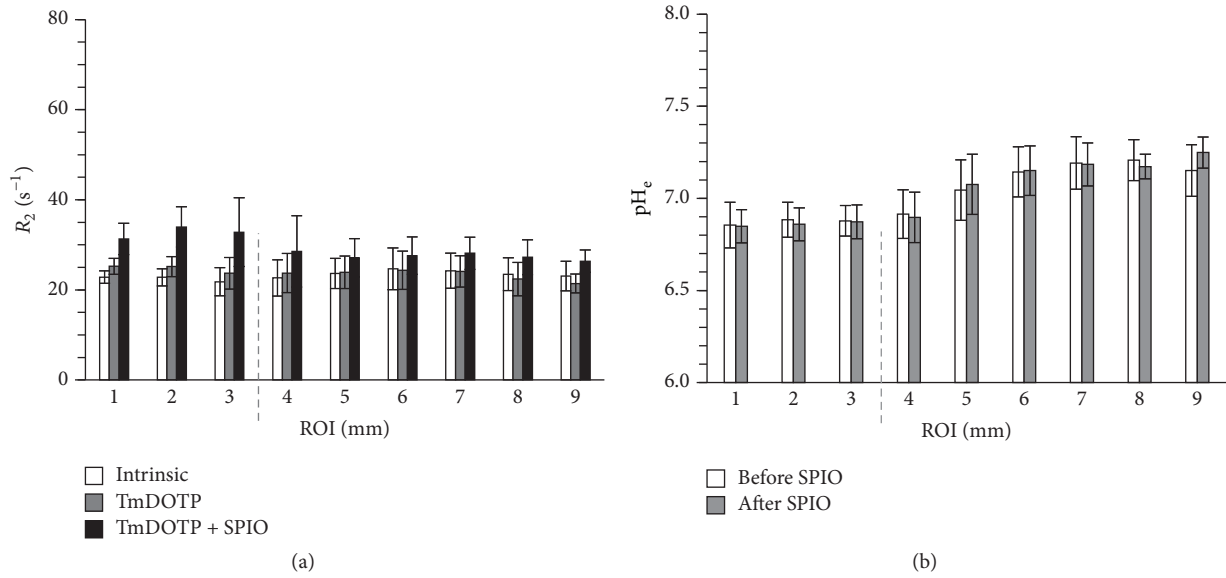


FIGURE 3: Region of interest (ROI) analysis for the average relaxation rate (R_2) and extracellular pH (pH_e) before and after infusion of SPIO-NPs for all RG2 tumor-bearing rats that underwent coinfusion of TmDOTP⁵⁻ and probenecid ($n = 5$). The ROI analysis is based on concentric 1 mm circular rings drawn from the center of mass of the tumor. (a) Average R_2 values in different ROIs for intrinsic contrast, after infusion of TmDOTP⁵⁻, and after infusion of TmDOTP⁵⁻ with SPIO-NPs. The average R_2 enhancement was highest inside the tumor (ROIs 1-3) compared to tumor edge (ROI 4) and nontumor regions (ROIs 5-9). The dashed line represents the tumor edge. Small R_2 enhancement was observed after infusion of TmDOTP⁵⁻. However, much higher R_2 enhancement was observed upon infusion of SPIO-NPs. See Table 1 for details. (b) The average pH_e values in different ROIs before and after infusion of SPIO-NPs. The pH_e values measured before and after infusion of SPIO-NPs were similar, both inside and outside the tumor. The pH_e was lowest in the tumor and highest in the healthy/nontumor tissue farthest from the tumor. Low pH_e was also measured on the tumor margin. See Table 2 for details.

TABLE 2: Regional analysis for extracellular pH (pH_e) imaging before and after infusion of SPIO-NPs for all RG2 tumor-bearing rats that underwent coinfusion of TmDOTP⁵⁻ and probenecid ($n = 5$). See Figure 3(b) for details. The pH_e was measured inside the MRI-defined tumor core (see Figure S2), at the tumor edge (regions 1 mm outside the tumor boundary), and in the healthy/nontumor tissue before and after the infusion of SPIO-NPs. Data shown are mean and standard deviation (SD).

pH_e	Before SPIO-NPs		After SPIO-NPs	
	Mean	SD	Mean	SD
Tumor core	6.9	0.1	6.9	0.1
Tumor's edge	6.9	0.1	6.9	0.1
Nontumor tissue	7.2	0.1	7.2	0.1

relative to healthy/nontumor tissue, the R_2 enhancement between the tumor edge and the healthy/nontumor tissue were similar, suggesting that the vasculature in the tumor margin was still intact despite the acidic transformation of their microenvironment. Future experiments should look at the vascularization inside, around, and far beyond the tumor boundary, for example, with dynamic contrast enhanced MRI and with epidermal growth factor receptor staining.

In addition to measurements obtained in the aggressive RG2 glioma, we also acquired pH_e maps before and after infusion of SPIO-NPs in rats bearing the less aggressive 9L gliosarcoma ($n = 4$) using coinfusion of TmDOTP⁵⁻

and probenecid (Figure 4). The pH_e maps of the aggressive RG2 tumor (Figure 4(a)(i) before versus Figure 4(a)(ii) after infusion of SPIO-NPs) showed a lower pH_e within the tumor region, but the acidification was diffuse and occurred also beyond the MRI-defined tumor boundary (see also Figures 2 and S3). Previously, it was reported that the diffuse acidification of pH_e beyond the RG2 tumor boundary correlated with increased expression of the proliferation marker Ki-67 [57]. In contrast, the pH_e maps of the less aggressive 9L gliosarcoma showed lower pH_e only within the MRI-defined tumor core (Figure 4(b)(i) before versus Figure 4(b)(ii) after SPIO-NPs). A detailed ROI analysis of the pH_e maps shows that, for the RG2, the pH_e slowly increases with the distance from the tumor core (Figure 4(a)(iii)), whereas for the 9L tumor the pH_e is highest outside the tumor boundary and is distance-independent (Figure 4(b)(iii)). Moreover, the regional pH_e trends observed with BIRDS were not dependent on the type of infusion method, that is, coinfusion of TmDOTP⁵⁻ and probenecid versus infusion of TmDOTP⁵⁻ after renal ligation (Figure S4).

4. Discussion

Elevated aerobic glycolysis in gliomas leads to elevated lactic acid and proton production, which upon extrusion from the intracellular compartment results in acidification of the extracellular milieu [44]. Additionally, because the BBB is disrupted in gliomas, NPs loaded with imaging agents

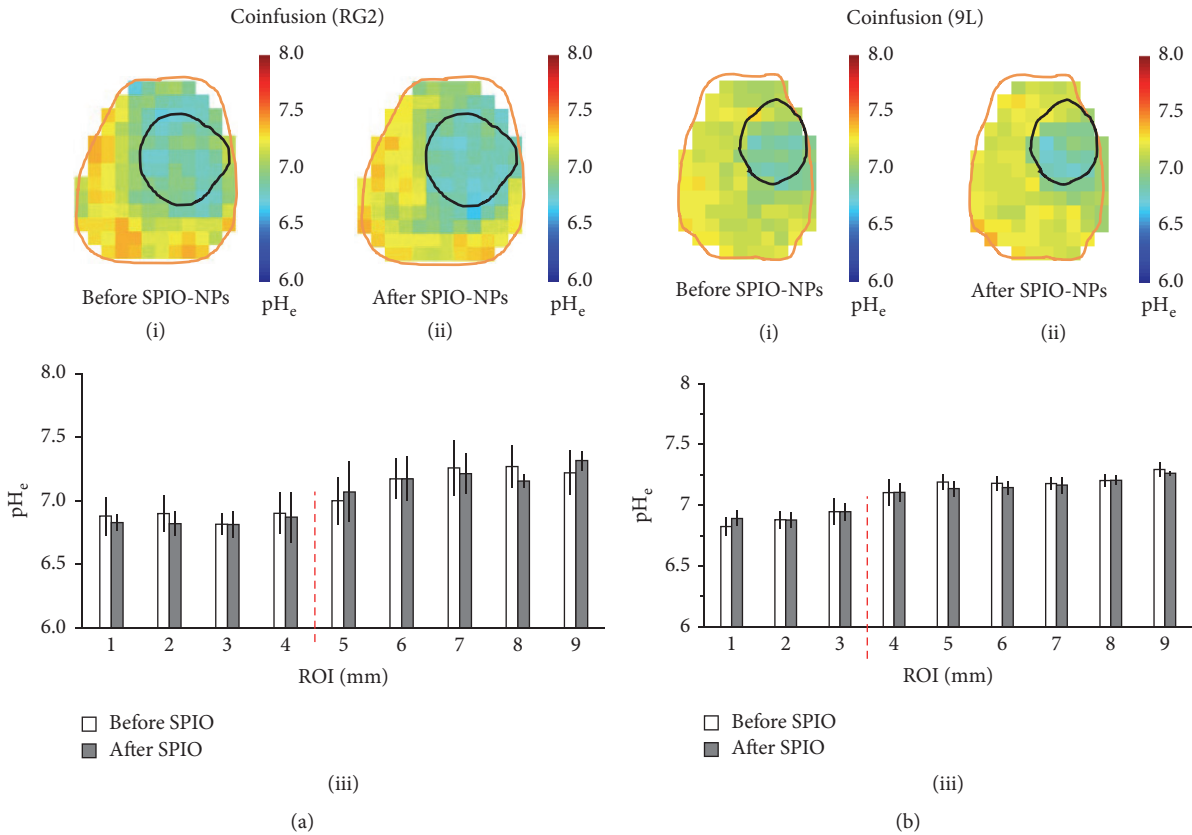


FIGURE 4: Comparison of pH_e maps for (a) RG2 glioma and (b) 9L gliosarcoma before and after infusion of SPIO-NPs in rats that underwent coinfusion of TmDOTP⁵⁻ and probenecid. In both (a) and (b), (i) and (ii) represent the pH_e maps before and after SPIO-NPs infusion, respectively, while (iii) depicts a detailed ROI analysis. See Figure 1 for details of the ROI mask. In (a), the pH_e inside the more aggressive RG2 glioma was typically lower than in the healthy/nontumor tissue, but diffuse acidification was observed well-beyond the MRI-defined tumor boundary. Thus the pH_e slowly increased as the distance from the tumor core increased. In (b), the pH_e inside the less aggressive 9L gliosarcoma was also lower than in the healthy/nontumor tissue, but the acidification did not extend beyond the MRI-defined tumor boundary, before and after infusion of SPIO-NPs. See Figure S4 for a comparison of regional pH_e dependence on the method used for inhibition of renal clearance (renal ligation versus probenecid).

(e.g., SPIO-NPs) selectively permeate into and accumulate within tumors. In the present study, a region-specific R_2 enhancement from extravasation of SPIO-NPs was observed, with higher R_2 increases inside the tumor and smaller R_2 increases outside the tumor. Although SPIO-NPs affected MRI contrast in all tissues, excellent SPIO-induced MRI contrast delineated the glioma boundary due to greater extravasation of SPIO-NPs from the vasculature into the tumor relative to healthy/nontumor tissue. We also measured pH_e with BIRDS using TmDOTP⁵⁻ before and after infusion of SPIO-NPs in rats bearing 9L and RG2 brain tumors. The results demonstrate that the pH_e readout was unaffected by the presence of SPIO-NPs, because the intratumoral-peritumoral pH_e gradients were essentially identical before and after the infusion of SPIO-NPs, despite slight variations in LWs of the proton peaks for TmDOTP⁵⁻. The measured pH_e was lowest inside the tumor and increased with the distance from the center of mass of the tumor in the more aggressive RG2 tumors. However, in the less aggressive 9L tumors, pH_e was notably higher immediately outside the tumor boundary. We envisage coinjection of BIRDS agents

(e.g., TmDOTP⁵⁻) and NPs containing drugs and SPIO, as a new methodology that can deliver high drug payloads to the tumor, image drug distribution, and track tumor location/size (by MRI), and at the same time monitor pH_e response to therapy (by BIRDS) [74].

The brain's microvasculature is either degraded or immature in several neuropathologies, including glioblastomas. Breakthroughs in glioma imaging and therapy exploit the fact that NPs, containing either SPIO (for MRI) or drugs (for therapy), can extravasate through the leaky microvasculature. The SPIO-NPs extravasate into the tumor to generate superior MRI contrast while tumor-targeted D-NPs safely deliver high payloads of drugs to the tumor [74].

In the present study, the highest R_2 enhancement (from TmDOTP⁵⁻ and SPIO-NPs) occurred in the tumor and was lowest in healthy/nontumor tissue farthest from the tumor. Because the R_2 enhancement comes entirely from the infused agents, this region-specific enhancement suggests a corresponding spatial variation in vascular permeability and consequent extravasation. In addition to the enhanced extravasation, the chaotic vascular architecture in tumors

contributes to poor clearance leading to increased retention of SPIO-NPs in the interstitial space of the tumor core. By using the R_2 enhancement and the relaxivity of Molday ION (SPIO-NPs), we calculated that the amount of SPIO-NPs in the tumor was 2 to 4 times higher than in healthy/nontumor tissue. The EPR in tumors has been widely utilized to preferentially deliver high amounts of imaging agents and D-NPs, both passively and actively [75, 76].

High-grade solid brain tumors tend to develop necrotic cores due to a combination of poor vascularization and inadequate perfusion [77–79]. Because gliomas like RG2 are very aggressive, they rapidly invade to induce severe neurological problems. As a consequence the rodent reaches terminal situations before the tumor cores are able to become necrotic. For example, these rodent brain tumors grow within a few weeks, whereas in the human brain gliomas develop necrotic foci after many months, if not longer. Tumor necrosis has very likely not yet occurred in these rodent tumors at the time points of our experiments. The observed higher R_2 in the center relative to the periphery suggests higher permeation and accumulation of SPIO-NPs in the center of the tumor due to greater extent of BBB disruption within the tumor niche. Prior studies support these observations. Beaumont et al. did not observe any necrosis in their RG2 rat gliomas at similar time points as our experiments [16]. Their staining results also showed that the BBB was significantly disrupted at the center of the tumor in RG2 tumors. While the vasculature at the primary tumor site/core is leaky, the blood vessels at the tumor infiltration sites (i.e., periphery) are often immature, which may slow the extravasation of SPIO-NPs out of the blood into these new tumor sites. Uehara et al. also showed that necrosis of tumor cores is minimal or absent in RG2 tumors at time points less than 4 weeks following inoculation [80]. Therefore based on the information regarding RG2 tumor growth from prior work in this and other laboratories, we expect the tumor cores to be non-necrotic, and thus higher R_2 increase from the SPIO-NPs would be observed in the tumor core. Additionally, because gliomas including RG2 are known to have an increased presence of macrophages relative to healthy brain tissue, the higher amount of SPIO-NPs in the tumor could be due in part to macrophage phagocytosis [16].

4.1. Superparamagnetic Iron Oxide Nanoparticles in Cancer Theranostics. Owing to their strong superparamagnetic properties, tunable size, shape, coating, and magnetic susceptibility, SPIO-NPs have gained utility as therapeutic agents in alternating magnetic field hyperthermia [81–85], as MRI contrast agents for cell tracking [86–89], and for imaging tumor location/size as well as drug delivery [40, 74, 90]. Drug delivery imaging with SPIO-NPs is often accomplished by coencapsulating drugs and SPIO into a given nanocarrier platform (e.g., micelles or liposomes). In liposomes, for example, SPIO-NPs and hydrophilic drugs can be encapsulated inside the nanocarrier, whereas hydrophobic drugs can be incorporated on the nanocarrier membrane. Recent advances also involve coating the surface of SPIO-NPs itself with drugs [11, 12]. Entry and accumulation of these drug-containing and SPIO-containing NPs into the tumor have been achieved by passive targeting, whereby the

NPs are small enough to extravasate through leaky tumor vasculature, but large enough not to cross the intact vessels in healthy/nontumor tissue. However, better and more selective targeting is achieved when the NPs are coated with ligands that are specific to receptors and/or transporters that are overexpressed on tumor cells and vasculature. Examples of such targets include transferrin receptors, epidermal growth factor receptors, folate receptors, vascular endothelial growth factor receptors, monocarboxylate transporters, and glucose transporters [29, 91–96]. In all these cases, the delivery and biodistribution of D-NPs are visualized and quantified through signal attenuation (negative contrast) of the R_2 -weighted MRI resulting from the strong superparamagnetic fields generated by SPIO-NPs. Because both the drugs and SPIO-NPs are contained in the same nanocarrier, the location and distribution of the SPIO-NPs, as observed by MRI, reflect the biodistribution of D-NPs. By quantifying the SPIO-induced MRI contrast attenuation, it is possible to quantify the D-NPs delivered to the tumor.

Currently, measurement of tumor size is the only FDA-approved method to assess the response to therapy noninvasively. Because changes in tumor size following treatment may take up to a month to manifest, this method is not ideal for aggressive brain cancers, especially when the treatment is later found not to have been effective. Thus a clear need exists for methods that can provide prompt assessment of therapeutic efficacy so that treatment can be altered quickly if desired. Recently, it was shown that quantitative monitoring of the tumor microenvironment following a pharmacologic challenge provides a better way to monitor therapeutic efficacy [97]. Because acidification of pH_e promotes drug resistance, degradation of the extracellular matrix, angiogenesis, tumor invasion, and metastasis, drugs that raise (or neutralize) pH_e by targeting the acid-generating glycolysis in tumors have demonstrated significant inhibition of tumor growth and enhanced apoptosis [45, 46, 48, 72, 98, 99]. Additionally, drugs that directly raise tumor pH_e (e.g., bicarbonate treatment) inhibit tumor invasion and metastasis [100, 101]. Because bicarbonate and drugs that inhibit glycolysis elevate pH_e in a few days, methods that quantitatively measure tumor pH_e longitudinally may provide an effective evaluation of their therapeutic efficacy and allow for prompt modification of therapy if the initial treatment is not working. A recent study has reported that temozolomide, which is an alkylating agent and is adjuvant chemotherapy used to clinically treat glioblastomas, arrests glioma growth and normalizes intratumoral pH_e [102].

4.2. Combining Drug Delivery Imaging with pH_e Imaging to Assess Therapy. Given the significant relaxation enhancement of the nonexchangeable protons on the TmDOTP⁵⁻ agent [60, 103, 104] due to pseudocontact interactions with unpaired Tm³⁺ electrons, we hypothesized that BIRDS-based pH_e readout of TmDOTP⁵⁻ will remain uncompromised by SPIO-NPs. Although SPIO-NPs altered MRI contrast in all tissues, SPIO-based MRI contrast clearly demarcated the tumor boundary due to greater extravasation of NPs through leaky blood vessels. Nonetheless, the quality of BIRDS-based

pH_e readout with TmDOTP⁵⁻, for both intratumoral and peritumoral regions, was unaffected by the presence of the SPIO-NPs, since the pH_e maps obtained before and after the infusion of SPIO-NPs were very similar.

While separate infusions of TmDOTP⁵⁻ and SPIO-NPs were employed in the present study, future studies might assess the possibility of combining them [74]. Conjugating several monomers of the pH_e-sensitive agent on the surface of the NPs could possibly enhance the sensitivity of BIRDS to monitor the immediate environment of D-NPs and prolong their lifetime to enable multiple monitoring sessions at various treatment time points. Ordinarily, BIRDS agents have fast renal clearance owing to their small size and thus renal inhibition is necessary for accumulation [57, 58, 60, 105]. However, if conjugated to NPs, the BIRDS agents lifetime might increase significantly (i.e., to several days, which is the case for SPIO-NPs), thus allowing their use without inhibition of renal clearance and obviating the need for repeated infusions [106]. Towards this goal, it has been previously demonstrated in vitro that encapsulation of BIRDS agents in liposomal nanoparticles resulted in an MR signal amplification without impeding the local pH readout [62].

5. Summary

The treatment of brain gliomas is hampered in part by a limited availability of reliable in vivo methodologies that can simultaneously and noninvasively measure glioma invasion, drug delivery, and its therapeutic benefits. In this study, we demonstrated superb MRI contrast enhancement and tumor delineation with SPIO-NPs and quantitative imaging of intratumoral-peritumoral pH_e gradients using BIRDS in rat models of brain gliomas. Furthermore, we demonstrated that both the intratumoral and peritumoral pH_e readouts, measured with BIRDS using TmDOTP⁵⁻, are not compromised by the presence of SPIO-NPs. Thus, we propose a new cancer imaging protocol that can target high drug payloads (via D-NPs) to tumors and image the drug delivery (via SPIO-NPs), concurrently map tumor location and size (by MRI), and at the same time monitor therapeutic efficacy through drug-induced changes in pH_e (by BIRDS) [74].

Abbreviations

3-APP:	3-Aminopropyl phosphonate
BBB:	Blood brain barrier
BIRDS:	Biosensor imaging of redundant deviation in shifts
CEST:	Chemical exchange saturation transfer
CSI:	Chemical shift imaging
EPR:	Enhanced permeation and retention
FOV:	Field of view
LW:	Linewidth
MR:	Magnetic resonance
NPs:	Nanoparticles
pH _e :	Extracellular pH
ROI:	Region of interest
SD:	Standard deviation

SNR:	Signal-to-noise ratio
SLR:	Shinnar-Le Roux
SPIO:	Superparamagnetic iron oxide
TmDOTP ⁵⁻ :	Thulium 1,4,7,10-tetraazacyclododecane-1,4,7,10-tetrakis methylene phosphonate.

Disclosure

Parts of this work have previously been presented as a published abstract in BRAIN & BRAIN PET 2017 Poster Viewing Session III.

Conflicts of Interest

The authors declare no conflicts of interest.

Authors' Contributions

Samuel Maritim and Fahmeed Hyder designed research. Samuel Maritim, Daniel Coman, Yuegao Huang, Jyotsna U. Rao, John J. Walsh, and Fahmeed Hyder performed research. Samuel Maritim, Daniel Coman, Yuegao Huang, Jyotsna U. Rao, and Fahmeed Hyder analyzed data. Samuel Maritim, Daniel Coman, Yuegao Huang, Jyotsna U. Rao, and Fahmeed Hyder wrote the paper.

Acknowledgments

This paper is supported by NIH Grants (R01 EB-023366, R01 EB-011968, and R01 CA-140102).

References

- [1] J. Ferlay, H. R. Shin, F. Bray, D. Forman, C. Mathers, and D. M. Parkin, "Estimates of worldwide burden of cancer in 2008: GLOBOCAN 2008," *International Journal of Cancer*, vol. 127, no. 12, pp. 2893–2917, 2010.
- [2] H. Ohgaki, "Epidemiology of brain tumors," *Methods in Molecular Biology*, vol. 472, pp. 323–342, 2009.
- [3] H. F. Bradford, "Glutamate, GABA and epilepsy," *Progress in Neurobiology*, vol. 47, no. 6, pp. 477–511, 1995.
- [4] W. M. Pardridge, "Drug targeting to the brain," *Pharmaceutical Research*, vol. 24, no. 9, pp. 1733–1744, 2007.
- [5] W. M. Pardridge, "Blood-brain barrier delivery," *Drug Discovery Therapy*, vol. 12, no. 1-2, pp. 54–61, 2007.
- [6] H. Wolburg and A. Lippoldt, "Tight junctions of the blood-brain barrier: development, composition and regulation," *Vascular Pharmacol*, vol. 38, no. 6, pp. 323–337, 2002.
- [7] M. Demeule, A. Regina, J. Jodoin et al., "Drug transport to the brain: Key roles for the efflux pump P-glycoprotein in the blood-brain barrier," *Vascular Pharmacology*, vol. 38, no. 6, pp. 339–348, 2002.
- [8] W. Risau and H. Wolburg, "Development of the blood-brain barrier," *Trends in Neurosciences*, vol. 13, no. 5, pp. 174–178, 1990.
- [9] S.-W. Lee, J. K. Woo, J. A. Park, K. C. Yoon, Y.-W. Kwon, and K.-W. Kim, "Blood-brain barrier interfaces and brain tumors," *Archives of Pharmacol Research*, vol. 29, no. 4, pp. 265–275, 2006.

- [10] J. D. Huber, R. D. Egleton, and T. P. Davis, "Molecular physiology and pathophysiology of tight junctions in the blood-brain barrier," *Trends in Neurosciences*, vol. 24, no. 12, pp. 719–725, 2001.
- [11] P.-C. Liang, Y.-C. Chen, C.-F. Chiang et al., "Doxorubicin-modified magnetic nanoparticles as a drug delivery system for magnetic resonance imaging-monitoring magnet-enhancing tumor chemotherapy," *International Journal of Nanomedicine*, vol. 11, pp. 2021–2037, 2016.
- [12] Y. Ling, K. Wei, F. Zou, and S. Zhong, "Temozolomide loaded PLGA-based superparamagnetic nanoparticles for magnetic resonance imaging and treatment of malignant glioma," *International Journal of Pharmaceutics*, vol. 430, no. 1-2, pp. 266–275, 2012.
- [13] H. Sarin, "Physiologic upper limits of pore size of different blood capillary types and another perspective on the dual pore theory of microvascular permeability," *Journal of Angiogenesis Research*, vol. 2, no. 1, article no. 14, 2010.
- [14] D. J. Cox, G. J. Pilkington, and P. L. Lantos, "The fine structure of blood vessels in ethylnitrosourea-induced tumours of the rat nervous system: with special reference to the breakdown of the blood-brain barrier," *Journal of Experimental Pathology*, vol. 57, pp. 419–430, 1976.
- [15] K. E. Schlageter, P. Molnar, G. D. Lapin, and D. R. Groothuis, "Microvessel organization and structure in experimental brain tumors: Microvessel populations with distinctive structural and functional properties," *Microvascular Research*, vol. 58, no. 3, pp. 312–328, 1999.
- [16] M. Beaumont, B. Lemasson, R. Farion, C. Segebarth, C. Rémy, and E. L. Barbier, "Characterization of tumor angiogenesis in rat brain using iron-based vessel size index MRI in combination with gadolinium-based dynamic contrast-enhanced MRI," *Journal of Cerebral Blood Flow & Metabolism*, vol. 29, no. 10, pp. 1714–1726, 2009.
- [17] D. Feng, J. A. Nagy, A. M. Dvorak, and H. F. Dvorak, "Different pathways of macromolecule extravasation from hyperpermeable tumor vessels," *Microvascular Research*, vol. 59, no. 1, pp. 24–37, 2000.
- [18] D. Feng, J. A. Nagy, H. F. Dvorak, and A. M. Dvorak, "Ultrastructural studies define soluble macromolecular, particulate, and cellular transendothelial cell pathways in venules, lymphatic vessels, and tumor-associated microvessels in man and animals," *Microscopy Research and Technique*, vol. 57, no. 5, pp. 289–326, 2002.
- [19] H. Hashizume, P. Baluk, S. Morikawa et al., "Openings between defective endothelial cells explain tumor vessel leakiness," *The American Journal of Pathology*, vol. 156, no. 4, pp. 1363–1380, 2000.
- [20] N. A. Vick and D. D. Bigner, "Microvascular abnormalities in virally-induced canine brain tumors. Structural bases for altered blood-brain barrier function," *Journal of the Neurological Sciences*, vol. 17, no. 1, pp. 29–39, 1972.
- [21] R. G. Blasberg and D. R. Groothuis, "Chemotherapy of Brain Tumors - Physiological and Pharmacokinetic Considerations," *Seminars in Oncology*, vol. 13, pp. 70–82, 1986.
- [22] D. R. Groothuis, J. M. Fischer, G. Lapin, N. A. Vick, and D. D. Bigner, "Comparative Permeability of Different Glioma Models to Horseradish-Peroxidase," *Cancer Treat Rep*, vol. 65, pp. 13–18, 1982.
- [23] C. H. Tator, "Retention of tritiated methotrexate in a transplantable mouse glioma," *Cancer Research*, vol. 36, pp. 3058–3066, 1976.
- [24] W. L. Monsky, C. Mouta Carreira, Y. Tsuzuki, T. Gohongi, D. Fukumura, and R. K. Jain, "Role of host microenvironment in angiogenesis and microvascular functions in human breast cancer xenografts: mammary fat pad versus cranial tumors," *Clinical cancer research : an official journal of the American Association for Cancer Research*, vol. 8, pp. 1008–1013, 2002.
- [25] F. Yuan, H. A. Salehi, Y. Boucher, U. S. Vasthare, R. F. Tuma, and R. K. Jain, "Vascular permeability and microcirculation of gliomas and mammary carcinomas transplanted in rat and mouse cranial windows," *Cancer Research*, vol. 54, pp. 4564–4568, 1994.
- [26] A. G. De Boer and P. J. Gaillard, "Strategies to improve drug delivery across the blood-brain barrier," *Clinical Pharmacokinetics*, vol. 46, no. 7, pp. 553–576, 2007.
- [27] A. G. de Boer and P. J. Gaillard, "Drug targeting to the brain," *Annual Review of Pharmacology and Toxicology*, vol. 47, pp. 323–355, 2007.
- [28] F. M. Kievit, O. Veiseh, C. Fang et al., "Chlorotoxin labeled magnetic nanovectors for targeted gene delivery to glioma," *ACS Nano*, vol. 4, no. 8, pp. 4587–4594, 2010.
- [29] S. D. Weitman, K. M. Frazier, and B. A. Kamen, "The folate receptor in central nervous system malignancies of childhood," *Journal of Neuro-Oncology*, vol. 21, no. 2, pp. 107–112, 1994.
- [30] S. P. S. Howarth, T. Y. Tang, R. Trivedi et al., "Utility of USPIO-enhanced MR imaging to identify inflammation and the fibrous cap: A comparison of symptomatic and asymptomatic individuals," *European Journal of Radiology*, vol. 70, no. 3, pp. 555–560, 2009.
- [31] K. Motomura, M. Ishitobi, Y. Komoike et al., "SPIO-enhanced magnetic resonance imaging for the detection of metastases in sentinel nodes localized by computed tomography lymphography in patients with breast cancer," *Annals of Surgical Oncology*, vol. 18, no. 12, pp. 3422–3429, 2011.
- [32] K. Polakova, I. Mocikova, D. Purova et al., "Magnetic resonance cholangiopancreatography (MRCP) using new negative peroral contrast agent based on superparamagnetic iron oxide nanoparticles for extrahepatic biliary duct visualization in liver cirrhosis," *Biomedical Papers*, vol. 160, no. 4, pp. 512–517, 2016.
- [33] M. Sigovan, W. Gasper, H. F. Alley, C. D. Owens, and D. Saloner, "USPIO-enhanced MR angiography of arteriovenous fistulas in patients with renal failure," *Radiology*, vol. 265, no. 2, pp. 584–590, 2012.
- [34] T. Tang, S. P. S. Howarth, S. R. Miller et al., "Assessment of inflammatory burden contralateral to the symptomatic carotid stenosis using high-resolution ultrasmall, superparamagnetic iron oxide-enhanced MRI," *Stroke*, vol. 37, no. 9, pp. 2266–2270, 2006.
- [35] T. Y. Tang, A. J. Patterson, S. R. Miller et al., "Temporal dependence of in vivo USPIO-enhanced MRI signal changes in human carotid atheromatous plaques," *Neuroradiology*, vol. 51, no. 7, pp. 457–465, 2009.
- [36] T. Tourdias, S. Roggerone, M. Filippi et al., "Assessment of disease activity in multiple sclerosis phenotypes with combined gadolinium- and superparamagnetic iron oxide-enhanced MR imaging," *Radiology*, vol. 264, no. 1, pp. 225–233, 2012.
- [37] M. Wagner, S. Wagner, J. Schnorr et al., "Coronary MR angiography using citrate-coated very small superparamagnetic iron oxide particles as blood-pool contrast agent: Initial experience in humans," *Journal of Magnetic Resonance Imaging*, vol. 34, no. 4, pp. 816–823, 2011.

- [38] C. Sun, O. Veiseh, J. Gunn et al., "In vivo MRI detection of gliomas by chlorotoxin-conjugated superparamagnetic nanopores," *Small*, vol. 4, no. 3, pp. 372–379, 2008.
- [39] C. Sun, C. Fang, Z. Stephen et al., "Tumor-targeted drug delivery and MRI contrast enhancement by chlorotoxin-conjugated iron oxide nanoparticles," *Nanomedicine*, vol. 3, no. 4, pp. 495–505, 2008.
- [40] G. Strohbehn, D. Coman, L. Han et al., "Imaging the delivery of brain-penetrating PLGA nanoparticles in the brain using magnetic resonance," *Journal of Neuro-Oncology*, vol. 121, no. 3, pp. 441–449, 2015.
- [41] W. Li, Z. Zhang, A. C. Gordon et al., "SPIO-labeled yttrium microspheres for MR imaging quantification of transcatheter intrahepatic delivery in a rodent model," *Radiology*, vol. 278, no. 2, pp. 405–412, 2016.
- [42] M. Stubbs, P. M. J. McSheehy, J. R. Griffiths, and C. L. Bashford, "Causes and consequences of tumour acidity and implications for treatment," *Molecular Medicine Today*, vol. 6, no. 1, pp. 15–19, 2000.
- [43] R. A. Cardone, V. Casavola, and S. J. Reshkin, "The role of disturbed pH dynamics and the NA⁺/H⁺ exchanger in metastasis," *Nature Reviews Cancer*, vol. 5, no. 10, pp. 786–795, 2005.
- [44] R. A. Gatenby, E. T. Gawlinski, A. F. Gmitro, B. Kaylor, and R. J. Gillies, "Acid-mediated tumor invasion: a multidisciplinary study," *Cancer Research*, vol. 66, no. 10, pp. 5216–5223, 2006.
- [45] A. I. Hashim, X. Zhang, J. W. Wojtkowiak, G. V. Martinez, and R. J. Gillies, "Imaging pH and metastasis," *NMR in Biomedicine*, vol. 24, no. 6, pp. 582–591, 2011.
- [46] R. Martinez-Zaguilan, E. A. Seftor, R. E. Seftor, Y. W. Chu, R. J. Gillies, and M. J. Hendrix, "Acidic pH enhances the invasive behavior of human melanoma cells," *Clinical & Experimental Metastasis*, vol. 14, pp. 176–186, 1996.
- [47] R. A. Gatenby and R. J. Gillies, "Why do cancers have high aerobic glycolysis?" *Nature Reviews Cancer*, vol. 4, no. 11, pp. 891–899, 2004.
- [48] J. Barar and Y. Omid, "Dysregulated pH in tumor microenvironment checkmates cancer therapy," *Bioimpacts*, vol. 3, no. 4, pp. 149–162, 2013.
- [49] J. L. Wike-Hooley, J. Haveman, and H. S. Reinhold, "The relevance of tumour pH to the treatment of malignant disease," *Radiotherapy & Oncology*, vol. 2, no. 4, pp. 343–366, 1984.
- [50] A. De Milito, R. Canese, M. L. Marino et al., "pH-dependent antitumor activity of proton pump inhibitors against human melanoma is mediated by inhibition of tumor acidity," *International Journal of Cancer*, vol. 127, no. 1, pp. 207–219, 2010.
- [51] P. M. J. McSheehy, M. Stubbs, and J. R. Griffiths, "Role of pH in tumor-trapping of the anticancer drug 5-fluorouracil," *Advances in Enzyme Regulation*, vol. 40, pp. 63–80, 2000.
- [52] R. J. Gillies, N. Raghunand, M. L. Garcia-Martin, and R. A. Gatenby, "pH imaging. A review of pH measurement methods and applications in cancers," *IEEE engineering in medicine and biology magazine : the quarterly magazine of the Engineering in Medicine & Biology Society*, vol. 23, pp. 57–64, 2004.
- [53] K. M. Ward, A. H. Aletras, and R. S. Balaban, "A new class of contrast agents for MRI based on proton chemical exchange dependent saturation transfer (CEST)," *Journal of Magnetic Resonance*, vol. 143, no. 1, pp. 79–87, 2000.
- [54] M. L. Garcia-Martin, G. Herigault, C. Remy et al., "Mapping extracellular pH in rat brain gliomas in vivo by 1H magnetic resonance spectroscopic imaging: comparison with maps of metabolites," *Cancer Research*, vol. 61, pp. 6524–6531, 2001.
- [55] R. J. Gillies, Z. Liu, and Z. Bhujwala, "31P-MRS measurements of extracellular pH of tumors using 3-aminopropylphosphonate," *American Journal of Physiology-Cell Physiology*, vol. 267, pp. C195–C203, 1994.
- [56] Z. Zhang, B. Hancock, S. Leen et al., "Compatibility of superparamagnetic iron oxide nanoparticle labeling for 1H MRI cell tracking with 31P MRS for bioenergetic measurements," *NMR in Biomedicine*, vol. 23, no. 10, pp. 1166–1172, 2010.
- [57] D. Coman, Y. Huang, J. U. Rao et al., "Imaging the intratumoral-peritumoral extracellular pH gradient of gliomas," *NMR in Biomedicine*, vol. 29, no. 3, pp. 309–319, 2016.
- [58] Y. Huang, D. Coman, P. Herman, J. U. Rao, S. Maritim, and F. Hyder, "Towards longitudinal mapping of extracellular pH in gliomas," *NMR in Biomedicine*, vol. 29, no. 10, pp. 1364–1372, 2016.
- [59] D. Coman, H. K. Trubel, and F. Hyder, "Brain temperature by Biosensor Imaging of Redundant Deviation in Shifts (BIRDS): Comparison between TmDOTP5- and TmDOTMA-," *NMR in Biomedicine*, vol. 23, no. 3, pp. 277–285, 2010.
- [60] D. Coman, H. K. Trubel, R. E. Rycyna, and F. Hyder, "Brain temperature and pH measured by 1H chemical shift imaging of a thulium agent," *NMR in Biomedicine*, vol. 22, no. 2, pp. 229–239, 2009.
- [61] D. Coman, R. A. De Graaf, D. L. Rothman, and F. Hyder, "In vivo three-dimensional molecular imaging with Biosensor Imaging of Redundant Deviation in Shifts (BIRDS) at high spatiotemporal resolution," *NMR in Biomedicine*, vol. 26, no. 11, pp. 1589–1595, 2013.
- [62] S. Maritim, Y. Huang, D. Coman, and F. Hyder, "Characterization of a lanthanide complex encapsulated with MRI contrast agents into liposomes for biosensor imaging of redundant deviation in shifts (BIRDS)," *Journal of Biological Inorganic Chemistry*, vol. 19, no. 8, pp. 1385–1398, 2014.
- [63] G. Liu, R. Y. Hong, L. Guo, Y. G. Li, and H. Z. Li, "Preparation, characterization and MRI application of carboxymethyl dextran coated magnetic nanoparticles," *Applied Surface Science*, vol. 257, no. 15, pp. 6711–6717, 2011.
- [64] D. Coman, G. E. Kiefer, D. L. Rothman, A. D. Sherry, and F. Hyder, "A lanthanide complex with dual biosensing properties: CEST (chemical exchange saturation transfer) and BIRDS (biosensor imaging of redundant deviation in shifts) with europium DOTA-tetraglycinate," *NMR in Biomedicine*, vol. 24, no. 10, pp. 1216–1225, 2011.
- [65] H. K. F. Trübel, P. K. Maciejewski, J. H. Farber, and F. Hyder, "Brain temperature measured by 1H-NMR in conjunction with a lanthanide complex," *Journal of Applied Physiology*, vol. 94, no. 4, pp. 1641–1649, 2003.
- [66] M. W. Brightman, "The Intracerebral Movement of Proteins Injected into Blood and Cerebrospinal Fluid of Mice," *Progress in Brain Research*, vol. 29, no. C, pp. 19–40, 1968.
- [67] A. K. Johnson and P. M. Gross, "Sensory circumventricular organs and brain homeostatic pathways," *The FASEB Journal*, vol. 7, pp. 678–686, 1993.
- [68] O. M. Girard, R. Ramirez, S. McCarty, and R. F. Mattrey, "Toward absolute quantification of iron oxide nanoparticles as well as cell internalized fraction using multiparametric MRI," *Contrast Media & Molecular Imaging*, vol. 7, pp. 411–417, 2012.
- [69] A. Taylor, A. Herrmann, D. Moss et al., "Assessing the efficacy of nano- and micro-sized magnetic particles as contrast agents for MRI cell tracking," *PLoS ONE*, vol. 9, no. 6, Article ID e100259, 2014.

- [70] S. H. Crayton and A. Tsourkas, "PH-titratable superparamagnetic iron oxide for improved nanoparticle accumulation in acidic tumor microenvironments," *ACS Nano*, vol. 5, no. 12, pp. 9592–9601, 2011.
- [71] C. Y. Shu, B. G. Sanganahalli, D. Coman, P. Herman, D. L. Rothman, and F. Hyder, "Quantitative β mapping for calibrated fMRI," *NeuroImage*, vol. 126, pp. 219–228, 2016.
- [72] F. Kallinowski and P. Vaupel, "Ph distributions in spontaneous and isografted rat tumours," *British Journal of Cancer*, vol. 58, no. 3, pp. 314–321, 1988.
- [73] I. F. Tannock and D. Rotin, "Acid pH in tumors and its potential for therapeutic exploitation," *Cancer Research*, vol. 49, pp. 4373–4384, 1989.
- [74] F. Hyder and S. M. Hoque, "Brain tumor diagnostics and therapeutics with superparamagnetic ferrite nanoparticles," *Contrast Media & Molecular Imaging*, Article ID 6387217, In press.
- [75] D. Barbaro, L. Di Bari, V. Gandin et al., "Glucose-coated superparamagnetic iron oxide nanoparticles prepared by metal vapour synthesis are electively internalized in a pancreatic adenocarcinoma cell line expressing GLUT1 transporter," *PLoS ONE*, vol. 10, no. 4, Article ID e0123159, 2015.
- [76] X. H. Shan, P. Wang, F. Xiong et al., "MRI of High-Glucose Metabolism Tumors: a Study in Cells and Mice with 2-DG-Modified Superparamagnetic Iron Oxide Nanoparticles," *Molecular Imaging and Biology*, vol. 18, no. 1, pp. 24–33, 2016.
- [77] J. M. Brown and A. J. Giaccia, "The unique physiology of solid tumors: opportunities (and problems) for cancer therapy," *Cancer Research*, vol. 58, pp. 1408–1416, 1998.
- [78] D. J. Chaplin, P. L. Olive, and R. E. Durand, "Intermittent blood flow in a murine tumor: radiobiological effects," *Cancer Research*, vol. 47, pp. 597–601, 1987.
- [79] T. P. Padera, B. R. Stoll, J. B. Tooredman, D. Capen, E. Di Tomaso, and R. K. Jain, "Cancer cells compress intratumour vessels," *Nature*, vol. 427, article 695, 2004.
- [80] H. Uehara, T. Miyagawa, J. Tjuvajev et al., "Imaging experimental brain tumors with 1-aminocyclopentane carboxylic acid and alpha-aminoisobutyric acid: comparison to fluorodeoxyglucose and diethylenetriaminepentaacetic acid in morphologically defined tumor regions," *Journal of Cerebral Blood Flow & Metabolism*, vol. 17, pp. 1239–1253, 1997.
- [81] S. M. Hoque, Y. Huang, E. Cocco et al., "Improved specific loss power on cancer cells by hyperthermia and MRI contrast of hydrophilic Fe₃O₄ nanoensembles," *Contrast Media & Molecular Imaging*, vol. 11, pp. 514–526, 2016.
- [82] A. Jordan and K. Maier-Hauff, "Magnetic nanoparticles for intracranial thermotherapy," *Journal of Nanoscience and Nanotechnology*, vol. 7, pp. 4604–4606, 2007.
- [83] B. Thiesen and A. Jordan, "Clinical applications of magnetic nanoparticles for hyperthermia," *International Journal of Hyperthermia*, vol. 24, no. 6, pp. 467–474, 2008.
- [84] F. K. H. van Landeghem, K. Maier-Hauff, A. Jordan et al., "Post-mortem studies in glioblastoma patients treated with thermotherapy using magnetic nanoparticles," *Biomaterials*, vol. 30, no. 1, pp. 52–57, 2009.
- [85] K. Maier-Hauff, R. Rothe, and R. Scholz, "Intracranial thermotherapy using magnetic nanoparticles combined with external beam radiotherapy: results of a feasibility study on patients with glioblastoma multiforme," *Journal of Neuro-Oncology*, vol. 81, no. 1, pp. 53–60, 2007.
- [86] J. W. M. Bulte and D. L. Kraitchman, "Monitoring cell therapy using iron oxide MR contrast agents," *Current Pharmaceutical Biotechnology*, vol. 5, no. 6, pp. 567–584, 2004.
- [87] H. E. Daldrup-Link, R. Meier, M. Rudelius et al., "In vivo tracking of genetically engineered, anti-HER2/neu directed natural killer cells to HER2/neu positive mammary tumors with magnetic resonance imaging," *European Radiology*, vol. 15, no. 1, pp. 4–13, 2005.
- [88] H. E. Daldrup-Link, M. Rudelius, G. Piontek et al., "Migration of iron oxide-labeled human hematopoietic progenitor cells in a mouse model: In vivo monitoring with 1.5-T ME imaging equipment," *Radiology*, vol. 234, no. 1, pp. 197–205, 2005.
- [89] L. Kostura, D. L. Kraitchman, A. M. Mackay, M. F. Pittenger, and J. M. W. Bulte, "Feridex labeling of mesenchymal stem cells inhibits chondrogenesis but not adipogenesis or osteogenesis," *NMR in Biomedicine*, vol. 17, no. 7, pp. 513–517, 2004.
- [90] C. H. Fan, C. Y. Ting, H. J. Lin et al., "SPIO-conjugated, doxorubicin-loaded microbubbles for concurrent MRI and focused-ultrasound enhanced brain-tumor drug delivery," *Biomaterials*, vol. 34, no. 14, pp. 3706–3715, 2013.
- [91] P. Zhang, L. Hu, Q. Yin, L. Feng, and Y. Li, "Transferrin-modified c[RGDfK]-paclitaxel loaded hybrid micelle for sequential blood-brain barrier penetration and glioma targeting therapy," *Molecular Pharmaceutics*, vol. 9, no. 6, pp. 1590–1598, 2012.
- [92] P. Zhang, L. Hu, Q. Yin, Z. Zhang, L. Feng, and Y. Li, "Transferrin-conjugated polyphosphoester hybrid micelle loading paclitaxel for brain-targeting delivery: Synthesis, preparation and in vivo evaluation," *Journal of Controlled Release*, vol. 159, no. 3, pp. 429–434, 2012.
- [93] Z. Zhen, W. Tang, H. Chen et al., "RGD-modified apoferritin nanoparticles for efficient drug delivery to tumors," *ACS Nano*, vol. 7, no. 6, pp. 4830–4837, 2013.
- [94] Z. Zhen, W. Tang, C. Guo et al., "Ferritin nanocages to encapsulate and deliver photosensitizers for efficient photodynamic therapy against cancer," *ACS Nano*, vol. 7, no. 8, pp. 6988–6996, 2013.
- [95] L. Qin, C.-Z. Wang, H.-J. Fan et al., "A dual-targeting liposome conjugated with transferrin and arginine-glycine-aspartic acid peptide for glioma-targeting therapy," *Oncology Letters*, vol. 8, no. 5, pp. 2000–2006, 2014.
- [96] J. U. Rao, U. F. H. Engelke, F. C. G. J. Sweep et al., "Genotype-specific differences in the tumor metabolite profile of pheochromocytoma and paraganglioma using untargeted and targeted metabolomics," *The Journal of Clinical Endocrinology & Metabolism*, vol. 100, no. 2, pp. E214–E222, 2015.
- [97] T. Inai, M. Mancuso, H. Hashizume et al., "Inhibition of vascular endothelial growth factor (VEGF) signaling in cancer causes loss of endothelial fenestrations, regression of tumor vessels, and appearance of basement membrane ghosts," *The American journal of pathology*, vol. 165, pp. 35–52, 2004.
- [98] R. J. Gillies and R. A. Gatenby, "Adaptive landscapes and emergent phenotypes: Why do cancers have high glycolysis?" *Journal of Bioenergetics and Biomembranes*, vol. 39, no. 3, pp. 251–257, 2007.
- [99] R. J. Gillies, I. Robey, and R. A. Gatenby, "Causes and consequences of increased glucose metabolism of cancers," *Journal of Nuclear Medicine*, vol. 49, supplement 2, pp. 24S–42S, 2008.
- [100] I. F. Robey, B. K. Baggett, N. D. Kirkpatrick et al., "Bicarbonate increases tumor pH and inhibits spontaneous metastases," *Cancer Research*, vol. 69, no. 6, pp. 2260–2268, 2009.
- [101] A. Ibrahim-Hashim, D. Abrahams, P. M. Enriquez-Navas, K. Luddy, R. A. Gatenby, and R. J. Gillies, "Tris-base buffer: a promising new inhibitor for cancer progression and metastasis," *Cancer Medicine*, vol. 6, pp. 1720–1729, 2017.

- [102] J. U. Rao, D. Coman, J. J. Walsh, M. M. Ali, Y. Huang, and F. Hyder, "Temozolomide arrests glioma growth and normalizes intratumoral extracellular pH," *Scientific Reports*, vol. 7, article 7865, 2017.
- [103] K. -. C. Chu, Y. Xu, J. A. Balschi, and C. S. Springer, "Bulk magnetic susceptibility shifts in nmr studies of compartmentalized samples: use of paramagnetic reagents," *Magnetic Resonance in Medicine*, vol. 13, no. 2, pp. 239–262, 1990.
- [104] A. D. Sherry, P. Caravan, and R. E. Lenkinski, "Primer on gadolinium chemistry," *Journal of Magnetic Resonance Imaging*, vol. 30, no. 6, pp. 1240–1248, 2009.
- [105] E. Ledneva, S. Karié, V. Launay-Vacher, N. Janus, and G. Deray, "Renal safety of gadolinium- Based contrast media in patients with chronic renal insufficiency," *Radiology*, vol. 250, no. 3, pp. 618–628, 2009.
- [106] J. Zhou, T. R. Patel, R. W. Sirianni et al., "Highly penetrative, drug-loaded nanocarriers improve treatment of glioblastoma," *Proceedings of the National Academy of Sciences of the United States of America*, vol. 110, no. 29, pp. 11751–11756, 2013.

Review Article

Iron Oxide Nanoradiomaterials: Combining Nanoscale Properties with Radioisotopes for Enhanced Molecular Imaging

Juan Pellico,¹ Jordi Llop,² Irene Fernández-Barahona,¹ Riju Bhavesh,¹
Jesús Ruiz-Cabello,^{3,4} and Fernando Herranz¹

¹Centro Nacional de Investigaciones Cardiovasculares Carlos III (CNIC) and Centro de Investigación Biomédica en Red de Enfermedades Respiratorias (CIBERES), 28029 Madrid, Spain

²Radiochemistry and Nuclear Imaging Group, CIC biomaGUNE, Paseo Miramon 182, 20009 Donostia, Spain

³Departamento Química Física II, Facultad de Farmacia, Universidad Complutense de Madrid, 28040 Madrid, Spain

⁴Centro de Investigación Biomédica en Red de Enfermedades Respiratorias (CIBERES), 28029 Madrid, Spain

Correspondence should be addressed to Fernando Herranz; fherranz@cnic.es

Received 21 July 2017; Accepted 1 October 2017; Published 21 November 2017

Academic Editor: Giancarlo Pascoli

Copyright © 2017 Juan Pellico et al. This is an open access article distributed under the Creative Commons Attribution License, which permits unrestricted use, distribution, and reproduction in any medium, provided the original work is properly cited.

The combination of the size-dependent properties of nanomaterials with radioisotopes is emerging as a novel tool for molecular imaging. There are numerous examples already showing how the controlled synthesis of nanoparticles and the incorporation of a radioisotope in the nanostructure offer new features beyond the simple addition of different components. Among the different nanomaterials, iron oxide-based nanoparticles are the most used in imaging because of their versatility. In this review, we will study the different radioisotopes for biomedical imaging, how to incorporate them within the nanoparticles, and what applications they can be used for. Our focus is directed towards what is new in this field, what the nanoparticles can offer to the field of nuclear imaging, and the radioisotopes hybridized with nanomaterials for use in molecular imaging.

1. Nanoplatform-Based Molecular Imaging

Molecular imaging (MI) is the remote sensing and quantification of the biochemical processes in a living organism at a cellular and molecular level. The interest in the use of nanomaterials (NM) for MI is explained by several factors. Firstly, due to the available variety in composition and size, it is possible to produce probes for every imaging modality (Figure 1). Secondly, the hybrid molecular imaging experiments are much easier to develop due to the intrinsic multifunctional character of most NM. Thirdly, the tailored synthesis of these materials permits fine-tuning the critical parameters like the pharmacokinetics of the probe or the ligand payload. This justifies why most of the NM are used in MI experiments. Examples include, but are not limited to, quantum dots [1, 2], gold nanoparticles [3, 4], upconverting nanophosphors [5, 6], liposomes [7, 8], dendrimers [9, 10], carbon nanotubes [11, 12], silica nanoparticles [13, 14], and perfluorocarbon nanoparticles [15, 16].

The combination of micro/nanoparticles with radioisotopes has long since been used. For example, it is well known that the combination of albumin aggregates with ^{99m}Tc for lung perfusion studies [17]. However, the newly developed nanoradiomaterials present a key difference, the precise control over the nanomaterial size (Table 1). The current trend is to combine the size-dependent properties of nanomaterials with the radioisotopes, rather than just using a nanoscaffold.

A particularly important kind of NM in molecular imaging, being the focus here, is iron oxide nanoparticles (IONP). There are many reasons that justify the preferential use of these NM in molecular imaging, like the possibility of getting positive or negative signal in magnetic resonance imaging, tunability of size, the ease of functionalizing their surface, and their biocompatibility or new imaging techniques like magnetic particle imaging [18]. Furthermore, IONP are probably the best example of a new approach in MI, as the combination of nanotechnology and radiochemistry. The combination

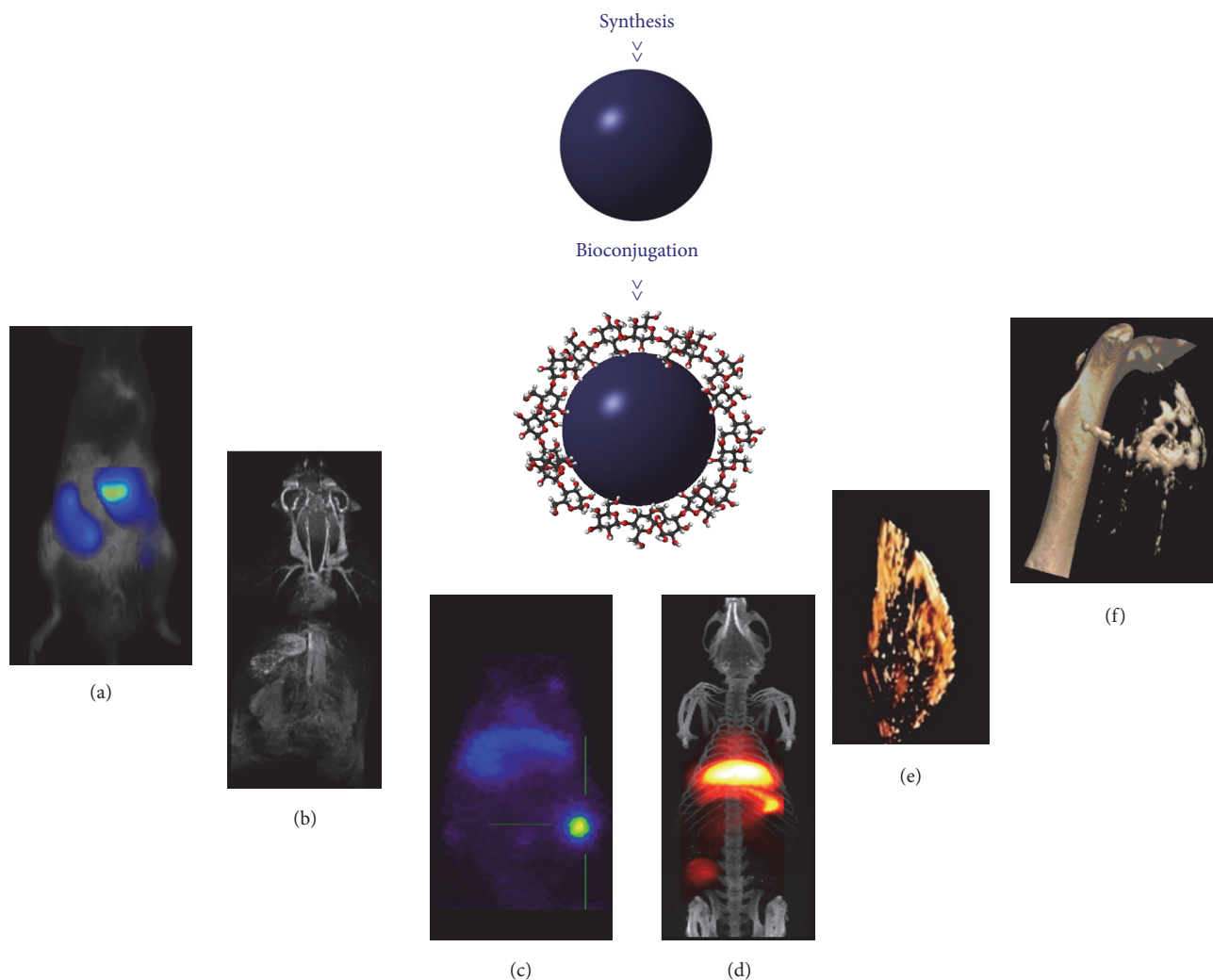


FIGURE 1: The synthesis and bioconjugation of different nanoparticles enable molecular imaging experiments with different modalities: (a) fluorescence, (b) magnetic resonance imaging, (c) positron emission tomography, (d) magnetic particle imaging/computed tomography, adapted from [18] with permission of the American Chemical Society, (e) photoacoustic imaging, and (f) computed tomography. Panel (d) is adapted from [19], with permission of the Royal Society of Chemistry. Panel (e) is adapted from [20] with permission of Elsevier.

of the size-dependent properties of nanomaterials and the exquisite sensitivity of nuclear imaging techniques creates a new paradigm in molecular imaging. These new features extend to most of the typical issues when developing tracers for biomedical imaging like the concept of multifunctionality, biodistribution, pharmacokinetics, and the administered dosage.

In this work we will review the synthesis, characterization, and application of iron oxide-based nanoradiomaterials (NRM), focusing on how this is a synergistic approach, beyond the classical attachment of different, independent parts that characterize many multifunctional nanomaterials.

2. Iron Oxide Nanoparticles for Molecular Imaging

Iron oxide nanoparticles (IONP) are one of the most used nanomaterials for biomedical applications. They show some

remarkable properties explaining their preferential status, such as their size-dependent MRI properties, superparamagnetic behavior, biocompatibility, and chemical stability [24]. They present a magnetic core, typically magnetite (Fe_3O_4), maghemite ($\gamma\text{-Fe}_2\text{O}_3$), or a mixture of both forming a crystalline structure. To avoid aggregation due to surface tension at nanometric scale, magnetic cores are usually accompanied by a coating that reduces surface tension forces, ensuring, hence, the colloidal stability of the sample. The properties of the final formulation depend on the combination of magnetic core and the coating. The selection of the appropriate synthetic method is therefore crucial in obtaining IONP with the desired features [25]. The most commonly used methods are discussed below.

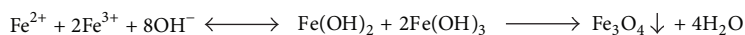
2.1. Synthetic Methods. In the last two decades, a variety of synthetic methods have been developed to produce IONP. We can divide the different approaches into two groups:

TABLE 1: Examples on the combined use of nanomaterials and radioisotopes.

Radioisotope	Nanomaterial	Radiolabeling method	Imaging techniques	Application	Reference
^{64}Cu	Fe_3O_4 -polyaspartic acid	Chelate approach (DOTA)	PET/MRI	Imaging of tumor integrin $\alpha_v\beta_3$ expression	[26]
^{64}Cu	γ - Fe_2O_3 -polyethylene glycol	Chelate approach (DOTA)	PET/MRI	Biodistribution studies	[27]
^{64}Cu	Fe_3O_4 -dopamine-human serum albumin	Chelate approach (DOTA)	PET/MRI	U87MG tumor imaging	[28]
^{64}Cu	Fe_3O_4 -dextran	Chelate approach (DOTA)	PET/MRI	Cardiovascular plaque imaging	[29]
^{64}Cu	Poly(lactic-co-glycolic acid)- Fe_3O_4 -polyethylene glycol	Chelate approach (DOTA)	PET/MRI	Tumor imaging in breast cancer models	[30]
^{64}Cu	Fe_3O_4 -dextran	Chelate approach (DOTA)	PET/MRI	Activated macrophage detection in atherosclerotic plaques	[31]
^{64}Cu	Fe_3O_4 -dextran	Chelate approach (DTCBP)	PET/MRI	Lymph node imaging	[32]
^{64}Cu	$(\text{Fe}_2\text{O}_3)_m(\text{Fe}_3\text{O}_4)_n$ -dextran	Chelate approach (DTPA)	PET/MRI	Activated macrophage detection in atherosclerotic plaques	[33]
^{64}Cu	$(\text{Fe}_2\text{O}_3)_m(\text{Fe}_3\text{O}_4)_n$ -dextran	Chelate approach (DTPA)	PET/MRI	Myeloid cell detection in cardiac allografts	[34]
^{64}Cu	Fe_3O_4 -polyethylene glycol	Chelate approach (NOTA)	PET/MRI	Combined targeted anticancer drug delivery and tumor imaging	[35]
^{64}Cu	Melanin-Fe-polyethylene glycol	Chelate approach (Melanin)	PET/MRI	Imaging of tumor integrin $\alpha_v\beta_3$ expression	[36]
^{64}Cu	Fe_3O_4 - MoS_2 -polyethylene glycol	Chelate-free synthesis	PET/MRI	Combined photothermal therapy and imaging of tumors in breast cancer models	[37]
^{68}Ga	Fe_3O_4 -polyethylene glycol	Chelate-free synthesis	PET/MRI	Lymph node imaging	[38]
^{68}Ga	Fe_3O_4 -polyethylene glycol	Chelate approach (NOTA)	PET/MRI	Tumor imaging of HT-29 xenografts	[39]
^{68}Ga	Fe_3O_4 -polyethylene glycol	Chelate approach (NOTA)	PET/MRI	Lymph node imaging	[40]
^{68}Ga	γ - Fe_2O_3 -poly(lactic-co-glycolic acid)-b-polyethylene glycol	Chelate approach (NODA)	PET/MRI	Biodistribution studies	[41]

TABLE I: Continued.

Radioisotope	Nanomaterial	Radiolabeling method	Imaging techniques	Application	Reference
^{68}Ga	Fe_3O_4 -polyethylene glycol	Chelate approach (DOTA)	PET/MRI	PSMA-positive tumor imaging	[42]
^{68}Ga	γ - Fe_2O_3 -dextran	Core-doping approach	PET/MRI	Imaging of tumor integrin $\alpha_v\beta_3$ expression	[23]
^{18}F	$(\text{Fe}_2\text{O}_3)_m(\text{Fe}_3\text{O}_4)_n$ -dextran	Click chemistry (copper-catalyzed azide-alkyne cycloaddition)	PET/MRI	Biodistribution studies	[43]
^{18}F	Fe_3O_4 -oleyamine branched polyacrylic acid	Chelate approach (NOTA)	PET/MRI	Biodistribution studies	[44]
^{18}F	$(\text{Fe}_2\text{O}_3)_m(\text{Fe}_3\text{O}_4)_n$ -dextran	Click chemistry (copper-catalyzed azide-alkyne cycloaddition)	PET/MRI	Macrophage detection in aortic aneurysms	[45]
^{124}I	Fe_3O_4 -polyethylene glycol	Surface labeling	PET/MRI	Lymph node imaging	[46]
^{124}I	MnFe_2O_4 -serum albumin	Surface labeling	PET/MRI	Lymph node imaging	[47]
^{11}C	Fe_3O_4 -COOH	Surface labeling	PET/MRI	Biodistribution studies	[48]
^{89}Zr	Fe_3O_4 -dextran	Chelate approach (DFO)	PET/MRI	Lymph node imaging	[49]
^{69}Ge	Fe_3O_4 -polyethylene glycol	Core-doping approach	SPECT/MRI	Lymph node imaging	[50]
^{99m}Tc	Fe_3O_4 -dextran	Chelate approach (DPA)	SPECT/MRI	Biodistribution studies	[22]
^{99m}Tc	Fe_3O_4 -dopamine-lactobionic acid	Chelate approach (DTPA)	SPECT/MRI	Liver imaging	[51]
^{99m}Tc	Fe_3O_4 -polyethylene glycol	Chelate approach (pertechnetate)	SPECT/MRI	Lymph node imaging	[52]
^{125}I	Fe_3O_4 -dextran	Chelate approach (CMD)	SPECT/MRI	Tumor imaging of breast cancer models	[53]



SCHEME 1: The reaction mechanism of the method developed by Massart.

aqueous and nonaqueous methods. Aqueous methods like coprecipitation, hydrothermal synthesis, and sol-gel synthesis produce physiologically stable IONP in a single step. On the other hand, nonaqueous methods produce stable IONP in nonpolar solvents, with better crystallinity and size homogeneity, in comparison with aqueous methods.

2.1.1. Coprecipitation Method. Coprecipitation is the most used aqueous method to obtain IONP. The first protocol, developed by Massart in 1981, involved the reaction between $\text{Fe}^{2+}/\text{Fe}^{3+}$ salt solutions at basic pH [54]. Under these conditions, with a molar ratio of 1:2, ferrous and ferric hydroxides are formed, which finally results in the formation of a Fe_3O_4 precipitate (Scheme 1).

Coprecipitation is a straightforward methodology that has been extensively used due to the possibility of producing IONP on a large scale [55]. The main advantage of this method is the production of nanoparticles with colloidal stability in water in a single step. However, the attachment of the surfactant is usually weak, resulting in poor bioconjugation efficiencies.

2.1.2. Thermal Decomposition. Among nonaqueous methods, thermal decomposition of organic precursors is the preferred one. In this method, an organometallic compound together with several surfactants is exposed to high temperatures, leading to decomposition, nucleation, and growth to form the core of the nanoparticle [56, 57]. Organometallic precursors used in this kind of synthesis are $\text{Fe}(\text{cup})_3$, $\text{Fe}(\text{CO})_5$, $\text{Fe}(\text{oleate})_3$, $\text{FeO}(\text{OH})$, and $\text{Fe}(\text{acac})_3$. One of the most successful combinations was proposed by Sun and Zeng in 2002. In this synthesis, $\text{Fe}(\text{acac})_3$ is heated in diphenyl ether in the presence of oleylamine, oleic acid, and a diol as surfactants [58]. This combination results in highly homogenous and monodisperse, magnetite nanoparticles. The size of the core can be controlled, by adjusting the heating temperature, the reaction time, and/or the concentration of the surfactant, to a range of 3–20 nm. The main advantage of thermal decomposition method is the control over size and shape, due to the fine-tuning of kinetic and thermodynamic parameters. The main drawback of this approach is the hydrophobic character of the nanomaterial that requires a further synthetic step to get water stable nanoparticles. On the other hand, this mandatory second step has also been used for the simultaneous incorporation of hydrophilic character and biological activity with interesting results [59].

2.1.3. Microwave Synthesis. Recently, microwave-driven synthesis has been applied for the development of diverse iron oxide formulations [60–62]. This method offers two key advantages, homogeneous heating and a significantly higher speed of reaction, considerably important for our topic here. In the traditional heat transfer equipment such as heating

jackets, oil baths, or sand baths, the sample temperature increases as a consequence of heat exchange through an external source. The process is often slow and the temperature gradients occur within the sample, which implicates local overheating spots. The dielectric heating characteristic of this microwave, on the other hand, prevents temperature gradients and therefore produces highly homogeneous NPs. Furthermore, the use of a microwave oven reduces user dependency while increasing the reproducibility. The usefulness of this approach for biomedical applications has already been proved [60–62].

2.2. Iron Oxide for Magnetic Resonance Imaging. Magnetic resonance imaging (MRI) is based on the physical principles of nuclear magnetic resonance (NMR). Briefly, it consists in measuring the evolution of the net magnetic vector generated after placing the sample (the patient) in a large magnetic field. After perturbation of this vector with a radiofrequency pulse, the magnetic vector goes back to the equilibrium state, that is, aligned with the external magnetic field. The recovery of the longitudinal magnetization and the loss of the transversal one are governed by two values, T_1 for the longitudinal and T_2 for the transversal. Contrast agents for MRI reduce both relaxation times; the change of T_1 or T_2 as a function of the concentration of the contrast agent, r_1 or r_2 , is what determines the classification of the compound as T_1 or T_2 contrast agent. Large r_1 values brighten the tissue, a “positive” contrast, while very large r_2 values darken the tissue, a “negative” contrast (Figure 2(a)).

IONP are extensively used in the field of biomedicine, as biosensors, in stem cell tracking, magnetic hyperthermia and drug delivery [63–66]. In terms of imaging IONP are well known as contrast agents for magnetic resonance imaging (MRI). IONP are very efficient T_2 contrast agents, due to their superparamagnetic behavior, showing very large r_2 values [67], therefore darkening the tissue surrounding the nanoparticles. However, the diagnosis for many pathologies is complicated by the use of negative contrast agents due to endogenous hypointense signals caused, for instance, by bleeding, metal deposits, or calcifications. In these cases, organs appear completely black, making IONP indistinguishable from endogenous signal. These reasons have, hence, motivated a research interest in finding the methods to obtain IONP for positive contrast agents. We, amongst others, have demonstrated how the use of IONP showing large r_1 values and r_2/r_1 ratios smaller than 3 can be used for T1-MR targeted image [68, 69]. The strategy to develop IONP for T_1 contrast lies in the reduction of the core size down to 2–3 nm. In these conditions, nanoparticles show magnetic behavior much similar to a paramagnetic than to a superparamagnetic compound (Figure 2(b)). Most recently, we have studied the possibility of changing from T_2 to T_1 contrast, by modifying just the thickness of the coating. IONP modified this way show completely different performance *in vivo*, with long

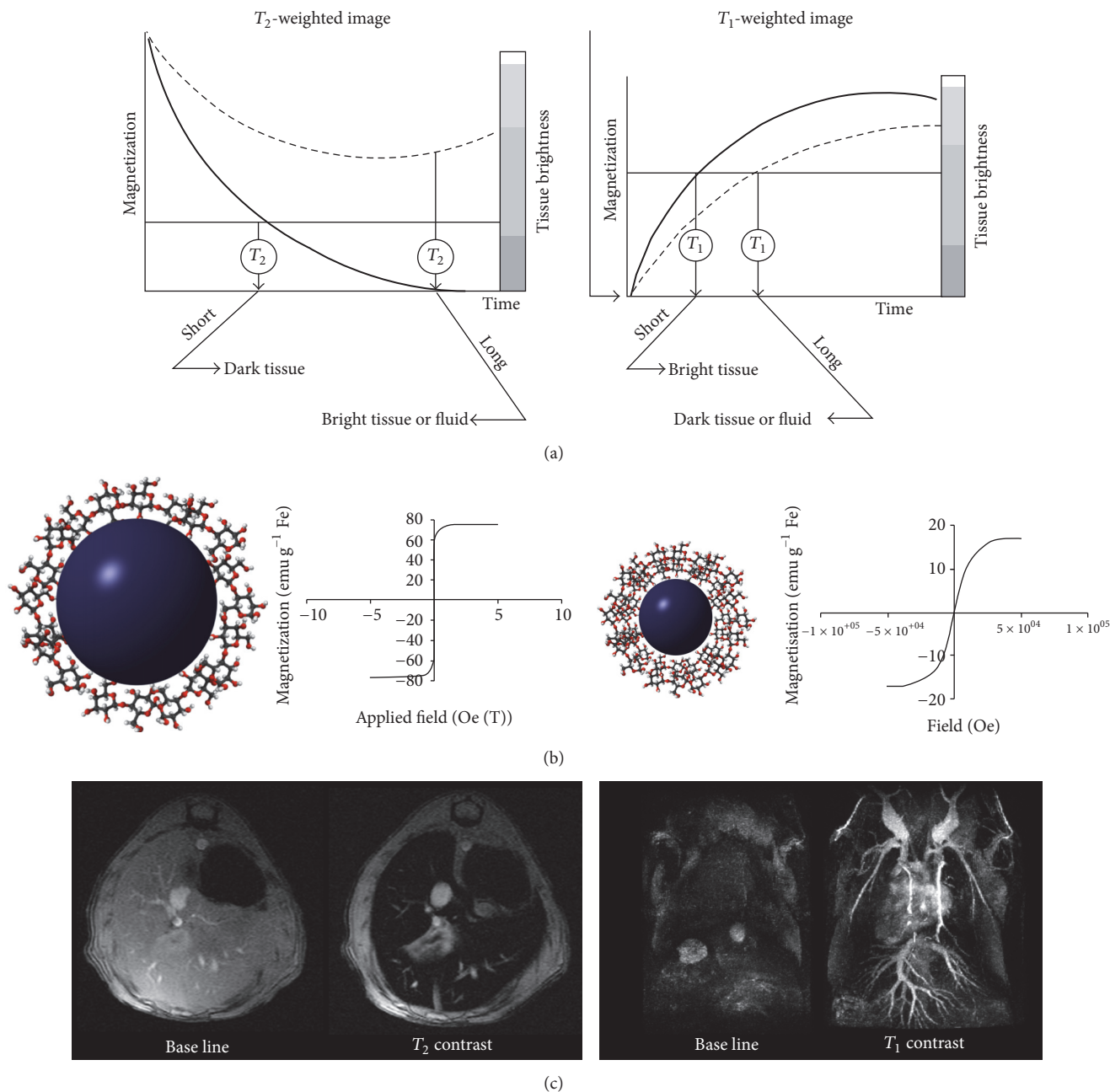


FIGURE 2: (a) Transversal and longitudinal relaxation times evolution in the presence or absence of contrast agents. (b) Change in the magnetic behavior of iron oxide nanoparticles with the core size, from superparamagnetic (left) to paramagnetic (right). (c) T_2 -weighted MRI of the liver using iron oxide nanoparticles with thick organic coating (left), T_1 -weighted MR angiography using iron oxide nanoparticles with thin organic coating (right).

circulating times and positive contrast, when the organic coating is thin (about 4 nm), and short circulating times and negative contrast, when the coating layer is thick (about 17 nm, Figure 2(c)), while core size is the same for both (about 4 nm) [70].

2.3. Why Still Far from a Clinical Routine Yet? IONP have long been used in clinic as T_2 contrast agents. Due to their excretion route, mainly by liver and spleen, these contrast agents are used in the clinic to visualize pathologies

in these regions [71–73]. For instance, IONP have been used for diagnosis of hepatocellular carcinoma, colorectal hepatic metastases, pancreatic islet inflammation, and splenic lymphoma [74–77]. However, IONP contrast agents are still far from clinical routine. A variety of iron oxide-based commercial products existed until a few years ago: ferumoxytol (Feraheme®), ferumoxides (Endorem®, Feridex®), ferucarbotran (Resovist®), ferumoxtran-10 (Combidex®, Sinerem®), feruglose (Clariscan®), and ferumoxsil (Lumirem®). The production of some agents such as Sinerem, Feridex, and

Clariscan has been discontinued for different reasons, mainly due to regulatory and marketing issues. Currently the only IONP approved for clinical use, Ferumoxytol (Feraheme), was in fact designed as iron supplement for patients with anemia and kidney chronic diseases [78]. After many years of research on the development of IONP, we have a biocompatible, multifunctional nanomaterial with quite a strong signal in T_2 -MRI which, however, has not yet found its place in medical imaging within the clinical spectra. Several reasons can be argued to explain this situation, like the hepatic elimination of the particles that produce large accumulations of Fe in the liver, which is a problem especially if repeated doses were necessary [79]. However, in our opinion, the main reason is precisely the claim that its eminent property is the very large negative contrast in MRI. Many times and for most diseases the identification of negative contrast in the image is not straightforward. Anyone who has worked with this kind of material in molecular imaging would agree that being able to differentiate between endogenous hypointense signals and the contrast provided by IONP is nothing but difficult. This difficulty in a clinical environment displaces its usage with Gd-based positive contrast probes, even if this will be at the expense of the inherent toxicity of these compounds. This is one of the most important reasons that explain the interest in combining IONP and radioisotopes. The possibility of combining all the interesting properties of IONP with that of the clear signal from nuclear imaging techniques solves the major part of the problem.

3. Radiochemistry for Molecular Imaging

3.1. Nuclear Imaging. Nuclear imaging techniques, which comprise positron emission tomography (PET), single photon emission computerized tomography (SPECT), and planar gamma-camera imaging or 2D-scintigraphy, are *in vivo*, ultrasensitive, and minimally invasive imaging modalities which allow the determination of the spatiotemporal distribution of positron- or gamma-emitter labeled tracers (radiotracers) after administration to a living organism. The principle behind PET and SPECT is relatively intuitive: positron emitters undergo spontaneous radioactive decay by emission of a positron, which ultimately interacts with an electron of a surrounding atom in a process called annihilation. This process results in the emission of a pair of gamma rays with energies of 511 keV each and travelling 180° apart. Gamma emitters undergo spontaneous radioactive decay by (β^- , γ) emission, through electron capture (EC, γ), emission, or isometric transition (IT). When a positron- or gamma-emitter labeled radiotracer is administered to an organism, the high-energy gamma rays escape from the body and are detected by external detectors. All the detected events are finally reconstructed into two-dimensional (2D) or three-dimensional (3D) images, which contain information about the spatiotemporal distribution of the radiotracer within the organism.

Nuclear imaging techniques are extremely sensitive and minimally invasive (the required administration dosage for obtaining an image is limited to a precisely minute quantity of the radiotracer). Hence, repeated studies can be conducted

within the same subject over time. The main drawbacks of these techniques are that they require the use of ionizing radiation and the spatial resolution is usually low (in the range of 0.5–1 mm for small animal scanners and a few mm for clinical scanners). Positron emitters typically used in the medical or biomedical fields have shorter half-lives than single photon emitters. Historically, the most commonly used radionuclides have been fluorine-18, carbon-11, nitrogen-13, and oxygen-15, which can be readily produced in small-sized biomedical cyclotrons. Recently, gallium-68 has gained relevance as it can be easily produced in $^{68}\text{Ge}/^{68}\text{Ga}$ generators, which are currently commercially available from different suppliers. However, all these radionuclides have a major limitation: its short half-life, which ranges from 122 s (oxygen-15) to 109.7 min (fluorine-18). Longer-lived positron emitters include zirconium-89 (^{89}Zr , $T_{1/2} = 78.41$ h), copper-64 (^{64}Cu , $T_{1/2} = 12.7$ h), and iodine-124 (^{124}I , $T_{1/2} = 100.22$ h).

3.2. Isotopes for SPECT and PET

3.2.1. The Need for Radiolabeling. One of the main drawbacks to consolidating the use of nanomaterials in biomedical applications is the difficulty associated with their tracking, after *in vivo* administration to a living organism. Indeed, the determination of the biodistribution, biological fate, or stability of NPs *in vivo* is extremely challenging. One alternative to gain information regarding the *in vivo* behavior of NPs is to incorporate a radioactive atom into the NP, namely, a positron or gamma emitter. Incorporation of a radionuclide enables the execution of *in vivo* imaging studies using nuclear imaging techniques. The major advantages of radionuclide-based NP tracking are the high sensitivity, the quantitative nature of the detection techniques, and the wide range of radioisotopes available, with different physical properties (see below). However, incorporation of the radioactive atom is usually far from trivial, and the first decision to be made is the selection of the radionuclide. An appropriate selection of the radionuclide requires careful consideration of many different factors, including its physicochemical properties.

As a general rule, the positron or gamma emitters are ideally suited to track NPs *in vivo*, because gamma rays have a high penetration capacity and can easily escape from the body and reach the detectors. However, potential attenuation of the radiation within the organism (which can be significant for low energy gamma emitters and large animal species/humans) may have an effect in the quantification process, and appropriate correction tools need to be considered. Another important factor to consider is the time window in which the NPs should be tracked. If the physical half-life of the radioisotope is too short, the biological process will only be partially investigated. On the other hand, if the physical half-life is too long, high radiation doses might be administered into the organism under investigation and the waste disposal will become more difficult. Finally, the radiochemical integrity of the radiolabeled NP is also paramount. The chemical route to incorporate the radiolabel has to be designed so as to minimize potential loss of the label during subsequent use. Both PET and SPECT rely on the detection of the gamma rays, which are originated in the

radioactive atom. If the label (radionuclide) and the NP are not together (due to, e.g., detachment or degradation of the NP), the interpretation of the data will lead to completely wrong conclusions.

With these considerations in mind, the number of positron and gamma emitters that can be principally used for the radiolabeling of NPs is huge. However, in practical terms only a few radionuclides have found real applicability in the field of bionanotechnology. The physical characteristics such as production processes and chemical possibilities for the most relevant positron and gamma emitters in the context of nanomedicine are discussed in the next subsections.

3.2.2. Radiohalogens. Radiohalogens have been used widely for decades due to their well-known chemistry and the wide range of half-lives and emission modes that they offer. Hence, radiohalogens are one of the first options to be considered when approaching the radiolabeling of NPs.

Fluorine-18. Fluorine-18 is an accelerator-produced radionuclide, with a decay mode close to 100% positron emission, and it can be generated in two chemical forms (F^- and $[^{18}F]F_2$) by using the $^{18}O(p,n)^{18}F$ nuclear reaction. The production of $[^{18}F]F^-$ is usually achieved by irradiation of ^{18}O -enriched water (95–98%) with protons in the energy range of 8–18 MeV, to obtain the radioactive anion as an aqueous solution. The production of $[^{18}F]F_2$ is based on the so-called “double-shot method” and consists of two irradiation steps. In the first step, pure $[^{18}O]O_2$ is irradiated with protons to produce ^{18}F which remains adsorbed on the walls of the target chamber. The oxygen is then removed by cryogenic retrieval, the target is refilled with a mixture of Ne/F_2 , and a second irradiation is carried out. During the second irradiation, an isotopic exchange reaction between the ^{18}F adsorbed on the walls of the target and F_2 occurs, yielding $[^{18}F]F_2$.

The main synthetic strategies behind ^{18}F -labeling can be crudely divided into two distinct areas. (i) The first area is direct fluorination, where the ^{18}F isotope is introduced “directly” into the target molecule of interest in one step via nucleophilic or electrophilic fluorination reactions. Nucleophilic $^{18}F^-$ is used to perform aliphatic or aromatic nucleophilic substitution reactions on different leaving groups. This approach is currently used in most of the PET centers worldwide for the daily production of 2-deoxy-2- $[^{18}F]$ fluoro-D-glucose ($[^{18}F]$ FDG or FDG), a radiofluorinated glucose metabolism marker, which has made an unparalleled contribution in the early diagnosis and evaluation of the response to treatment of a variety of tumors. For electrophilic fluorinations, the most commonly used reagent is $[^{18}F]F_2$, which can be used directly or converted into less reactive derivatives, such as acetyl hypofluorite ($CH_3COO[^{18}F]F$), $[^{18}F]$ fluoropyridinium [80], and $[^{18}F]$ fluoro-N-sulfonamides [81], or other ^{18}F -fluorinating N–F reagents such as $[^{18}F]$ selectfluor [82]. (ii) The second area is indirect fluorination, which exploits ^{18}F -labeled prosthetic groups and is usually applied to radiolabeling of biomolecules which might be unstable under the harsh reaction conditions required for direct fluorination. A large

number of ^{18}F -labeled prosthetic groups have been developed and applied to ^{18}F -fluoroalkylation, ^{18}F -fluoroacylation, or ^{18}F -fluoroamidation of primary amino groups or thiol residues or used to conduct Huisgen cycloaddition reactions (see [83] for a recent review on ^{18}F -fluorination chemistry). Indirect labeling has been applied to the preparation of different ^{18}F -labeled NPs [84, 85].

Radioiodine: ^{123}I , ^{124}I , ^{125}I , and ^{131}I . Iodine-123 is widely used in nuclear imaging; it has a relatively long half-life (13.22 hours) and decays by electron capture to ^{123}Te resulting in the emission of gamma rays with a major peak at 159 keV. It is usually produced using the $^{124}Te(p,2n)^{123}I$ nuclear reaction using solid, liquid, or gaseous targets, although solid and gas targets are the most commonly used. Radionuclidic impurities can be formed during the production, that is, ^{124}I via the (p,n) reaction on ^{124}Te or the (p,2n) reaction on ^{125}Te [86]. Therefore, the use of ^{124}Te with high purity is recommended. When solid targets are used, the irradiated material is elemental tellurium or tellurium oxide [86]. After irradiation, the ^{123}I is isolated by distillation and then trapped in a basic solution. Alternatively, the irradiated target can be dissolved in an oxidizing alkaline solution, followed by reduction of the enriched tellurium to the elemental state and iodine to I^- with aluminium powder. Precipitated tellurium metal is removed through filtration, and iodide is purified using a cation exchange resin.

Iodine-124 is a positron emitter with a long half-life (4.17 days) and a complex decay scheme, with many high energy γ -emissions and high energy positron emission ($E_{\beta_{max}} = 2.14$ MeV, 23% abundance) [87]. It can be produced using different nuclear reactions, with the $^{124}Te(p,n)^{124}I$ reaction being currently the most commonly used [86]. For the production, electroplated elemental tellurium or tellurium oxide melted and introduced in the target cavity is used in the solid state. After irradiation, ^{124}I is recovered by dry distillation [88] or by dissolution of the irradiated target in an oxidizing alkaline medium followed by reduction of iodine to the I^- state by aluminium powder, which can be finally purified by cation exchange chromatography.

Iodine-125 has a half-life of 59.49 days and decays by electron capture to an excited state of ^{125}Te , which decays immediately accompanied by emission of gamma rays with a maximum energy of 35.5 keV. Due to the low energy of the emitted gamma rays, attenuation becomes an issue *in vivo* and this radionuclide is mainly used for *in vitro* and *ex vivo* applications. It is produced in nuclear reactors via the $^{124}Xe(n, \gamma)^{125m}Xe$ and $^{124}Xe(n, \gamma)^{125g}Xe$ nuclear reactions. ^{125m}Xe and ^{125g}Xe are unstable and decay to ^{125}I with 57 s and 16.9 h half-lives, respectively. After neutron beam, short-lived radionuclides produced during the irradiation are allowed to decay. During this period, the newly created ^{125g}Xe becomes ^{125}I , which is then collected with aqueous NaOH solution and purified using ion-exchange resins.

Iodine-131 has a half-life of 8.02 days and exhibits 100% decay by electron emission, resulting also in the emission of gamma rays with a maximum of 364.5 keV (81.7%). Due to the simultaneous gamma and β^- emission, this radionuclide

is used in therapeutic applications. It can be produced using two different nuclear reactions, either by neutron irradiation of natural tellurium via the $^{130}\text{Te}(n, \gamma)^{131}\text{Te}$ nuclear reaction (^{131}Te decays to ^{131}I with a half-life of 25 min) or by irradiation of uranium and chemical recovery from the fission products. Currently, all the above-mentioned radioisotopes of iodine can be obtained from commercial suppliers.

Radioiodination has been extensively used for decades for the radiolabeling of a wide range of molecular formats, ranging from small molecules to peptides, antibodies, proteins, and nanoparticles. Such labeling can be achieved using mainly three different strategies: (i) In situ oxidation of I^- using an oxidizing agent such as *N*-chloro tosylamide or chloramine-T [89], followed by aromatic electrophilic substitution in an activated aromatic ring. This method has been widely used for the radiolabeling of peptides, proteins, and antibodies containing tyrosine residues. As the years pass, more convenient and mild oxidizing agents such as 1,3,4,6-tetrachloro-3 α ,6 α -diphenyl glycoluril (Iodogen) have been developed [90]. This reagent is insoluble in water and can be deposited on the walls of the reaction vessel, enabling termination of the reaction by removal of the reaction crude. (ii) Indirect methods: They consist of preparing a pre-labeled, chemically active group which can be attached to the molecule of interest in a second step. The most widely used conjugation reagent is *N*-succinimidyl 3-(4-hydroxyphenyl) propionate (Bolton–Hunter reagent) [91], which readily forms amides with primary amines. (iii) Isotopic exchange: It is conducted under catalytic conditions. This method requires the presence of a iodine atom in the molecule to be labeled and usually leads to low molar activity values [92]. A summary of the most commonly used strategies is schematized in Figure 3.

Aromatic electrophilic substitution [93] and indirect labeling [47, 94] have been used to date for the preparation of different types of labeled NPs using different radioisotopes of iodine. Additionally, direct adsorption of I^- on the surface of certain metallic NPs has also been exploited for imaging purposes [95, 96].

Radiometals

Technetium-99m. Technetium-99m ($^{99\text{m}}\text{Tc}$) accounts for nearly 80% of nuclear medicine imaging procedures in the clinical field. It has a favourable γ -energy (141 keV), a suitable half-life (6.02 h), and well-known coordination chemistry and can easily be obtained as $^{99\text{m}}\text{TcO}_4^-$ in aqueous buffer from commercially available $^{99}\text{Mo}/^{99\text{m}}\text{Tc}$ generators. In such generators, ^{99}Mo ($T_{1/2} = 67$ h) is held as $^{99}\text{MoO}_4^{2-}$ on acidic alumina. The ^{99}Mo decays forming $[^{99\text{m}}\text{Tc}]\text{TcO}_4^-$, which can be eluted on a periodic basis (see Figure 4 for a schematic representation of a standard $^{99}\text{Mo}/^{99\text{m}}\text{Tc}$ generator).

The production of the ^{99}Mo for the preparation of $^{99}\text{Mo}/^{99\text{m}}\text{Tc}$ generators can be achieved via the $^{98}\text{Mo}(n, \gamma)^{99}\text{Mo}$ nuclear reaction (which leads to low molar activity values) or by irradiation of highly enriched uranium (HEU) with neutrons, which produces the nuclear fission of ^{235}U yielding a small fraction of ^{99}Mo , the latter being with high molar

activity. However, numerous other radionuclides on top of ^{99}Mo are produced in this process [97] and the purification is challenging and time consuming [98]. Additionally, a large volume of radioactive waste is generated, and the reactors producing ^{99}Mo , having been in operation for a considerable time, need decommissioning or refurbishment [99]. As a consequence, alternative strategies for the direct production of $^{99\text{m}}\text{Tc}$ via the $^{100}\text{Mo}(p, 2n)^{99\text{m}}\text{Tc}$ nuclear reaction have been and are currently being explored [100].

Most of the synthetic methods used in the preparation of $^{99\text{m}}\text{Tc}$ -labeled radiotracers start from $^{99\text{m}}\text{TcO}_4^-$, a tetrahedral, d^0 ion. In aqueous solution, Tc can exist in any oxidation state from VII to I. Ligands that use simple sigma donation from nitrogen, oxygen, and sulphur lead almost exclusively to Tc(V) complexes, which are almost exclusively square pyramidal when the overall charge on the complex is negative or neutral. When the overall charge is positive, the geometry is usually octahedral. Inclusion of mixed ligand systems involving sigma donors and pi acceptors leads to Tc(I), Tc(II), Tc(III), or Tc(IV) complexes. The radiolabeling using $^{99\text{m}}\text{Tc}$ is based on the formation of complexes, and the synthetic process usually involves TcO_4^- , a reducing agent (i.e., Sn^{2+} , Fe^{2+} , Cu^+), and a ligand. In the presence of the reducing agent, TcO_4^- is reduced in first instance to a metastable species, which is captured by the ligand. If complexation is weak or slow, TcO_2 might be formed. In these cases, intermediate complexes with weak ligands can be formed first and the final complex can be achieved by ligand displacement in a second step. In the context of NPs, the most widely used chelator is hydrazinonicotinamide (HYNIC), a complexing agent that acts as a mono- or bidentate ligand, requires coligands such as tricine or *N,N'*-ethylenediaminediacetic acid (EDDA) to stabilize the radiometal, and has been used to label gold NPs of different nature [101, 102]. Using a completely different approach, superparamagnetic iron oxide nanoparticles (SPIOs) could be labeled using $^{99\text{m}}\text{Tc}$ -prelabeled bisphosphonates [22].

Gallium-68 and Gallium-67. Gallium-68 ($T_{1/2} = 67.7$ min) can be obtained from the parent radionuclide germanium-68 (^{68}Ge , $T_{1/2} = 270.8$ days), which decays via electronic capture to ^{68}Ga , which subsequently decays to the stable isotope ^{68}Zn . Gallium-68 has 89% positron branching and a physical half-life matching the pharmacokinetics of small molecules. This, together with the development of ^{68}Ge - ^{68}Ga generators, which allows daily production of ^{68}Ga in ionic form without the need for a cyclotron, has boosted the use of this radionuclide [103]. Before the development of the first ^{68}Ge - ^{68}Ga generator, ^{68}Ga was extracted (using liquid-liquid extraction) from irradiated targets in which ^{68}Ge was produced via irradiation of natural gallium [104] or gallium/nickel alloys [105]. Due to the unease of this process, the first generators appeared already in the 1960s [106]. In this pioneering work, alumina (Al_2O_3) was used to retain ^{68}Ge , and ^{68}Ga could be eluted from the column using ethylenediaminetetraacetic acid (EDTA) solution. This process has the drawback that the chemical species eluted

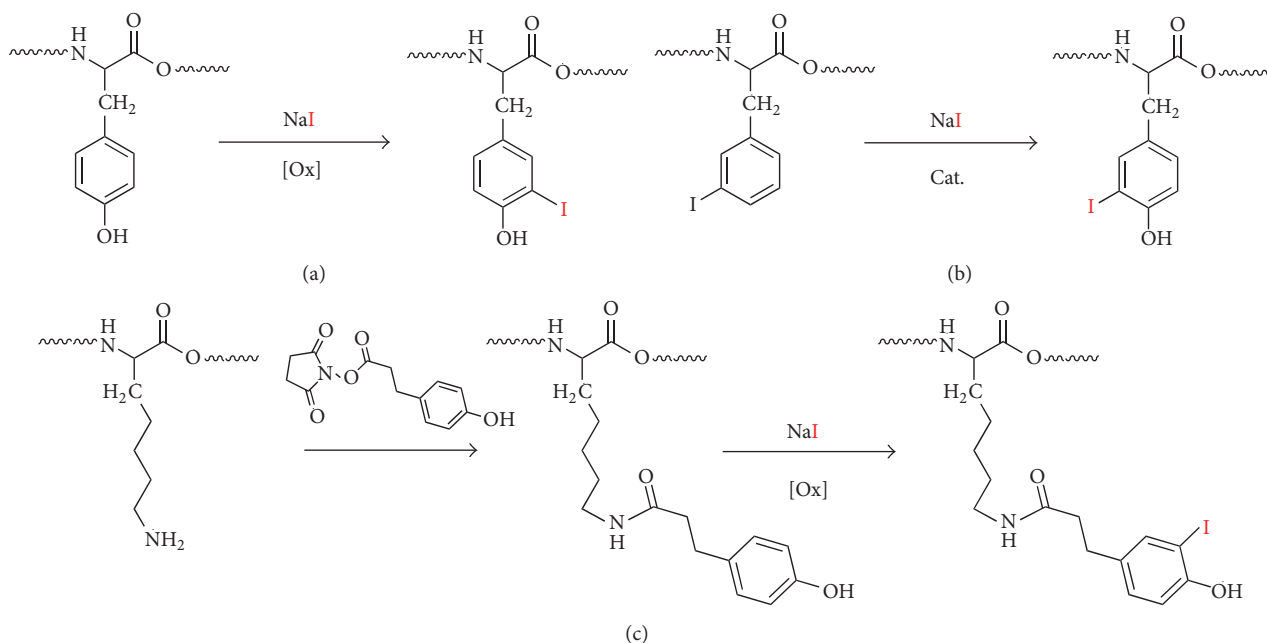


FIGURE 3: Schematic representation of the main strategies used for the radioiodination: (a) electrophilic substitution, (b) isotopic substitution, and (c) indirect labeling. The red atom represents any radioisotope of iodine.

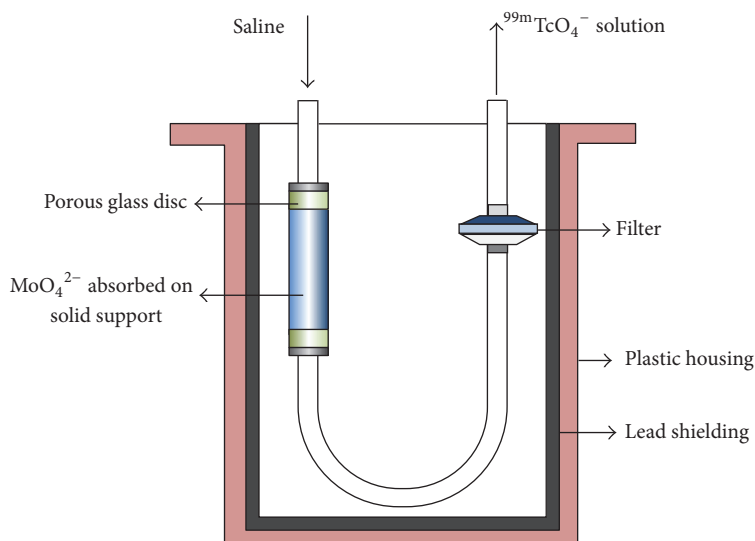


FIGURE 4: General scheme of a $^{99}\text{Mo}/^{99m}\text{Tc}$ generator.

from the generator is inconvenient to approach subsequent labeling processes; as a consequence, a second generation of “ionic” generators has been developed over the years. Currently, several generators are commercially available, and they differ in the solid support material and the solution used to “milk” the ^{68}Ga out of the column. They also show different properties in terms of ^{68}Ge breakthrough and presence of metallic impurities. The presence of ^{68}Ge and metal ions in the eluted gallium usually requires the

implementation of a purification process, which can be achieved by (i) separating the eluate in different fractions and using only those containing the highest concentration of ^{68}Ga ; (ii) using an anion-exchange resin to selectively trap the anionic chloro complexes of $^{68}\text{Ga}^{3+}$ formed under strong acidic conditions (5.5 M HCl) [107], which can be later eluted with small volumes of H_2O ; (iii) selectively retaining ^{68}Ga in a cation exchange cartridge by elution using diluted HCl [108]. Metallic impurities can be removed from the cartridge using

80% acetone/0.15 N HCl solution, and elution of the ^{68}Ga can be finally achieved by elution with 98% acetone/0.05 N HCl [109].

Gallium-68 has a relatively short half-life that does not match the biological half-life of some macromolecules or NPs. Hence, examples of the use of this radionuclide to label NPs are scarce in the literature [110]. In this context, the use of ^{67}Ga might be more convenient. Gallium-67 is a gamma emitter with a long half-life (3.26 d); it decays to stable Zn by electron capture without β emission. It can be produced in particle accelerators using different nuclear reactions: $^{67}\text{Zn}(p,n)^{67}\text{Ga}$, $^{68}\text{Zn}(p,2n)^{67}\text{Ga}$ [111], $^{66}\text{Zn}(d,n)^{67}\text{Ga}$, and $^{67}\text{Zn}(d,2n)^{67}\text{Ga}$ [112, 113]. Gallium can be finally separated from Zn by ion-exchange chromatography or by liquid extraction [114].

The gallium ion occurring in a solution solely in (III) oxidation state is a hard acid metal and has simple aqueous coordination chemistry. Hence, labeling molecules with ^{68}Ga or ^{67}Ga is usually performed via chelation. The most widely used chelating agents are 1,4,7,10-tetraazacyclododecane-tetraacetic acid (DOTA), 1,4,7-triazacyclononane-1,4,7-triacetic acid (NOTA), and 1,4,7-triazacyclononane,1-glutaric acid-4,7-acetic acid (NODAGA), all of which are cyclic azacyclo acetic acid compounds. Gallium chemistry is highly influenced by pH change. Labeling at a pH value above 5 is inhibited by formation of stable $\text{Ga}(\text{OH})_3$, while labeling at very acidic pH values may lead to protonation of the coordinating sites, hence diminishing the coordinative capacity and preventing the formation of the complex. Several examples of radiolabeling of NPs using Gallium-67 and chelators anchored to the NP surface have been described in the literature [115]. Alternative methods based on direct absorption of the Ga^{3+} ion on the surface of metal oxide NPs have also been described (see Section 4.3).

Copper-64. Copper-64 has a relatively long half-life (12.7 h) and can undergo electron capture (ϵ , 43.8%), β^+ emission to ^{64}Ni (17.8%), and β^- emission to ^{64}Zn (38.4%) [116]. The beta-minus branch along with the emission of Auger electrons makes it an attractive candidate for therapy.

Copper-64 can be effectively produced in nuclear reactors and accelerators. By using reactors, ^{64}Cu can be produced via the $^{63}\text{Cu}(n,\gamma)^{64}\text{Cu}$ nuclear reaction by irradiation of stable ^{63}Cu (69.1% natural abundance) with thermal neutrons. This leads to low specific activity values. For the production of high specific activity ^{64}Cu , fast neutrons can be used, for example, via the $^{64}\text{Zn}(n,p)^{64}\text{Cu}$ nuclear reaction [117]. However, the presence of thermal neutrons, which are always present together with fast neutrons, produces significant quantities of other radionuclides, for example, ^{65}Zn ($T_{1/2} = 243.7$ d). Copper-64 can be also produced using cyclotrons via the $^{64}\text{Ni}(p,n)^{64}\text{Cu}$ nuclear reaction. After being first proposed [118], this methodology has been continuously improved. Currently, enriched nickel is first electroplated on a gold disk, which is irradiated with protons. After irradiation, the target material is dissolved in concentrated HCl, and copper and nickel are separated by using an anion-exchange column [119, 120].

Copper-64 exhibits relatively simple chemistry. In solution, it is present in two oxidation states (I and II), and there is a large variety of chelator systems which can form stable complexes with copper [121, 122]. Amongst them, DOTA and NOTA are the most widely used to approach ^{64}Cu -radiolabeling. These chelators and others have been used to incorporate ^{64}Cu in silica-gold core-shell NPs, [123], quantum dots [124], SWCNTs [125], and monocrystalline IONP [33].

Zirconium-89. Zirconium-89 exhibits a decay scheme with 23% positron branching and it has a relatively long half-life (78.4 h). However, the simultaneous emission of a high energy gamma ray with a high branching ratio (99.0%) has negative implications in terms of the effective dose administered into the subject under investigation, limiting its use in certain scenarios. It can be produced by proton irradiation of natural yttrium via the $^{89}\text{Y}(p,n)^{89}\text{Zr}$ nuclear reaction [126], and although radioactive impurities can be formed during irradiation (i.e., $^{89\text{m}}\text{Zr}$, ^{88}Zr , and ^{88}Y), high radionuclidic purity can be achieved using ~ 15 MeV protons. Separation of ^{89}Zr was first achieved by using different solid phase extraction methods [127]. Nowadays, purification is achieved by using an hydroxamate column [128], because, contrary to yttrium, zirconium is able to form complexes with hydroxamates at high acid concentration [129]. With this method, high radionuclidic and radiochemical purities can be achieved with excellent recovery.

In contrast to other radioisotopes previously described, ^{89}Zr forms poorly stable complexes with diethylenetriaminepentaacetic acid (DTPA) [130] and ethylenediaminetetraacetic acid (EDTA) [131] and does not fit in chelators such as NOTA or DOTA. In practice, only desferrioxamine (DFO) is currently used in the radiolabeling of biomolecules with ^{89}Zr and has been recently applied to the preparation of labeled NPs [132]. However, experimental data suggests that $^{89}\text{Zr}^{4+}$ is released from DFO *in vivo*, and hence the development of chelators forming complexes with improved stability is highly desirable. Recently, 3,4,3-(LI-1,2-HOPO) has been suggested as an alternative to DFO with improved chelating properties [133].

4. Combined Iron Oxide Nanoparticles and Radioisotopes

4.1. What Nanoparticles Change in Nuclear Imaging? There are several benefits for nuclear imaging, when using nanoparticles, with the most prominent two being pharmacokinetics (PK) and multifunctionality (MF). In the first case, changing the PK of a "traditional" radiotracer is not straightforward, with most of the examples relying on the use of polyethylene glycol chains to, for example, increase the hydrophilicity of the compound (but at the cost of numerous time-consuming steps and reduced radiolabeling yield). The concept of incorporating small molecules in nanocarriers, so that the PK is then that of the nanoparticles, is not new, being one of the key aspects in nanoplatform-based drug delivery. The same idea applies here; upon incorporation of the radioisotope

in the NP, the PK is no longer that of the radiotracer, but that of the nanoparticle. Thanks to the nanometric control over the size of the particles and over surface composition the PK can be easily tailored. This allows, for example, obtaining nanoparticles with “à la carte” renal or hepatic excretion. The second aspect, multifunctionality, is an essential aspect of nanoparticles but is seldom found in traditional radiotracers. For example, the synthesis of a nanoradiotracer for PET/MRI/fluorescence and biological activity can be easily done by combining radioisotope core-doped IONP and surface functionalizing with a fluorophore and a peptide [23]. To achieve such complexity with traditional radiotracers would be a tremendous and time-consuming challenge due to the lack of a nanoplatform.

4.2. What Radioisotopes Change in Nanoparticles? Also, here there are several benefits, with sensitivity being the most remarkable one. This applies both to imaging experiments and, as we said before, to the study of nanoparticles' biodistribution. In terms of imaging, the use of nuclear imaging techniques expands, by one or two orders of magnitude, the concentration limit that can be used compared to MRI. Furthermore, when using NP for “negative” contrast in MRI, the identification of the negative signal coming from the nanoparticles is not always straightforward. The incorporation of radioactive signal completely changes this situation. The combined use of PET and MRI helps for much easier localization of the tracer. For the same reasons the study of nanoparticles' biodistribution completely changes upon incorporation of a radioisotope, when it is then possible to quantitatively account for all the injected nanomaterials. These combined advantages explain the large number of already published examples (Table 1). However, a fundamental requisite for this is robust radiolabeling.

4.3. Radiolabeling Approaches. There are two important issues to take into account during the development of dual nanoradiotracers based on iron oxide nanoparticles: which radioisotope to take and where to incorporate it within the nanoparticle. The selection of the radioisotope mainly depends on the required half-life time for further imaging experiments and the imaging equipment available. Regarding the localization of the radioisotope, there are two possibilities: either the radioisotope is tagged on the surface of the nanoparticle or it is incorporated directly within the core of the nanoparticle. Irrespectively of the labeling method employed (*vide infra*), the incorporation of radionuclides into NPs modifies the chemical composition of the NPs. Such modifications can have an effect on the surface of the NPs (e.g., incorporation of a chelate or pre-labeled tag, which can ultimately modify the surface properties and zeta potential of the NPs) or the core (when the radionuclide is incorporated by ion/neutron beam or core doping). Thanks to the high sensitivity of nuclear imaging techniques, the mass amount of the radionuclide is usually extremely low (especially if radioisotopes with high specific activity are used). As a consequence, the modifications produced on the NPs are expected to be negligible on a macroscopic scale. In any case, it is convenient to investigate the effect of the labeling

process on the physicochemical and biological properties of the labeled particles.

Some of the reported methods for both the approaches, surface labeling and core doping, are listed below.

(i) Radiolabeling of Nanoparticles on the Surface. To produce dual iron oxide nanoradiotracers by surface labeling strategies, two approaches can be followed. One of the most used is the chelate approach in which the nanoparticle is functionalized with a ligand able to complex with the radioisotope (Figure 5(a)). A relatively new approach, chelate-free strategy, comprises the addition of the radioisotope to the surface of the nanoparticles without a chelate ligand (Figure 5(b)). In the latter case, the surface must show some affinity towards the radioisotope enabling, hence, the purification and *in vivo* use.

(i.i) Chelate Approach. This is a classical strategy where well-known ligands are added to the surface of the IONP to form a complex with the radioisotope.

The development of these probes involves at least three steps: synthesis of IONP, functionalization with the chelate ligand, and finally incorporation of the radioisotope. To select the ligand several features must be considered. First, the ligand should be attached to the surface of the nanoparticles in order to avoid *in vivo* desorption, preferably by covalent bonding. Moreover, the attachment of the ligand should not modify the colloidal properties of the nanoparticles. Finally, the selected ligand must produce a stable coordination complex with the required radioisotope. The stable coordination complex between the radioisotope and the ligand is the key and most problematic point in this method. Once the formulation is intravenously injected, many of the cations present in the bloodstream, like Ca^{2+} , Mg^{2+} , and Zn^{2+} , can trigger a transmetallation reaction, displacing the radioisotope from the coordination complex. If this occurs, the signal recovered in the nuclear imaging equipment comes from the free radioisotope and not from the IONP nanoradiotracer, which may cause a problem in the interpretation of the imaging results.

Among the many ligands studied, a family of cyclic compounds, based on heterocyclic N-dodecane or nonane moieties, has received special attention in the functionalization of the nanoparticles. These ligands, also known as DOTA or NOTA, present tetra or triacetic acids that form a very stable coordination complex with different radioisotopes such as ^{64}Cu or ^{68}Ga . Macrocyclic ligands are preferred because they present slower dissociation rates than their linear analogous [134]. Examples with this approach have been described for SPECT/MRI or PET/MRI [135, 136]. Concerning SPECT/MRI, $^{99\text{m}}\text{Tc}$ is the most used radioisotope. Successful radiolabeling is carried out using chelates such as diethylene triamine pentaacetic acid (DTPA) and NOTA. For instance, Madru et al. have describe the synthesis of IONP radiolabeled with $^{99\text{m}}\text{Tc}$ for the detection of lymph nodes obtaining a 99% of radiolabeling yield [52]. Other SPECT radioisotopes are also used with IONP. Some studies have shown efficient methodologies for the radiolabeling of IONP with longer half-life radioisotopes. Misri et al. produced dual

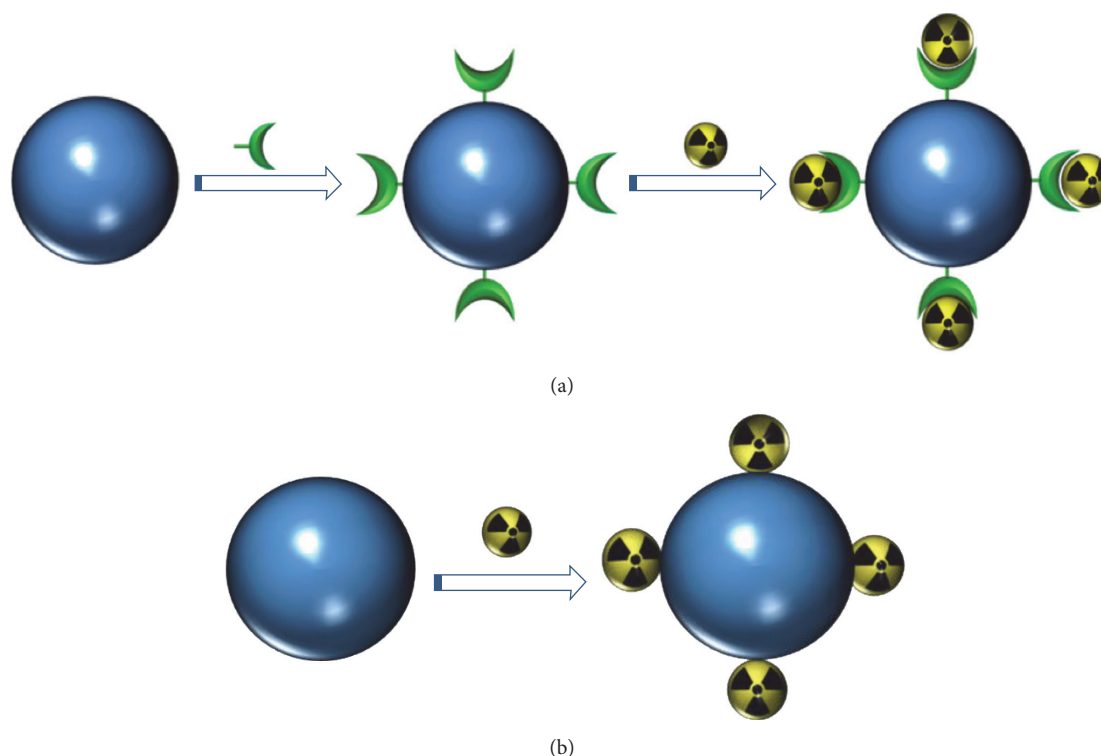


FIGURE 5: Surface radiolabeling strategies: (a) chelate approach, (b) chelate-free approach.

SPECT/MRI probes using DTPA as chelator to incorporate ^{111}In -labeled antibody into the IONP [137]. ^{125}I has also been used to produce a trimodal SPECT/MRI/Optical imaging probe, based on IONP [138]. Most of examples for PET/MRI probes synthesized by chelator approach use ^{64}Cu as positron emitter. DOTA or NOTA is incorporated in the surface of the nanoparticle and then radiolabeled with ^{64}Cu . Yang et al. showed a synthesis of IONP radiolabeled with ^{64}Cu by coordination with NOTA chelate. They incorporated cRGD into targeted integrins in tumor model and conjugated doxorubicin for drug delivery and treatment of the tumor [35]. Another example uses a DOTA amine derivate chelator to avoid cross-linking side reactions, increasing, hence, the stability of the nanoparticles and radiolabeling yield [139]. Although ^{64}Cu is the main radioisotope to produce PET/MRI nanoradiotracers, formulations with ^{68}Ga have been already prepared by chelate approach. Kim et al. produced an IONP functionalized with oleanolic acid for tumor targeting and conjugated with NOTA chelate for the radiolabeling with ^{68}Ga [39].

Chelate approach is a straightforward synthetic protocol and allows multifunctionalization of the IONP before the radiolabeling, being probably the major advantage of the method. Nevertheless, it is a time-consuming methodology as it requires a multiple-step protocol. This disadvantage has promoted the research on methods to incorporate the radioisotope directly in the surface of the nanoparticle without a chelate ligand.

(i.ii) *Chelate-Free Synthesis.* Chelate-free approach takes advantage of the affinity of some elements towards iron oxide

to incorporate the radioisotope directly on the surface of the nanoparticle. It is a relatively new methodology and only a few examples have been reported. For instance, it is known that arsenic presents high affinity towards magnetite [140]. Chen et al. exploited this affinity to incorporate radioactive arsenic into magnetite nanoparticles to produce PET/MRI nanoparticles by chelate-free synthesis [141]. In another example, ^{69}Ge is adsorbed on the surface of IONP. This property is frequently used to produce $^{68}\text{Ge}/^{68}\text{Ga}$ generators and it has been used for the radiolabeling of IONP with ^{69}Ge on the surface of the nanoparticle [50, 142].

In this approach, the main advantage is that in just one step the radioisotope is incorporated in the nanoparticles. However, there are some inconveniences to be considered. For example, reported examples use radioisotopes that arguably show reduced utility *in vivo*, compared to the radioisotopes employed in other methods. In addition, *in vivo* desorption of the radioisotope from the nanoparticle can occur decreasing signal-to-noise ratio in the imaging experiments and causing toxicity problems in case of arsenic. Recently, Nguyen Pham et al. described the synthesis of chelator-free IONP radiolabeled with PET or SPECT emitters providing available probes for SPECT/PET-MRI [143]. Other examples applied direct radiolabeling of IONP coated with functionalized polyethylene glycol with ^{68}Ga resulting in high radiolabeling yields (95%) and good serum stability [144, 145].

(ii) *Radiolabeling of Nanoparticles by Core Doping.* In this method the synthesis of the nanoparticle and the incorporation of the radioisotope are performed simultaneously

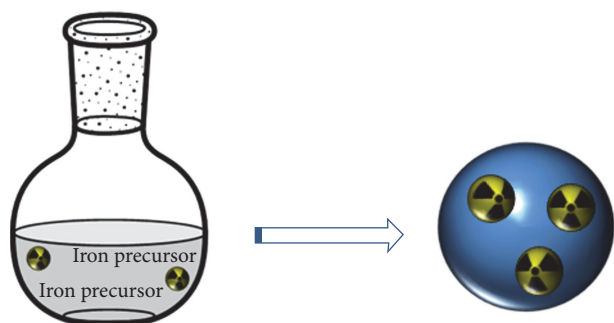


FIGURE 6: One-step core-doping synthesis of nanoradiomaterials.

(Figure 6). Carefully choosing the radioisotopes and synthesis condition permits the incorporation of the isotope within the crystal structure of the iron oxide and not just a simple adsorption or entrapment upon formation of the nanoparticle [23].

Core-doped nanoparticles prevent *in vivo* desorption of the radioisotope from the surface of the nanoparticle and transmetallation reactions, providing excellent radiochemical properties to the nanoradiotracer.

A key point in the core-doping approach is the synthesis technique of the IONP. A fast methodology is required especially if short half-life radioisotope is used for doping. Therefore, reported examples of core-doping approach use microwave-driven synthesis of IONP. As we mentioned before, microwave-driven synthesis allows obtaining IONP in few minutes with highly reproducible results.

Wong et al. reported the first example of core-doped IONP in 2012. They produced IONP coated with dextran and doped with ^{64}Cu in 5 minutes using microwave synthesis [146]. They obtained colloiddally stable nanoparticles with a modest radiolabeling yield. Most recently, we have described a microwave synthesis of IONP doped with a short half-life isotope, ^{68}Ga [23]. We obtained colloiddally stable nanoparticles with large radiolabeling yield (~93%) giving an excellent specific activity of 7.6 GBq/mmol Fe, in 15 min total reaction time and complete purification [23]. Nanoparticles, coated with dextran, showed extremely small core size of 2.5 nm and hydrodynamic size around 20 nm. Magnetic characterization revealed T_1 contrast capabilities of the formulation with large r_1 value and modest r_2 value, showcasing this work as the first example of IONP for PET/(T_1) MRI.

(iii) *Radiolabeling of Nanoparticles by Neutron and Ion Irradiation.* Irradiation with accelerated subatomic particles such as neutrons, protons, or deuterons can be used as a general method for the radiolabeling of nanoparticles. This methodology relies on the *in situ* formation of a radionuclide as a result of a nuclear reaction produced by the interaction of the accelerated particle and one stable isotope present in the NP. This strategy has been used, for example, for the activation of aluminium oxide NPs using proton irradiation [147], the activation of cerium oxide NPs using deuteron irradiation [148], or the activation of gold NPs via the $^{197}\text{Au}(n, \gamma)^{198}\text{Au}$ nuclear reaction [149].

Radiolabeling of NPs by particle irradiation has two main advantages: first, it can be used to activate NPs after their preparation, including industrially produced NPs; second, it can be applied to any NP containing atoms susceptible to nuclear reactions. However, there are two drawbacks that severely limit the applicability of this methodology, requiring careful consideration, and mainly apply to ion irradiation: (i) The activation of one particle is produced by recoil implantation of the radioisotope generated in a different particle. In other words, the radionuclide produced as a consequence of the nuclear reaction travels a few micrometers until its kinetic energy is lost. This means that ion irradiation of NPs can only be carried out in the solid state. When applied to a solution, the radionuclide will have many chances to end up in the solvent. (ii) The nuclear reaction generated by ion irradiation of NPs results in the release of a significant amount of energy, which in turn produces a macroscopic temperature increase limiting the methodology to the activation of NPs that do not contain temperature-sensitive components, for example, organic shells; besides the macroscopic effect, local heating at the nanoscale also requires consideration, because small NPs can be vaporized or promote the formation of aggregates with surrounding particles. Therefore, appropriate cooling during beaming and careful selection of the irradiation conditions are paramount to prevent significant alteration of the physicochemical properties of the NPs. Targets using liquid or gas/liquid cooling have been successfully employed towards the activation of NPs using ion irradiation (Figure 7). The target has to be appropriately designed to ensure effective cooling, especially taking into account the fact that, as mentioned above, NPs in the solid state (powders) need to be irradiated, and the thermal conductivity of powders is usually poor.

In practical terms, the two limitations mentioned above have restricted the application of ion-beam activation of NPs to a few examples in the literature, with all being metal and metal oxide NPs. Due to potential alteration during beam, it is extremely important to investigate potential physicochemical or structural alterations induced on the NPs during beam.

The first example on proton activation of NPs was published by Abbas et al. and described the activation of two types of TiO_2 which were activated using capsules with different thicknesses, and the effects of the irradiation were evaluated [150]. Local heating on the thick capsules led to phase transition in a fraction of the material. Temperature control of nanoparticulate material by using appropriate target design enabled stable radiolabeling of the NPs without alteration in the state of aggregation [151]. The same strategy was used for the activation of ^{18}O -enriched titanium oxide NPs [152]. In this work, the irradiation resulted in the formation of ^{18}F via the $^{18}\text{O}(p, n)^{18}\text{F}$ nuclear reaction, although the simultaneous formation of other radioisotopes by activation of titanium, that is, ^{48}V , ^{47}V , and ^{44g}Sc , was observed by high-resolution gamma spectrometry. The radiolabeling of the NPs did not significantly alter the morphological properties of the NPs, as demonstrated by transmission electron microscopy (TEM) and dynamic light scattering (DLS) measurements. Thanks to the presence of ^{18}F , short-term *in vivo* biodistribution

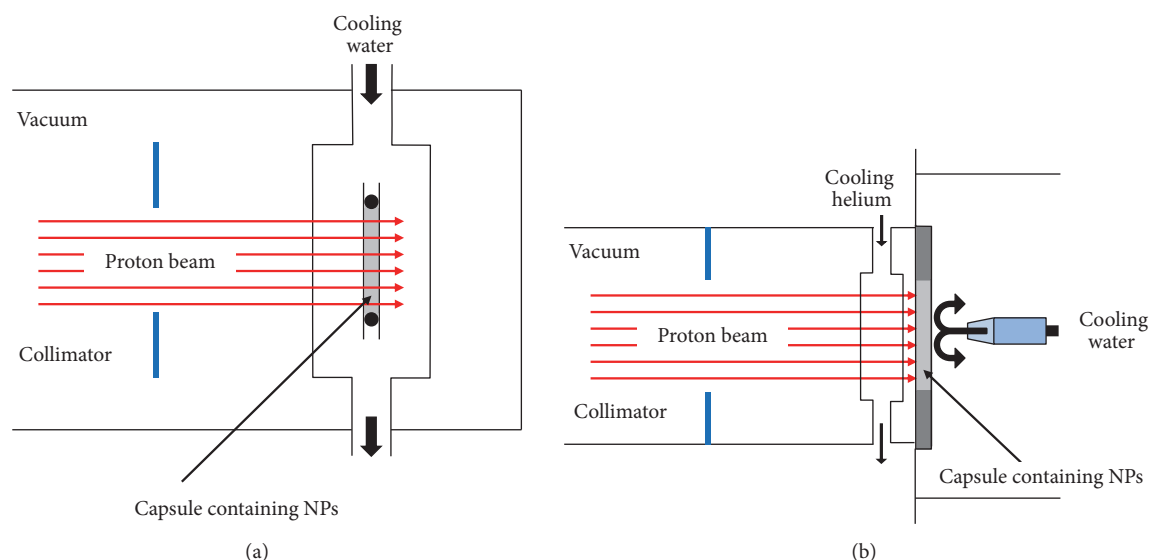


FIGURE 7: Schematic diagram of the target system used for direct ion-beam activation of NPs using water cooling (a) and water-helium cooling (b). Adapted from [21].

studies of the metal oxide NPs in rats could be conducted after intravenous and oral administration using PET. The same group also reported the activation of aluminium oxide NPs by proton irradiation via the $^{16}\text{O}(p,\alpha)^{13}\text{N}$ nuclear reaction [153]. In this work, different-sized NPs were introduced in an aluminium capsule and irradiated with cyclotron-accelerated protons at $5\ \mu\text{A}$, to produce ^{13}N -labeled NPs. Despite the short half-life of ^{13}N (9.97 min), the activation was sufficient to determine the biodistribution pattern after intravenous injection in rodents up to 1 hour. The authors could establish a relationship between the nominal size of the NPs and the organs where accumulation of the NPs took place.

Direct activation of carbon-based NPs by proton irradiation can also be achieved, although relatively high energies ($>29\ \text{MeV}$, which cannot be achieved by most of the biomedical cyclotrons) are required. Activation occurs via the $(p,3p3n)$ reaction leading to the creation of ^7Be . By using protons of energy above $35\ \text{MeV}$, it has been shown that specific activities of some hundreds of kBq/mg can be obtained in carbon black and carbon nanotubes in a reasonable irradiation time [154]. However, the effects of the irradiation on the physicochemical properties of the irradiated material were not investigated.

Proton irradiation can also be employed to the activation of iron oxide NPs, because the most abundant stable isotope of iron (^{56}Fe , natural abundance of 91.75%) can undergo the $^{56}\text{Fe}(p,n)^{56}\text{Co}$ nuclear reaction in the energy range $5\text{--}30\ \text{MeV}$ [155], with ^{56}Co being a positron emitter with a half-life of 77.2 days. This nuclear reaction has been employed for the activation of Fe_3O_4 (magnetite) NPs using accelerated protons with energy in the range $12\text{--}14\ \text{MeV}$ [156]. Although other nuclear reactions may occur during proton irradiation, that is, $^{57}\text{Fe}(p,2n)^{56}\text{Co}$ and $^{58}\text{Fe}(p,3n)^{56}\text{Co}$, their contribution to the overall formation of ^{56}Co can be neglected at the above-mentioned proton energies due to the low reaction cross

sections and the low natural abundances of ^{57}Fe and ^{58}Fe (2.2% and 0.28%, resp.). X-ray diffraction (XRD), dynamic light scattering (DLS), and zeta potential measurements before and after activation demonstrated that no changes took place in the crystalline structure, and no alterations were observed in terms of size and zeta potential.

If the material of the NPs cannot be activated by proton irradiation, other accelerated ions might be used, that is, deuterons. Deuteron irradiation was used to create ^{141}Ce -labeled NPs via the (d,p) reaction from ^{140}Ce [148]. Low beam currents ($2\ \mu\text{A}$) were used to prevent thermal damage of the NPs. DLS and zeta potential measurements confirmed negligible structural and morphological changes in the NPs due to the irradiation procedure.

As mentioned above, irradiation with accelerated ions can pose severe damage to the irradiated particles. As an alternative, neutron irradiation can be used. Neutron activation is mainly performed by exposing the NPs to the intense neutron flux of a nuclear research reactor, resulting generally in (n,γ) or (n,p) nuclear reactions, although the latter presents lower cross section values (and hence is less efficient). The yield for neutron capture by (n,γ) reactions depends on the neutron energy; in general, the reaction cross section rises as the neutron energy is reduced, following a good approximation of $E_n^{-1/2}$ up to energies of about $10^3\ \text{keV}$, but the cross section value at a given energy can vary several orders of magnitude from one atomic species to another. In practical terms, only a few atoms can undergo neutron activation, including among others ^{151}Eu , ^{165}Ho , ^{187}Re , and ^{197}Au , which yield ^{152}Eu , ^{166}Ho , ^{188}Re , and ^{198}Au , respectively. Other atoms like Fe can be also activated, but cross section values are much lower. In contrast to ion irradiation, in neutron activation the neutron capture occurs preferentially at low neutron energies, and it can generally be assumed that the activated nucleus remains very close to its original position. As a consequence,

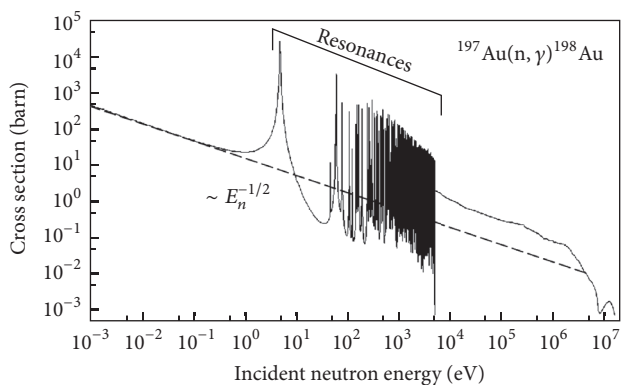


FIGURE 8: Excitation function for the neutron capture reaction $^{197}\text{Au}(n,\gamma)^{198}\text{Au}$. The oscillations of the reaction cross section in the energy range between 5 and 5000 eV are referred to as resonances (data from JEFF 3.1.1 (OECD-NEA 2009)).

irradiation of NPs in solution is feasible with little risk for the radionuclide to end up in the solvent [21], and hence cooling of the irradiated material is more effective than in ion activation, in which powders are usually irradiated.

One of the main limitations of neutron activation is the need to conduct activation in a nuclear research reactor. To mitigate this drawback, alternative methods have been developed, with one of them being the use of accelerators taking advantage of the adiabatic resonance crossing (ARC). This method relies on gradually slowing down fast neutrons emitted from ion-induced nuclear reactions with high neutron yield. If the neutron moderator is properly designed, the energy of the neutrons can be tuned to match the energy range in which target atoms exhibit resonances in their neutron capture (resonances are energy ranges in which the probability for the neutron capture to occur is very high; see Figure 8 for gold). In this way, the small neutron flux (compared to that obtained in a nuclear reactor) can be compensated by making more efficient use of the neutron-energy regime. Experimental setups have been tested at different locations including CERN [157], Louvain-la-Neuve [158], and JRC Ispra [159] with promising results.

There are a few examples in the literature describing neutron activation of NPs. The preparation of ^{166}Ho -labeled holmium acetylacetonate NPs could be achieved by neutron activation using neutron flux of $5 \times 10^{12} \text{ cm}^{-2} \text{ s}^{-1}$ during 60 minutes. In this case, specific activities of 12 MBq/mg could be achieved [160]. Because ^{166}Ho emits beta particles, the activated NPs were suggested as potential radiotherapeutic agents for the treatment of solid cancers. In a different study, ^{198}Au -labeled gold NPs were labeled by neutron activation. In this case, thiol-functionalized gold NPs were activated by neutron irradiation at neutron flux of $10^{14} \text{ cm}^{-2} \text{ s}^{-1}$ at a research reactor. The amount of radioactivity was sufficient to approach subsequent *in vivo* studies using dissection and gamma counting. Importantly, the NPs were not altered by the neutron irradiation, despite the presence of organic functional groups on the surface of the gold core.

If the NPs to be investigated do not contain any atom susceptible to activation neither via neutron nor via ion, there

is one alternative method, which can be assayed; the so-called recoil implantation. It relies on intimately mixing the NPs with a powder containing an atom, which can undergo a nuclear reaction under ion beam and hence act as a radio-labeling source. The high energy of the activated atom results in recoil implantation somewhere else, for example, in one of the NPs. This strategy has been used so far for the preparation of ^7Be -labeled industrially manufactured SiO_2 NPs [161].

5. Applications

IONP have emerged as a very interesting platform into which radionuclides and targeting moieties can be incorporated. This combination expands the field of application of IONP. Thanks to the hybrid nature of these particles, they can be used in PET/MRI and SPECT/MRI experiments [162, 163] or directly in PET/CT when MRI is not needed. In this sense, IONP can be used as a new kind of “chelate ligand” for radioisotopes but with size-dependent properties.

5.1. Biodistribution. IO-based nanoradiotracers have been reportedly tried *in vivo* in preclinical models to ensure biocompatibility and evaluate biodistribution. Devaraj et al. [43] synthesized cross-linked dextran-coated IONP radiolabeled with ^{18}F via *click chemistry* and tried them in mice to determine biodistribution and blood clearance time of the NPs.

Stelter et al. [164] tried *in vivo* ^{68}Ga -DTPA-IONP in rats. PET and MR imaging determined hepatic and splenic accumulation of the NPs. The same NP accumulation trend was reported by Sharma et al. [48], who injected ^{11}C -labeled IONP in healthy mice.

Glaus et al. [27] obtained IONP micelles radiolabeled with ^{64}Cu via DOTA chelating agent and studied their biodistribution *in vivo* by PET and MRI in mice. Probe showed a circulation half-life of 143 min and hepatic and splenic accumulation 24 h after NP injection.

Sun et al. [44] radiolabeled comb-like oleylamine polyacrylic acid (COBP) IONP with ^{18}F using NOTA. *In vivo* PET and MR imaging in mice revealed hepatic and splenic NP uptake and no accumulation in bone.

De Rosales et al. [22] radiolabeled Endorem (liver MRI contrast agent) with $^{99\text{m}}\text{Tc}$ -DPA-alendronate (bisphosphonate SPECT agent), which bound directly the core of the IONP. *In vivo* SPECT and MR imaging revealed hepatic and splenic accumulation, meaning that the biodistribution of this complex is more similar to that of Endorem than to $^{99\text{m}}\text{Tc}$ -DPA-alendronate, which accumulates in bone tissue (Figure 9).

Lee et al. [51] targeted asialoglycoprotein receptor in hepatocytes using lactobionic acid-functionalized $^{99\text{m}}\text{Tc}$ -DTPA-IONP. *In vivo* SPECT in mice revealed hepatic NP accumulation.

5.2. Oncology. The availability of new and enhanced technologies allowing gene and protein expression study triggered immense progress in cancer biology and pharmacology, as well as clinical oncology [165]. Yet the absence of

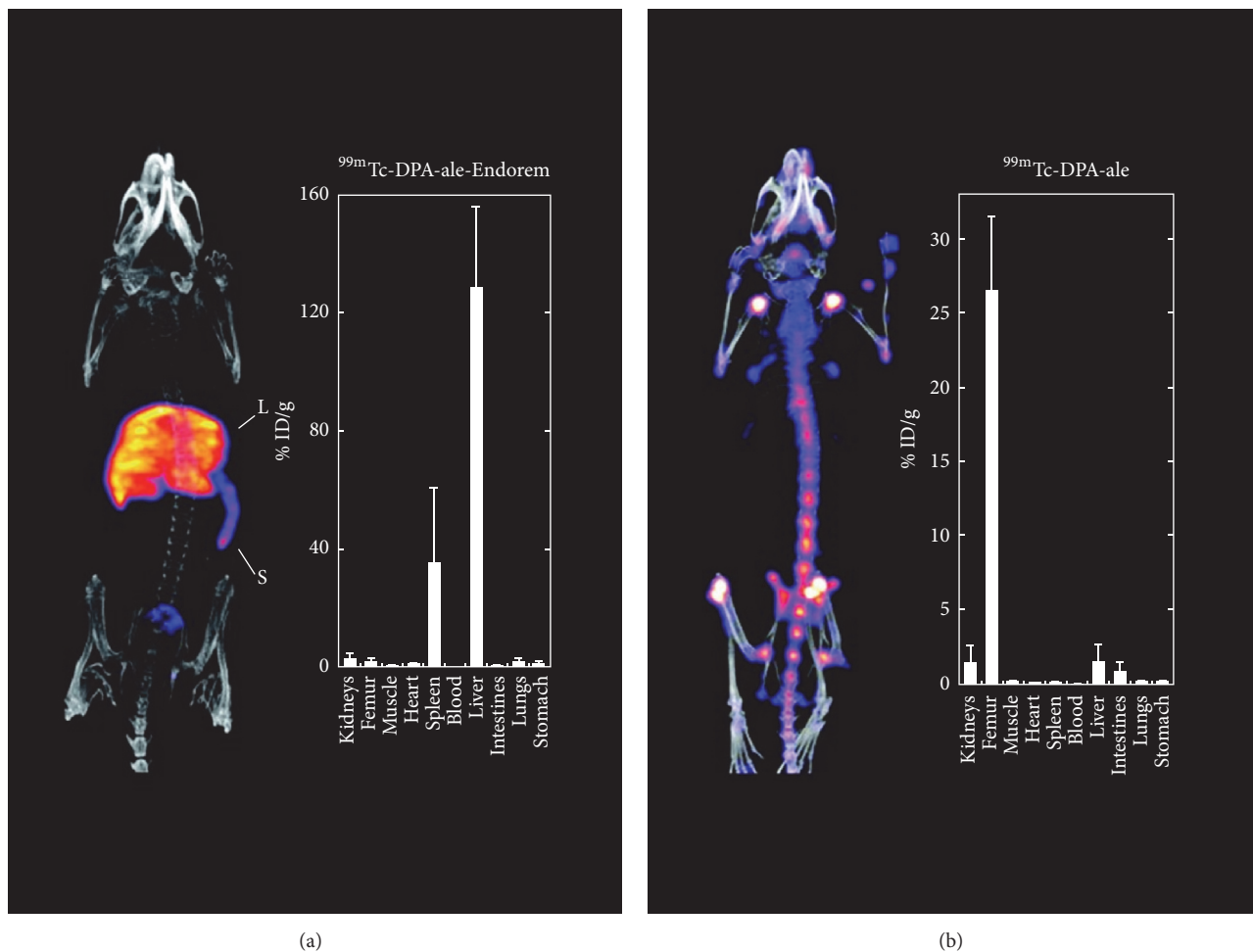


FIGURE 9: *In vivo* SPECT/CT maximum intensity projection (left) and biodistribution studies (right) of (a) $^{99m}\text{Tc-DPA-alendronate-Endorem}$ and (b) $^{99m}\text{Tc-DPA-alendronate}$. Reproduced, with permission, from [22].

technology to study *in vivo* molecular events in depth has motivated the quest for novel approaches [166]. The combination of nanotechnology and radiochemistry, although quite novel, has already provided further enlightenment of cancer molecular mechanisms. It is not surprising that oncology is one of the main fields of research for these multimodal probes.

Aryal et al. [30] took advantage of the long circulating lifetime of their ^{64}Cu -labeled PLGA-coated IONP clusters and the EPR effect in tumors to successfully locate breast cancer cells in mouse xenograft models using PET and T_2 -weighted MRI. Passive tumor accumulation strategy was used in another study carried out by Liu et al. [37] using PEG-coated ^{64}Cu -radiolabeled MoS_2 sheets containing IONP, which allowed tumor visualization and posterior tumor ablation by photothermal therapy in 4T1 tumor-bearing mice.

Lee et al. [26] labeled polyaspartic acid-coated IONP with ^{64}Cu via DOTA chelator and conjugated them to RGD peptide to achieve targeted visualization of tumor integrin $\alpha_v\beta_3$ expression in murine models bearing U87MG tumors, by both PET and MRI. RGD peptide was also chosen by

Yang et al. [35] to direct SPIO nanocarriers, radiolabeled with ^{64}Cu and containing doxorubicin, for tumor-targeted drug delivery and PET/MRI of U87MG-tumor-bearing mice. Deng et al. [53] used RDG-conjugated ^{125}I -labeled IONP to target tumor cells for *in vivo* SPECT and MRI visualization in a breast cancer mouse model. Pellico et al. [23] obtained via microwave-assisted synthesis a chelator-free hybrid nanoradiotracer, ^{68}Ga core-doped dextran-coated IONP, that was posteriorly conjugated to RGD peptide to target angiogenesis in a subcutaneous melanoma murine model. *In vivo* PET and T_1 -weighted MRI experiments confirmed specific tumor accumulation of the $^{68}\text{Ga-C-IONP-RGD}$ probe (Figure 10).

Kim et al. [39] conjugated PEG-coated ^{68}Ga -NOTA-IONP with oleanolic acid to specifically target HT-29 cells in a murine model and visualize tumor *in vivo* by PET and MRI.

To target prostate-specific membrane antigen (PSMA), Moon et al. [42] encapsulated IONP with amphiphiles containing PEG, DOTA, and PSMA-targeting ligand and radiolabeled them with ^{68}Ga . *In vivo* PET and MR imaging experiments in mouse prostate cancer xenograft models revealed specific probe accumulation at tumor site.

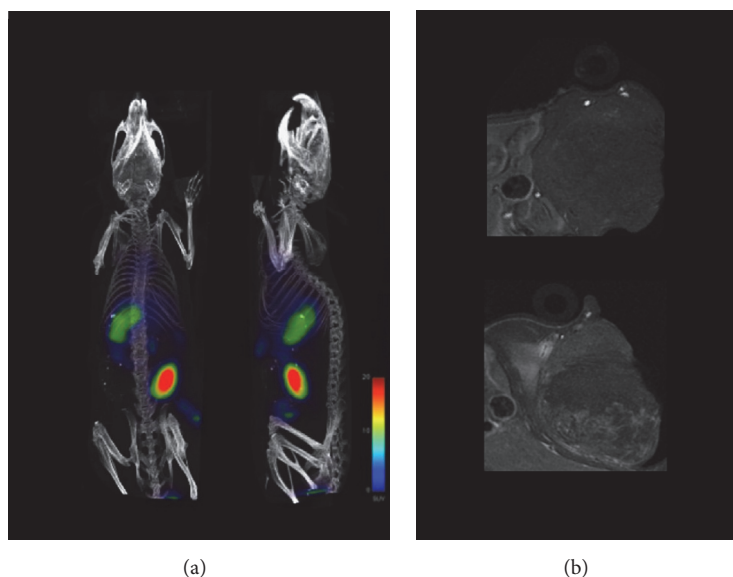


FIGURE 10: (a) PET/CT imaging of subcutaneous melanoma bearing mice 1 hour after injection of ^{68}Ga -C-IONP-RGD. (b) Axial T_1 -weighted MRI of the tumor area in a mouse before the injection of ^{68}Ga -C-IONP-RGD (top) and 24 hours after injection (bottom). Reproduced, with permission, from [23].

Lymph nodes play a key role in cancer cell metastasis; for this reason numerous studies have focused on these structures to design novel hybrid probes for cancer staging. ^{64}Cu -labeled IONP were synthesized by Torres Martin de Rosales et al. [32] to track lymph nodes *in vivo* in murine models. ^{68}Ga -labeled IONP have been used in different studies to track lymph nodes using PET and MRI [38, 40, 145, 167]. Choi et al. [168] coated ^{124}I -labeled IONP with serum albumin for the same purpose. Cross-linked PEG-coated IONP radiolabeled with ^{124}I were selected by Park et al. [46] to track sentinel lymph nodes in murine 4T1 tumor xenograft model. Ferumoxytol was chosen by Thorek et al. [49] to synthesize a PET/MRI dual probe labeled with ^{89}Zr via DFO chelator to track lymphatic drainage in murine diseased models. Cui et al. [169] reported synthesis and *in vivo* evaluation of $\text{Co}_x\text{Fe}_{3-x}\text{O}_4@/\text{NaYF}_4$ core-shell NPs labeled with ^{18}F to track lymph nodes in murine inflammation models. Chakravarty et al. [50] intrinsically labeled PEG-coated IONP with ^{69}Ge to map lymph nodes in healthy mice. Madru et al. [52] used PEG-coated IONP labeled with $^{99\text{m}}\text{Tc}$ and for imaging lymph nodes in rats using SPECT and MRI.

5.3. Cardiovascular Diseases. Cardiovascular diseases are the leading cause of death worldwide, accounting for more than 17 million deaths per year; a figure which is expected to keep rising in the coming years [170]. Most relevant advances in the treatment of these diseases have been focused on early diagnosis, for which molecular imaging is a key element.

Nahrendorf et al. [45] developed a multifunctional probe to detect macrophages in aortic aneurysms in using ^{18}F -labeled cross-linked dextran-coated IONP. *In vivo* imaging

experiments in murine models revealed specific probe accumulation in aneurysmatic aorta.

Ueno et al. [34] synthesized ^{64}Cu -labeled IONP coated with cross-linked dextran to quantify infiltration of myeloid cells in mouse cardiac allografts.

Atherosclerotic plaque vulnerability to rupture is of paramount importance, as is it correlated to the risk of adverse coronary events. Dextran-coated IONP radiolabeled with ^{64}Cu have been used in several studies to assess atherosclerotic plaque vulnerability targeting activated macrophages [29, 31, 33].

6. Conclusions

Nanomaterials in combination with radioisotopes are used more and more in molecular imaging. They show enhanced performance for hybrid imaging. Furthermore, it is possible to design them for tailored pharmacokinetics, for controlled biodistribution, and for the combination of diagnosis and therapy. In our opinion, new developments should focus on producing nanoradiomaterials showing features that are more intriguing than just the simple addition of their constituent parts. They should show synergistic behavior. Ideally, new features should appear from the combination of nanomaterials and radioisotopes. We have shown some of the most recent examples of this, but with the development of new materials and with their combination with different isotopes, the future of this combined approach seems promising both for preclinical imaging and for the patients.

Conflicts of Interest

The authors declare no conflicts of interest.

Acknowledgments

The authors are thankful for the financial support by the Spanish Ministry for Economy and Competitiveness (MEyC) (Grant no. SAF2016-79593-P) and by Carlos III Health Research Institute (Grant no. DTS16/00059). The CNIC is supported by the Spanish Ministry of Economy, Industry and Competitiveness (MEIC) and the Pro CNIC Foundation and is a Severo Ochoa Centre of Excellence (MEIC award SEV-2015-0505).

References

- [1] S. M. Wichner, V. R. Mann, A. S. Powers et al., “Covalent Protein Labeling and Improved Single-Molecule Optical Properties of Aqueous CdSe/CdS Quantum Dots,” *ACS Nano*, vol. 11, no. 7, pp. 6773–6781, 2017.
- [2] D. Bhatia, S. Arumugam, M. Nasilowski et al., “Quantum dot-loaded monofunctionalized DNA icosahedra for single-particle tracking of endocytic pathways,” *Nature Nanotechnology*, vol. 11, no. 12, pp. 1112–1119, 2016.
- [3] J. Song, X. Yang, Z. Yang et al., “Rational Design of Branched Nanoporous Gold Nanoshells with Enhanced Physico-Optical Properties for Optical Imaging and Cancer Therapy,” *ACS Nano*, vol. 11, no. 6, pp. 6102–6113, 2017.
- [4] J. L. Campbell, E. D. SoRelle, O. Ilovich et al., “Multimodal assessment of SERS nanoparticle biodistribution post ingestion reveals new potential for clinical translation of Raman imaging,” *Biomaterials*, vol. 135, pp. 42–52, 2017.
- [5] H. S. Park, S. H. Nam, J. Kim, H. S. Shin, Y. D. Suh, and K. S. Hong, “Clear-cut observation of clearance of sustainable upconverting nanoparticles from lymphatic system of small living mice,” *Scientific Reports*, vol. 6, Article ID 27407, 2016.
- [6] T. Wu, B. Johnsen, Z. Qin et al., “Two-colour fluorescent imaging in organisms using self-assembled nano-systems of upconverting nanoparticles and molecular switches,” *Nanoscale*, vol. 7, no. 26, pp. 11263–11266, 2015.
- [7] S. Edmonds, A. Volpe, H. Shmeeda et al., “Exploiting the Metal-Chelating Properties of the Drug Cargo for in Vivo Positron Emission Tomography Imaging of Liposomal Nanomedicines,” *ACS Nano*, vol. 10, no. 11, pp. 10294–10307, 2016.
- [8] Y. Duan, L. Wei, J. Petryk, and T. D. Ruddy, “Formulation, characterization and tissue distribution of a novel pH-sensitive long-circulating liposome-based theranostic suitable for molecular imaging and drug delivery,” *International Journal of Nanomedicine*, vol. 11, pp. 5697–5708, 2016.
- [9] Y. Huang, D. Coman, F. Hyder, and M. M. Ali, “Dendrimer-Based Responsive MRI Contrast Agents (G1-G4) for Biosensor Imaging of Redundant Deviation in Shifts (BIRDS),” *Bioconjugate Chemistry*, vol. 26, no. 12, pp. 2315–2323, 2015.
- [10] H. Mendoza-Nava, G. Ferro-Flores, F. d. Ramirez et al., “Fluorescent, Plasmonic, and Radiotherapeutic Properties of the,” *Molecular Imaging*, vol. 16, p. 153601211770476, 2017.
- [11] L. Xie, G. Wang, H. Zhou et al., “Functional long circulating single walled carbon nanotubes for fluorescent/photoacoustic imaging-guided enhanced phototherapy,” *Biomaterials*, vol. 103, pp. 219–228, 2016.
- [12] J. Budhathoki-Uprety, R. E. Langenbacher, P. V. Jena, D. Roxbury, and D. A. Heller, “A Carbon Nanotube Optical Sensor Reports Nuclear Entry,” *ACS Nano*, vol. 11, no. 4, pp. 3875–3882, 2017.
- [13] M. Di Paola, A. Quarta, F. Conversano et al., “Human Hepatocarcinoma Cell Targeting by Glypican-3 Ligand Peptide Functionalized Silica Nanoparticles: Implications for Ultrasound Molecular Imaging,” *Langmuir*, vol. 33, no. 18, pp. 4490–4499, 2017.
- [14] P. Rainone, B. Riva, S. Belloli et al., “Development of ^{99m}Tc -radiolabeled nanosilica for targeted detection of HER2-positive breast cancer,” *International Journal of Nanomedicine*, vol. Volume 12, pp. 3447–3461, 2017.
- [15] M. Srinivas, J. Tel, G. Schreiber et al., “PLGA-encapsulated perfluorocarbon nanoparticles for simultaneous visualization of distinct cell populations by 19F MRI,” *Nanomedicine*, vol. 10, no. 15, pp. 2339–2348, 2015.
- [16] S. Mastrogriaco, W. Dou, O. Koshkina et al., “Perfluorocarbon/Gold Loading for Noninvasive in Vivo Assessment of Bone Fillers Using,” *ACS Applied Materials & Interfaces*, vol. 9, no. 27, pp. 22149–22159, 2017.
- [17] M. M. Gwyther and E. O. Field, “Aggregated Tc99m-labelled albumin for lung scintiscanning,” *The International Journal of Applied Radiation and Isotopes*, vol. 17, no. 8, pp. 485–486, 1966.
- [18] E. Y. Yu, M. Bishop, B. Zheng et al., “Magnetic Particle Imaging: A Novel in Vivo Imaging Platform for Cancer Detection,” *Nano Letters*, vol. 17, no. 3, pp. 1648–1654, 2017.
- [19] H. Wang, C. Liu, X. Gong et al., “In vivo photoacoustic molecular imaging of breast carcinoma with folate receptor-targeted indocyanine green nanoprobes,” *Nanoscale*, vol. 6, no. 23, pp. 14270–14279, 2014.
- [20] R. Meir, O. Betzer, M. Motiei, N. Kronfeld, C. Brodie, and R. Popovtzer, “Design principles for noninvasive, longitudinal and quantitative cell tracking with nanoparticle-based CT imaging,” *Nanomedicine: Nanotechnology, Biology and Medicine*, vol. 13, no. 2, pp. 421–429, 2017.
- [21] N. Gibson, U. Holzwarth, K. Abbas et al., “Radiolabelling of engineered nanoparticles for in vitro and in vivo tracing applications using cyclotron accelerators,” *Archives of Toxicology*, vol. 85, no. 7, pp. 751–773, 2011.
- [22] R. T. M. De Rosales, R. Tavaré, A. Glaria, G. Varma, A. Protti, and P. J. Blower, “ ^{99m}Tc -bisphosphonate-iron oxide nanoparticle conjugates for dual-modality biomedical imaging,” *Bioconjugate Chemistry*, vol. 22, no. 3, pp. 455–465, 2011.
- [23] J. Pellico, J. Ruiz-Cabello, M. Saiz-Alía et al., “Fast synthesis and bioconjugation of ^{68}Ga core-doped extremely small iron oxide nanoparticles for PET/MR imaging,” *Contrast Media & Molecular Imaging*, vol. 11, no. 3, pp. 203–210, 2016.
- [24] X. Liu, Z. Zhong, Y. Tang, and B. Liang, “Review on the synthesis and applications of Fe_3O_4 nanomaterials,” *Journal of Nanomaterials*, vol. 2013, Article ID 902538, 7 pages, 2013.
- [25] A. K. Gupta and M. Gupta, “Synthesis and surface engineering of iron oxide nanoparticles for biomedical applications,” *Biomaterials*, vol. 26, no. 18, pp. 3995–4021, 2005.
- [26] H. Lee, Z. Li, K. Chen et al., “PET/MRI dual-modality tumor imaging using arginine-glycine-aspartic (RGD)-conjugated radiolabeled iron oxide nanoparticles,” *Journal of Nuclear Medicine*, vol. 49, no. 8, pp. 1371–1379, 2008.
- [27] C. Glaus, R. Rossin, M. J. Welch, and G. Bao, “In vivo evaluation of ^{64}Cu -labeled magnetic nanoparticles as a dual-modality PET/MR imaging agent,” *Bioconjugate Chemistry*, vol. 21, no. 4, pp. 715–722, 2010.
- [28] J. Xie, K. Chen, J. Huang et al., “PET/NIRF/MRI triple functional iron oxide nanoparticles,” *Biomaterials*, vol. 31, no. 11, pp. 3016–3022, 2010.

- [29] B. R. Jarrett, C. Correa, K. L. Ma, and A. Y. Louie, "In vivo mapping of vascular inflammation using multimodal imaging," *PLoS ONE*, vol. 5, no. 10, Article ID e13254, 2010.
- [30] S. Aryal, J. Key, C. Stigliano, M. D. Landis, D. Y. Lee, and P. Decuzzi, "Positron emitting magnetic nanoconstructs for PET/MR imaging," *Small*, vol. 10, no. 13, pp. 2688–2696, 2014.
- [31] C. Tu, T. S. Ng, R. E. Jacobs, and A. Y. Louie, "Multimodality PET/MRI agents targeted to activated macrophages," *JBIC Journal of Biological Inorganic Chemistry*, vol. 19, no. 2, pp. 247–258, 2014.
- [32] R. Torres Martin de Rosales, R. L. Tavar, M. Paul et al., "Synthesis of 64 Cu II -Bis(dithiocarbamatebisphosphonate) and its conjugation with superparamagnetic iron oxide nanoparticles: in vivo evaluation as dual-modality pet-mri agent," *Angewandte Chemie International Edition*, vol. 50, pp. 5509–5513, 2011.
- [33] M. Nahrendorf, H. Zhang, S. Hembrador et al., "Nanoparticle PET-CT imaging of macrophages in inflammatory atherosclerosis," *Circulation*, vol. 117, no. 3, pp. 379–387, 2008.
- [34] T. Ueno, P. Dutta, E. Keliher et al., "Nanoparticle PET-CT detects rejection and immunomodulation in cardiac allografts," *Circulation: Cardiovascular Imaging*, vol. 6, no. 4, pp. 568–573, 2013.
- [35] X. Yang, H. Hong, J. J. Grailer et al., "CRGD-functionalized, DOX-conjugated, and 64Cu-labeled superparamagnetic iron oxide nanoparticles for targeted anticancer drug delivery and PET/MR imaging," *Biomaterials*, vol. 32, no. 17, pp. 4151–4160, 2011.
- [36] Q. Fan, K. Cheng, X. Hu et al., "Transferring biomarker into molecular probe: Melanin nanoparticle as a naturally active platform for multimodality imaging," *Journal of the American Chemical Society*, vol. 136, no. 43, pp. 15185–15194, 2014.
- [37] T. Liu, S. Shi, C. Liang et al., "Iron oxide decorated MoS₂ nanosheets with double PEGylation for chelator-free radiolabeling and multimodal imaging guided photothermal therapy," *ACS Nano*, vol. 9, no. 1, pp. 950–960, 2015.
- [38] R. Madru, T. A. Tran, J. Axelsson et al., "(68)Ga-Labeled Superparamagnetic Iron Oxide Nanoparticles (SPIONs) for Multi-Modality PET/MR/Cherenkov Luminescence Imaging of Sentinel Lymph Nodes," *American Journal of Nuclear Medicine and Molecular Imaging*, vol. 4, pp. 60–69, 2013.
- [39] S.-M. Kim, M. K. Chae, M. S. Yim et al., "Hybrid PET/MR imaging of tumors using an oleanolic acid-conjugated nanoparticle," *Biomaterials*, vol. 34, no. 33, pp. 8114–8121, 2013.
- [40] B. Y. Yang, S.-H. Moon, S. R. Seelam et al., "Development of a multimodal imaging probe by encapsulating iron oxide nanoparticles with functionalized amphiphiles for lymph node imaging," *Nanomedicine*, vol. 10, no. 12, pp. 1899–1910, 2015.
- [41] E. Locatelli, L. Gil, L. L. Israel et al., "Biocompatible nanocomposite for PET/MRI hybrid imaging," *International Journal of Nanomedicine*, vol. 7, pp. 6021–6033, 2012.
- [42] S.-H. Moon, B. Y. Yang, Y. J. Kim et al., "Development of a complementary PET/MR dual-modal imaging probe for targeting prostate-specific membrane antigen (PSMA)," *Nanomedicine: Nanotechnology, Biology and Medicine*, vol. 12, no. 4, pp. 871–879, 2016.
- [43] N. K. Devaraj, E. J. Keliher, G. M. Thurber, M. Nahrendorf, and R. Weissleder, "18F labeled nanoparticles for in Vivo PET-CT imaging," *Bioconjugate Chemistry*, vol. 20, no. 2, pp. 397–401, 2009.
- [44] Z. Sun, K. Cheng, F. Wu et al., "Robust surface coating for a fast, facile fluorine-18 labeling of iron oxide nanoparticles for PET/MR dual-modality imaging," *Nanoscale*, vol. 8, no. 47, pp. 19644–19653, 2016.
- [45] M. Nahrendorf, E. Keliher, B. Marinelli et al., "Detection of macrophages in aortic aneurysms by nanoparticle positron emission tomography-computed tomography," *Arteriosclerosis, Thrombosis, and Vascular Biology*, vol. 31, no. 4, pp. 750–757, 2011.
- [46] J. C. Park, M. K. Yu, G. I. An et al., "Facile preparation of a hybrid nanoprobe for triple-modality optical/PET/MR imaging," *Small*, vol. 6, no. 24, pp. 2863–2868, 2010.
- [47] J.-S. Choi, J. C. Park, H. Nah et al., "A hybrid nanoparticle probe for dual-modality positron emission tomography and magnetic resonance imaging," *Angewandte Chemie International Edition*, vol. 47, no. 33, pp. 6259–6262, 2008.
- [48] R. Sharma, Y. Xu, S. W. Kim et al., "Carbon-11 radiolabeling of iron-oxide nanoparticles for dual-modality PET/MR imaging," *Nanoscale*, vol. 5, no. 16, pp. 7476–7483, 2013.
- [49] D. L. J. Thorek, D. Ulmert, N.-F. M. Diop et al., "Non-invasive mapping of deep-tissue lymph nodes in live animals using a multimodal PET/MRI nanoparticle," *Nature Communications*, vol. 5, pp. 2166–2171, 2014.
- [50] R. Chakravarty, H. F. Valdovinos, F. Chen et al., "Intrinsically germanium-69-labeled iron oxide nanoparticles: Synthesis and in-vivo dual-modality PET/MR imaging," *Advanced Materials*, vol. 26, no. 30, pp. 5119–5123, 2014.
- [51] C.-M. Lee, H.-J. Jeong, E.-M. Kim et al., "Superparamagnetic iron oxide nanoparticles as a dual imaging probe for targeting hepatocytes in vivo," *Magnetic Resonance in Medicine*, vol. 62, no. 6, pp. 1440–1446, 2009.
- [52] R. Madru, P. Kjellman, F. Olsson et al., "99mTc-labeled superparamagnetic iron oxide nanoparticles for multimodality SPECT/MRI of sentinel lymph nodes," *Journal of Nuclear Medicine*, vol. 53, no. 3, pp. 459–463, 2012.
- [53] S. Deng, W. Zhang, B. Zhang et al., "Radiolabeled cyclic arginine-glycine-aspartic (RGD)-conjugated iron oxide nanoparticles as single-photon emission computed tomography (SPECT) and magnetic resonance imaging (MRI) dual-modality agents for imaging of breast cancer," *Journal of Nanoparticle Research*, vol. 17, no. 1, 2015.
- [54] R. Massart, "Preparation of aqueous magnetic liquids in alkaline and acidic media," *IEEE Transactions on Magnetics*, vol. 17, no. 2, pp. 1247–1248, 1981.
- [55] J. Park, K. An, Y. Hwang et al., "Ultra-large-scale syntheses of monodisperse nanocrystals," *Nature Materials*, vol. 3, no. 12, pp. 891–895, 2004.
- [56] A. Lassenberger, T. A. Grünwald, P. D. van Oostrum et al., "Monodisperse Iron Oxide Nanoparticles by Thermal Decomposition: Elucidating Particle Formation by Second-Resolved in Situ Small-Angle X-ray Scattering," *Chemistry of Materials*, vol. 29, no. 10, pp. 4511–4522, 2017.
- [57] R. Hufschmid, H. Arami, R. M. Ferguson et al., "Synthesis of phase-pure and monodisperse iron oxide nanoparticles by thermal decomposition," *Nanoscale*, vol. 7, no. 25, pp. 11142–11154, 2015.
- [58] S. Sun and H. Zeng, "Size-controlled synthesis of magnetite nanoparticles," *Journal of the American Chemical Society*, vol. 124, no. 28, pp. 8204–8205, 2002.
- [59] B. Salinas, J. Ruiz-Cabello, M. P. Morales, and F. Herranz, "Olefin metathesis for the functionalization of superparamagnetic nanopar," *Bioinspired, Biomimetic and Nanobiomaterials*, vol. 1, no. 3, pp. 166–172, 2012.

- [60] W.-W. Wang, Y.-J. Zhu, and M.-L. Ruan, "Microwave-assisted synthesis and magnetic property of magnetite and hematite nanoparticles," *Journal of Nanoparticle Research*, vol. 9, no. 3, pp. 419–426, 2007.
- [61] J. Pellico, A. V. Lechuga-Vieco, M. Benito et al., "Microwave-driven synthesis of bisphosphonate nanoparticles allows in vivo visualisation of atherosclerotic plaque," *RSC Advances*, vol. 5, no. 3, pp. 1661–1665, 2015.
- [62] J. G. Parsons, C. Luna, C. E. Botez, J. Elizalde, and J. L. Gardea-Torresdey, "Microwave-assisted synthesis of iron(III) oxyhydroxides/oxides characterized using transmission electron microscopy, X-ray diffraction, and X-ray absorption spectroscopy," *Journal of Physics and Chemistry of Solids*, vol. 70, no. 3–4, pp. 555–560, 2009.
- [63] I. Koh and L. Josephson, "Magnetic Nanoparticle Sensors," *Sensors*, vol. 9, no. 10, pp. 8130–8145, 2009.
- [64] Jasmin, G. T. de Souza, R. A. Louzada, P. H. Rosado-de-Castro, R. Mendez-Otero, and A. C. C. de Carvalho, "Tracking stem cells with superparamagnetic iron oxide nanoparticles: Perspectives and considerations," *International Journal of Nanomedicine*, vol. 12, pp. 779–793, 2017.
- [65] P. Kaur, M. L. Aliru, A. S. Chadha, A. Asea, and S. Krishnan, "Hyperthermia using nanoparticles - Promises and pitfalls," *International Journal of Hyperthermia*, vol. 32, no. 1, pp. 76–88, 2016.
- [66] M. Bietenbeck, A. Florian, C. Faber, U. Sechtem, and A. Yilmaz, "Remote magnetic targeting of iron oxide nanoparticles for cardiovascular diagnosis and therapeutic drug delivery: Where are we now?" *International Journal of Nanomedicine*, vol. 11, pp. 3191–3203, 2016.
- [67] N. Lee and T. Hyeon, "Designed synthesis of uniformly sized iron oxide nanoparticles for efficient magnetic resonance imaging contrast agents," *Chemical Society Reviews*, vol. 41, no. 7, pp. 2575–2589, 2012.
- [68] B. H. Kim, N. Lee, H. Kim et al., "Large-scale synthesis of uniform and extremely small-sized iron oxide nanoparticles for high-resolution T1 magnetic resonance imaging contrast agents," *Journal of the American Chemical Society*, vol. 133, no. 32, pp. 12624–12631, 2011.
- [69] F. Hu, Q. Jia, Y. Li, and M. Gao, "Facile synthesis of ultrasmall PEGylated iron oxide nanoparticles for dual-contrast T1-and T2-weighted magnetic resonance imaging," *Nanotechnology*, vol. 22, no. 24, Article ID 245604, 2011.
- [70] J. Pellico, J. Ruiz-Cabello, I. Fernández-Barahona et al., "One-Step Fast Synthesis of Nanoparticles for MRI: Coating Chemistry as the Key Variable Determining Positive or Negative Contrast," *Langmuir*, vol. 33, no. 39, pp. 10239–10247, 2017.
- [71] Y.-X. J. Wang, "Superparamagnetic iron oxide based mri contrast agents: current status of clinical application," *Quantitative Imaging in Medicine and Surgery*, vol. 1, pp. 35–44, 2011.
- [72] P. Reimer and T. Balzer, "Ferucarbotran (Resovist): a new clinically approved RES-specific contrast agent for contrast-enhanced MRI of the liver: properties, clinical development, and applications," *European Radiology*, vol. 13, no. 6, pp. 1266–1276, 2003.
- [73] C. Corot, P. Robert, J.-M. Idée, and M. Port, "Recent advances in iron oxide nanocrystal technology for medical imaging," *Advanced Drug Delivery Reviews*, vol. 58, no. 14, pp. 1471–1504, 2006.
- [74] Y. K. Kim, H. S. Kwak, C. S. Kim, G. H. Chung, Y. M. Han, and J. M. Lee, "Hepatocellular carcinoma in patients with chronic liver disease: Comparison of SPIO-enhanced MR imaging and 16-detector row CT," *Radiology*, vol. 238, no. 2, pp. 531–541, 2006.
- [75] J. Ward, J. A. Guthrie, D. Wilson et al., "Colorectal hepatic metastases: Detection with SPIO-enhanced breath-hold MR imaging - Comparison of optimized sequences," *Radiology*, vol. 228, no. 3, pp. 709–718, 2003.
- [76] J. L. Gaglia, A. R. Guimaraes, M. Harisinghani et al., "Noninvasive imaging of pancreatic islet inflammation in type 1A diabetes patients," *The Journal of Clinical Investigation*, vol. 121, no. 1, pp. 442–445, 2011.
- [77] R. Weissleder, G. Elizondo, D. D. Stark et al., "The diagnosis of splenic lymphoma by MR imaging: Value of superparamagnetic iron oxide," *American Journal of Roentgenology*, vol. 152, no. 1, pp. 175–180, 1989.
- [78] M. Lu, M. H. Cohen, D. Rieves, and R. Pazdur, "FDA report: ferumoxytol for intravenous iron therapy in adult patients with chronic kidney disease," *American Journal of Hematology*, vol. 85, no. 5, pp. 315–319, 2010.
- [79] M. Levy, N. Luciani, D. Alloyeau et al., "Long term in vivo biotransformation of iron oxide nanoparticles," *Biomaterials*, vol. 32, no. 16, pp. 3988–3999, 2011.
- [80] F. Oberdorfer, E. Hofmann, and W. Maier-Borst, "Preparation of 18F-labelled N-fluoropyridinium triflate," *Journal of Labelled Compounds and Radiopharmaceuticals*, vol. 25, no. 9, pp. 999–1005, 1988.
- [81] N. Satyamurthy, G. T. Bida, M. E. Phelps, and J. R. Barrio, "N-[18F]fluoro-N-alkylsulfonamides: Novel reagents for mild and regioselective radiofluorination," *International Journal of Radiation Applications and Instrumentation*, vol. 41, no. 8, pp. 733–738, 1990.
- [82] H. Teare, E. G. Robins, A. Kirjavainen et al., "Radiosynthesis and evaluation of [18F]Selectfluor bis(triflate)," *Angewandte Chemie International Edition*, vol. 49, no. 38, pp. 6821–6824, 2010.
- [83] O. Jacobson, D. O. Kiesewetter, and X. Chen, "Fluorine-18 radiochemistry, labeling strategies and synthetic routes," *Bioconjugate Chemistry*, vol. 26, no. 1, pp. 1–18, 2015.
- [84] S. Rojas, J. D. Gispert, C. Menchón et al., "Novel methodology for labelling mesoporous silica nanoparticles using the 18F isotope and their in vivo biodistribution by positron emission tomography," *Journal of Nanoparticle Research*, vol. 17, no. 3, 2015.
- [85] P. P. Di Mauro, V. Gómez-Vallejo, Z. Baz Maldonado, J. Llop Roig, and S. Borrós, "Novel 18F Labeling Strategy for Polyester-Based NPs for in Vivo PET-CT Imaging," *Bioconjugate Chemistry*, vol. 26, no. 3, pp. 582–592, 2015.
- [86] K. Kondo, R. M. Lambrecht, and A. P. Wolf, "Iodine-123 production for radiopharmaceuticals-XX. Excitation functions of the $^{124}\text{Te}(p, 2n)^{123}\text{I}$ and $^{124}\text{Te}(p, n)^{124}\text{I}$ reactions and the effect of target enrichment on radionuclidic purity," *The International Journal of Applied Radiation and Isotopes*, vol. 28, no. 4, pp. 395–401, 1977.
- [87] V. Preylowski, S. Schlögl, F. Schoenahl et al., "Is the Image Quality of I-124-PET Impaired by an Automatic Correction of Prompt Gammas?" *PLoS ONE*, vol. 8, no. 8, Article ID e71729, 2013.
- [88] R. Weinreich and E. J. Knust, "Quality assurance of iodine-124 produced via the nuclear reaction $^{124}\text{Te}(d, 2n)^{124}\text{I}$," *Journal of Radioanalytical and Nuclear Chemistry*, vol. 213, no. 4, pp. 253–261, 1996.

- [89] W. M. Hunter and F. C. Greenwood, "Preparation of iodine-131 labelled human growth hormone of high specific activity," *Nature*, vol. 194, no. 4827, pp. 495-496, 1962.
- [90] P. J. Fraker and J. C. Speck Jr., "Protein and cell membrane iodinations with a sparingly soluble chloroamide, 1,3,4,6-tetrachloro-3a,6a-diphenylglycoluril," *Biochemical and Biophysical Research Communications*, vol. 80, no. 4, pp. 849-857, 1978.
- [91] A. E. Bolton and W. M. Hunter, "The labelling of proteins to high specific radioactivities by conjugation to a 125I containing acylating agent. Application to the radioimmunoassay," *Biochemical Journal*, vol. 133, no. 3, pp. 529-538, 1973.
- [92] M. Breslav, A. McKinney, J. M. Becker, and F. Naider, "Preparation of radiolabeled peptides via an iodine exchange reaction," *Analytical Biochemistry*, vol. 239, no. 2, pp. 213-217, 1996.
- [93] J. Llop, P. Jiang, M. Marradi et al., "Visualisation of dual radio-labelled poly(lactide-co-glycolide) nanoparticle degradation in vivo using energy-discriminant SPECT," *Journal of Materials Chemistry B*, vol. 3, no. 30, pp. 6293-6300, 2015.
- [94] E. A. Simone, B. J. Zern, A.-M. Chacko et al., "Endothelial targeting of polymeric nanoparticles stably labeled with the PET imaging radioisotope iodine-124," *Biomaterials*, vol. 33, no. 21, pp. 5406-5413, 2012.
- [95] X. Shao, A. Agarwal, J. R. Rajian, N. A. Kotov, and X. Wang, "Synthesis and bioevaluation of 125I-labeled gold nanorods," *Nanotechnology*, vol. 22, no. 13, Article ID 135102, 2011.
- [96] N. Eskandari, K. Yavari, M. Outokesh, S. Sadjadi, and S. J. Ahmadi, "Iodine-131 radiolabeling of poly ethylene glycol-coated gold nanorods for in vivo imaging," *Journal of Labelled Compounds and Radiopharmaceuticals*, vol. 56, no. 1, pp. 12-16, 2013.
- [97] T. N. Van Der Walt and P. P. Coetzee, "The isolation of 99Mo from fission material for use in the 99Mo/99mTc generator for medical use," *Radiochimica Acta*, vol. 92, no. 4-6, pp. 251-257, 2004.
- [98] A. Dash, F. F. Knapp, and M. R. A. Pillai, "99Mo/99mTc separation: An assessment of technology options," *Nuclear Medicine and Biology*, vol. 40, no. 2, pp. 167-176, 2013.
- [99] F. Tárkányi, A. Hermanne, S. Takács et al., "Investigation of alternative production routes of 99mTc: Deuteron induced reactions on 100Mo," *Applied Radiation and Isotopes*, vol. 69, no. 1, pp. 18-25, 2011.
- [100] B. Guérin, S. Tremblay, S. Rodrigue et al., "Cyclotron production of 99mTc: an approach to the medical isotope crisis," *Journal of nuclear medicine : official publication, Society of Nuclear Medicine*, vol. 51, no. 4, 2010.
- [101] E. Morales-Avila, G. Ferro-Flores, B. E. Ocampo-García et al., "Multimeric system of 99mTc-labeled gold nanoparticles conjugated to c[RGDfK(C)] for molecular imaging of tumor $\alpha(v)\beta(3)$ expression," *Bioconjugate Chemistry*, vol. 22, no. 5, pp. 913-922, 2011.
- [102] B. Ocampo-García, G. Ferro-Flores, E. Morales-Avila, and F. D. M. Ramírez, "Kit for preparation of multimeric receptor-specific 99mTc- radiopharmaceuticals based on gold nanoparticles," *Nuclear Medicine Communications*, vol. 32, no. 11, pp. 1095-1104, 2011.
- [103] P. J. Riss, C. Kroll, V. Nagel, and F. Rösch, "NODAPA-OH and NODAPA-(NCS)n: Synthesis, 68Ga-radiolabelling and in vitro characterisation of novel versatile bifunctional chelators for molecular imaging," *Bioorganic & Medicinal Chemistry Letters*, vol. 18, no. 20, pp. 5364-5367, 2008.
- [104] T. N. Van der Walt and C. Vermeulen, "Thick targets for the production of some radionuclides and the chemical processing of these targets at iThemba LABS," *Nuclear Instruments and Methods in Physics Research Section A: Accelerators, Spectrometers, Detectors and Associated Equipment*, vol. 521, no. 1, pp. 171-175, 2004.
- [105] C. Loc'h, B. Maziere, D. Comar, and R. Knipper, "A new preparation of germanium 68," *The International Journal of Applied Radiation and Isotopes*, vol. 33, no. 4, pp. 267-270, 1982.
- [106] Y. Yano and H. O. Anger, "A Gallium-68 Positron Cow for Medical Use," *Journal of Nuclear Medicine*, vol. 5, pp. 484-487, 1964.
- [107] E. de Blois, H. S. Chan, C. Naidoo, D. Prince, E. P. Krenning, and W. A. P. Breeman, "Characteristics of SnO₂-based ⁶⁸Ge/⁶⁸Ga generator and aspects of radiolabelling DOTA-peptides," *Applied Radiation and Isotopes*, vol. 69, no. 2, pp. 308-315, 2011.
- [108] K. P. Zhernosekov, D. V. Filosofov, R. P. Baum et al., "Processing of generator-produced ⁶⁸Ga for medical application," *Journal of Nuclear Medicine*, vol. 48, no. 10, pp. 1741-1748, 2007.
- [109] F. W. E. Strelow, A. H. Victor, C. R. van Zyl, and C. Eloff, "Distribution Coefficients and Cation Exchange Behavior of Elements in Hydrochloric Acid-Acetone," *Analytical Chemistry*, vol. 43, no. 7, pp. 870-876, 1971.
- [110] J. Frigell, I. García, V. Gómez-Vallejo, J. Llop, and S. Penadés, "68Ga-labeled gold glyconanoparticles for exploring blood-brain barrier permeability: Preparation, biodistribution studies, and improved brain uptake via neuropeptide conjugation," *Journal of the American Chemical Society*, vol. 136, no. 1, pp. 449-457, 2014.
- [111] F. E. Little and M. C. Lagunas-Solar, "Cyclotron production of 67Ga. Cross sections and thick-target yields for the 67Zn (p,n) and 68Zn (p,2n) reactions," *The International Journal of Applied Radiation and Isotopes*, vol. 34, no. 3, pp. 631-637, 1983.
- [112] J. Steyn and B. R. Meyer, "Production of 67Ga by deuteron bombardment of natural zinc," *The International Journal of Applied Radiation and Isotopes*, vol. 24, no. 7, pp. 369-372, 1973.
- [113] M. U. Khandaker, H. Haba, and H. A. Kassim, "Cyclotron produced 67Ga, a potential radionuclide for diagnostic and therapeutic applications," in *AIP Conference Proceedings*, November 2015.
- [114] T. N. Van Der Walt and F. W. E. Strelow, "Quantitative separation of gallium from other elements by cation-exchange chromatography," *Analytical Chemistry*, vol. 55, no. 2, pp. 212-216, 1983.
- [115] Y. K. Kim, C. S. Kim, Y. M. Han, G. Park, S. B. Hwang, and H. C. Yu, "Comparison of gadoteric acid-enhanced MRI and superparamagnetic iron oxide-enhanced MRI for the detection of hepatocellular carcinoma," *Clinical Radiology*, vol. 65, no. 5, pp. 358-365, 2010.
- [116] M.-M. Bé, P. Cassette, M. C. Lépy et al., "Standardization, decay data measurements and evaluation of 64Cu," *Applied Radiation and Isotopes*, vol. 70, no. 9, pp. 1894-1899, 2012.
- [117] K. R. Zinn, T. R. Chaudhuri, T. Cheng, J. Steven Morris, and W. A. Meyer, "Production of no-carrier-added 64Cu from zinc metal irradiated under boron shielding," *Cancer*, vol. 73, no. 3 S, pp. 774-778, 1994.
- [118] F. Szelecsényi, G. Blessing, and S. M. Qaim, "Excitation functions of proton induced nuclear reactions on enriched 61Ni and 64Ni: Possibility of production of no-carrier-added 61Cu and 64Cu at a small cyclotron," *Applied Radiation and Isotopes*, vol. 44, no. 3, pp. 575-580, 1993.
- [119] D. W. McCarthy, R. E. Shefer, R. E. Klinkowstien et al., "Efficient production of high specific activity 64Cu using a biomedical

- cyclotron,” *Nuclear Medicine and Biology*, vol. 24, no. 1, pp. 35–43, 1997.
- [120] Q. Xie, H. Zhu, F. Wang et al., “Establishing Reliable Cu-64 Production Process: From Target Plating to Molecular Specific Tumor Micro-PET Imaging,” *Molecules*, vol. 22, no. 4, p. 641, 2017.
- [121] C. J. Anderson and R. Ferdani, “Copper-64 radiopharmaceuticals for PET imaging of cancer: advances in preclinical and clinical research,” *Cancer Biotherapy and Radiopharmaceuticals*, vol. 24, no. 4, pp. 379–393, 2009.
- [122] D. Krajčiová, M. Melník, E. Havránek, A. Forgáčsová, and P. Mikuš, “Copper compounds in nuclear medicine and oncology,” *Journal of Coordination Chemistry*, vol. 67, no. 9, pp. 1493–1519, 2014.
- [123] H. Xie, Z. J. Wang, A. Bao, B. Goins, and W. T. Phillips, “In vivo PET imaging and biodistribution of radiolabeled gold nanoshells in rats with tumor xenografts,” *International Journal of Pharmaceutics*, vol. 395, no. 1-2, pp. 324–330, 2010.
- [124] K. Chen, Z.-B. Li, H. Wang, W. Cai, and X. Chen, “Dual-modality optical and positron emission tomography imaging of vascular endothelial growth factor receptor on tumor vasculature using quantum dots,” *European Journal of Nuclear Medicine and Molecular Imaging*, vol. 35, no. 12, pp. 2235–2244, 2008.
- [125] Z. Liu, W. B. Cai, L. N. He et al., “In vivo biodistribution and highly efficient tumour targeting of carbon nanotubes in mice,” *Nature Nanotechnology*, vol. 2, no. 1, pp. 47–52, 2007.
- [126] B. Dutta, M. Maiti, and S. Lahiri, “Production of $^{88,89}\text{Zr}$ by proton induced activation of natY and separation by SLX and LLX,” *Journal of Radioanalytical and Nuclear Chemistry*, vol. 281, no. 3, pp. 663–667, 2009.
- [127] J. M. Link, K. A. Krohn, and J. F. Eary, “ ^{89}Zr for Antibody Labeling and Positron Emission Tomography,” *J. Label. Compd. Radiopharm.*, vol. 23, pp. 1297–1298, 1986.
- [128] J. P. Holland, Y. Sheh, and J. S. Lewis, “Standardized methods for the production of high specific-activity zirconium-89,” *Nuclear Medicine and Biology*, vol. 36, no. 7, pp. 729–739, 2009.
- [129] V. I. Fadeeva, T. I. Tikhomirova, I. B. Yuferova, and G. V. Kudryavtsev, “Preparation, properties and analytical application of silica with chemically grafted hydroxamic acid groups,” *Analytica Chimica Acta*, vol. 219, no. C, pp. 201–212, 1989.
- [130] W. E. Meijs, J. D. M. Herscheid, H. J. Haisma, and H. M. Pinedo, “Evaluation of desferal as a bifunctional chelating agent for labeling antibodies with Zr-89,” *International Journal of Radiation Applications and Instrumentation*, vol. 43, no. 12, pp. 1443–1447, 1992.
- [131] T. J. Wadas, E. H. Wong, G. R. Weisman, and C. J. Anderson, “Coordinating radiometals of copper, gallium, indium, yttrium, and zirconium for PET and SPECT imaging of disease,” *Chemical Reviews*, vol. 110, no. 5, pp. 2858–2902, 2010.
- [132] C. Truillet, E. Thomas, F. Lux, L. T. Huynh, O. Tillement, and M. J. Evans, “Synthesis and characterization of ^{89}Zr -labeled ultrasmall nanoparticles,” *Molecular Pharmaceutics*, vol. 13, no. 7, pp. 2596–2601, 2016.
- [133] M. A. Deri, S. Ponnala, B. M. Zeglis et al., “Alternative chelator for ^{89}Zr radiopharmaceuticals: Radiolabeling and evaluation of 3,4,3-(LI-1,2-HOPO),” *Journal of Medicinal Chemistry*, vol. 57, no. 11, pp. 4849–4860, 2014.
- [134] V. Alexander, “Design and synthesis of macrocyclic ligands and their complexes of lanthanides and actinides,” *Chemical Reviews*, vol. 95, no. 2, pp. 273–342, 1995.
- [135] A. Lahooti, S. Sarkar, S. Laurent, and S. Shanehsazzadeh, “Dual nano-sized contrast agents in PET/MRI: a systematic review,” *Contrast Media & Molecular Imaging*, vol. 11, no. 6, pp. 428–447, 2016.
- [136] P. Bouziotis, D. Psimadas, T. Tsotakos, D. Stamopoulos, and C. Tsoukalas, “Radiolabeled iron oxide nanoparticles as dual-modality SPECT/MRI and PET/MRI agents,” *Current Topics in Medicinal Chemistry*, vol. 12, no. 23, pp. 2694–2702, 2012.
- [137] R. Misri, D. Meier, A. C. Yung, P. Kozlowski, and U. O. Häfeli, “Development and evaluation of a dual-modality (MRI/SPECT) molecular imaging bioprobe,” *Nanomedicine: Nanotechnology, Biology and Medicine*, vol. 8, no. 6, pp. 1007–1016, 2012.
- [138] Y. Tang, C. Zhang, J. Wang et al., “MRI/SPECT/fluorescent tri-modal probe for evaluating the homing and therapeutic efficacy of transplanted mesenchymal stem cells in a rat ischemic stroke model,” *Advanced Functional Materials*, vol. 25, no. 7, pp. 1024–1034, 2015.
- [139] B. R. Jarrett, B. Gustafsson, D. L. Kukis, and A. Y. Louie, “Synthesis of ^{64}Cu -labeled magnetic nanoparticles for multimodal imaging,” *Bioconjugate Chemistry*, vol. 19, no. 7, pp. 1496–1504, 2008.
- [140] G. Morin, Y. Wang, G. Ona-Nguema et al., “EXAFS and HRTEM evidence for As(III)-containing surface precipitates on nanocrystalline magnetite: Implications for as sequestration,” *Langmuir*, vol. 25, no. 16, pp. 9119–9128, 2009.
- [141] F. Chen, P. A. Ellison, C. M. Lewis et al., “Chelator-free synthesis of a dual-modality PET/MRI agent,” *Angewandte Chemie International Edition*, vol. 52, no. 50, pp. 13319–13323, 2013.
- [142] R. Chakravarty, R. Shukla, R. Ram, A. K. Tyagi, A. Dash, and M. Venkatesh, “Development of a nano-zirconia based $^{68}\text{Ge}/^{68}\text{Ga}$ generator for biomedical applications,” *Nuclear Medicine and Biology*, vol. 38, no. 4, pp. 575–583, 2011.
- [143] T. H. Nguyen Pham, N. A. Lengkeek, I. Greguric et al., “Tunable and noncytotoxic PET/SPECT-MRI multimodality imaging probes using colloiddally stable ligand-free superparamagnetic iron oxide nanoparticles,” *International Journal of Nanomedicine*, vol. 12, pp. 899–909, 2017.
- [144] R. Madru, T. A. Tran, J. Axelsson et al., “Ga-Labeled Superparamagnetic Iron Oxide Nanoparticles (SPIONs) for Multimodality PET/MR/Cherenkov Luminescence Imaging of Sentinel Lymph Nodes,” *American Journal of Nuclear Medicine and Molecular Imaging*, vol. 4, pp. 60–69, 2014.
- [145] M. Evertsson, P. Kjellman, M. Cinthio et al., “Combined Magnetomotive ultrasound, PET/CT, and MR imaging of ^{68}Ga -labelled superparamagnetic iron oxide nanoparticles in rat sentinel lymph nodes in vivo,” *Scientific Reports*, vol. 7, no. 1, 2017.
- [146] R. M. Wong, D. A. Gilbert, K. Liu, and A. Y. Louie, “Rapid size-controlled synthesis of dextran-coated, ^{64}Cu -doped iron oxide nanoparticles,” *ACS Nano*, vol. 6, no. 4, pp. 3461–3467, 2012.
- [147] C. Pérez-Campaña, V. Gómez-Vallejo, A. Martin et al., “Tracing nanoparticles in vivo: A new general synthesis of positron emitting metal oxide nanoparticles by proton beam activation,” *Analyst*, vol. 137, no. 21, pp. 4902–4906, 2012.
- [148] F. Simonelli, P. Marmorato, K. Abbas et al., “Cyclotron production of radioactive CeO_2 nanoparticles and their application for in vitro uptake studies,” *IEEE Transactions on NanoBioscience*, vol. 10, no. 1, pp. 44–50, 2011.
- [149] J. Ponti, R. Colognato, F. Franchini et al., “A quantitative in vitro approach to study the intracellular fate of gold nanoparticles:

- From synthesis to cytotoxicity," *Nanotoxicology*, vol. 3, no. 4, pp. 296–306, 2009.
- [150] K. Abbas, I. Cydzik, R. Del Torchio et al., "Radiolabelling of TiO₂ nanoparticles for radiotracer studies," *Journal of Nanoparticle Research*, vol. 12, no. 7, pp. 2435–2443, 2010.
- [151] U. Holzwarth, A. Bulgheroni, N. Gibson et al., "Radiolabelling of nanoparticles by proton irradiation: Temperature control in nanoparticulate powder targets," *Journal of Nanoparticle Research*, vol. 14, no. 6, article no. 880, 2012.
- [152] C. Pérez-Campaña, F. Sansaloni, V. Gómez-Vallejo et al., "Production of ¹⁸F-labeled titanium dioxide nanoparticles by proton irradiation for biodistribution and biological fate studies in rats," *Particle & Particle Systems Characterization*, vol. 31, no. 1, pp. 134–142, 2014.
- [153] C. Pérez-Campaña, V. Gómez-Vallejo, M. Puigivila et al., "Biodistribution of different sized nanoparticles assessed by positron emission tomography: A general strategy for direct activation of metal oxide particles," *ACS Nano*, vol. 7, no. 4, pp. 3498–3505, 2013.
- [154] K. Abbas, F. Simonelli, U. Holzwarth et al., "Feasibility study of production of radioactive carbon black or carbon nanotubes in cyclotron facilities for nanobioscience applications," *Applied Radiation and Isotopes*, vol. 73, pp. 44–48, 2013.
- [155] I. L. Jenkins and A. G. Wain, "Excitation functions for the bombardment of ⁵⁶Fe with protons," *Journal of Inorganic and Nuclear Chemistry*, vol. 32, no. 5, pp. 1419–1425, 1970.
- [156] P. Marmorato, F. Simonelli, K. Abbas et al., "⁵⁶Co-labelled radioactive Fe₃O₄ nanoparticles for in vitro uptake studies on Balb/3T3 and Caco-2 cell lines," *Journal of Nanoparticle Research*, vol. 13, no. 12, pp. 6707–6716, 2011.
- [157] A. Abánades, J. Aleixandre, S. Andriamonje et al., "Results from the TARC experiment: Spallation neutron phenomenology in lead and neutron-driven nuclear transmutation by adiabatic resonance crossing," *Nuclear Instruments and Methods in Physics Research Section A: Accelerators, Spectrometers, Detectors and Associated Equipment*, vol. 478, no. 3, pp. 577–730, 2002.
- [158] I. Tilquin, P. Froment, M. Cogneau, T. Delbar, J. Vervier, and G. Ryckewaert, "Experimental measurements of neutron fluxes produced by proton beams (23–80 MeV) on Be and Pb targets," *Nuclear Instruments and Methods in Physics Research Section A: Accelerators, Spectrometers, Detectors and Associated Equipment*, vol. 545, no. 1–2, pp. 339–343, 2005.
- [159] K. Abbas, S. Buono, N. Burgio et al., "Development of an accelerator driven neutron activator for medical radioisotope production," *Nuclear Instruments and Methods in Physics Research Section B: Beam Interactions with Materials and Atoms*, vol. 601, no. 3, pp. 223–228, 2009.
- [160] W. Bult, R. Varkevisser, F. Soulimani et al., "Holmium nanoparticles: Preparation and in vitro characterization of a new device for radioablation of solid malignancies," *Pharmaceutical Research*, vol. 27, no. 10, pp. 2205–2212, 2010.
- [161] U. Holzwarth, E. Bellido, M. Dalmiglio, J. Kozempel, G. Cotogno, and N. Gibson, "⁷Be-recoil radiolabelling of industrially manufactured silica nanoparticles," *Journal of Nanoparticle Research*, vol. 16, no. 9, article no. 2574, 2014.
- [162] A. Kiani, A. Esquevin, N. Lepareur, P. Bourguet, F. Le Jeune, and J. Gauvrit, "Main applications of hybrid PET-MRI contrast agents: A review," *Contrast Media & Molecular Imaging*, vol. 11, no. 2, pp. 92–98, 2016.
- [163] F. Ai, C. A. Ferreira, F. Chen, and W. Cai, "Engineering of radiolabeled iron oxide nanoparticles for dual-modality imaging," *Wiley Interdisciplinary Reviews: Nanomedicine and Nanobiotechnology*, vol. 8, no. 4, pp. 619–630, 2016.
- [164] L. Stelter, J. G. Pinkernelle, R. Michel et al., "Modification of aminosilanized superparamagnetic nanoparticles: Feasibility of multimodal detection using 3T MRI, small animal PET, and fluorescence imaging," *Molecular Imaging and Biology*, vol. 12, no. 1, pp. 25–34, 2010.
- [165] S. S. Gambhir, "Molecular imaging of cancer with positron emission tomography," *Nature Reviews Cancer*, vol. 2, no. 9, pp. 683–693, 2002.
- [166] M. Marciello, J. Pellico, I. Fernandez-Barahona, F. Herranz, J. Ruiz-Cabello, and M. Filice, "Recent advances in the preparation and application of multifunctional iron oxide and liposome-based nanosystems for multimodal diagnosis and therapy," *Interface Focus*, vol. 6, no. 6, Article ID 20160055, 2016.
- [167] J. S. Kim, Y.-H. Kim, J. H. Kim et al., "Development and in vivo imaging of a PET/MRI nanoprobe with enhanced NIR fluorescence by dye encapsulation," *Nanomedicine*, vol. 7, no. 2, pp. 219–229, 2012.
- [168] J. Choi, J. Park, H. Nah et al., "A Hybrid Nanoparticle Probe for Dual-Modality Positron Emission Tomography and Magnetic Resonance Imaging," *Angewandte Chemie*, vol. 120, no. 33, pp. 6355–6358, 2008.
- [169] X. Cui, D. Mathe, N. Kovács et al., "Synthesis, Characterization, and Application of Core-Shell Co_{0.16}Fe_{2.84}O₄@NaYF₄(Yb, Er) and Fe₃O₄@NaYF₄(Yb, Tm) Nanoparticle as Trimodal (MRI, PET/SPECT, and Optical) Imaging Agents," *Bioconjugate Chemistry*, vol. 27, no. 2, pp. 319–328, 2016.
- [170] D. Mozaffarian, E. J. Benjamin, A. S. Go et al., "Heart disease and stroke statistics—2015 update: a report from the American Heart Association," *Circulation*, vol. 131, no. 4, pp. e29–e322, 2015.

Research Article

Erbium-Based Perfusion Contrast Agent for Small-Animal Microvessel Imaging

Justin J. Tse,^{1,2} P. Joy Dunmore-Buyze,¹ Maria Drangova,^{1,2,3} and David W. Holdsworth^{1,4}

¹Imaging Research Laboratories, Robarts Research Institute, Western University, London, ON, Canada N6A 5B7

²Department of Medical Biophysics, Western University, London, ON, Canada N6A 5C1

³Department of Medical Imaging, Western University, London, ON, Canada N6A 5B7

⁴Department of Surgery, Western University, London, ON, Canada N6A 5B7

Correspondence should be addressed to Justin J. Tse; tse.jjp@gmail.com and David W. Holdsworth; dholdsworth@robarts.ca

Received 11 July 2017; Revised 11 September 2017; Accepted 2 October 2017; Published 15 November 2017

Academic Editor: Pedro Moreno Pimentel-Coelho

Copyright © 2017 Justin J. Tse et al. This is an open access article distributed under the Creative Commons Attribution License, which permits unrestricted use, distribution, and reproduction in any medium, provided the original work is properly cited.

Micro-computed tomography (micro-CT) facilitates the visualization and quantification of contrast-enhanced microvessels within intact tissue specimens, but conventional preclinical vascular contrast agents may be inadequate near dense tissue (such as bone). Typical lead-based contrast agents do not exhibit optimal X-ray absorption properties when used with X-ray tube potentials below 90 kilo-electron volts (keV). We have developed a high-atomic number lanthanide (erbium) contrast agent, with a K-edge at 57.5 keV. This approach optimizes X-ray absorption in the output spectral band of conventional microfocus spot X-ray tubes. Erbium oxide nanoparticles (nominal diameter < 50 nm) suspended in a two-part silicone elastomer produce a perfusable fluid with viscosity of 19.2 mPa-s. Ultrasonic cavitation was used to reduce aggregate sizes to <70 nm. Postmortem intact mice were perfused to investigate the efficacy of contrast agent. The observed vessel contrast was >4000 Hounsfield units, and perfusion of vessels < 10 μ m in diameter was demonstrated in kidney glomeruli. The described new contrast agent facilitated the visualization and quantification of vessel density and microarchitecture, even adjacent to dense bone. Erbium's K-edge makes this contrast agent ideally suited for both single- and dual-energy micro-CT, expanding potential preclinical research applications in models of musculoskeletal, oncological, cardiovascular, and neurovascular diseases.

1. Introduction

It is increasingly important in preclinical research to study the vasculature in both soft tissue and bone [1–5]. This includes visualization, quantification, and characterization of microvessels (i.e., vessels less than 10 μ m in diameter). Micro-computed tomography (micro-CT) can provide images with spatial resolution better than 5 μ m in both intact specimens and in *ex vivo* small animals [6–8]. However, blood-filled vessels lack inherent radiographic contrast, requiring the use of an exogenous contrast agent that can pass through capillaries and be retained within the vascular system. The increased contrast provided by such an agent facilitates automated (or semi-automated) segmentation (i.e., separation) of the perfused vasculature from surrounding tissues.

The performance (sensitivity, specificity, and accuracy) of vessel segmentation algorithms has been shown to be dependent on the signal-to-noise ratio (SNR, defined as the ratio of the vessel signal to background noise) between the contrast-enhanced vasculature and surrounding tissue in the micro-CT image [9]. Higher SNR results in a more robust and objective classification of the perfused vessels, leading to a more accurate assessment of their microarchitecture. The SNR can be increased by either reducing background noise or increasing the signal intensity within the vessel. However, decreasing micro-CT image noise is typically impractical, as it is achieved through much longer scan times [10]. Therefore, the most effective method to increase vessel SNR is to increase the contrast within the vasculature, using a radio-opaque exogenous contrast agent.

Several formulations of exogenous vascular contrast agents are commonly available. Most clinical contrast agents for *in vivo* use are iodine-based; however, their small molecular size of <800 Da results in rapid clearance (i.e., within minutes) via the kidneys [11, 12]. Even in postmortem studies with increased iodine concentrations and scan times, the short retention time of these iodine-based agents makes them unsuitable for microvessel studies. Preclinical exogenous agents, of larger molecular sizes (i.e., >1100 Da), can remain within the blood pool for hours [13, 14]. These contrast agents are typically iodine-, barium-, or lead-based and have been used effectively to study vessel microarchitecture in the heart [15, 16], kidney [17, 18], tumours [19, 20], nerves [21–23], and long bones [24, 25]. However, these preclinical contrast agents do not exhibit optimal X-ray absorption (and hence do not optimize SNR) on a large installed base of micro-CT machines that typically operate at a maximum of 90 kilo-electron volts (keV).

X-ray absorption, responsible for observed contrast within X-ray images, is influenced by the K-edge of the contrast material (i.e., the energy required to eject an inner K-shell electron). The K-edges for common preclinical contrast agents are 33 keV for iodine, 37.4 keV for barium, and 88 keV for lead. These K-edge energies are not optimally matched for typical micro-focus tubes operating at a peak potential of 90 kVp, as the K-edge energies are located either at the low- or high-energy range of the output spectrum of the tube. Ideally, a contrast agent with a K-edge closer to the mean energy of the output spectrum of these micro-CT machines (i.e., ~50 keV) would provide enhanced X-ray absorption.

The lanthanide erbium (Er), with a K-edge at 57.5 keV, would provide the contrast necessary for micro-CT scanners operating at 90 kVp. An Er-based contrast agent would also provide an additional benefit for dual-energy micro-CT studies, which require CT scans above and below the K-edge of the material of interest [26]. In this study, we describe a novel contrast agent based on erbium oxide (Er_2O_3) nanoparticles (nominal diameter of ~50 nm) and illustrate a process by which Er_2O_3 nanoparticles form a colloidal suspension in a continuous-phase fluid (i.e., two-part liquid silicone elastomer). This methodology of contrast agent fabrication resulted in a high-atomic number (and consequently highly X-ray attenuating) *ex vivo* vascular perfusion contrast agent, with sufficiently low viscosity (19.2 mPa·s) to ensure the perfusion of the microvascular network (<10 μm).

Using micro-CT, we demonstrate the efficacy of the custom contrast agent in a postmortem murine model. The contrast agent perfused the smallest vessels (i.e., capillaries) and provided increased SNR, facilitating the visualization of microvessels with diameter < 10 μm . The Er-based contrast agent provided a greater SNR than commercially available agents, while also possessing a more appropriate absorption K-edge energy (57.5 keV). The resulting increase in vessel contrast would enhance the performance and automation of segmentation algorithms in all types of vascular networks and small-animal models (for both single- and dual-energy studies). This approach will be applicable in many preclinical studies, including musculoskeletal, cardiovascular, neurovascular, and oncological research programs.

2. Materials and Methods

2.1. Er-Based Contrast Agent Preparation. Erbium oxide (Er_2O_3) nanoparticles (NPs) were chosen as the main constituent of the contrast agent, due to their high X-ray attenuation and availability in a nanoparticulate powder (nominal diameter ~ 50 nm). To deliver the Er_2O_3 NPs throughout the vascular network, a commercially available two-part silicone elastomer (commonly used for vascular perfusion, Microfil MV-132, Flowtech Inc., Carver, MA, USA) was chosen as the carrier matrix. Uncured, this silicone elastomer has a manufacturer-reported viscosity of 20 mPa·s and when cured, the silicone matrix entrains the suspended Er_2O_3 NPs to form a stable silicone cast of the perfused vasculature. Initial experiments revealed difficulties incorporating the Er_2O_3 NPs within the two-part silicone elastomer. Analysis, via confocal fluorescence microscopy, of the uncoated Er_2O_3 powder revealed the tendency of the NPs to naturally aggregate into clusters > 1 μm , due to van der Waals forces—nanoparticulate powders have been shown to naturally clump and form much larger particle sizes when left uncoated or untreated [27, 28]. Large aggregates such as these could clump together and prevent the perfusion of arterioles and capillaries, inhibiting perfusion of the venous system. Thus, to address the fact that uncoated nanoparticles tend to aggregate into large clumps (i.e., >100 μm) a method was devised to ensure the size of the Er_2O_3 NPs in the final product remained smaller than 100 nm, as follows.

2.1.1. Er_2O_3 NP Silicone Elastomer Suspension. Uncoated Er_2O_3 NPs of ~50 nm nominal diameter (Nanostructured and Amorphous Materials, Houston, TX, USA) were ground using a mortar and pestle for ~5 minutes to break down large aggregates. The ground powder was then mixed with an additive-free clear two-part silicone elastomer (Microfil MV-132, Carver, MA, USA), which is mixed in a ratio of two-part MV-Diluent to one-part MV-132. To prepare 30 mL of contrast agent, 4.0 g of ground Er_2O_3 (i.e., 13.3% w/v) was added to 17.47 mL of MV-Diluent and 8.73 mL of MV-132; the remaining 3.8 mL was comprised of the curing agent described below, which was added immediately prior to perfusion into the animal. The uncured suspension of Er_2O_3 powder and silicone elastomer was probe sonicated (Branson Digital Sonifier 450D, standard 13 mm tapped horn, Crystal Electronics, Newmarket, ON, Canada) for a total of 35 minutes with 25% amplitude and a duty cycle of 30 s ON to 10 s OFF. Due to the intense heat generated during sonication, the samples were immersed in an ice bath and sonication was performed in three intervals interspersed with 5–10-minute cool-down periods. The Er_2O_3 NP silicone elastomer suspension was prepared several hours prior to perfusion, to allow particle aggregates to settle, and then decanted prior to use. If prepared further in advance, sonication of the suspension of 5–10 minutes is required to ensure particle resuspension.

2.1.2. Curing Agent. To facilitate consistent and controlled curing of the Er_2O_3 NP silicone elastomer suspension, a tin-based curing agent was prepared in-house. The curing agent comprised a solution of 40% (w/w) dibutyltin dilaurate

(Sigma Aldrich, St. Louis, MI, USA) in tetraethyl orthosilicate (Sigma Aldrich, St. Louis, MI, USA), which was mixed using a magnetic stirrer for several hours until it became a homogeneous pale-yellow transparent solution.

2.2. Er-Based Contrast Agent Characterization. Particle and aggregate sizes of the “raw” and sonicated Er_2O_3 powder were evaluated visually using confocal fluorescence microscopy. Prior to sonication, drops of raw Er_2O_3 powder mixed within the two-part silicone elastomer were dispensed on a glass bottom microwell dish (MatTek Corporation, Ashland, MA, USA). Following sonication, drops of the prepared Er-based suspension were placed on a separate microwell dish. Samples were analyzed using confocal fluorescence microscopy (Leica DMI8, Wetzlar, Germany), an Ar 488 nm laser for excitation, and emission bandwidths of 493–739 nm. To visualize particle sizes within the nonsonicated “raw” sample and sonicated suspension, a 20x (HC PL APO CS2 20x/0.75 DRY) and 63x (HC PL APO CS2 63x/1.40 OIL) objective lens were used, respectively.

Dynamic light scattering (DLS) was used to quantify the size distribution of the prepared Er-based suspension. A 10% (v/v) dilution of the suspension in MV-Diluent was prepared and analyzed with DLS (ZetaSizer Nano Instrument, Malvern Instruments Ltd., Malvern, UK). Measurements were performed at room temperature (25°C) in a quartz cuvette (1 mg/mL).

The viscosity of the contrast agent was measured using a lab-based Modular Compact Rheometer (MCR 302, Anton Paar, Graz, Austria); the measured viscosity was used to correct the DLS measurements.

2.3. Animals. All animal studies were approved by the Animal Use Subcommittee at Western University (protocol #2015-018). Five male C57BL/6 mice (~30 g) were used for this study. The mouse model was selected to demonstrate the capability of the Er_2O_3 contrast agent to perfuse the microvasculature of the smallest of the commonly used small-animal models. Anesthetized mice were first exsanguinated with sterile saline followed by perfusion with the Er contrast agent. To prevent blood clot formation during exsanguination, sterile 0.9% (w/v) saline was heparinized to 0.4% (1 mL of heparin (Sandoz, QC, Canada) in 250 mL saline). Sterile tubing (Baxter Canada, Mississauga, ON, Canada), 1.8 m in length, was used to connect the saline bag to a blunted 21 G \times 3/4” butterfly catheter (BD, Franklin Lakes, NJ, USA). The saline IV bag was hung 127 cm above the surgery table, thereby providing a pressure of 94 mmHg. Five minutes prior to the start of the procedure the mice were given a 100 μ l intraperitoneal injection of heparin. After induction of anesthesia (3% isoflurane (Baxter Canada, Mississauga, ON, Canada) in O_2 at a rate of 2 mL/min) an incision was made along the thoracic cavity exposing the heart. The butterfly catheter was carefully inserted into the left ventricle parallel to the septum. A drop of cyanoacrylate (Krazy Glue, Elmer’s Products, Atlanta, GA, USA) was applied at the entry point of the catheter into the left ventricle to avoid accidental piercing of the septum. The right atrium was clipped to allow for circulatory system drainage. The heparinized saline

solution was perfused throughout the circulatory system for 10 minutes to ensure complete removal of the blood.

During saline perfusion, 3.8 mL (12.7% v/v) of curing agent was added to 36.2 mL Er_2O_3 -based silicone elastomer suspension and vortexed (VWR® Fixed Speed Vortex Mixer, Radnor, PA, USA) continuously for 8 minutes. The contrast agent was injected into an empty IV bag (with separate 1.8 m of surgical tubing) and hung 160 cm above the mice (129 mm Hg). While this value is greater than the mean arterial pressure (MAP) of mice (~103 mm Hg) [29, 30], it was chosen to ensure complete perfusion of the animal before the contrast agent cured. Furthermore, the perfusion pressure used in this study is significantly lower than the >150 mmHg used in prior studies using the lead-based Microfil agent [22, 31–33]. Perfusion at a pressure more closely matched to peak systolic pressure (i.e., ~120 mmHg) reduces the risk of vascular dilation and capillary rupture. The contrast agent was let to freely perfuse through the animal until completely cured, which occurred approximately ~35 minutes after start of perfusion. Following contrast agent curing, mice were placed in 10% neutral buffered formalin overnight, prior to micro-CT scanning.

2.4. Data Collection and Analysis. Whole body mouse scans were acquired with a preclinical micro-CT scanner (Vision 120, GE Healthcare, London, ON, Canada). The scan parameters were 90 kVp (no added filtration), 40 mA, 900 views, 0.4° increment angle over 360°, geometric magnification of 1.13, and 16 ms exposure, resulting in a total exposure time of 14.4 s and 576 mAs. Including the time required for gantry motion and recording of image projections, the total acquisition time was 5 minutes. The projection images were binned 2 \times 2 prior to reconstruction for a final isotropic voxel spacing of 100 μ m.

Higher resolution scans of the hindlimb regions were acquired on a specimen scanner (Locus, GE Healthcare, London, ON, Canada) using a 3 hr scan protocol (900 views, 80 kVp, 80 μ A, no added filtration, 0.4° increment angle over 360°, geometric magnification of 1.41, 15-frame averaging, and 2 \times 2 binning for a final isotropic voxel spacing of 40 μ m). To prevent sample motion during these high-resolution image acquisitions, the perfused mouse was placed in a 50 mL tube.

Confirmation of perfusion of microvessels (i.e., <10 μ m) was achieved by high-resolution micro-CT. Fabricated microvessel constructs or synthetic capillaries have been utilized to evaluate microvessel perfusions in the past [34, 35], but fabricating synthetic vessels with diameters on the order of 10 μ m remains technically challenging. Fortunately, the mouse kidney is a well-characterized organ system, with known vessel diameters ranging from the renal artery (~0.3 mm) to capillaries (~10 μ m) [36, 37]. The kidney contains many glomeruli (responsible for the waste removal and blood filtering), which are comprised of capillaries in a bundle of ~75 μ m diameter [38]. Therefore, an excised Er_2O_3 -perfused kidney was embedded in paraffin in a 1.2 mL tube (Corning®, Corning, NY, USA) and scanned with a specimen scanner (Locus SP, GE Healthcare, London, ON, Canada), using a 16 hr protocol. Scan parameters were 80 kVp, 80 μ A, 900 projections, no added filtration, 0.4° increment angle over 360°,

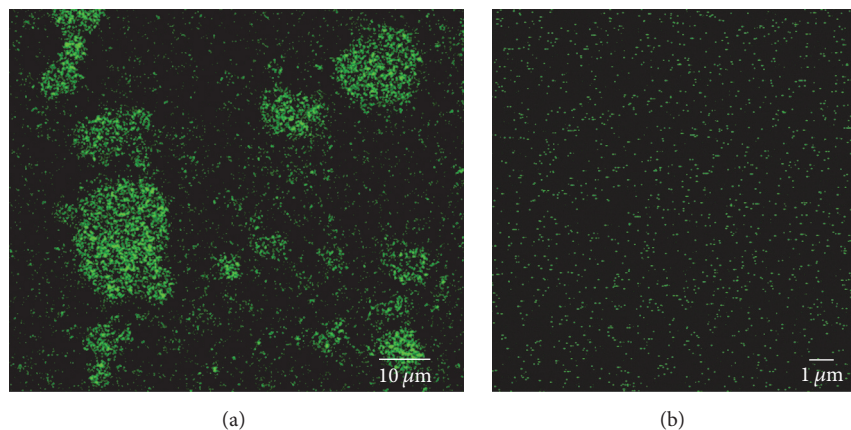


FIGURE 1: Confocal fluorescence microscopy images of (a) nonsonicated raw Er_2O_3 powder naturally aggregated to large microsized ($>10\ \mu\text{m}$) particles when mixed within the two-part silicone elastomer, making the suspension not suitable for microvascular perfusion. However, with sonication, nanosized ($\sim 70\ \text{nm}$) particles were achieved (b).

geometric magnification of 3.83, 14-frame averaging, and 1×1 binning for a final isotropic spatial resolution of $4.8\ \mu\text{m}$.

The micro-CT scanners used in this study were all equipped with a CsI-based energy-weighted detector. It has been shown that the peak response of these detectors [39] is very close to the absorption K-edge of Er (57.5 keV), making them ideally suited for detection of an erbium-based contrast agent.

Each of the scans contained calibrators of water and air, which were used for image calibration and conversion into Hounsfield units (HU). This allowed us to quantify the amount of contrast enhancement of perfused vasculature, based on the the CT signal level in HU within various organs throughout the vascular system. Using 3D visualization and analysis software (MicroView, GE Healthcare, London, ON, Canada), regions of interest (ROI) $500 \times 500 \times 500\ \mu\text{m}$ were generated in each region and the mean HU values recorded. Specifically, for all mice, the mean HU was determined from the heart (left ventricle), testes, and inferior vena cava (IVC), as they represented the beginning, middle, and end of the perfusion pathway, respectively. The CT signal levels within the selected organs were compared to cortical bone within the diaphysis region (i.e., the densest endogenous contrast) and a commercially available lead-based contrast agent. A rat hindlimb previously perfused with the widely used and commercially available lead-based contrast agent (Microfil MV-122, Flowtech Inc., Caver, MA, USA) was scanned using the $100\ \mu\text{m}$ acquisition protocol.

All statistical analyses were performed using Prism 6 (GraphPad Software Inc., La Jolla, CA, USA). Repeated measures ANOVA was used to test for statistical differences between all Er-based contrast-enhanced regions (i.e., heart, testes, and IVC) and cortical bone. In a separate test, one-way unpaired ANOVA was performed to compare the mean attenuation in Er-perfused vessels against cortical bone and the Microfil MV122-perfused rat femoral artery. Statistical differences were noted if a $p < 0.05$ was achieved.

3. Results

3.1. Efficacy of an Ex Vivo Er-Based Contrast Agent for Vascular Perfusion. An effective preclinical postmortem X-ray compatible vascular contrast agent must be comprised of small, X-ray attenuating particles homogeneously suspended within a low viscosity medium. These characteristics will ensure uniform contrast enhancement of perfused vasculature, including microvessels with diameter $< 10\ \mu\text{m}$ (i.e., capillaries). Automated segmentation algorithms, which are typically based on grey-scale levels, require homogeneous perfusion of microvessels to effectively separate perfused vasculature from surrounding tissues, so it is essential to employ an appropriate particle size, uniformly distributed in the carrier medium.

Ultrasonic cavitation (sonication) was used to successfully break up large aggregates of Er_2O_3 to nm-sized aggregates, which could be homogeneously incorporated within the two-part silicone matrix. Following intense sonication, a visually homogeneous suspension of 13.3% w/v Er_2O_3 within the two-part silicone elastomer was achieved. The Er_2O_3 NPs were found to remain in suspension for several days, allowing for the contrast agent to be prepared several days prior to use. Confocal fluorescence microscopy visually confirmed that the size of the sonicated nanoparticles within the Er_2O_3 contrast agent suspension (Figure 1(b)) was less than $100\ \text{nm}$ —a size that can pass easily through the microvessels of any vascular system.

The ability of a contrast agent to perfuse the microvasculature also depends on its viscosity. Measuring the viscosity of the uncured Er-based contrast agent—at $19.2\ \text{mPa}\cdot\text{s}$ —demonstrated agreement with the $20\ \text{mPa}\cdot\text{s}$ viscosity reported by the manufacturer of the two-part silicone elastomer, confirming that the uncured Er_2O_3 contrast agent is able to pass through small vessels under standard perfusion pressures.

Based on the measured viscosity of $19.2\ \text{mPa}\cdot\text{s}$, the DLS measurement reported a Gaussian particle size distribution

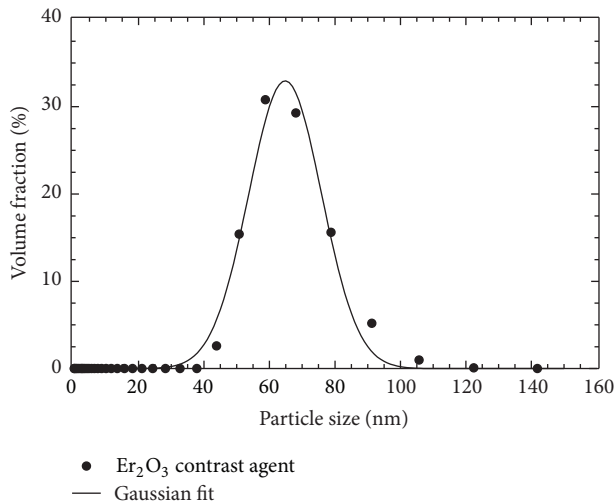


FIGURE 2: Dynamic light scattering (DLS) results demonstrating the particle size distribution of a sample of the Er_2O_3 contrast agent. Average particle size is 72.2 ± 2.2 nm. Results of a suspension that was mixed and subsequently stored for 2 years are shown in S1.

with mean hydrodynamic diameter of 64.8 nm, standard deviation of 11.1 nm, and a range from 44 to 122 nm (Figures 2 and S1; see Supplementary Material available online at <https://doi.org/10.1155/2017/7368384>). Measurements of particle size and carrier viscosity indicated that the prepared Er_2O_3 suspension should easily pass through microvessels; this aspect of performance was further evaluated by micro-CT imaging of intact perfused mice.

Whole Er_2O_3 -perfused C57Bl/6 mice scanned with $50 \mu\text{m}$ isotropic voxel spacing, and rebinned 2×2 to a final resolution of $100 \mu\text{m}$, revealed a uniform and homogeneous distribution of the cured Er_2O_3 contrast agent within the vasculature throughout the entire perfused mouse (Figure 3). The vasculature displayed enhanced contrast in comparison to surrounding tissues throughout an intact animal; importantly the attenuation of the contrasted vessels was higher than that of bone.

Scans of Er contrast-perfused hindlimbs were acquired with $20 \mu\text{m}$ isotropic voxel spacing and subsequently rebinned 2×2 for a final resolution of $40 \mu\text{m}$ (Figure 4), to observe the smaller vasculature next to the dense bony structures of the femur and tibia. From these results, we were able to clearly see a feeding artery that runs within (Figure 4(a)) and along (Figure 4(b)) the entire length of each long bone. At this higher resolution, smaller structures such as a foramen (i.e., an opening for blood vessels to enter bone) can be visualized (Figure 4(c)). The ability to differentiate the foramen from the vessel running through it is particularly noteworthy, as this is not possible with other contrast agents that have lower attenuation coefficients. The observed perfusion of the venous system (Figure 4(a) yellow arrows) suggests successful perfusion of the capillaries, which is further supported by the lack of visible contrast agent pooling within the interstitial space (pooling might have been observed if overpressurization during perfusion had caused microvessel rupture).

3.2. Visualization of Capillary Bed Perfusion. The results of the high-resolution micro-CT scan revealed that the Er_2O_3 contrast agent successfully perfused the entire continuous, well-ordered vascular tree of the kidney (Figure 5). The contrast enhancement of the vasculature was sufficiently high, such that a single grey-scale threshold separated perfused vasculature from surrounding tissues, allowing for the generation of 3D images of the kidney vessel microarchitecture (Figure 5(b)). The virtual Er_2O_3 vascular “cast” (Figures 5(a) and 5(b)) showed complete perfusion from the abdominal aorta (i.e., the main feeding vessel) down to the 6th and 7th arterial branches (i.e., glomeruli afferent arterioles). Previous research has shown that mouse glomeruli afferent arterioles can be as small as $\sim 13 \mu\text{m}$ [36]; thus, visualization of individual glomeruli (i.e., several capillaries) suggests that our contrast agent is able to perfuse structures $< 13 \mu\text{m}$ (Figures 5(c) and 5(d)). While previous research has shown perfusion of the kidney down to the afferent arterioles [36, 40–42] using a commercially available lead-based contrast agent, the main advantage of the Er_2O_3 -based contrast agent is its ability to provide higher contrast and SNR.

3.3. Contrast Enhancement Provided by the Er-Based Contrast Agent in Micro-CT. The measured mean CT values for the heart (4094 ± 264 HU), testes (4107 ± 182 HU), and IVC (4001 ± 305 HU), compared in Figure 6, showed no significant difference ($p = 0.3940$) between these three regions. On the other hand, the mean signal from cortical bone (2359 ± 207 HU) and the lead-based contrast agent Microfil MV-122 (2683 ± 77.6 HU) were significantly lower than the signal from the Er contrast-agent perfused vasculature ($p < 0.006$ and $p < 0.0001$ for bone and Microfil, respectively). The approximately 1400 HU difference in signal between that provided by the Er_2O_3 -based contrast agent and cortical bone will aid in facilitating the automatic segmentation of vessels from surrounding bone, which is not possible when commercially available contrast agents, such as Microfil MV 122, are used.

4. Discussion

We have demonstrated a methodology for the homogeneous incorporation of Er_2O_3 nanoparticles within a two-part silicone elastomer, forming a colloidal suspension capable of providing high X-ray attenuation that can facilitate the visualization and characterization of microvessels within a small-animal model. In this study, we characterized and investigated the capabilities of the custom *ex vivo* Er-based vascular perfusion contrast agent.

Ultrasonic cavitation successfully broke down large naturally occurring Er_2O_3 aggregates (i.e., $> 100 \mu\text{m}$) into nm-sized particles (Figures 1(b) and 2) suspended within a silicone carrier. The prepared suspension was determined to possess low viscosity and a narrow particle size distribution that would facilitate the perfusion of intact whole body mice (Figure 3). Micro-CT scans acquired with both 50 and $20 \mu\text{m}$ isotropic voxel spacings revealed whole-mouse perfusion and higher-ordered vascular branching (i.e., 1st to 3rd order) and visualization of vessels within bone (Figures 3 and 4).

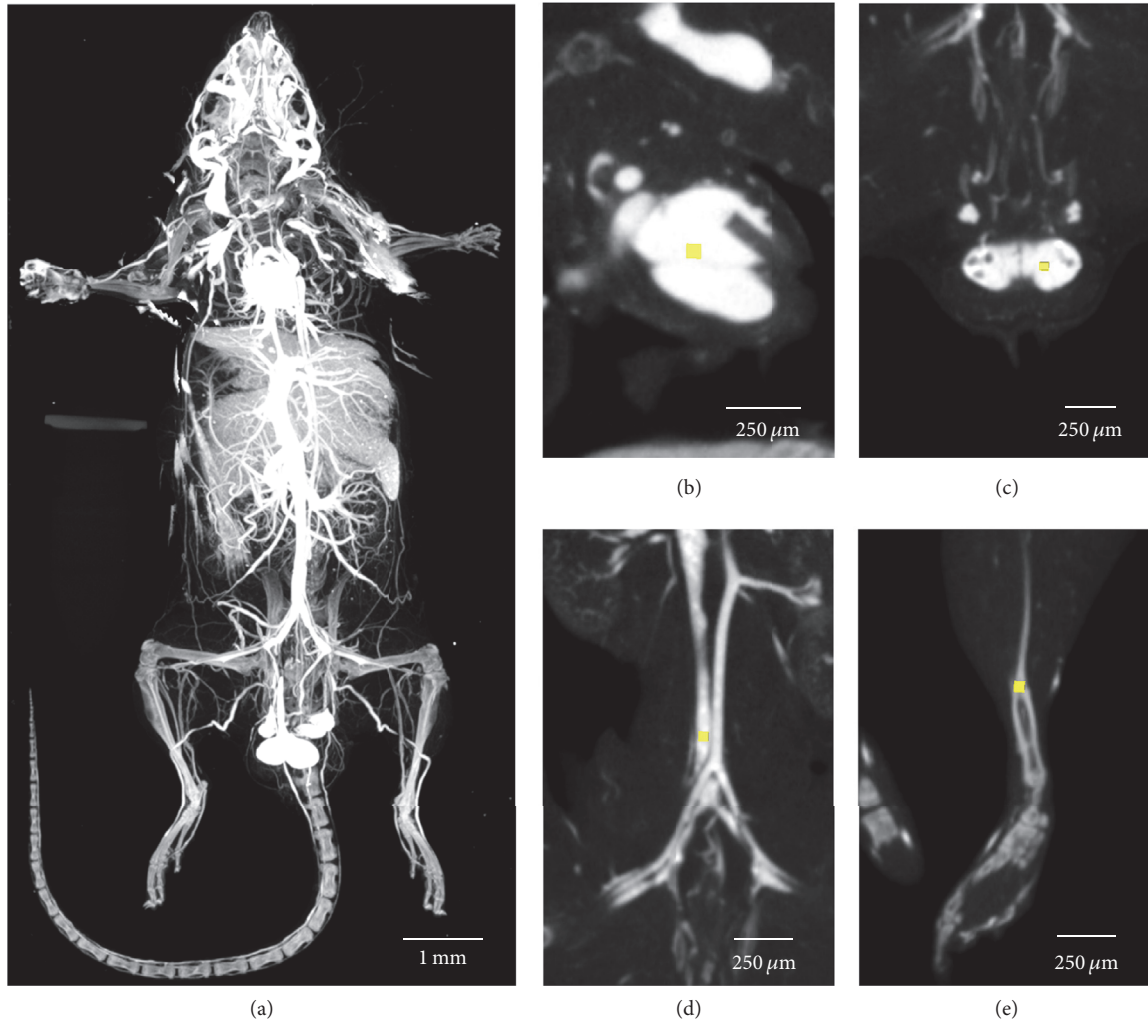


FIGURE 3: Rebinned $100\ \mu\text{m}$ voxel images where the (a) maximum intensity projection (MIP) of a whole body perfused mouse demonstrates that the attenuation of the Er_2O_3 contrast agent in the vasculature is higher than the mouse's skeletal structure. Quantitative measurements of attenuation (in HU) were obtained from regions drawn within heart (b), testes (c), inferior vena cava (d), and cortical bone (e).

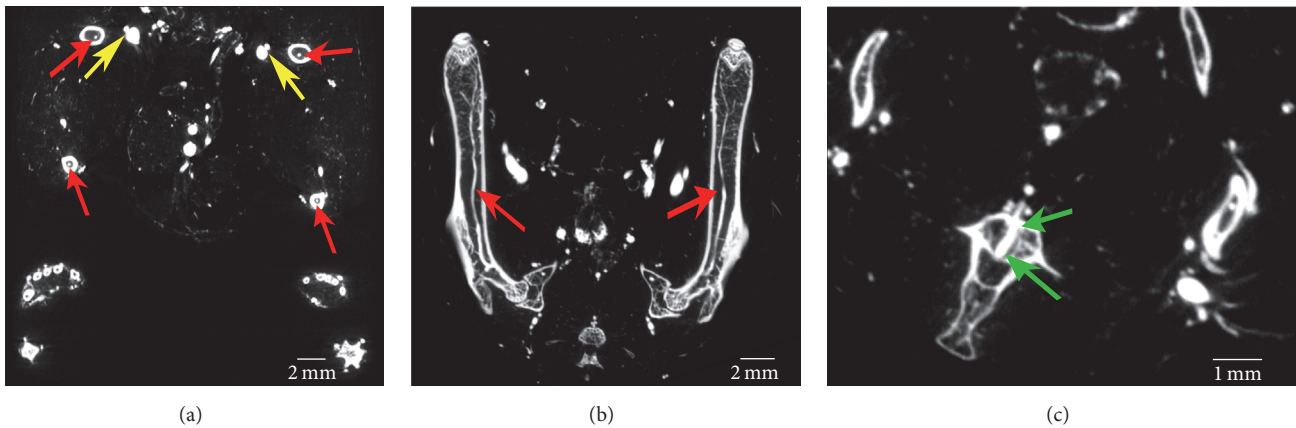


FIGURE 4: Multiplanar reformatted images at $40\ \mu\text{m}$, resulting from 2×2 rebinning of $20\ \mu\text{m}$ acquired micro-CT scans, clearly depict the ability to visualize the extent of the nutrient arteries, which run along the tibia and femur. Red arrows highlight the nutrient arteries in cross-section in (a) and along their entire length in (b). At this resolution the depiction of parallel arteries and veins (yellow arrows) indicates successful perfusion through the capillary network. The ability to visualize vessels as they pass through a foramen (green arrows) into bone is depicted in (c).

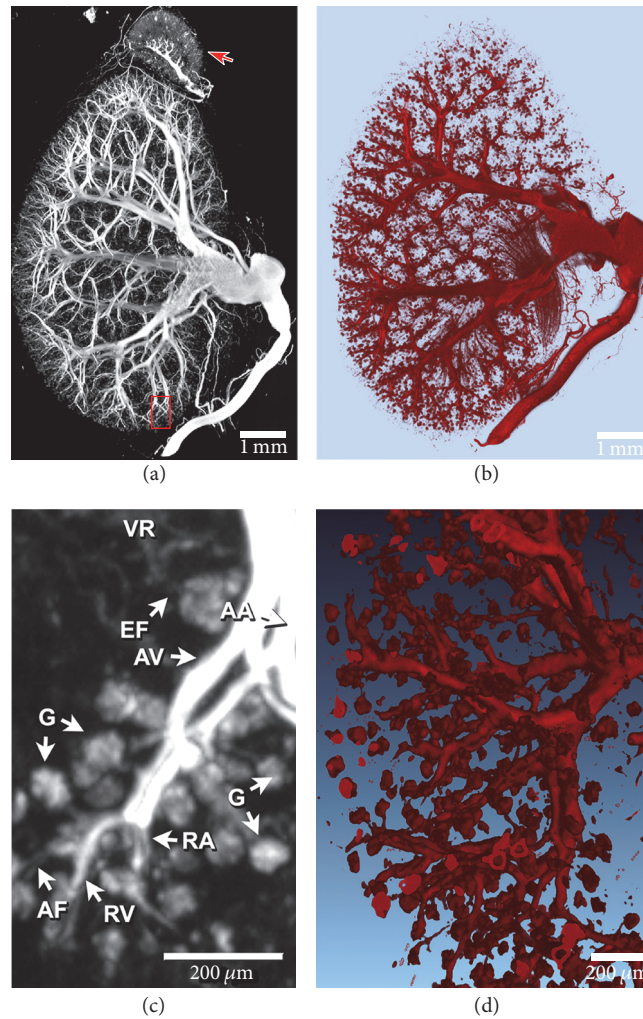


FIGURE 5: (a) MIP of an entire mouse kidney and attached adrenal gland (arrow) perfused with the new Er contrast agent. (b) 3D rendering of the perfused kidney with a plane cut to demonstrate an entire intact vascular tree. (c) Magnified 0.35 mm thick slice MIP of the area outlined in red in (a), demonstrating 6-7th level arterial branching. (d) 3D rendering of the terminal arteriole branches, ending in the glomeruli (the kidney's spherical capillary bed). G: glomeruli; AF: afferent arteriole; EF: efferent arteriole; RA: cruciate radial artery; RV: cruciate radial vein; AA: arcuate artery; AV: arcuate vein; and VR: vasa recta.

High-resolution scans with $5\ \mu\text{m}$ spatial resolution demonstrated well-characterized vascular microarchitecture within a perfused kidney, with observed vascular filling down to vessels $<13\ \mu\text{m}$ in diameter and contrast enhancement of capillary beds (i.e., glomeruli, Figure 5). Additionally, the attenuation of the Er-based contrast agent was found to be significantly higher than that of cortical bone (i.e., the densest naturally occurring substance within our samples) and the commonly used lead-based Microfil (MV-122) vascular contrast agent (Figure 6). This study clearly demonstrates the efficacy of the custom Er-based suspension as an *ex vivo* micro-CT vascular perfusion contrast agent.

An important benefit of the presented Er-based contrast agent is an X-ray attenuation coefficient that is significantly higher than that of both bone and other existing contrast agents. This difference facilitates the separation of microvessels from both soft tissue and bone in the images and can also

result in a reduction of scan time. While shorter scans result in a greater amount of noise [10], the higher contrast between the Er contrast agent within the vasculature and surrounding tissue ensures that SNR remains high despite the shorter scan times. The approach used to incorporate the Er nanoparticles within the suspension (i.e., ultrasonic cavitation) renders the approach amenable to the production of custom contrast agents of varying elemental compositions and concentrations. Furthermore, silicone-compatible colorants can also be introduced within the silicone media to allow for the customization of the contrast agents' visual appearance against tissue; this may be useful for macroscopic visualization and postmortem histological analysis.

In the current implementation, each working volume of contrast agent (i.e., 30 ml) is prepared individually, requiring approximately one hour of operator time. Larger volumes of contrast agent could be prepared in advance, with the

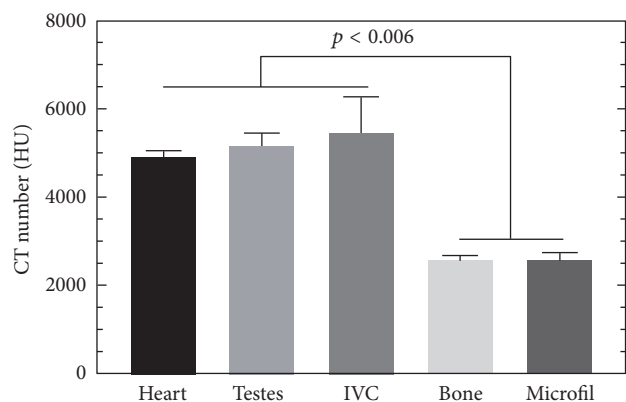


FIGURE 6: Heart, testes, and inferior vena cava (IVC) were chosen to represent the start, middle, and end of the perfusion route. The attenuation (HU) of the Er_2O_3 -based contrast agent in all three regions was significantly higher than that of cortical bone ($p < 0.006$, repeated measures ANOVA). Importantly, the attenuation of the Er_2O_3 -enhanced vasculature was significantly higher than that commercially available lead-based Microfil MV122 (one-way ANOVA, $p < 0.0001$), while there was no difference between Microfil MV122 and cortical bone ($p > 0.9999$).

curing catalyst being added just prior to usage. In this case, additional sonication may be required to ensure resuspension of aggregated particles (Figure S1).

As with other cast-forming contrast agents (e.g., Microfil) the new Er-based contrast agent is limited to applications of postmortem vascular analysis at study endpoints. This limitation requires that larger cohorts of animals are needed to assess changes to the vasculature over periods of time. An *in vivo* contrast agent would make investigations with reduced sample size possible and allow for the study of vascular changes within the same animal over time; however, development of an *in vivo* contrast agent is not within the scope of this study. Currently, there exist *in vivo* contrast agents that reside within the blood pool for extended periods of time [43, 44]; thus, we expect that the incorporation of Er into an *in vivo* agent is possible.

5. Conclusions

We have demonstrated the effectiveness of an Er-based suspension as a single-energy X-ray vascular contrast agent that significantly enhances the contrast—in comparison to surrounding dense bone and commercially available lead-based contrast agents (Figure 6)—of perfused vasculature within small animals (Figures 3–5). With an absorption K-edge at 57.5 keV, the Er-based contrast agent is also ideally suited for dual-energy micro-computed tomography (DECT) on a large installed base of high-resolution preclinical micro-CT machines that operate at up to 90 kVp. The combination of the Er_2O_3 -based vascular perfusion contrast agent with optimized DECT scan protocols and spectral shaping (using X-ray filtration) would facilitate rapid and automatic quantitative segmentation of perfused vasculature from surrounding tissues [26], a process that is otherwise difficult due to partial volume effects that can limit traditional single-energy CT

scans. Dual-energy CT-based material separation has been shown to be beneficial in studying a range of diseases in clinical applications (i.e., gout, cardiovascular, and cancer) [45–47], by allowing for the quantitative separation of the material of interest from surrounding tissues. The novel contrast agent that we describe has the potential to provide these advantages of DECT-based quantification and segmentation for preclinical investigations of vascular changes in small-animal models.

Data Access

All data needed to evaluate the conclusions in the paper are present in the paper and/or the Supplementary Materials. Additional data related to this paper may be requested from the authors.

Conflicts of Interest

The authors declare that they have no conflicts of interest.

Authors' Contributions

Justin J. Tse developed the concept, performed the experiments, collected and analyzed the results, and wrote the manuscript. P. Joy Dunmore-Buyze aided in experiments and data collection. Maria Drangova and David W. Holdsworth helped devise the experiments. All authors have read, edited, and approved the completed manuscript.

Acknowledgments

This work was supported in part by grants from the Canadian Institute for Health Research (CIHR) Grant no. 133575 and FDN 148474, the Heart and Stroke Foundation of Canada Grant G-14-005959, and the Ontario Research Fund. Justin J. Tse is a CIHR Graduate Fellow in Musculoskeletal Health Research and has received funding from the Joint Motion Program (JuMP)—a CIHR training program in Musculoskeletal Health Research and leadership and part of a collaborative graduate program in Musculoskeletal Health Research; Justin J. Tse is also a Member of the Bone and Joint Institute at Western University, Canada; and Justin J. Tse is a recipient of the Natural Sciences and Engineering Research Council of Canada Alexander Graham Bell Canada graduate scholarship (NSERC CGS-D) and an Ontario Graduate Scholarship (OGS). Maria Drangova is Career Scientist of the Heart and Stroke Foundation of Ontario. The authors would like to thank Dr. Elizabeth Gillies, Dr. Solmaz Karamdoust, and Charmaine Cruje for their technical assistance and for providing the probe sonicator and DLS machine. They also thank Dr. Flávio Beraldo for his assistance in the collection of confocal fluorescence microscopy images and Dr. John de Bruyn for performing the viscosity measurements. Much appreciation is also given to Zhang Nong and Matthew Lowerison for mouse surgeries/perfusions and Dr. Geoff Pickering for the use of his animal perfusion laboratory.

References

- [1] A. J. LeBlanc and J. B. Hoying, "Adaptation of the coronary microcirculation in aging," *Microcirculation*, vol. 23, no. 2, pp. 157–167, 2016.
- [2] C. T. Ambrose, "The role of capillaries in the lesser ailments of old age and in Alzheimer's disease and vascular dementia: The potential of pro-therapeutic angiogenesis," *Journal of Alzheimer's Disease*, vol. 54, no. 1, pp. 31–43, 2016.
- [3] Z. Emrani, A. Karbalaie, A. Fatemi, M. Etehadtavakol, and B.-E. Erlandsson, "Capillary density: An important parameter in nailfold capillaroscopy," *Microvascular Research*, vol. 109, pp. 7–18, 2017.
- [4] C. N. Hall, C. Reynell, B. Gesslein et al., "Capillary pericytes regulate cerebral blood flow in health and disease," *Nature*, vol. 508, no. 1, pp. 55–60, 2014.
- [5] G. Katsuumi, I. Shimizu, Y. Yoshida, and T. Minamino, "The pathological role of vascular aging in cardio-metabolic disorder," *Inflammation and Regeneration*, vol. 36, article 16, 2016.
- [6] N. L. Ford, K. C. Graham, A. C. Groom, I. C. MacDonald, A. F. Chambers, and D. W. Holdsworth, "Time-course characterization of the computed tomography contrast enhancement of an iodinated blood-pool contrast agent in mice using a volumetric flat-panel equipped computed tomography scanner," *Investigative Radiology*, vol. 41, no. 4, pp. 384–390, 2006.
- [7] C. T. Badea, M. Drangova, D. W. Holdsworth, and G. A. Johnson, "In vivo small-animal imaging using micro-CT and digital subtraction angiography," *Physics in Medicine and Biology*, vol. 53, no. 19, pp. R319–R350, 2008.
- [8] L. Zagorchev, P. Oses, Z. W. Zhuang et al., "Micro computed tomography for vascular exploration," *Journal of Angiogenesis Research*, vol. 2, no. 1, article 7, 2010.
- [9] Y. Ding, W. O. C. Ward, T. Wästerlid et al., "Three-dimensional vessel segmentation using a novel combinatory filter framework," *Physics in Medicine and Biology*, vol. 59, no. 22, pp. 7013–7029, 2014.
- [10] N. L. Ford, M. M. Thornton, and D. W. Holdsworth, "Fundamental image quality limits for microcomputed tomography in small animals," *Medical Physics*, vol. 30, no. 11, pp. 2869–2877, 2003.
- [11] G. J. Schwartz and S. L. Furth, "Glomerular filtration rate measurement and estimation in chronic kidney disease," *Pediatric Nephrology*, vol. 22, no. 11, pp. 1839–1848, 2007.
- [12] T. S. Desser, D. L. Rubin, H. Muller, G. L. McIntire, E. R. Bacon, and J. L. Toner, "Blood pool and liver enhancement in CT with liposomal iodixanol: Comparison with iohexol," *Academic Radiology*, vol. 6, no. 3, pp. 176–183, 1999.
- [13] S. A. Detombe, J. Dunmore-Buyze, and M. Drangova, "Evaluation of eXIA 160XL cardiac-related enhancement in C57BL/6 and BALB/c mice using micro-CT," *Contrast Media & Molecular Imaging*, vol. 7, no. 2, pp. 240–246, 2012.
- [14] P. Blery, P. Pilet, A. V. Bossche et al., "Vascular imaging with contrast agent in hard and soft tissues using microcomputed-tomography," *Journal of Microscopy*, vol. 262, no. 1, pp. 40–49, 2016.
- [15] S. A. Detombe, N. L. Ford, F. Xiang, X. Lu, Q. Feng, and M. Drangova, "Longitudinal follow-up of cardiac structure and functional changes in an infarct mouse model using retrospectively gated micro-computed tomography," *Investigative Radiology*, vol. 43, no. 7, pp. 520–529, 2008.
- [16] A. Y. Sheikh, K. E. A. van der Bogt, T. C. Doyle et al., "Micro-CT for characterization of murine CV disease models," *JACC: Cardiovascular Imaging*, vol. 3, no. 7, pp. 783–785, 2010.
- [17] M. D. Bentley, M. C. Ortiz, E. L. Ritman, and J. C. Romero, "The use of microcomputed tomography to study microvasculature in small rodents," *American Journal of Physiology—Regulatory, Integrative and Comparative Physiology*, vol. 282, no. 5, pp. R1267–R1279, 2002.
- [18] D. S. Perrien, M. A. Saleh, K. Takahashi et al., "Novel methods for microCT-based analyses of vasculature in the renal cortex reveal a loss of perfusable arterioles and glomeruli in eNOS-/- mice," *BMC Nephrology*, vol. 17, no. 1, pp. 17–24, 2016.
- [19] K. C. Graham, N. L. Ford, L. T. MacKenzie et al., "Noninvasive quantification of tumor volume in preclinical liver metastasis models using contrast-enhanced X-ray computed tomography," *Investigative Radiology*, vol. 43, no. 2, pp. 92–99, 2008.
- [20] H. Nyangoga, P. Mercier, H. Libouban, M. F. Baslé, and D. Chappard, "Three-dimensional characterization of the vascular bed in bone metastasis of the rat by microcomputed tomography (MicroCT)," *PLoS ONE*, vol. 6, no. 3, Article ID e17336, 2011.
- [21] M. Zamir, J. Twynstra, A. J. Vercnocke et al., "Intrinsic microvasculature of the sciatic nerve in the rat," *Journal of the Peripheral Nervous System*, vol. 17, no. 4, pp. 377–384, 2012.
- [22] S. Ghanavati, L. X. Yu, J. P. Lerch, and J. G. Sled, "A perfusion procedure for imaging of the mouse cerebral vasculature by X-ray micro-CT," *Journal of Neuroscience Methods*, vol. 221, pp. 70–77, 2014.
- [23] M. Cavaglia, S. M. Dombrowski, J. Drazba, A. Vasanji, P. M. Bokesch, and D. Janigro, "Regional variation in brain capillary density and vascular response to ischemia," *Brain Research*, vol. 910, no. 1–2, pp. 81–93, 2001.
- [24] C. L. Duvall, W. R. Taylor, D. Weiss, and R. E. Guldberg, "Quantitative microcomputed tomography analysis of collateral vessel development after ischemic injury," *American Journal of Physiology—Heart and Circulatory Physiology*, vol. 287, no. 1, pp. H302–H310, 2004.
- [25] L. Józsa, M. U. K. Lehto, M. Järvinen, M. Kvist, A. Réffy, and P. Kannus, "A comparative study of methods for demonstration and quantification of capillaries in skeletal muscle," *Acta Histochemica*, vol. 94, no. 1, pp. 89–96, 1993.
- [26] P. V. Granton, S. I. Pollmann, N. L. Ford, M. Drangova, and D. W. Holdsworth, "Implementation of dual- and triple-energy cone-beam micro-CT for postreconstruction material decomposition," *Medical Physics*, vol. 35, no. 11, pp. 5030–5042, 2008.
- [27] H.-Y. Kim, J. O. Sofo, D. Velegol, M. W. Cole, and A. A. Lucas, "Van der waals dispersion forces between dielectric nanoclusters," *Langmuir*, vol. 23, no. 4, pp. 1735–1740, 2007.
- [28] N. M. Kovalchuk and V. M. Starov, "Aggregation in colloidal suspensions: effect of colloidal forces and hydrodynamic interactions," *Advances in Colloid and Interface Science*, vol. 179–182, pp. 99–106, 2012.
- [29] X. Zhao, D. Ho, S. Gao, C. Hong, D. E. Vatner, and S. F. Vatner, "Arterial pressure monitoring in mice," *Current Protocols in Mouse Biology*, vol. 1, pp. 105–122, 2011.
- [30] T. L. Cunliffe-Beamer, "Health delivery and quality assurance programs for mice," in *The Mouse in Biomedical Research*, J. D. Small and J. G. Fox, Eds., pp. 401–437, Academic Press, 1983.
- [31] M. Marxen, M. M. Thornton, C. B. Chiarot et al., "MicroCT scanner performance and considerations for vascular specimen imaging," *Medical Physics*, vol. 31, no. 2, pp. 305–313, 2004.
- [32] A. Dorr, J. G. Sled, and N. Kabani, "Three-dimensional cerebral vasculature of the CBA mouse brain: a magnetic resonance imaging and micro computed tomography study," *NeuroImage*, vol. 35, no. 4, pp. 1409–1423, 2007.

- [33] D. Sarhaddi, B. Poushanchi, M. Merati et al., "Validation of histologic bone analysis following Microfil vessel perfusion," *Journal of Histotechnology*, vol. 35, no. 4, pp. 180–183, 2012.
- [34] D. B. Berry, S. You, J. Warner, L. R. Frank, S. Chen, and S. R. Ward, "A 3D tissue-printing approach for validation of diffusion tensor imaging in skeletal muscle," *Tissue Engineering Part A*, vol. 23, no. 17-18, pp. 980–988, 2017.
- [35] K. Sarveswaran, V. Kurz, Z. Dong, T. Tanaka, S. Penny, and G. Timp, "Synthetic capillaries to control microscopic blood flow," *Scientific Reports*, vol. 6, Article ID 21885, 2016.
- [36] S. X. Vasquez, F. Gao, F. Su et al., "Optimization of microCT imaging and blood vessel diameter quantitation of preclinical specimen vasculature with radiopaque polymer injection medium," *PLoS ONE*, vol. 6, no. 4, Article ID e19099, 2011.
- [37] B. J. Hillman, S. M. Lee, and G. Wilson, "In vivo barium microangiography in the mouse," *Investigative Radiology*, vol. 15, no. 2, pp. 145–147, 1980.
- [38] D. A. Rytand, "The number and size of mammalian glomeruli as related to kidney and to body weight, with methods for their enumeration and measurement," *American Journal of Anatomy*, vol. 62, no. 4, pp. 507–520, 1938.
- [39] P. V. Granton, M. Podesta, G. Landry, S. Nijsten, G. Bootsma, and F. Verhaegen, "A combined dose calculation and verification method for a small animal precision irradiator based on onboard imaging," *Medical Physics*, vol. 39, no. 7, pp. 4155–4166, 2012.
- [40] R. Xu, F. Franchi, B. Miller et al., "Polycystic kidneys have decreased vascular density: a micro-CT study," *Microcirculation*, vol. 20, no. 2, pp. 183–189, 2013.
- [41] R. Savai, A. C. Langheinrich, R. T. Schermuly et al., "Evaluation of angiogenesis using micro-computed tomography in a xenograft mouse model of lung cancer," *Neoplasia*, vol. 11, no. 1, pp. 48–56, 2009.
- [42] A. Garcia-Sanz, A. Rodriguez-Barbero, M. D. Bentley, E. L. Ritman, and J. C. Romero, "Three-dimensional microcomputed tomography of renal vasculature in rats," *Hypertension*, vol. 31, no. 1, pp. 440–444, 1998.
- [43] S. You, H.-Y. Jung, C. Lee et al., "High-performance dendritic contrast agents for X-ray computed tomography imaging using potent tetraiodobenzene derivatives," *Journal of Controlled Release*, vol. 226, pp. 258–267, 2016.
- [44] Y. Zou, Y. Wei, G. Wang et al., "Nanopolymersomes with an ultrahigh iodine content for high-performance X-ray computed tomography imaging in vivo," *Advanced Materials*, vol. 29, no. 10, Article ID 1603997, 2017.
- [45] M. Uhrig, D. Simons, D. Bonekamp, and H.-P. Schlemmer, "Improved detection of melanoma metastases by iodine maps from dual energy CT," *European Journal of Radiology*, vol. 90, pp. 27–33, 2017.
- [46] I. Danad, B. Ó. Hartaigh, and J. K. Min, "Dual-energy computed tomography for detection of coronary artery disease," *Expert Review of Cardiovascular Therapy*, vol. 13, no. 12, pp. 1345–1356, 2015.
- [47] Y. H. Lee and G. G. Song, "Diagnostic accuracy of dual-energy computed tomography in patients with gout: a meta-analysis," *Seminars in Arthritis and Rheumatism*, vol. 47, no. 1, pp. 95–101, 2017.

Research Article

One-Pot Aqueous Synthesis of Fluorescent Ag-In-Zn-S Quantum Dot/Polymer Bioconjugates for Multiplex Optical Bioimaging of Glioblastoma Cells

Alexandra A. P. Mansur,¹ Herman S. Mansur,¹
Sandhra M. Carvalho,^{1,2,3} and Anderson J. Caires¹

¹Center of Nanoscience, Nanotechnology and Innovation (CeNano²I), Federal University of Minas Gerais (UFMG), Belo Horizonte, MG, Brazil

²Department of Preventive Veterinary Medicine, Veterinary School, Federal University of Minas Gerais (UFMG), Belo Horizonte, MG, Brazil

³Department of Physiology and Biophysics, ICB, Federal University of Minas Gerais (UFMG), Belo Horizonte, MG, Brazil

Correspondence should be addressed to Herman S. Mansur; hmansur@demet.ufmg.br

Received 20 July 2017; Revised 4 September 2017; Accepted 13 September 2017; Published 13 November 2017

Academic Editor: Maria P. Morales

Copyright © 2017 Alexandra A. P. Mansur et al. This is an open access article distributed under the Creative Commons Attribution License, which permits unrestricted use, distribution, and reproduction in any medium, provided the original work is properly cited.

Cancer research has experienced astonishing advances recently, but cancer remains a major threat because it is one of the leading causes of death worldwide. Glioblastoma (GBM) is the most malignant brain tumor, where the early diagnosis is vital for longer survival. Thus, this study reports the synthesis of novel water-dispersible ternary AgInS₂ (AIS) and quaternary AgInS₂-ZnS (ZAIS) fluorescent quantum dots using carboxymethylcellulose (CMC) as ligand for multiplexed bioimaging of malignant glioma cells (U-87 MG). Firstly, AgInS₂ core was prepared using a one-pot aqueous synthesis stabilized by CMC at room temperature and physiological pH. Then, an outer layer of ZnS was grown and thermally annealed to improve their optical properties and split the emission range, leading to core-shell alloyed nanostructures. Their physicochemical and optical properties were characterized, demonstrating that luminescent monodispersed AIS and ZAIS QDs were produced with average sizes of 2.2 nm and 4.3 nm, respectively. Moreover, the results evidenced that they were cytocompatible using *in vitro* cell viability assays towards human embryonic kidney cell line (HEK 293T) and U-87 MG cells. These AIS and ZAIS successfully behaved as fluorescent nanoprobe (red and green, resp.) allowing multiplexed bioimaging and biolabeling of costained glioma cells using confocal microscopy.

1. Introduction

Despite indisputable progress in medicine in the recent decades, cancer remains as one of the most devastating diseases of the 21st century challenging scientists and professionals as the word “cancer” covers approximately 200 different types of disease [1–3]. In fact, it is far more likely that advances in science for early diagnosis will result in threatening more cancers as “manageable” chronic diseases with patients maintaining a relative satisfactory quality of life [4].

Brain tumors are the most common cancer occurring among children (age 0–14) and the leading cause of cancer-related deaths at that age, above leukemia statistics. Brain tumors are a diverse group of neoplasms that frequently carry

a poor prognosis for patients [5, 6]. Glioblastoma (GBM, World Health Organization grade IV glioma) is the most prevalent and lethal primary intrinsic brain tumor. Unlike other solid tumor cell types, GBM widely and aggressively invades the surrounding brain but hardly metastasizes to other organs [7, 8]. Despite tremendous efforts to develop diagnostic tools and therapeutic avenues, the accurate early detection and effective treatment of brain tumors remains a difficult challenge to be overcome in the field of neurooncology. Currently, the prognosis for GBM tumor is at the extreme worst with mortality greater than 90% at 5 years, with a median survival of 12.6 months [9–11].

Modern neuroimaging tools are being applied to diagnose and grade brain tumors preoperatively, to plan and

direct surgery intraoperatively, and to monitor and assess treatment response and estimating patient prognosis [12, 13]. Current research in brain tumor imaging attempts to develop, validate, and clinically implement advanced neuroimaging techniques that can benefit in the diagnosis and the detection of early treatment inefficiencies [12]. Imaging techniques including magnetic resonance imaging (MRI), computed tomography (CT), and positron-emission tomography (PET) are the most common modalities for brain tumor diagnosis, characterization, and intraoperative imaging. Other techniques such as fluorescence imaging have been developed for intraoperative fluorescence-guided tumor resection. These imaging modalities can aid in delineating the boundaries between neoplastic and normal tissue, helping doctors determine the most suitable sequence of treatment [9, 10]. Recently, theranostics, which is the combination of therapy and diagnosis, has become one of the primary keywords in cancer research, taking into account the fact that if cancer growth can be hampered during the diagnostic procedure, the subsequent cancer treatment would be facilitated because cancer growth is delayed or cancer burden is reduced [14].

To this end, nanotechnology offers a promising platform for the evolution of cancer molecular imaging strategies where nanomaterials can be used in the development of novel theranostic systems in oncology. Quantum dots (QDs) are being intensively studied as innovative class of nanoprobe for biomedical imaging because of their unique optical and electronic properties. Multiplexed molecular imaging relying on fluorescent QDs can reveal the temporal relationship among molecules by simultaneously staining several tumor biomarkers [6]. To overcome the obstacles of QDs for biomedical imaging, the physicochemical properties of QDs such as composition, size, shape, and surface characteristics associated with cytotoxicity have been comprehensively investigated [6, 15, 16]. However, despite the intense research in the realm of quantum dots for nanomedicine applications, the large majority of studies are based on Cd-containing semiconductor core (i.e., CdS, CdSe, and CdTe) synthesized using organometallic process at high temperature [17, 18]. For that reason, their potential toxicity has become a subject of serious discussion and debate, without a definitive conclusion yet. Some studies have demonstrated that Cd-based QDs can degrade in a biological environment, releasing highly cytotoxic Cd²⁺ ions [18, 19]. Therefore, over the past few years, a variety of Cd-free QDs have been produced from materials including zinc chalcogenides (i.e., ZnSe, ZnS), copper indium sulfide (CuInS₂), silver indium sulfide (AgInS₂, AIS), silver sulfide (Ag₂S), and core-shell nanostructures (AgInS₂-ZnS, ZAIS) [17, 19–21]. Importantly, some of these QDs share many of the advantages of commonly used Cd-based QDs regarding their optical properties and photoluminescence stability, surface biochemistry, and colloidal stability. Hence, QD-based probes that comply with the full set of requirements for biomedical applications can be used to target cancer molecules with high specificity [22–24]. Although ternary semiconductor QDs (e.g., Ag-In-S) have been already prepared in water medium for biomedical applications [19, 20, 25–28] no report was found in the consulted literature where they were directly synthesized using polysaccharide-based

biopolymers as surface capping ligands for *in vitro* imaging GBM cells.

Thus, in this study, a facile one-pot synthesis of novel Cd-free QDs based on AIS and ZAIS semiconductor nanocrystals produced by an eco-friendly aqueous process using carboxymethylcellulose simultaneously as stabilizing ligand and for surface biofunctionalization is presented. These colloidal nanoconjugates were cytocompatible and demonstrated fluorescent activity for effective multiplexed bioimaging of malignant glioma cells *in vitro*, as schematically depicted in Figure 1S (Graphical Abstract, Supplementary Material available online at <https://doi.org/10.1155/2017/3896107>). We endeavor that this research paves the way to develop new fluorescent biomarkers in nanomedicine for diagnosis, targeting and therapy of brain cancer tumors.

2. Materials and Methods

2.1. Materials. Zinc nitrate hydrate (Zn(NO₃)₂·6H₂O, >99%), indium nitrate hydrate (In(NO₃)₃·xH₂O, In = 28.5% wt), carboxymethylcellulose sodium salt (CMC, degree of substitution: 0.7; average molecular mass = 90,000 Da; medium viscosity: 180 cps, 4% in H₂O at 25°C), 3-(4,5-dimethylthiazol-2-yl) 2,5-diphenyltetrazolium bromide (MTT, >98%), Triton™ X-100, sodium dodecyl sulfate (SDS, ≥99.0%), paraformaldehyde (95%), and hydrochloric acid (HCl, 37%) were purchased from Sigma-Aldrich (USA). Silver nitrate (AgNO₃, 99.9%) and sodium sulfide hydrate (Na₂S·9H₂O, >98%) were purchased from Synth (Brazil). Dulbecco's Modified Eagle Medium (DMEM), fetal bovine serum (FBS), phosphate buffered saline (PBS), penicillin G sodium, streptomycin sulfate, and amphotericin-b were supplied by Gibco BRL (USA). Hydromount was purchased from Fisher Scientific Ltd. (UK). Human embryonic kidney (HEK 293T, American Type Culture Collection, ATCC® CRL-1573™) cells were kindly provided by Professor M.F Leite (Department of Physiology and Biophysics, UFMG). Malignant glioma (U-87 MG) cells were purchased from Rio de Janeiro Cell Bank (ATCC® HTB-14™).

Aforementioned chemicals were used without further purification, deionized water (DI water, Millipore Simplicity™) with a resistivity of 18 MΩ cm was used to prepare the solutions, and the procedures were performed at room temperature (RT, 23 ± 2°C), unless specified otherwise.

2.2. Synthesis of Quantum Dot Conjugates

2.2.1. Synthesis of AIS QDs (QD1 and QD2). CMC solution (1% w/v) was prepared by adding sodium carboxymethylcellulose powder (0.5 g) to a 50 mL of water and stirring at room temperature until complete solubilization occurred. AgInS₂ (QD1) conjugates were synthesized *via* an aqueous route at room temperature as follows: 2 mL of CMC solution and 48 mL of deionized water were added to a flask and the solution stabilized at physiological pH (7.5 ± 0.2). Under magnetic stirring, 0.33 mL of the silver precursor solution (AgNO₃, 1 × 10⁻³ mol·L⁻¹) and 1.33 mL of indium precursor solution (In(NO₃)₃·xH₂O, 1 × 10⁻³ mol·L⁻¹) were added to the flask and stirred for 1 min. This stoichiometry of Ag : In

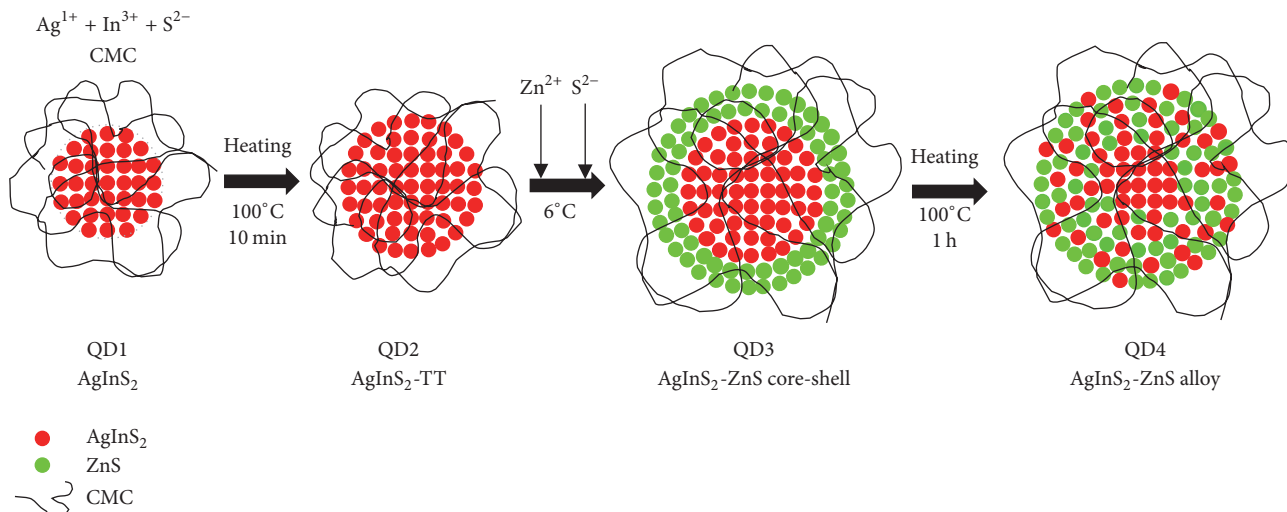


FIGURE 1: Procedure for fabrication Ag-In-S and Ag-In-Zn-S quantum dots.

molar ratio of 1 : 4 gives the most intense emission for AgInS₂ nanocrystals [20, 29, 30]. In the sequence, under vigorous stirring, 2.0 mL of sulfur solution precursor (Na₂S·9H₂O, 1×10^{-3} mol·L⁻¹) was dropped into the flask and stirred for 10 min.

In order to improve the optical properties of AgInS₂ cores (referred to as QD1 or AgInS₂), some procedures were taken in following sequence: (a) thermal treatment (TT) of AgInS₂ cores at $100 \pm 5^\circ\text{C}$ for 10 min to annealing/growth of AgInS₂ QDs (referred to as QD2 or AgInS₂-TT); (b) ZnS shell growth overlaying AgInS₂-TT cores (referred to as QD3 or AgInS₂-ZnS core-shell); and (c) thermal treatment of AgInS₂-ZnS core-shell structure at $100 \pm 5^\circ\text{C}$ for 60 min leading to alloying (referred to as QD4 or AgInS₂-ZnS alloy). Figure 1 summarizes the steps for the preparation of ZAIS QDs from AIS QDs that are described in Section 2.2.2.

2.2.2. Synthesis of ZAIS QDs (AgInS₂-ZnS, QD3, and QD4).

In this step, initially an “adlayer” of ZnS was grown onto AgInS₂-TT core reaching a core-shell nanostructure (AgInS₂-ZnS core-shell or QD3). Therefore, the previous AIS solution (QD2) was refrigerated at $6 \pm 2^\circ\text{C}$ for at least 6 h. Then, at $6 \pm 2^\circ\text{C}$ and under stirring, a 1.25 mL of zinc precursor (Zn(NO₃)₂·6H₂O, 1×10^{-3} mol·L⁻¹) was added dropwise (10 μL at each 10 s) into 50 mL of QD2 suspension followed by addition of 1.25 mL of sulfur precursor (Na₂S·9H₂O, 1×10^{-3} mol·L⁻¹) in the same way (dropwise, 10 μL at each 10 s) and stirred for 20 min. The resulting suspension (QD3, AgInS₂-ZnS) was reserved for 24 h at $6 \pm 2^\circ\text{C}$.

In the sequence, the QD3 suspension was heated for 1 h at $100 \pm 5^\circ\text{C}$ to allow interdiffusion of Zn²⁺ ions from shell into the core and annealing, leading to the formation of AgInS₂-ZnS alloys (QD4).

All of the QDs colloidal dispersions produced were stable, homogeneous, and light brown. The QD colloids were dialyzed for 24 h (with water changes after 2 h and 4 h) against 3 L of DI water using a Pur-A-Lyzer™ Mega Dialysis Kit (Sigma, cellulose membrane with molecular weight cut-off

filter, MWCO of 12,000 Da) under moderate stirring at room temperature. After purification, the QD dispersions were stored at RT until further use. Colloidal dispersions were concentrated using an Amicon® Ultra Filter (Millipore) with a 100,000 molecular mass (M_w) cut-off cellulose membrane.

2.3. Characterization of Quantum Dot Conjugates. Ultraviolet-visible (UV-vis) spectroscopy measurements were performed using Perkin-Elmer, Inc. (USA) equipment (Lambda EZ-210) in transmission mode with samples in a quartz cuvette over a wavelength range between 600 and 190 nm. All of the experiments were conducted in triplicate ($n = 3$) unless specifically noted, and the data were presented as the mean \pm standard deviation.

The photoluminescence spectroscopy (PL) of the conjugates was performed based on spectra acquired at RT using a violet diode laser module at 405 nm excitation wavelength (λ_{exc}) (150 mW, Roithner Laser Technik, Germany) coupled to a USB4000 VIS-NIR (visible-near infrared) spectrophotometer (Ocean Optics, Inc., USA). All of the tests were performed using a minimum of four repetitions ($n \geq 4$). Quantum yield (QY) was measured according to the procedure using Rhodamine 6G (Sigma, USA) in ethanol as the standard at $\lambda_{\text{exc}} = 405$ nm [31]. Additionally, QD colloidal media were placed inside a “darkroom-chamber” where they were illuminated by a UV (ultraviolet) radiation emission bulb ($\lambda_{\text{exc}} = 365$ nm, 6 W, Boitton Instruments). Digital color images were collected when the QDs fluoresced in the visible range of the spectra.

Morphological characterization of QD nanostructures was based on the images, electron diffraction patterns (ED), and energy-dispersive X-ray spectra (EDX) using Tecnai G2-20-FEI (FEI Company, USA) transmission electron microscope (TEM) at an accelerating voltage of 200 kV. In all of the TEM analyses, the samples were prepared by placing a drop of a dilute QD suspension onto carbon-coated copper grids (Electron Microscopy Sciences, USA) and allowing them to dry at room temperature overnight. The QD size

and size-distribution data were obtained based on the TEM images by measuring at least 150 randomly selected nanoparticles using image processing program (ImageJ, version 1.50, public domain, National Institutes of Health) [32].

X-ray diffraction (XRD) patterns were recorded using PANalytical (UK) Empyrean diffractometer (Cu-K α radiation with $\lambda = 1.5406 \text{ \AA}$). Measurements were performed in the 2θ range from 6 to 60° with steps of 0.017°. For the sample preparation, concentrated colloidal QD dispersions were placed onto glass slides and oven-dried at $40 \pm 1^\circ\text{C}$ for 12 h.

Dynamic light scattering (DLS) and zeta potential (ZP) analyses were performed using ZetaPlus instrument (Brookhaven Instruments Corporation, 35 mW red diode laser light, wavelength $\lambda = 660 \text{ nm}$) with a minimum of ten replicates. The ZP measurements were performed at $25 \pm 2^\circ\text{C}$ under the Smoluchowski approximation method with a minimum of ten replicates.

2.4. Biological Characterization of QD Conjugates. All of the biological tests were conducted according to ISO 10993-5:2009/(R)2014 (Biological evaluation of medical devices: tests for *in vitro* cytotoxicity) using kidney cell line of a human embryonic culture (HEK 293T) and malignant glioma cells (U-87 MG). HEK 293T (passage 18) and U-87 MG (passage 8) cells were cultured in DMEM with 10% FBS, penicillin G sodium (10 units mL^{-1}), streptomycin sulfate (10 mg mL^{-1}), and amphotericin-b (0.025 mg mL^{-1}) in a humidified atmosphere of 5% CO₂ at 37°C.

2.4.1. Evaluation of Cytotoxicity by MTT Cell Viability Assay. MTT (3-(4,5-dimethylthiazol-2yl) 2,5-diphenyl tetrazolium bromide) experiments were performed to evaluate the toxicity of QDs dispersions. HEK 293T and U-87 MG cells were plated (1×10^4 cells/well) in 96-well plates. Cell populations were synchronized in serum-free media for 24 h. After that, the media volume was suctioned and replaced with DMEM media containing 10% FBS for 24 h. The samples of QD1, QD2, QD3, and QD4 colloidal solutions were added to individual wells at final concentrations of $2.5 \text{ nmol}\cdot\text{L}^{-1}$ of QD nanoparticles ($\sim 1 \text{ mg mL}^{-1}$). For MTT assay, control samples were designed as follows: control group (cell culture with DMEM medium); positive control (1.0% v/v Triton™ X-100 in PBS); and negative control (chips of sterile polypropylene Eppendorf, 1 mg mL^{-1} , Eppendorf, Germany). After 24 h, all media were aspirated and replaced with $60 \mu\text{L}$ of culture media containing serum to each well and images of cells were acquired on an Leica DMIL LED (Germany) inverted microscope. Then $50 \mu\text{L}$ of MTT (5 mg mL^{-1}) was added to each well and incubated for 4 h in an oven at 37°C and 5% CO₂. Next, $40 \mu\text{L}$ SDS solution/4% HCl was placed in each well and incubated for 16 h in an oven at 37°C and 5% CO₂. Then, $100 \mu\text{L}$ was removed from each well and transferred to a 96-well plate. The absorbance was measured at 595 nm on iMark™ Microplate Absorbance Reader (Bio-Rad) with a 595 nm filter. Percentage cell viability was calculated according to (1). The values of the controls

(wells with cells and no samples) were set to 100% cell viability.

$$\text{Cell viability} = \frac{(\text{Absorbance of sample and cells})}{(\text{Absorbance of control})} \times 100\%. \quad (1)$$

2.4.2. Cellular Uptake of QD Conjugates by Laser Scanning Confocal Microscopy: Internalization, Kinetics, and Multiplexed Images. The evaluation of the QDs conjugates as fluorescent biological probes was performed using confocal laser scanning microscopy after exposing HEK 293T and U-87 MG cells to QD1 and QD4 samples. QD1 (AIS) with the lowest QY was chosen for cell imaging with two cell lines and cellular uptake kinetics to demonstrate the feasibility of using these QD conjugates for cell imaging due their unique optical emission properties. QD1 (AIS) and QD4 (ZAIS) were selected as the fluorescent species for spectrally multiplexed imaging of cells considering the detectable wavelength of PL emission. HEK 293T cells on passage 19 and U-87 MG cells on passage 9 were plated (5×10^5 cells per well) in 6-well plate. The cells were incubated for 4 days in 5% CO₂ at 37°C and synchronized for 24 h. Then, QD colloidal suspensions with the medium solution (DMEM with 10% FBS) were added to the cells and incubated in 5% CO₂ at 37°C from 30 min up to 120 min (in cellular uptake kinetics study), followed by washing with PBS. For evaluation of internalization and kinetics, QD1 was incubated at final concentration of $50 \text{ nmol}\cdot\text{L}^{-1}$ of QD nanoparticles. For costained multiplexed imaging, QD1 and QD4 were incubated separately at final concentration of $50 \text{ nmol}\cdot\text{L}^{-1}$ or QD1 and QD4 were incubated together, at the same concentration of each. In the sequence, the cells were fixed with paraformaldehyde (4%) for 30 min and washed three times with PBS, and cover slips were mounted with Hydromount. Images were obtained with a Zeiss LSM Meta 510 confocal microscope (Carl Zeiss, Germany) using the water immersion (objective 63x Plan-Apo/1.4 NA, Numerical Aperture). For green-emission, argon laser was used to excite at $\lambda_{\text{exc}} = 488 \text{ nm}$ and emission was collected at 505–550 nm. For red-emitting QD, excitation was at $\lambda_{\text{exc}} = 568 \text{ nm}$ and emission at LP 585 nm (LP = low pass). For the reference control, cells were incubated only with the original medium with 10% FBS (autofluorescence). Plot of intensity profiles and measurements of mean fluorescence intensity were performed using public domain image processing software (ImageJ software, version 1.50).

3. Results and Discussion

3.1. Characterization of Quantum Dot Conjugates. Here, carboxymethylcellulose was used as the ligand for stabilizing the ultra-small semiconductor nanocrystals in water media, which were characterized *in situ* by UV-vis spectroscopy. These QDs presented broad UV-vis absorption spectra with an onset at approximately 650 nm (Figure 2(a)). This relatively broad absorption edge has been reported in literature [27, 33, 34] for AIS and ZAIS nanoparticles, which was generally associated with size distribution of QD produced

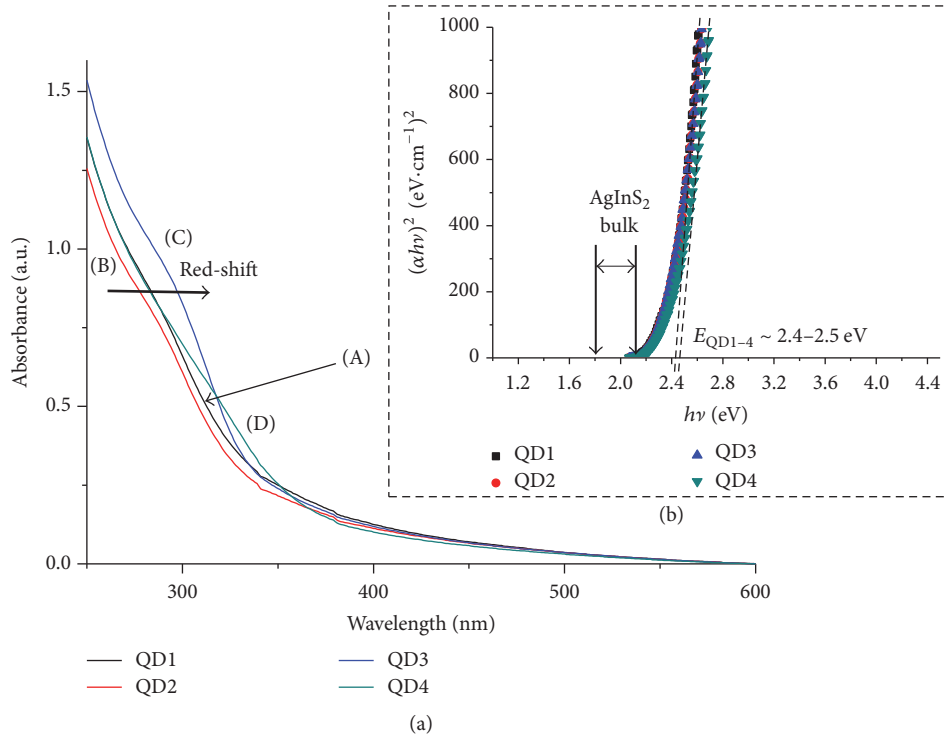


FIGURE 2: UV-vis absorption spectra (a) and optical absorption spectra (Tauc relation) (b) for QD1 (A), QD2 (B), QD3 (C), and QD4 (D).

[35, 36]. The arrow in Figure 2(a) shows the “red-shift” in the absorption spectra of QD2 after overcoating with the ZnS passivating shell (QD3). Such behavior is caused by the growth of the wider bandgap (ZnS, bulk band gap (E_g) = 3.61 eV [37]) semiconductor, which may be interpreted as a partial leakage of the exciton from the AgInS₂-core (h^+/e^- , holes/electrons) into the ZnS shell through the heterojunction [38].

Band gap values for the prepared QDs were extracted from the UV-vis absorbance curves using the “Tauc relation” (Figure 2(b)). AgInS₂ (AIS) is a direct bandgap semiconductor with E_g ranging from 1.8 eV (tetragonal) to 2.1 eV (orthorhombic) [27, 39]. The estimated E_{QD} (QD band gap) values were between 2.4 eV and 2.5 eV, which are larger than that of the bulk values ($E_g = 1.8-2.1$ eV) due to the quantum confinement effect.

In order to access the morphological features, the sizes, and the elemental composition of the QDs, TEM analysis coupled with EDX was performed. AgInS₂ core (AIS, QD1, Figure 3(a)) and quaternary alloyed AgInS₂-ZnS (ZAIS, QD4, Figure 3(b)) typical images revealed the formation of relatively monodispersed nanoparticles with reasonable spherical shape. The clear continuous lattice fringes obtained by electron diffraction in the HRTEM (high-resolution transmission electron microscopy) images demonstrated the single-crystalline nature of the QDs. The histograms of nanoparticle size distributions (Figures 3(c) and 3(d)) indicated the average size of 2.2 ± 0.4 nm and 4.3 ± 0.5 nm for QD1 and QD4, respectively. The observed increasing in diameter was expected by considering the growth of the ZnS shell over the nanocrystal core. EDX measurements

confirmed the presence of Ag, In, and S in ternary QD1 and the incorporation of Zn in the alloyed QD4 (Figures 3(e) and 3(f)). For QD1, EDX analysis indicated an average molar ratio of [Ag] : [In] = 1 : 4.3, which is in good agreement with the precursor molar ratio for metal cations [1 : 4].

The XRD pattern indicated three broadened and weak reflections in ternary core (QD1, Figure 4(b)) and quaternary alloyed (QD4, Figure 4(c)) samples, due to the small particle size, overlapped with the broad band present at $2\theta \sim 21.8^\circ$ (Figure 4(a)) that is characteristic of the CMC polymer used for the chemical stabilization of the QDs [40]. Based on reflection positions, the orthorhombic crystal phase was suggested for AgInS₂ nanoparticles. However, as reported in literature [27, 41], the occurrence of other AIS phases cannot be either ruled out or confirmed due to the large width of the reflections. It is clear that the diffraction peaks of ZAIS nanocrystals (QD4) were shifted to higher angles in comparison to AgInS₂ core (QD1) due to ZnS alloying with the reflections located between the corresponding peaks of the bulk orthorhombic AgInS₂ (International Centre for Diffraction Data, ICDD 25-1328) and cubic ZnS (ICDD 80-0020). Therefore, this feature confirmed that the QD4 (Figure 4(c)) formed an alloyed solid solution and not a mixture of AgInS₂ and ZnS nanoparticles [21, 42].

Typical room temperature PL spectra of the quantum dots and QY results of QD1 to QD4 are presented in Figure 5. The spectra (Figure 5(a)) indicated that luminescence is based on defect-activated sites, where no excitonic emission was observed. In addition, “Full Width at Half Maximum” (FWHM) was larger than 100 nm, which is consistent with

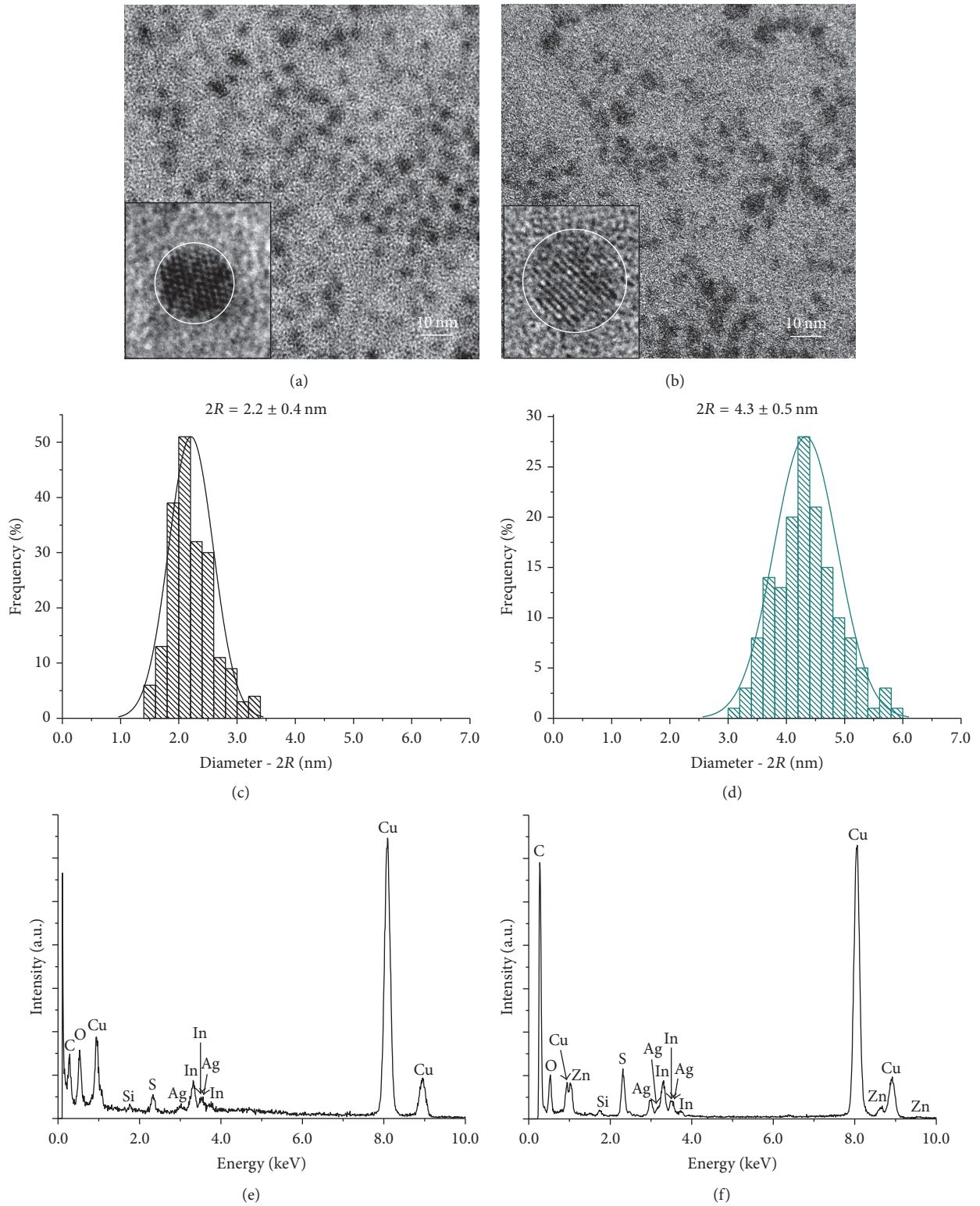


FIGURE 3: TEM image (inset: HRTEM picture) for QD1, AIS core (a) and QD4, ZAIS (b), histograms of size distribution for QD1 (c) and QD4 (d), and EDX spectra for QD1 (e) and QD4 (f).

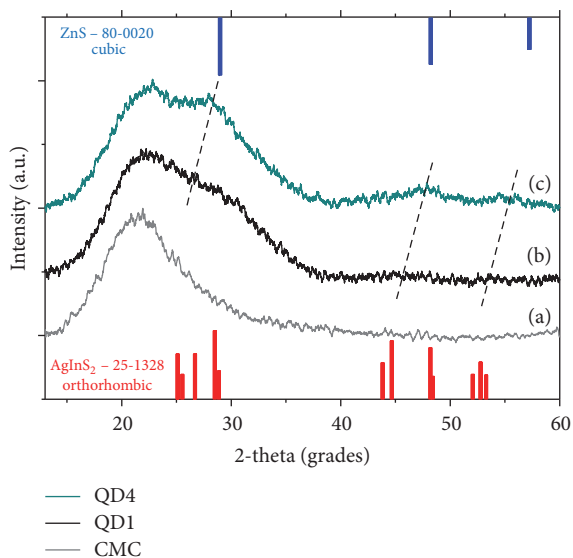


FIGURE 4: XRD patterns of CMC ligand (a), QD1 (AIS) (b), and QD4 (ZAIS) (c).

previous reports for Ag-In-S- and Zn-Ag-In-S semiconductor nanocrystals [43, 44].

According to the literature [29, 41] emissions of I-III-VI nanocrystals are dominated by radiative recombination related to intrinsic donor-acceptor defects due to the failure of aligned orientation between Ag and In, in addition to nonradiative pathways from surface defects due to the high surface to volume ratio of QDs. Thermal treatment (QD1 \rightarrow QD2) and shell growth (QD2 \rightarrow QD3) reduced the surface trap states that cause the nonradiative pathways increasing the radiative emissions, as could be clearly seen by the increase of the PL intensity (Figure 5(a)) and QY values (Figure 5(b)). Besides passivating dangling bonds on QD surface, ZnS adlayer also promoted a blue-shift of the emission spectrum. Finally, thermal treatment of core-shell structure (QD3 \rightarrow QD4) greatly improved photoluminescence intensity associated with interdiffusion of Zn ions into the AIS lattice upon alloying process and further annealing [20]. In this sense, the proposed strategy of improving optical properties of AgInS₂ by a sequence of steps was effective. Despite the relative low values of QY (*ca.* 0.2%–1.0%), which is commonly observed for QD produced in water medium at room temperature mostly due to the density of crystalline and surface defects, the drastic increase of approximately 200% and 400% after the formation of the core-shell nanostructure and after the alloying-annealing process, respectively, is remarkable.

Thus, it is important to highlight that, compared with previous reported studies [20, 27, 28], mostly based on heating up, hot injection, and organic processes, these AgInS₂ QDs were produced using a facile one-step synthesis in aqueous media based on carboxymethylcellulose as polymer stabilizer, which offer several advantages: (a) more reproducible; (b) low-cost; (c) environment friendly; (d) commercially availability and abundance; (e) biocompatibility for further biomedical applications. However, a facile and “green” mild process using aqueous medium for the

preparation of AgInS₂/polymer nanoconjugates with high luminescent properties (*i.e.*, PL quantum yield, QY > 40%) for augmenting bioimaging sensitivity is beyond the scope of the current study and remains a challenge for the future researches. Nonetheless, this is not a restriction, and QDs produced by aqueous processes with lower values of QY (*i.e.*, typically < 5%) have been successfully applied for numerous applications in bioimaging (*e.g.*, confocal microscopy, flow cytometry) [16, 24, 45].

For biological applications, it widely known that size, shape, composition, and surface chemistry of nanoparticles have important roles in the biological responses of cells, tissues, and organs. Nanoparticle surface charge was determined by zeta potential (ξ) measurements. The ξ -values for the synthesized nanoconjugates were between -43 mV and -46 mV, which indicated the predominance of negatively charged surface due to the carboxylic groups (R-COO⁻) of anionic CMC ligand at physiological pH ($pK_a \sim 4.3$) [46, 47]. In addition, the zeta potential (ξ -values) values lower than -40 mV indicated that the nanoparticles were electrostatically stabilized by the cellulose-modified polymer ligand as a colloidal nanoconjugate. The DLS technique was used to evaluate hydrodynamic sizes of the colloidal QDs in the medium. After the synthesis, in water medium at physiological pH, the sum of contribution of QD inorganic core with the CMC organic shell and its interactions with the surrounding medium resulted in a hydrodynamic diameter ranging from 38 nm to 48 nm. These results indicated that colloidal QD nanoconjugate suspensions contain individual nanoparticles electrostatically stabilized with negative surface charge.

In order to investigate the possible changes of surface charges and hydrodynamic sizes of QD1 and QD4 nanoconjugates immersed in the biological media for MTT and cellular uptake assays, ZP and DLS measurements were performed after 30 min of incubation (DMEM with 10% FBS). The DMEM contains inorganic salts, amino acids, vitamins, and D-glucose and is usually supplemented with FBS, which is a complex mixture (*i.e.*, growth factors, proteins, vitamins, trace elements, and hormones) important for the growth and maintenance of cells [48–50]. After incubation with DMEM (with 10% FBS), the average zeta potential measured for both systems decreased from *ca.* -45.0 mV to -5.0 mV and the hydrodynamic radius was reduced from *ca.* 40 nm to 20 nm. These changes are associated with the overall balance of the neutralization of CMC polymer surface charges by inorganic salts and interaction of QD polymeric shell with the biomolecules from DMEM and FBS. Thus, QDs in the medium of biological assays are not agglomerated and coated with an hybrid shell (CMC-biomolecules-ions) that stabilize the near neutral QD surfaces by steric hindrance at sizes of approximately 20 nm [51, 52].

3.2. Biological Characterization of QD Conjugates

3.2.1. Evaluation of Cytotoxicity by MTT Cell Viability Assay. The cytotoxicity of the heavy-metal free AIS (QD1 and QD2) and ZAIS (QD3 and QD4) nanoconjugates was assessed using the enzyme-based MTT. According to the study

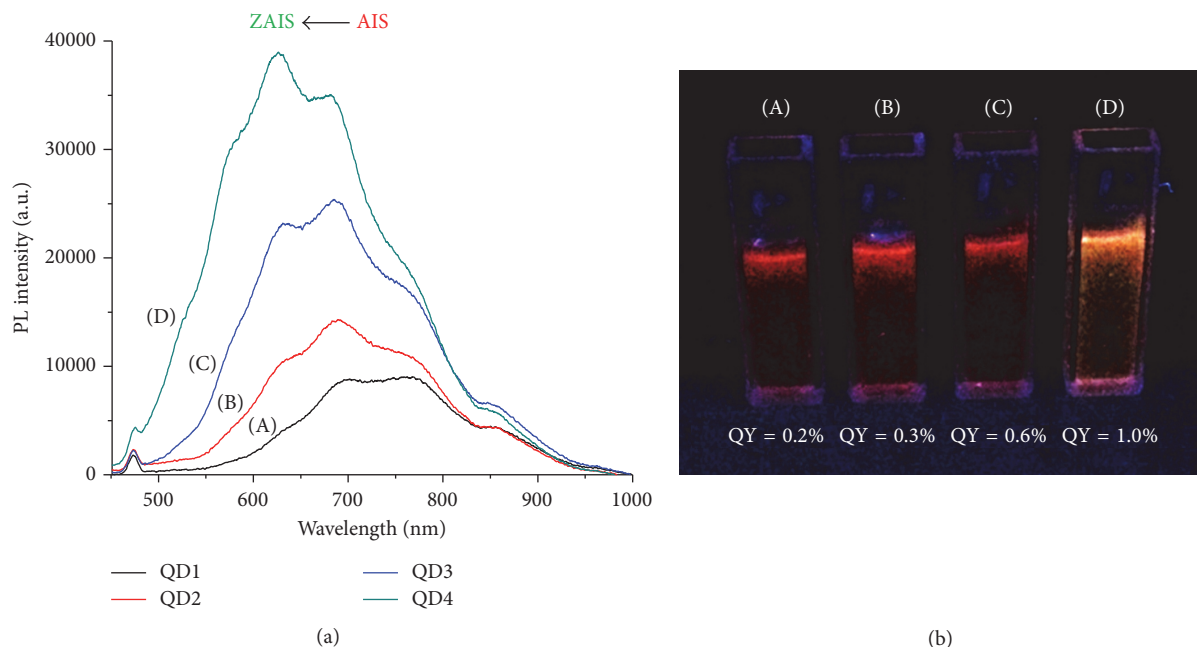


FIGURE 5: Photoluminescence spectra (a) and digital image of QD colloidal solutions excited by ultraviolet light ($\lambda_{\text{exc}} = 365 \text{ nm}$) and QY values (b) obtained from QD1 (A), QD2 (B), QD3 (C), and QD4 (D) nanoconjugates.

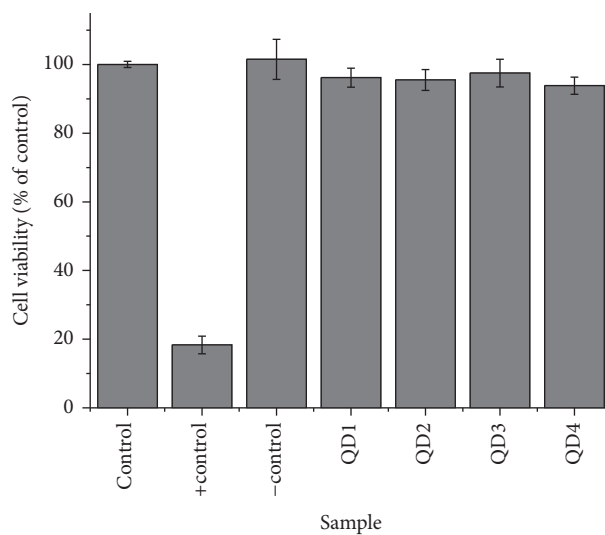
recently published [18], MTT assay has been the predominant assay for *in vitro* evaluation of nanomaterials for biomedical applications [53–55]. Two cell lines, HEK 293T and U-87 MG, were used in the experiments. HEK 293T is a permanent cell line established from primary embryonic human kidney that is widely used as cell model and is very useful for transfection experiments, as they have a higher transfection efficiency than other cell lines, making it a common choice of cultures for biological research. The U-87 MG cell line is human primary glioblastoma cell line that is commonly used for brain cancer research [56]. The choice of use malignant glioma cells is due to the high lethality of brain tumors and the limited treatment options currently available [57] that demands studies of novel nanomaterials for targeting, detection, and treatment of brain tumors at the same time, which will be helpful to the earliest diagnosis and prolong survivability for patients.

The results of HEK 293T (Figure 6(a)) and U-87 MG (Figure 7(a)) cell lines in contact with the quantum dot-CMC nanoconjugates demonstrated that no significant differences in the cell viability compared to the control were detected (within the statistical variation). All of the samples presented cell viability responses typically above 90%, indicating the nontoxicity of these bioconjugates. Even HEK 293T cells, which are more susceptible to be affected by the physicochemical characteristics of the nanoparticles due to the permeability of their membranes [58], presented cell viability higher than 94% at the concentration of nanoconjugates of 1.0 mg mL^{-1} after incubation for 24 h. Optical images of the cells before (Figure 6(b)) and after incubation with QD1 nanoconjugates are in agreement with MTT results presenting more than 90% of cell confluence for HEK 293T cells (Figure 6(c)) and above 80% for U-87 MG cells before

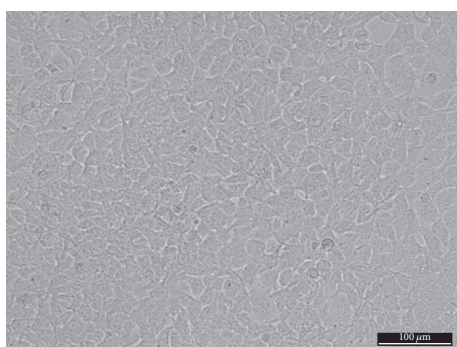
(Figure 7(b)) after (Figure 7(c)) incubation. Similar results of cell confluence were obtained for the other nanoconjugate samples in contact with HEK 293T and U-87 MG cells (Figures 2S and 3S, Supplementary Material). In addition, qualitative morphological evaluation of the cells after incubation for 24 h with QDs was performed in zoomed-in images of the cells (Figures 4S and 5S, Supplementary Material) according to the scoring system described in ISO 10933-5, where grade 0 corresponds to none reactivity and grade 4 corresponds to severe reactivity. The changes observed for all nanoconjugates and cell types under evaluation can be graded as 1 (Slight), which means “not more than 20% of the cells are round, loosely attached and without intracytoplasmic granules, or show changes in morphology; occasional lysed cells are present; only slight growth inhibition observable.” The evaluation of grade 1 of our samples is considered a noncytotoxic effect according to ISO 10933-5. Thus, these nanoconjugates designed and produced with Cd-free inorganic core (AIS and ZAIS) and directly stabilized with carboxymethylcellulose ligand *via* aqueous route at physiological pH hold promise for biomedical bioimaging and targeting of cancer cells. However, the *in vitro* MTT assay was specifically used to evaluate the mitochondrial function and cell viability as a preliminary quantitative assessment of the cytocompatibility towards these nanoconjugates and further studies are required before *in vivo* or clinical applications.

3.2.2. Cellular Uptake of QD Conjugates by Laser Scanning Confocal Microscopy

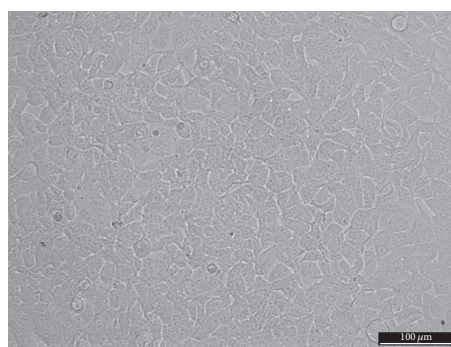
(1) *Cell Imaging and Kinetics of Cellular Uptake.* In this study, in order to demonstrate the unique optical properties of quantum dots as compared to conventional dyes, AIS



(a)



(b)



(c)

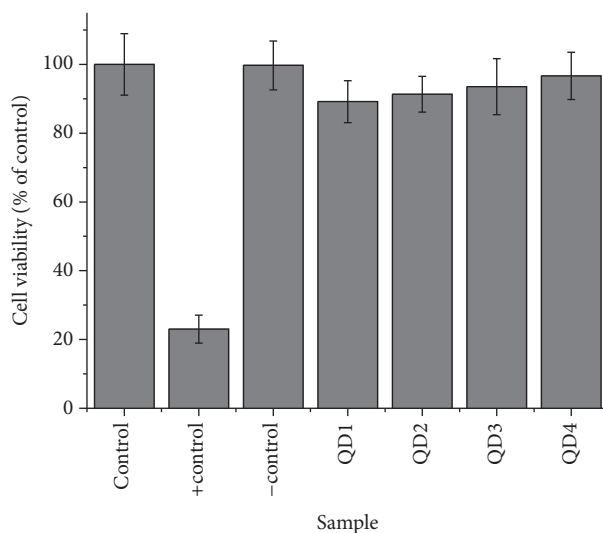
FIGURE 6: HEK 293T cell viability response by MTT assay after 24 h of incubation in direct contact with the QD nanoconjugate samples (a). HEK 293T cells images in control (b) and QD1 sample (c) (scale bar = 100 μm).

nanoparticles with low QY (QD1, AgInS_2 , QY = 0.2%) were used as biological biomarkers and for cellular uptake evaluation using confocal laser scanning microscopy performed after incubation with HEK 293T and U-87 MG cells.

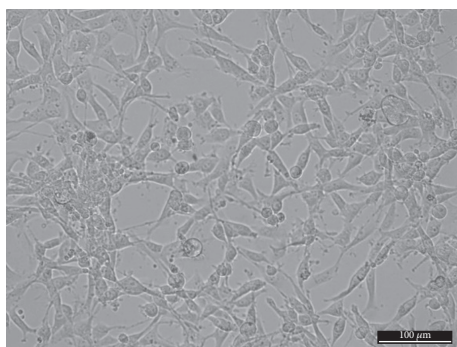
Distinct from AIS/ZAIS QDs reported in literature that required biological targeting vector and high quantum yield for allowing cellular imaging [20, 44], the novel AgInS_2 nanoconjugates developed in this study were effectively internalized by HEK 293T and U-87 MG cells, which showed clear PL red-emission after 30 min of incubation (Figure 8). For both cell lines, PL emission associated with cellular localization of AIS nanoconjugates was examined using intensity fluorescence profiles obtained using image process software (ImageJ, v1.50). Thirty minutes after cellular uptake of HEK 293T and U-87 MG cells, the distribution of AIS conjugates fluorescence emission was observed at cytosol with no obvious fluorescence in their nuclei (Detail I, Figure 8(a)) and no clear evidence of specific intracellular localization. In addition, despite the scattered red fluorescence in the cytoplasmic matrix, some high fluorescent areas were observed in the cytoplasm that may suggest the presence of vesicles filled with QDs (white arrows, Detail II, Figure 8(b)).

However, in order to prove this hypothesis, costaining vesicles components is necessary.

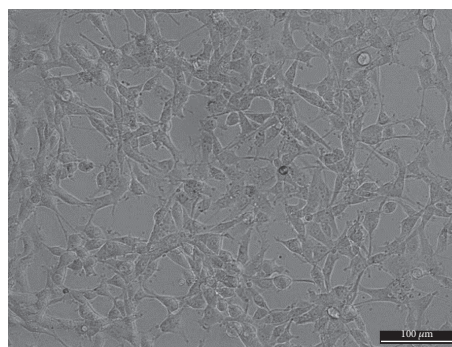
Also, the kinetics of cellular uptake of QD1 in glioblastoma cells (U-87 MG) were evaluated (Figure 9). Confocal fluorescent images (Figure 9(b)) were taken after 30 min, 60 min, and 120 min of incubation with the nanoconjugates and mean fluorescence intensity (MFI, Figure 9(c)) was calculated using image processing software (public domain, ImageJ, v1.5). A significant enhancement of the fluorescence intensities associated with the increase of incubation time from 30 min to 60 min (two-sample *t*-test, one tailed, with significance level (α) 0.025 at 29 degrees of freedom) was detected. It is demonstrated that these nanoparticulate systems not only effectively penetrated through cell membranes allowing biolabeling but also proved the continuing endocytosis by the cells with further intracellular scattered distribution within the cytoplasmic matrix after 60 min of contact of QD with cells. At 120 min of incubation, it was observed that the mean fluorescence intensity was not significantly distinct from the obtained at 60 min of incubation (two-sample *t*-test, one tailed, with significance level (α) 0.025 at 29 degrees of freedom), suggesting that the saturation stage



(a)



(b)



(c)

FIGURE 7: U-87 MG cell viability response by MTT assay after 24 h of incubation in direct contact with the QD nanoconjugate samples (a). U-87 MG cells images in control (b) and QD1 sample (c) (scale bar = 100 μm).

of intracellular uptake was reached [59]. In addition, for all evaluated incubation times, the cells demonstrate normal and clear morphology (Figure 9(a)).

(2) *Multiplexed Bioimaging.* The unique optical and electronic properties of quantum dots, such as high brightness, high chemical and photostability, continuous absorption, and relative narrow emission bandwidth, make them ideal choice as labels to develop fluorescent-based characterization techniques for detection and imaging cancer cells and tissues. In addition, QDs can be synthesized with distinct emission colors (i.e., multicolor nanoprobe *via* chemical composition and sizes) conjugated with functional biomolecules (e.g., antibodies and peptides) providing multiplexing capabilities to simultaneously identifying multiple biological targets of cancer cells and tissue for a myriad of applications in oncology [9, 10, 60–64]. In order to investigate the potential of the AIS (QD1) and the ZAIS (QD4) quantum dots for spectrally multiplexed imaging, the U-87 MG glioblastoma cells treated separately with these QDs were imaged by confocal microscopy and the fluorescent signals from the red-emitting (AIS) and the green-emitting (ZAIS) were resolved

by using spectrally matched filters (505/550 and LP 585). Based on the cell images depicted in Figure 10, the results demonstrated that the potential of using the 2-dimensional encoded QDs for spectrally multiplexed imaging and the images of cell costained with AIS + ZAIS (QD1 + QD4) is shown in Figure 11 that demonstrated the feasibility of combining these QDs for multiplexed bioimaging.

It is important to highlight that these results of multiplexed imaging by confocal microscopy relied on the exceptional optical properties of the water-soluble and cyto-compatible QD nanoconjugates (i.e., red-emitting, AIS, and green-emitting, ZAIS). This strategy can be transferred to other characterization techniques for cancer biomarker detection such as flow cytometry (FC), immunohistochemistry (IHC), immunohistofluorescence (IHF), image guided surgery, and steady state fluorescence [9, 10, 61–65]. Certainly, further studies are required to exploit the myriad of possibilities for producing cadmium-free QD nanoconjugates using aqueous processes with tunable PL properties (ranging from infrared to ultraviolet emission) *via* nanocrystal size and chemical composition, alloying and doping, core-shell nanostructures, processing routes, capping ligands, and

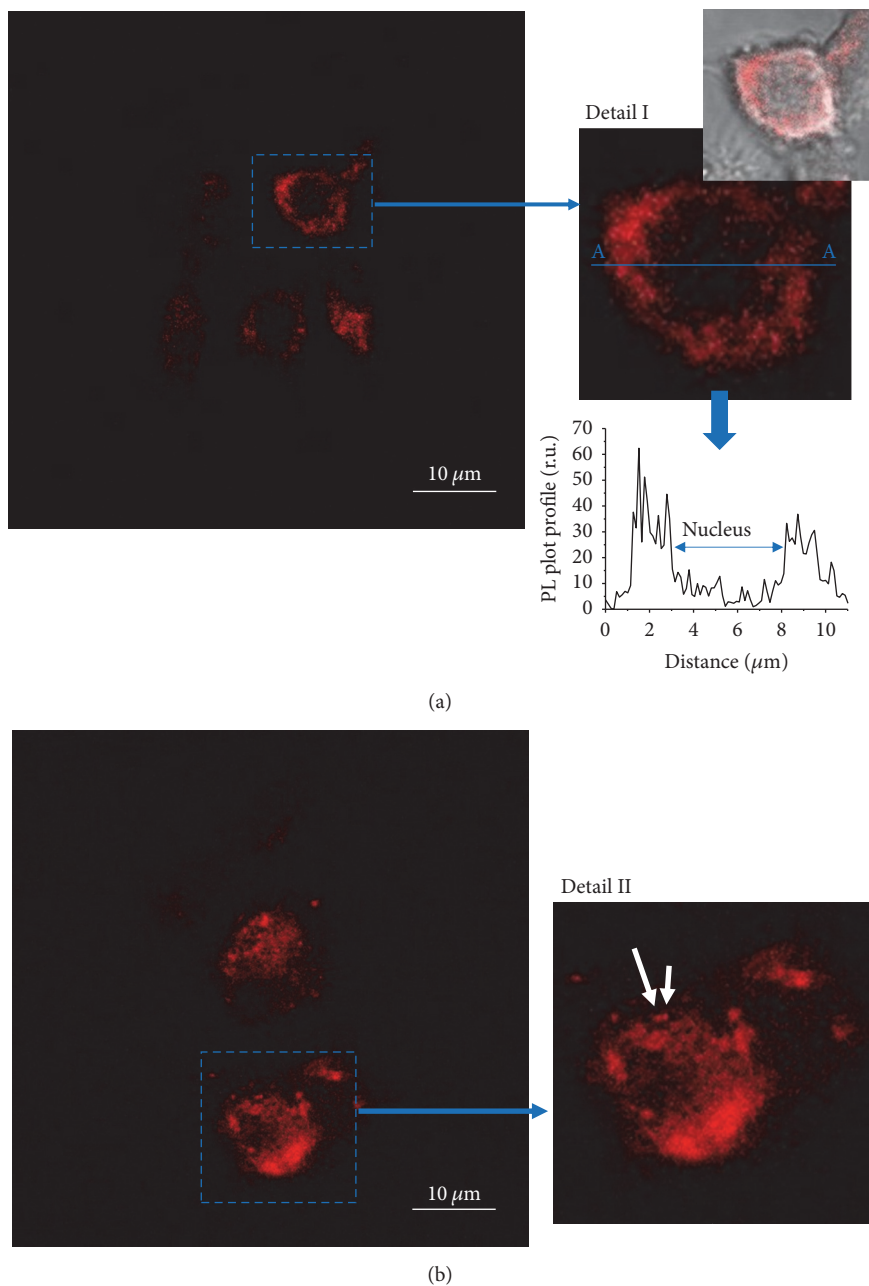


FIGURE 8: Confocal microscopy imaging of the cellular uptake of the AIS (QD1) nanoconjugates in the U-87 MG (a) and HEK 293T (b) cells. Detail I: intensity fluorescence profile along A-A line U-87 MG cell line indicating cellular localization of AIS nanoconjugates. Detail II: white arrows pointing out high fluorescent areas that may suggest the presence of vesicles filled with QDs.

others. To that end, a scenario could be envisioned for the future in which the use of multicolor QD-based fluorescent nanoconjugates could enhance the sensitivity, specificity, and multiplexing capabilities of molecular histopathology and early diagnosis of cancer for *in vitro*, *in vivo*, *ex vivo* applications. In particular, patients with glioblastoma (GBM), an extremely aggressive clinical phenotype of brain cancer, will undoubtedly benefit from the development of a new generation of diagnosis and therapies based on QD nanoconjugates with multiplexing technologies.

4. Conclusions

In this work a facile and eco-friendly method for synthesizing novel ternary AgInS_2 (AIS) and quaternary $\text{AgInS}_2\text{-ZnS}$ (ZAIS) fluorescent colloidal nanocrystals with carboxymethylcellulose (CMC) as capping ligand using a one-pot aqueous processing route at room temperature and physiological pH was developed. The formation of colloidal semiconductor solution was monitored *in situ* by UV-vis spectroscopy, where the initial blue-shift of spectrum indicated the production of stable AIS and the posterior

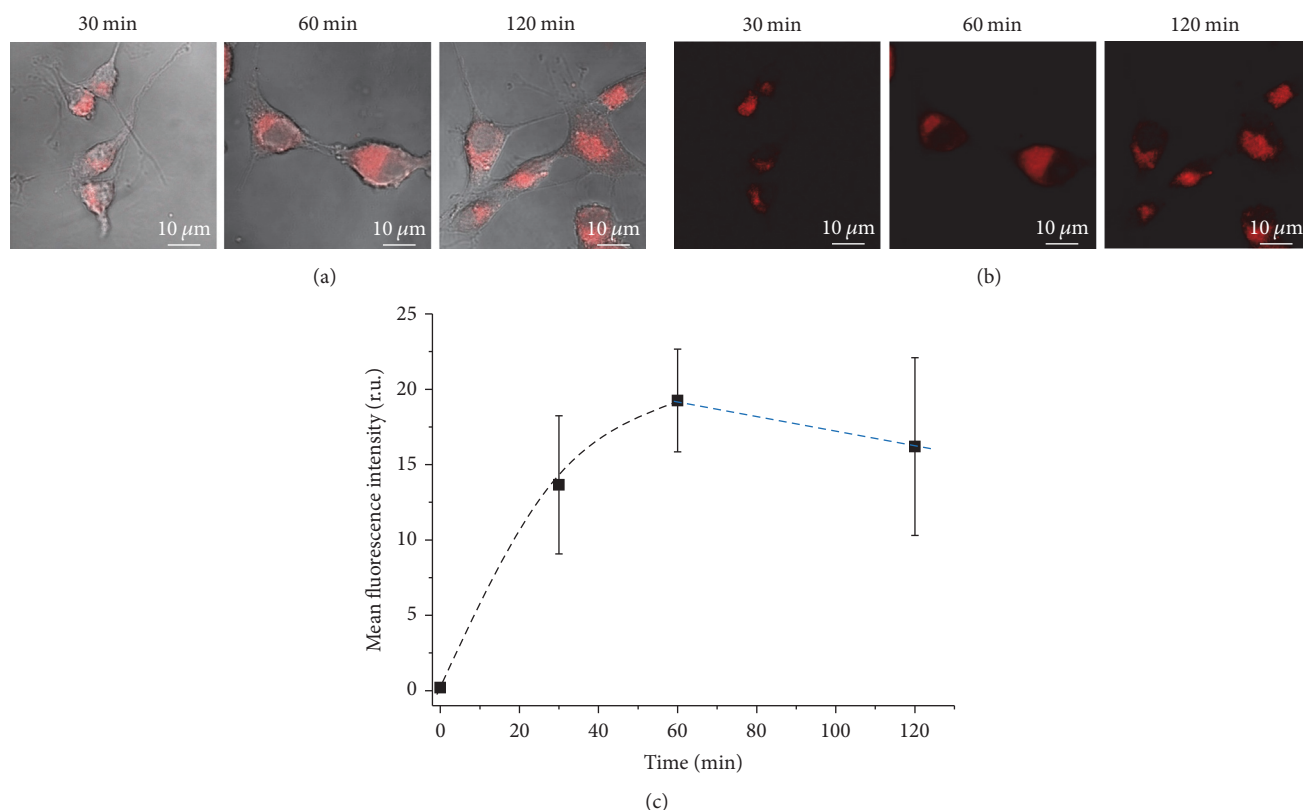


FIGURE 9: Confocal microscopy imaging of the cellular uptake of the AIS (QD1) nanoconjugates by U-87 MG cells *versus* incubation time (30 min, 60 min, and 120 min): PL + bright field image (a), PL image (b), and plot of MFI \times time (c).

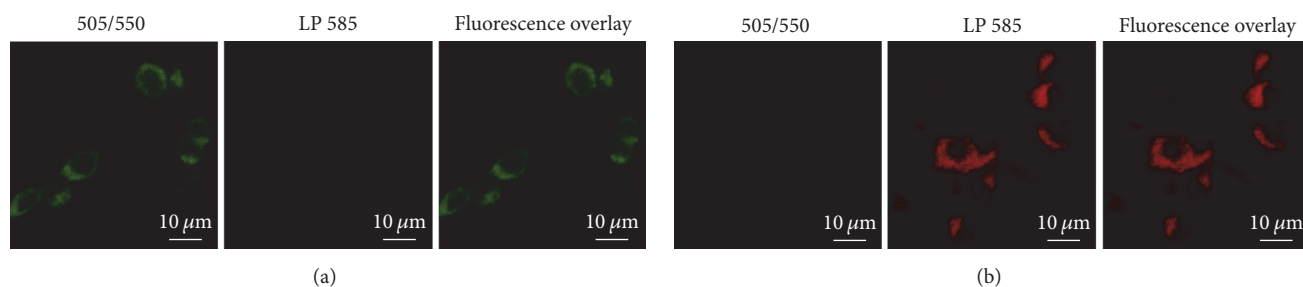


FIGURE 10: Fluorescence spectral imaging of U-87 MG cells separately treated for 30 min with green-emitting ZAIS (a) and red-emitting AIS (b) with PL emissions split by optical filters (green: 505/550 and red: LP 585) and overlaid PL image.

red-shift evidenced the growth of a ZnS layer resulting on the ZAIS core-shell nanostructures. TEM results indicated that monodispersed AIS and ZAIS QDs were produced with average sizes of 2.2 nm and 4.3 nm, respectively. In addition, these nanoconjugates showed surface charge determined by zeta potential measurements typically ranging from -43 mV to -46 mV and hydrodynamic diameter from 38 nm up to 48 nm assessed by the DLS method. These results indicated that colloidal QD nanoconjugates were electrostatically stabilized by negatively charged CMC polymer ligand (i.e., carboxylic groups, $R-COO^-$). Moreover, the MTT results evidenced that they were preliminarily cytocompatible using *in vitro* assay with HEK 293T and U-87 MG cells. Moreover,

these novel AIS and ZAIS QDs surface modified by CMC showed appropriate intracellular photoluminescence upon incubation with HEK 293T and U-87 MG cells, providing the effective function of cell bioimaging. Finally, these AIS and ZAIS QDs demonstrated red and green photoluminescent emissions, respectively, allowing effectively multiplexed bioimaging and biolabeling of costained glioma cells using confocal microscopy. Therefore, these bioconjugates offer promising nanoplatforams for potential *in vitro* and *in vivo* biomedical applications in multimodal bioimaging and targeting of cancer cells, opening a vast realm of possibilities to be explored in future researches.

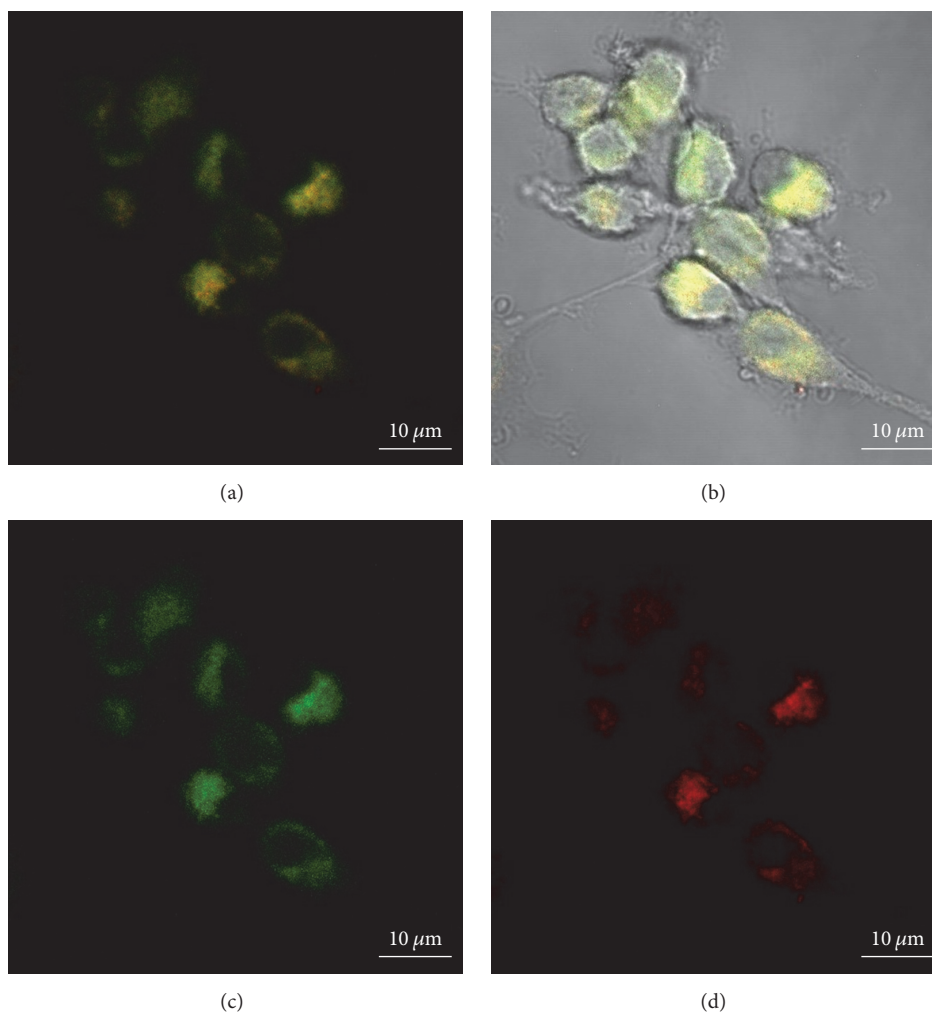


FIGURE 11: Multiplexed QD images of U-87 MG cells costained with AIS (QD1) + ZAIS (QD4): fluorescence overlay multicolor image (a); PL multicolor image overlaid with bright field image (b); PL image from filter 505/550 (green-emitting ZAIS) (c); and PL image from filter LP 585 (red-emitting AIS) (d).

Conflicts of Interest

The authors declare that there are no conflicts of interest regarding the publication of this article.

Acknowledgments

The authors acknowledge the financial support from the following Brazilian research agencies: CAPES (PROEX-433/2010; PNPd; PROINFRA2010–2014), FAPEMIG (PPM-00760-16; BCN-TEC 30030/12), CNPq (PQ1B–306306/2014-0; UNIVERSAL-457537/2014-0; PIBIC-2014/2015), and FIN-EP (CTINFRA-PROINFRA 2008/2010/2011). The authors express their gratitude to Professor Andréia Bicalho for the assistance with XRD analysis. Finally, the authors thank the staff at the Center of Nanoscience, Nanotechnology and Innovation (CeNano²I)/CEMUCASI/UFMG for the spectroscopy analyses.

References

- [1] K. Strebhardt and A. Ullrich, "Paul Ehrlich's magic bullet concept: 100 Years of progress," *Nature Reviews Cancer*, vol. 8, no. 6, pp. 473–480, 2008.
- [2] A. M. Scott, J. D. Wolchok, and L. J. Old, "Antibody therapy of cancer," *Nature Reviews Cancer*, vol. 12, no. 4, pp. 278–287, 2012.
- [3] H. Chen, W. Zhang, G. Zhu, J. Xie, and X. Chen, "Rethinking cancer nanotheranostics," *Nature Reviews Materials*, vol. 2, no. 7, p. 17024, 2017.
- [4] R. Weissleder and M. J. Pittet, "Imaging in the era of molecular oncology," *Nature*, vol. 452, no. 7187, pp. 580–589, 2008.
- [5] A. Jemal, F. Bray, M. M. Center, J. Ferlay, E. Ward, and D. Forman, "Global cancer statistics," *CA: A Cancer Journal for Clinicians*, vol. 61, no. 2, pp. 69–90, 2011.
- [6] M. Fang, C.-W. Peng, D.-W. Pang, and Y. Li, "Quantum dots for cancer research: current status, remaining issues, and future perspectives," *Cancer Biology & Medicine*, vol. 9, no. 3, pp. 151–163, 2012.

- [7] J. D. Lathia, S. C. Mack, E. E. Mulkearns-Hubert, C. L. L. Valentim, and J. N. Rich, "Cancer stem cells in glioblastoma," *Genes & Development*, vol. 29, no. 12, pp. 1203–1217, 2015.
- [8] H. Sontheimer, "Brain cancer: tumour cells on neighbourhood watch," *Nature*, vol. 528, no. 7580, pp. 49–50, 2015.
- [9] Y. Cheng, R. A. Morshed, B. Auffinger, A. L. Tobias, and M. S. Lesniak, "Multifunctional nanoparticles for brain tumor imaging and therapy," *Advanced Drug Delivery Reviews*, vol. 66, pp. 42–57, 2014.
- [10] W. Szopa, T. A. Burley, G. Kramer-Marek, and W. Kaspera, "Diagnostic and therapeutic biomarkers in glioblastoma: current status and future perspectives," *BioMed Research International*, vol. 2017, Article ID 8013575, 13 pages, 2017.
- [11] N. Kuthala, R. Vankayala, Y. Li, C. Chiang, and K. C. Hwang, "Engineering novel targeted boron-10-enriched theranostic nanomedicine to combat against murine brain tumors via mr imaging-guided boron neutron capture therapy," *Advanced Materials*, vol. 29, no. 31, Article ID 1700850, 2017.
- [12] M. C. Mabray, R. F. Barajas, and S. Cha, "Modern brain tumor imaging," *Brain Tumor Research and Treatment*, vol. 3, no. 1, pp. 8–23, 2015.
- [13] S. Cha, "Update on brain tumor imaging: from anatomy to physiology," *American Journal of Neuroradiology*, vol. 27, no. 3, pp. 475–487, 2006.
- [14] E.-K. Lim, T. Kim, S. Paik, S. Haam, Y.-M. Huh, and K. Lee, "Nanomaterials for theranostics: recent advances and future challenges," *Chemical Reviews*, vol. 115, no. 1, pp. 327–394, 2015.
- [15] Y. Wang and L. Chen, "Quantum dots, lighting up the research and development of nanomedicine," *Nanomedicine: Nanotechnology, Biology and Medicine*, vol. 7, no. 4, pp. 385–402, 2011.
- [16] H. Mansur, A. Mansur, S. Carvalho, Z. Lobato, M. I. Guedes, and M. d. Leite, "Surface biofunctionalized CdS and ZnS quantum dot nanoconjugates for nanomedicine and oncology: to be or not to be nanotoxic?" *International Journal of Nanomedicine*, vol. 11, pp. 4669–4690, 2016.
- [17] F. P. Ramanery, A. A. P. Mansur, and H. S. Mansur, "One-step colloidal synthesis of biocompatible water-soluble ZnS quantum dot/chitosan nanoconjugates," *Nanoscale Research Letters*, vol. 8, no. 1, pp. 1–13, 2013.
- [18] E. Oh, R. Liu, A. Nel et al., "Meta-analysis of cellular toxicity for cadmium-containing quantum dots," *Nature Nanotechnology*, vol. 11, no. 5, pp. 479–486, 2016.
- [19] G. Xu, S. Zeng, B. Zhang, M. T. Swihart, K.-T. Yong, and P. N. Prasad, "New generation cadmium-free quantum dots for biophotonics and nanomedicine," *Chemical Reviews*, vol. 116, no. 19, pp. 12234–12327, 2016.
- [20] M. D. Regulacio, K. Y. Win, S. L. Lo et al., "Aqueous synthesis of highly luminescent AgInS₂-ZnS quantum dots and their biological applications," *Nanoscale*, vol. 5, no. 6, pp. 2322–2327, 2013.
- [21] H. C. Yoon, J. H. Oh, M. Ko, H. Yoo, and Y. R. Do, "Synthesis and characterization of green Zn-Ag-In-S and red Zn-Cu-In-S quantum dots for ultrahigh color quality of down-converted white LEDs," *ACS Applied Materials & Interfaces*, vol. 7, no. 13, pp. 7342–7350, 2015.
- [22] H. S. Mansur, A. A. P. Mansur, A. Soriano-Araújo, and Z. I. P. Lobato, "Beyond biocompatibility: an approach for the synthesis of ZnS quantum dot-chitosan nano-immunoconjugates for cancer diagnosis," *Green Chemistry*, vol. 17, no. 3, pp. 1820–1830, 2015.
- [23] H. S. Mansur, A. A. P. Mansur, A. Soriano-Araújo, Z. I. P. Lobato, S. M. De Carvalho, and M. D. F. Leite, "Water-soluble nanoconjugates of quantum dot-chitosan-antibody for in vitro detection of cancer cells based on 'enzyme-free' fluoroimmunoassay," *Materials Science and Engineering: C*, vol. 52, pp. 61–71, 2015.
- [24] A. A. P. Mansur, H. S. Mansur, A. Soriano-Araújo, and Z. I. P. Lobato, "Fluorescent nano-hybrids based on quantum dot-chitosan-antibody as potential cancer biomarkers," *ACS Applied Materials & Interfaces*, vol. 6, no. 14, pp. 11403–11412, 2014.
- [25] W. Cai, D.-W. Shin, K. Chen et al., "Peptide-labeled near-infrared quantum dots for imaging tumor vasculature in living subjects," *Nano Letters*, vol. 6, no. 4, pp. 669–676, 2006.
- [26] W. Cai, K. Chen, Z.-B. Li, S. S. Gambhir, and X. Chen, "Dual-function probe for PET and near-infrared fluorescence imaging of tumor vasculature," *The Journal of Nuclear Medicine*, vol. 48, no. 11, pp. 1862–1870, 2007.
- [27] A. Raevskaya, V. Lesnyak, D. Haubold et al., "A fine size selection of brightly luminescent water-soluble Ag-In-S and Ag-In-S/ZnS quantum dots," *The Journal of Physical Chemistry C*, vol. 121, no. 16, pp. 9032–9042, 2017.
- [28] L. Borkovska, A. Romanyuk, V. Strelchuk et al., "Optical characterization of the AgInS₂ nanocrystals synthesized in aqueous media under stoichiometric conditions," *Materials Science in Semiconductor Processing*, vol. 37, pp. 135–142, 2015.
- [29] H. Zhong, Z. Bai, and B. Zou, "Tuning the luminescence properties of colloidal I–III–VI semiconductor nanocrystals for optoelectronics and biotechnology applications," *The Journal of Physical Chemistry Letters*, vol. 3, no. 21, pp. 3167–3175, 2012.
- [30] J. Y. Chang, G. Q. Wang, C. Y. Cheng, W. X. Lin, and J. C. Hsu, "Strategies for photoluminescence enhancement of AgInS₂ quantum dots and their application as bioimaging probes," *Journal of Materials Chemistry*, vol. 22, pp. 10609–10618, 2012.
- [31] D. F. Eaton, "Reference materials for fluorescence measurement," *Pure and Applied Chemistry*, vol. 60, no. 7, pp. 1107–1114, 1988.
- [32] C. A. Schneider, W. S. Rasband, and K. W. Eliceiri, "NIH Image to ImageJ: 25 years of image analysis," *Nature Methods*, vol. 9, no. 7, pp. 671–675, 2012.
- [33] T. Torimoto, T. Adachi, K.-I. Okazaki et al., "Facile synthesis of ZnS-AgInS₂ solid solution nanoparticles for a color-adjustable lumiphore," *Journal of the American Chemical Society*, vol. 129, no. 41, pp. 12388–12389, 2007.
- [34] J. Song, C. Ma, W. Zhang et al., "Bandgap and structure engineering via cation exchange: from binary Ag₂S to ternary AgInS₂, quaternary AgZnInS alloy and AgZnInS/ZnS core/shell fluorescent nanocrystals for bioimaging," *ACS Applied Materials & Interfaces*, vol. 8, no. 37, pp. 24826–24836, 2016.
- [35] A. E. Raevskaya, Y. V. Panasiuk, O. L. Stroyuk et al., "Spectral and luminescent properties of ZnO-SiO₂ core-shell nanoparticles with size-selected ZnO cores," *RSC Advances*, vol. 4, no. 108, pp. 63393–63401, 2014.
- [36] A. A. P. Mansur, F. P. Ramanery, L. C. Oliveira, and H. S. Mansur, "Carboxymethyl chitosan functionalization of Bi₂S₃ quantum dots: towards eco-friendly fluorescent core-shell nanoprobe," *Carbohydrate Polymers*, vol. 146, pp. 455–466, 2016.
- [37] K. Rajeshwar, N. R. De Tacconi, and C. R. Chenthamarakshan, "Semiconductor-based composite materials: preparation, properties, and performance," *Chemistry of Materials*, vol. 13, no. 9, pp. 2765–2782, 2001.
- [38] P. Reiss, M. Protière, and L. Li, "Core/shell semiconductor nanocrystals," *Small*, vol. 5, no. 2, pp. 154–168, 2009.

- [39] M. L. A. Aguilera, M. Ortega-López, V. M. Sánchez Resendiz, J. A. Hernández, and M. A. González Trujillo, "Some physical properties of chalcopyrite and orthorhombic AgInS₂ thin films prepared by spray pyrolysis," *Materials Science and Engineering: B*, vol. 102, no. 1-3, pp. 380–384, 2003.
- [40] V. Uskoković, "Composites comprising cholesterol and carboxymethyl cellulose," *Colloids and Surfaces B: Biointerfaces*, vol. 61, no. 2, pp. 250–261, 2008.
- [41] Y. J. Park, J. H. Oh, N. S. Han et al., "Photoluminescence of band gap states in AgInS₂ nanoparticles," *The Journal of Physical Chemistry C*, vol. 118, no. 44, pp. 25677–25683, 2014.
- [42] Y.-J. Yuan, D.-Q. Chen, M. Xiong et al., "Bandgap engineering of (AgIn)_xZn_{2(1-x)}S₂ quantum dot photosensitizers for photocatalytic H₂ generation," *Applied Catalysis B: Environmental*, vol. 204, pp. 58–66, 2017.
- [43] D. Deng, J. Cao, L. Qu, S. Achilefu, and Y. Gu, "Highly luminescent water-soluble quaternary Zn–Ag–In–S quantum dots for tumor cell-targeted imaging," *Physical Chemistry Chemical Physics*, vol. 15, no. 14, pp. 5078–5083, 2013.
- [44] J. Song, C. Ma, W. Zhang et al., "Tumor cell-targeted Zn₃In₂S₆ and Ag–Zn–In–S quantum dots for color adjustable luminophores," *Journal of Materials Chemistry B*, vol. 4, no. 48, pp. 7909–7918, 2016.
- [45] C. L. Salgado, A. A. P. Mansur, H. S. Mansur, and F. J. M. Monteiro, "Fluorescent bionanoprobes based on quantum dot-chitosan-O-phospho-l-serine conjugates for labeling human bone marrow stromal cells," *RSC Advances*, vol. 4, no. 90, pp. 49016–49027, 2014.
- [46] Y. Gong and D. Zhao, "In situ immobilization of mercury in water, soil, and sediment using carboxymethyl cellulose stabilized iron sulfide nanoparticles," in *Novel Solutions to Water Pollution*, vol. 1123 of *ACS Symposium Series*, pp. 61–77, American Chemical Society, Washington, DC, USA, 2013.
- [47] A. A. P. Mansur, F. G. de Carvalho, R. L. Mansur, S. M. Carvalho, L. C. de Oliveira, and H. S. Mansur, "Carboxymethyl-cellulose/ZnCdS fluorescent quantum dot nanoconjugates for cancer cell bioimaging," *International Journal of Biological Macromolecules*, vol. 96, pp. 675–686, 2017.
- [48] R. Dulbecco and G. Freeman, "Plaque production by the polyoma virus," *Virology*, vol. 8, no. 3, pp. 396–397, 1959.
- [49] J. van der Valk, D. Brunner, K. De Smet et al., "Optimization of chemically defined cell culture media—replacing fetal bovine serum in mammalian in vitro methods," *Toxicology in Vitro*, vol. 24, no. 4, pp. 1053–1063, 2010.
- [50] G. Gstraunthaler, "Alternatives to the use of fetal bovine serum: serum-free cell culture," *ALTEX: Alternativen zu Tierexperimenten*, vol. 20, no. 4, pp. 275–281, 2003.
- [51] N. Oh and J.-H. Park, "Endocytosis and exocytosis of nanoparticles in mammalian cells," *International Journal of Nanomedicine*, vol. 9, no. 1, pp. 51–63, 2014.
- [52] A. Albanese and W. C. W. Chan, "Effect of gold nanoparticle aggregation on cell uptake and toxicity," *ACS Nano*, vol. 5, no. 7, pp. 5478–5489, 2011.
- [53] S. Sharifi, S. Behzadi, S. Laurent, M. Laird Forrest, P. Stroeve, and M. Mahmoudi, "Toxicity of nanomaterials," *Chemical Society Reviews*, vol. 41, no. 6, pp. 2323–2343, 2012.
- [54] W. Jiang, B. Y. S. Kim, J. T. Rutka, and W. C. W. Chan, "Nanoparticle-mediated cellular response is size-dependent," *Nature Nanotechnology*, vol. 3, no. 3, pp. 145–150, 2008.
- [55] K. M. Tsoi, Q. Dai, B. A. Alman, and W. C. W. Chan, "Are quantum dots toxic? Exploring the discrepancy between cell culture and animal studies," *Accounts of Chemical Research*, vol. 46, no. 3, pp. 662–671, 2013.
- [56] M. Allen, M. Bjerke, H. Edlund, S. Nelander, and B. Westermarck, "Origin of the U87MG glioma cell line: good news and bad news," *Science Translational Medicine*, vol. 8, no. 354, Article ID 354re3, 2016.
- [57] J. L. Sowers, K. M. Johnson, C. Conrad, J. T. Patterson, and L. C. Sowers, "The role of inflammation in brain cancer," in *Inflammation and Cancer—Advances in Experimental Medicine and Biology*, vol. 816, Springer, Basel, Swiss, 2014.
- [58] S. Vaidyanathan, B. G. Orr, and M. M. Banaszak Holl, "Detergent induction of HEK 293A cell membrane permeability measured under quiescent and superfusion conditions using whole cell patch clamp," *The Journal of Physical Chemistry B*, vol. 118, no. 8, pp. 2112–2123, 2014.
- [59] L. Damalakiene, V. Karabanovas, S. Bagdonas, M. Valius, and R. Rotomskis, "Intracellular distribution of nontargeted quantum dots after natural uptake and microinjection," *International Journal of Nanomedicine*, vol. 8, pp. 555–568, 2013.
- [60] B. Zhang, C. Yang, Y. Gao et al., "Engineering quantum dots with different emission wavelengths and specific fluorescence lifetimes for spectrally and temporally multiplexed imaging of cells," *Nanotheranostics*, vol. 1, no. 1, pp. 131–140, 2017.
- [61] Y. Xing, Q. Chaudry, C. Shen et al., "Bioconjugated quantum dots for multiplexed and quantitative immunohistochemistry," *Nature Protocols*, vol. 2, no. 5, pp. 1152–1165, 2007.
- [62] F. T. Lee-Montiel, P. Li, and P. I. Imoukhuede, "Quantum dot multiplexing for the profiling of cellular receptors," *Nanoscale*, vol. 7, no. 44, pp. 18504–18514, 2015.
- [63] H. Xu, J. Xu, X. Wang, D. Wu, Z. G. Chen, and A. Y. Wang, "Quantum dot-based, quantitative, and multiplexed assay for tissue staining," *ACS Applied Materials Interfaces*, vol. 5, no. 8, pp. 2901–2907, 2013.
- [64] Q. T. Nguyen and R. Y. Tsien, "Fluorescence-guided surgery with live molecular navigation—a new cutting edge," *Nature Reviews Cancer*, vol. 13, no. 9, pp. 653–662, 2013.
- [65] A. Madhankumar, O. D. Mrowczynski, S. R. Patel et al., "Interleukin-13 conjugated quantum dots for identification of glioma initiating cells and their extracellular vesicles," *Acta Biomaterialia*, vol. 58, pp. 205–213, 2017.